TECHNISCHE UNIVERSITÄT DARMSTADT

The electron-gamma coincidence set-up at the S-DALINAC

vom Fachbereich Physik
der Technischen Universität Darmstadt

zur Erlangung des Grades
Doctor rerum naturalium
(Dr. rer. nat.)

genehmigte Dissertation
von Gerhart Steinhilber

Erstgutachter: Prof. Dr. Dr. h.c. mult. Norbert Pietralla
Zweitgutachter: Prof. Dr. Joachim Enders

Darmstadt 2022

Gerhart Steinhilber: The electron-gamma coincidence set-up at the S-DALINAC
Darmstadt, Technische Universität Darmstadt
Jahr der Veröffentlichung der Dissertation auf TUprints: 2023
URN: urn:nbn:de:tuda-tuprints-229937
Tag der mündlichen Prüfung: 06.07.2022

Veröffentlichung unter CC BY-SA 4.0 International
http://creativecommons.org/licenses/by-sa/4.0/

Erklärung laut Promotionsordnung

§8 Abs. 1 lit. c PromO

Ich versichere hiermit, dass die elektronische Version meiner Dissertation mit der schriftlichen Version übereinstimmt.

§8 Abs. 1 lit. d PromO

Ich versichere hiermit, dass zu einem vorherigen Zeitpunkt noch keine Promotion versucht wurde. In diesem Fall sind nähere Angaben über Zeitpunkt, Hochschule, Dissertationsthema und Ergebnis dieses Versuchs mitzuteilen.

§9 Abs. 1 PromO

Ich versichere hiermit, dass die vorliegende Dissertation selbstständig und nur unter Verwendung der angegebenen Quellen verfasst wurde.

§9 Abs. 2 PromO

Die Arbeit hat bisher noch nicht zu Prüfungszwecken gedient.

Darmstadt, den 07.06.2022

_____

Gerhart Steinhilber

Abstract

This work describes the development, construction and commissioning of a new setup for (e,e'γ)-coincidence measurements at the superconducting Darmstadt linear accelerator S-DALINAC. (e,e'γ) reactions are characterized by the pure electromagnetic interaction in the excitation and in the decay channels and thereby allow nuclear physics investigations with high precision. In contrast to inclusive electron scattering, this measurement method is directly sensitive to the interference of longitudinal and transverse form factors, which affects the angular distribution of the emitted photons.

To establish the new (e,e'γ) setup, the existing large acceptance QCLAM electron spectrometer was combined with a new setup consisting of $LaBr_3$:Ce detectors. For the readout of the γ-ray detectors, a new data acquisition system was developed and combined with the existing QCLAM data acquisition system to form a coincidence data acquisition. A software package for data analysis was developed.

In the first commissioning experiment on the 2_1^+ and 1_2^+ states of ^{12}C, the functionality of the (e,e'γ)-setup could be demonstrated. Findings from this and from a second commissioning experiment on ^{96}Ru, together with GEANT4 simulations, were used to optimize the setup with a particular focus on the reduction of background radiation in the γ-ray detectors. The full and optimized setup was used in a first production run on a ^{96}Ru target to measure the γ-decay behavior below and above the neutron separation threshold. Isolated states were observed to decay via the 2_1^+ state of ^{96}Ru. Above the neutron separation threshold, ^{96}Ru decays by emission of a neutron to ^{95}Ru. Depopulations of the low-lying states of ^{95}Ru were observed.

Zusammenfassung

Diese Arbeit beschreibt die Entwicklung, Konstruktion und Inbetriebnahme eines neuen Messsystems für (e,e'γ)-Koinzidenzmessungen am supraleitenden Elektronenlinear-beschleuniger S-DALINAC. (e,e'γ)-Reaktionen zeichnen sich durch eine rein elektromagnetische Wechselwirkung sowohl im Anregungs- als auch im Zerfallskanal aus und ermöglichen kernphysikalische Untersuchungen mit hoher Präzision. Zudem ist die Messmethode, im Gegensatz zur inklusiven Elektronenstreuung, durch Messung der Winkelverteilung der γ-Strahlung auf die Interferenz der longitudinalen und transversalen Formfaktoren sensitiv.

Für das neue Messsystem wurde das bestehende QCLAM Elektronenspektrometer, welches sich durch eine große Raumwinkelakzeptanz auszeichnet, mit einem neuen Aufbau bestehend aus $LaBr_3$:Ce Detektoren kombiniert. Zum Auslesen der Detektoren wurde ein neues Datenaufnahmesystem entwickelt, welches für (e,e'γ)-Koinzidenzmessungen mit dem QCLAM Datenaufnahmesystem zu einem Koinzidenzdatenaufnahmesystem kombiniert wurde. Für die Auswertung der gemessenen Daten wurde ein Softwarepaket entwickelt.

Im ersten Kommissionierungsexperiment an den 2_1^+ und 1_2^+ Zuständen von ^{12}C konnte die Funktionsweise des (e,e'γ)-Aufbaus demonstriert werden. Erkenntnisse aus dem ersten Kommissionierungsexperiment und einem weiteren Experiment an ^{96}Ru ermöglichten zusammen mit GEANT4-Simulationen die Optimierung des Experimentieraufbaus mit besonderem Fokus auf der Reduktion der Untergrundstrahlung in den γ-Detektoren. Der vollständige und optimierte Aufbau wurde in einem ersten Produktionsexperiment an einem ^{96}Ru Target zur Messung des γ-Zerfallsverhaltens unterhalb und oberhalb der Neutronenseparationsschwelle verwendet. Es wurden isolierte Zustände beobachtet, die über den 2_1^+ Zustand von ^{96}Ru zerfallen. Oberhalb der Neutronenseparationsschwelle zerfällt ^{96}Ru durch Emission eines Neutrons zu ^{95}Ru, dessen Depopulationen über die niedrig liegenden angeregten Zustände beobachtet wurde.

Content

1. Introduction

Since its introduction over 60 years ago, electron scattering [1] has become an important and well established tool to investigate nuclear structure. Ultra-relativistic electrons with a momentum of 100 MeV/c, as in typical electron scattering experiments, have a de Broglie wavelength [2] of 2 fm, which is in the order of the radius of nuclei. The radius of a nucleus with mass number A is approximately described by $1.2\,\mathrm{fm} \cdot A^{1/3}$ [3]. Hence, electron scattering can resolve the structure of nuclei.

In inclusive (e,e') electron scattering experiments, cross sections, which are a measure of the probability for an interaction of an electron with a nucleus, are measured. Cross sections contain information about the structure of the nucleus, which is accessible via a comparison of the experimentally determined differential cross sections $d\sigma_{exp}/d\Omega$ with the differential cross section of a theoretically calculated point-like and infinitely massive nucleus $d\sigma_{point}/d\Omega$ as shown in Equation (1.1).

$$\frac{d\sigma_{\mathrm{exp}}}{d\Omega} = \frac{d\sigma_{\mathrm{point}}}{d\Omega} R(E_x, q) \tag{1.1}$$

Ω is the solid angle in which electrons are detected, R denotes the nuclear response which depends on the excitation energy E_x, and the momentum transfer q, of the electron to the nucleus. R is a linear combination of the longitudinal and transverse form factors F_L and F_T, which contain the nuclear (electromagnetic) structure information. The terms longitudinal and transverse refer to the components of the virtual photons involved in the scattering process. Elastic scattering processes ($E_x = 0$) allow the investigation of the properties of ground states such as absolute charge radius measurements. For a spinless nucleus, $R(E_x = 0, q) = |F_L(q)|^2$ and F_L represents the Fourier transformed charge distribution of the ground state. If the nucleus is excited ($E_x > 0$) during the scattering process, it is called inelastic scattering and both form factors need to be considered. Form factors describe the variation of the excitation strength of a state as a function of the momentum transfer [3,4]. As an example, the form factor of the 1_2^+ state of energy 15.1 MeV of ^{12}C is shown in Figure 1. It shows the typical shape of a form factor of an M1 transition, which becomes zero for $q \to 0$. For elastic scattering processes, the minima give information about the size of the nucleus, assuming a sphere with a diffuse edge.

An advantage of using electrons for scattering experiments is their purely electromagnetic interaction through the exchange of virtual photons, which is described with high accuracy within the framework of quantum electrodynamics (QED). Since the electromagnetic interaction is relatively weak, measurements can be performed on atomic nuclei without greatly disturbing their structure and multiple scattering processes are reduced to an almost negligible level [5]. For achievable luminosities, the interaction is strong enough to obtain sufficiently high count rates in measurements. Aside from electron scattering, there are other methods to study atomic nuclei with electromagnetic probes such as photonuclear reactions [6] and Coulomb excitation by heavy charged particles [7].

Nuclear investigations by real photons of momentum ω can, in contrast to electron scattering, only be performed at the photon point ($E_x = \omega$) since photons are massless. Due to their transverse polarization, real photons can only interact transversely with nuclei, thus monopole excitations cannot be excited by real photons. Also, higher multipoles than E2/M1

are hardly excited by photons. Electrons are not restricted by these limitations and are capable of exciting higher multipoles [3].

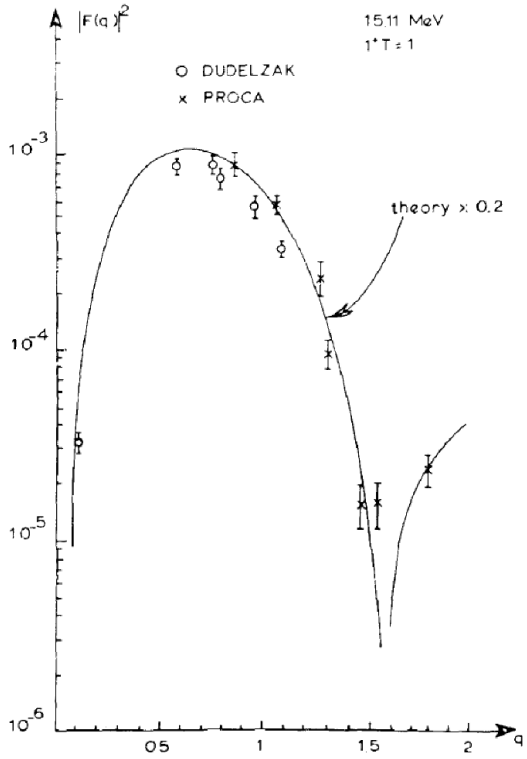

Figure 1: The form factor of the 1_2^+ state at 15.11 MeV of ^{12}C as a function of momentum transfer in the units of fm^{-1} measured in inelastic electron scattering is shown. Reprinted from [8]. Copyright 2022, with permission from Elsevier.

Coulomb excitations of nuclei induced by the electric field of ion beams are limited in kinetic energy by the height of the Coulomb barrier to reduce the effects of nuclear forces. In electron scattering, the maximum kinetic energy of electrons should not exceed 500 MeV to prevent complications from meson production [3]. Coulomb excitations were considered practically incapable of magnetic excitations [9]. With the development of the measurement method of relativistic Coulomb excitation, magnetic excitations can also be studied in Coulomb excitation [10]. Electrons are suitable for excitation of these transitions as well [11,12].

Inclusive electron scattering is an established method to study phenomena of isolated bound states of stable spin zero nuclei, which are excited by a single multipole using electromagnetic probes. A few unstable isotopes, ^3H [13], ^{14}C [14], and ^{41}Ca [15], have been studied in electron scattering, as this requires that the isotopes live long enough to produce a target out of them. An alternative to this approach, which can be used in the future to study the properties of short-lived isotopes, is the use of technological developments such as electron-ion colliders installed at radioactive beam facilities [4,16].

Exclusive (e,e'x) electron scattering experiments are a way to expand the potential of inclusive electron measurements and allowing for investigation of a large set of phenomena. Figure 2 schematically illustrates the measurement methods for inclusive and exclusive electron scattering. In contrast to inclusive electron scattering experiments, in coincidence experiments

the particle x (e.g. neutrons, protons, alpha particles, ...) emitted during the equilibration process of the excited nucleus is detected in a secondary detector in addition to the scattered electron. This makes it possible to study excitation and decay [17].

By measuring the angular distributions of the particles x, multipole strengths can be determined model independently [17]. An example of this type of coincidence experiment is the study of the strongly mixed E0-, E1-, and E2-multipole strengths in ^{40}Ca, which was studied using an ^{40}Ca(e,e'p)^{39}K reaction [18].

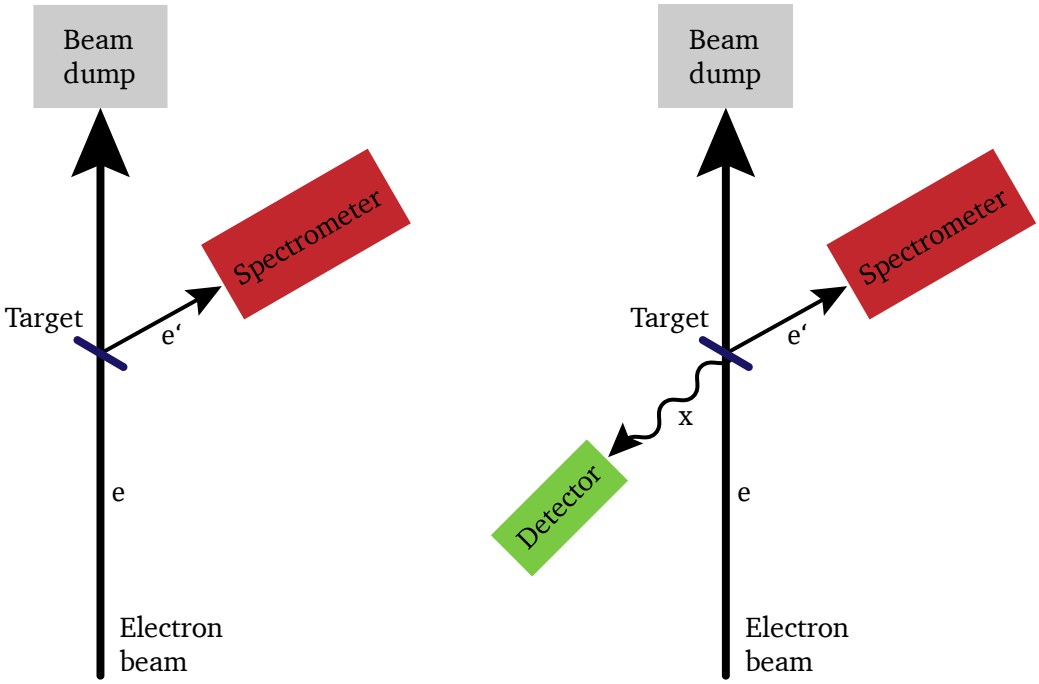

Figure 2: In electron scattering experiments, an electron beam impinges on the target. The non-scattered part of the electron beam is collected at the Faraday Cup. Left: In inclusive electron scattering, scattered electrons are detected by an electron spectrometer. Right: For the measurement of exclusive electron scattering, the setup is extended by a detector for the particle emitted during the decay of the excited nucleus.

The main background source in inelastic electron scattering is the radiative tail of elastically scattered electrons. A further advantage of coincidence measurements is the suppression of the radiative tail by the gating on the particle x. This was demonstrated in a ^{208}Pb(e,e'n) [19] measurement as shown in Figure 3. The ^{208}Pb(e,e') spectrum has a large background which disappears when the coincidence condition with the neutron is used.

Another example of possible measurements which can be performed using coincidence setups are electro-fission measurements. These measurements allow to study fission barriers through subthreshold fission [17] and the coupling of giant resonances in the actinide region in the fission channel [20,21].

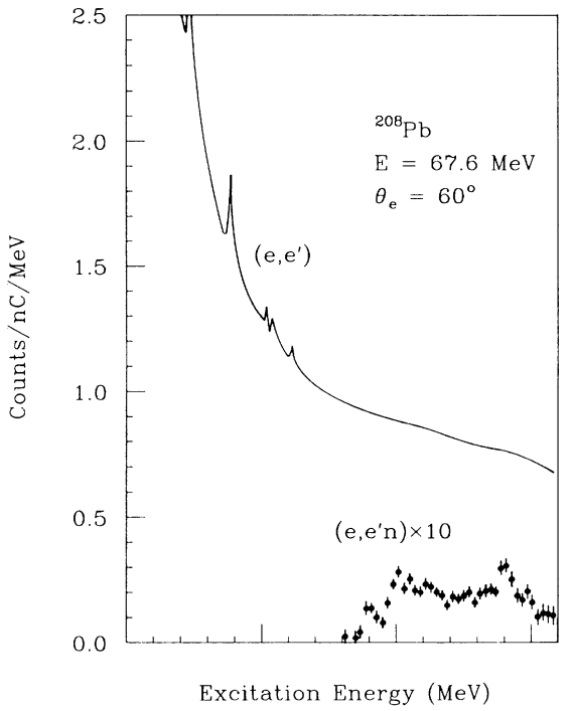

Figure 3: In inclusive (e,e') electron scattering experiments, the background is dominated by the radiative tail of the elastic line. By using the coincidence condition in exclusive (e,e'x) measurements, this background is suppressed. Reprinted Figure 3 with permission from [19] Copyright 2022 by the American Physical Society.

Electron-γ coincidence measurements represent a very interesting case of exclusive electron scattering as both reaction and decay channel are purely electromagnetic in nature which, in principle, makes it the "ultimate" electromagnetic probe [17]. The first (e,e'γ) measurement was performed on the 2_1^+ state of ^{12}C at the MUSL-2 accelerator at the University of Illinois [22,23]. This state was measured in inclusive electron scattering multiple times [24–27], extracting the longitudinal and transverse form factors through the Rosenbluth separation method [28]. An alternative for extraction of F_L and F_T (and the relative sign of their phase) is provided by (e,e'γ) measurements, which are sensitive to the interference term of F_L and F_T [23]. The result of this pioneering experiment is shown in Figure 4. The interference of the longitudinal and transverse form factors results in a rotation of the quadrupole pattern, with the relative sign of the form factors determining the direction of the rotation. From previously measured form factors, a rotation of 2.3° was calculated and the (e,e'γ) measurement provided a negative relative sign [23].

Longitudinal and transverse form factors were also studied for the 2_1^+, 3_1^- and 1_1^- states of ^{16}O [29]. (e,e'γ) measurements also allow the reconstruction of transition currents in non-zero spin nuclei by isolating each multipole form factor by its γ-decay, as demonstrated in an ^{15}N(e,e'γ) experiment [30]. Another application of (e,e'γ) experiments is the investigation of the electromagnetic decay of the Pygmy Dipole Resonance (PDR) and Giant Dipole Resonance (GDR) [17,31].

Despite the success of the early (e,e'γ) experiments, the full potential of the measurement method has not been fully exploited. Measurements are very limited in number and limited to light nuclei. To overcome the main challenge in (e,e'γ) measurements, the coincident bremsstrahlung background, advances in detector development are crucial for a modern

setup. The usage of fast timing, high efficiency $LaBr_3$:Ce scintillation detectors with a good energy resolution [32] are essential for the design of a new (e,e'γ) setup.

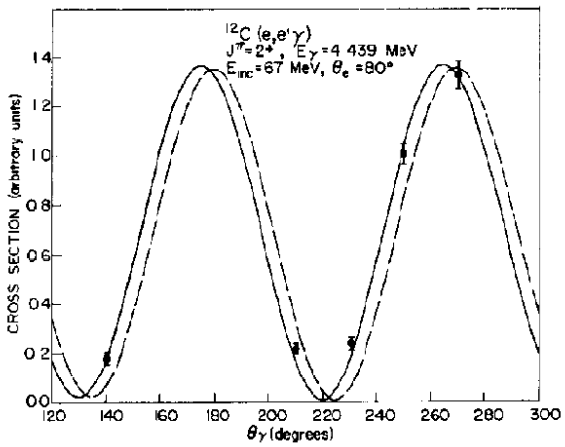

Figure 4: The ratio of $|F_T|^2/|F_L|^2$ rotates the measured quadrupole pattern by 2.3° relative to the momentum transfer axis. The solid line was calculated for negative relative signs and the dashed curve was calculated for positive relative signs. Reprinted Figure 4 with permission from [23] Copyright 2022 by the American Physical Society.

The **S**uperconducting **DA**rmstadt **LIN**ear **AC**celerator (S-DALINAC) at the Institute for Nuclear Physics at the Technische Universität Darmstadt [33] is an established facility for inclusive and exclusive electron scattering experiments. For example, the scissors mode, an isovector magnetic dipole mode, has been discovered [34,35] and one- and two-phonon symmetric and mixed-symmetric 2^+ states of ^{92}Zr [36] and ^{94}Mo [37] were successfully studied in inclusive electron scattering and exclusive measurements were conducted to study giant resonances in (e,e'n) [38] and (e,e'x; x=p,α) [18] reactions. Because of its existing infrastructure, especially the large acceptance **Q**uadrupole **CLAM**shell (QCLAM) spectrometer [39] and because of already existing experience in performing (e,e'x) measurements, the S-DALINAC facility is an ideal place for the development of a new (e,e'γ) setup. The new (e,e'γ) setup consisting of the mechanical setup, a data acquisition system and the analysis software was designed, constructed and commissioned within the scope of this work. This provides a new tool for nuclear physics studies at the S-DALINAC. A first test of the data acquisition was performed in a ^{12}C(e,e'γ) measurement, followed by a short ^{96}Ru(e,e'γ) test measurement for characterization of the new experimental setup, resulting in optimizations for background reduction. A first production run on ^{96}Ru(e,e'γ) was performed with the goal of measuring a γ-decay branch of the 2_3^+ state. A measurement to study dipole excitations such as PDR and GDR in ^{140}Ce by using the coincidence condition with γ-decay for selection of the multipolarity is planned. In addition, findings from the development of the electronics and data acquisition of the (e,e'γ) program will be integrated into the development of the planned electro-fission measurement setup [40].

Chapter 2 presents a formalism for describing the (e,e'γ) reactions and a description of the physics cases which can be studied in (e,e'γ). The S-DALINAC and the QCLAM spectrometer are described in chapter 3. The new (e,e'γ) experimental setup is presented in Chapter 4. The data acquisition system and analysis software are described in Chapters 5 and 6. Chapters 7 through 9 discuss the measurements performed with the new experimental setup. The first two measurement campaigns were commissioning experiments that provided important data

for further optimization of the experimental setup. The third measurement campaign represents the first production run of a (e,e'γ) measurement at S-DALINAC.

2. Physics Cases and the (e,e'γ) Formalism

In this chapter, the nuclei of interest, namely ^{12}C and ^{96}Ru, which were measured in this work (see Chapters 7 to 9), are discussed. Subsequently, a formalism for the description of (e,e'γ) reactions is presented. As an example, the double differential cross section for the nucleus ^{12}C was calculated. This will provide insights into the positioning of the γ-ray detectors of the new setup.

2.1. The ^{12}C Nucleus

The ^{12}C nucleus is of special importance for the evolution of carbon-based life and is also an interesting nuclide from a nuclear physics point of view. The Hoyle state at an excitation energy of 7.654 MeV, which is characterized by a triple α cluster configuration, plays a central role in the reaction of ^{4}He nuclei and therefore in the production of ^{12}C in stars [41]. In stars heavier than 1.3 solar masses, ^{12}C contributes dominantly to energy production in the carbon-nitrogen-oxygen (CNO) cycle through the emission of neutrinos [42]. In addition, natural carbon has high isotopic purity, self-supporting targets can be produced and it is easy to handle.

Table 1: Key properties of the states of ^{12}C observed in inclusive and exclusive electron scattering in this work. Listed are the excitation energy E_x, decay properties (IT: internal transition, α: α-decay, p: emission of a proton) and widths, photon energies E_γ of photons emitted in γ-decays and the relative intensities $I(\gamma)$ of the γ-decays. Data taken from [43].

State	E_x (MeV)	Decay	Width (eV)	E_γ (MeV)	$I(\gamma)$ (%)
0_1^+	0	Stable	Stable	Stable	Stable
2_1^+	4.43982 (21)	IT= 100 %	$\Gamma = 10.8 \cdot 10^{-3}$ (6)	4.43894	100
0_2^+	7.65407 (19)	IT: $4.16 \cdot 10^{-2}$ % $\alpha \approx 100$ %	Γ =9.3 (9)	3.21379	100
1_2^+	15.110 (3)	IT= 95.9 % α= 4.1 %	Γ=43.6 (10) $\Gamma_{\gamma 0}$=38.5 (8)	2.400 4.809 7.453 10.665 15.100	1.5 (4) 4.2 (15) 2.83 (36) 2.49 (34) 100 (2)
2_3^+	16.1060 (8)	IT= 0.27% p=0.41 % α=99.3 %	$\Gamma_\gamma = 5.3 \cdot 10^3$ (2)	3.396 5.257 6.463 11.6601 1.6944	1.5 (3) 3.8 (9) 2.4 (5) 100 (12) 4.6 (9)

For these reasons, the ^{12}C nucleus is frequently measured in electron scattering experiments and was also studied during the first (e,e'γ) experiment. ^{12}C has isolated states in a large energy interval and causes a small background from bremsstrahlung and elastically scattered

electrons due to its low atomic number. The states observed in this work and their most relevant properties are listed in Table 1. The 2_1^+ state of ^{12}C is located at an excitation energy of 4.4 MeV and decays to the ground state via a one-step γ-decay. The 1_2^+ state at an excitation energy of 15.1 MeV decays by 86 % directly to the ground state. Thus, these states are suitable for a commissioning experiment of the new (e,e'γ) setup. Moreover, the excitation energy of the 1_2^+ state of ^{12}C corresponds to the excitation energy of the GDR in heavier nuclei, so that an observation of this γ-decay can serve as a first test for possible future studies of the γ-decay of the GDR to the ground state or low-lying excited states. The 0_2^+ state and the 2_3^+ state decay predominantly by particle emission. Therefore, these states are unlikely to be observed in (e,e'γ) measurements, but they can be used together with the 0_1^+ ground state for calibration measurements in inclusive measurements.

2.2. The ^{96}Ru Nucleus and Mixed-Symmetric States

In the shell model [44,45] the protons and neutrons, which have spin S=1/2 and are therefore fermions, fill the shells in pairs due to the Pauli principle starting with the lowest shell until they are full and continuing with the next shell. The completely filled shells are called closed shells, whereas the nucleons in incompletely filled shells define the valence-space of a nucleus. The valence nucleons are responsible for the low-lying states of the nucleus, where a distinction is made between excitations in which only a single nucleon is involved and collective excitations in which many nucleons are involved. The low-energy nuclear excitations of even-even nuclei are dominated by simple collective excitations induced by the long-range quadrupole component of the nuclear force. Collective excitations can be described as a homogeneous system that vibrates and rotates. These surface vibrations are called phonons. As shown in Figure 5, for the example of a quadrupole excitation, collective excitations can occur by an oscillation of protons and neutrons in phase, for full-symmetric states (FSS), or out of phase, for mixed symmetric states (MSS) [46]. In an oscillation in phase, the protons and neutrons involved are indistinguishable. In contrast, out-of-phase oscillations give information about the proton-neutron degree of freedom. The nucleus ^{96}Ru, which was studied in this work, played an important role in the investigation of MSSs [47,48].

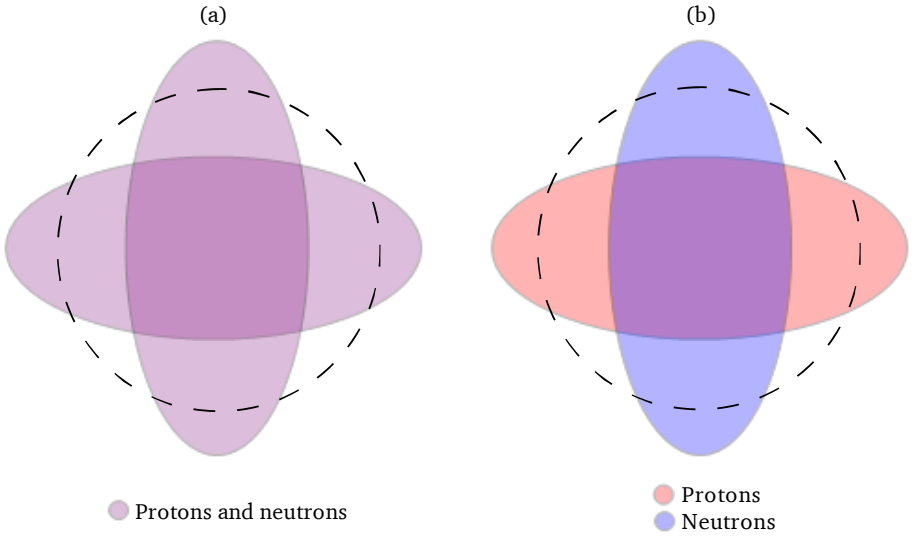

Figure 5: Collective quadrupole excitations of vibrational nuclei can be described by a motion of protons and neutrons in phase (a) and out of phase (b).

2.2.1. Mixed-Symmetric States

The interacting boson model (IBM) describes nucleons in the valence shell as bosons since the pairing force outside a closed shell preferentially couples the nucleons to pairs [49]. Since two protons (neutrons) in the same orbital can only couple to integer angular momentum, the lowest collective excitations of even-even nuclei can be described by bosons in valence space, neglecting the nucleons in the closed shells. In the original version (IBM-1) no distinction is made between protons and neutrons. A further development is IBM-2 [50], which introduces proton and neutron bosons to distinguish the proton-neutron degree of freedom and predicts MSSs.

In IBM-2, the F-spin quantum number is introduced, which is the bosonic analog of the isospin [50,51]. Proton and neutron bosons have $F = 1/2$ and the projection on the z-axis is $F_z = +1/2$ for proton bosons and $F_z = -1/2$ for neutron bosons. The maximum F-spin $F_{\max}$ satisfies the triangle inequality

$$F_{\max} = \frac{N_\pi + N_\nu}{2} \geq F \geq \frac{|N_\pi - N_\nu|}{2} \tag{2.1}$$

for a system of N_π proton bosons and N_ν neutron bosons. States with $F = F_{\max}$ are FSSs and states with $F < F_{\max}$ are MSSs. The latter give a new insight into the proton-neutron degree of freedom of heavy nuclei and are therefore of great interest.

Since in nearly all even-even nuclei the first excited state is a 2^+ state, considering the long-range quadrupole component of the nuclear force, an intuitive formalism for describing the low-lying states by excitations can be given by a quadrupole operator $\hat{Q}$. The resulting scheme, which is shown in Figure 6, is called the Q-phonon scheme [52–55]. This formalism can be extended to distinguish the proton-neutron degree of freedom by a quadrupole operator $\hat{Q}_\pi$ for proton bosons and the operator $\hat{Q}_\nu$ for neutron bosons. The resulting quadrupole operator for symmetric coupling of proton bosons and neutron bosons is given by

$$\hat{Q}_{\mathrm{s}} = \hat{Q}_\pi + \hat{Q}_\nu. \tag{2.2}$$

Analogously, the quadrupole operator for a mixed-symmetric coupling is given by

$$\hat{Q}_{\mathrm{ms}} = a\,\hat{Q}_\pi - b\,\hat{Q}_\nu, \tag{2.3}$$

where a and b ensure the orthogonality of the operator. The excited states are obtained by applying the quadrupole operators $\hat{Q}_{\mathrm{s}}$ and $\hat{Q}_{\mathrm{ms}}$ to the ground-state. Consequently, the first full-symmetric 2^+ state and the first mixed-symmetric 2^+ state are obtained by

$$\left|2^+_{1,\mathrm{FSS}}\right\rangle = N_{\mathrm{s}}\hat{Q}_{\mathrm{s}}|0^+_1\rangle \tag{2.4}$$

and

$$\left|2^+_{1,\mathrm{MSS}}\right\rangle = N_{\mathrm{ms}}\hat{Q}_{\mathrm{ms}}|0^+_1\rangle, \tag{2.5}$$

where N_{s} and N_{ms} are normalization constants [56]. Higher lying states are multi-phonon configurations, which are generated by coupling Q-phonons to total angular momentum J. The coupling of two symmetric Q-phonons results in the triplet

$$|J^+_{\mathrm{FSS}}\rangle \propto \left(\hat{Q}_{\mathrm{s}}\hat{Q}_{\mathrm{s}}\right)^{(J)}|0^+_1\rangle \tag{2.6}$$

with $J = 0, 2, 4$. The higher lying mixed-symmetric states are analogously obtained by coupling a mixed-symmetric Q_{ms}-phonon and a symmetric Q_{s}-phonon, resulting in the quintet given by

$$|J^+_{\mathrm{MSS}}\rangle \propto \left(\hat{Q}_{\mathrm{ms}}\hat{Q}_{\mathrm{s}}\right)^{(J)}|0^+_1\rangle \tag{2.7}$$

with J =0, 1, 2, 3, 4. The 1^+ state of this multiplet is known as the scissors mode. In IBM-2, these one- and two-phonon mixed-symmetric states have $F = F_{max} - 1$. Some typical properties arising from this model are (except for in the limit of well-deformed rotors) [56]:

- The lowest-lying state is the $2^+_{1,\mathrm{FSS}}$ state.
- The lowest-lying MMS is the $2^+_{1,\mathrm{MSS}}$ state.
- The $2^+_{1,\mathrm{MSS}}$ state decays to the $2^+_{1,\mathrm{FSS}}$ state by a strong M1 transition with a matrix element of the order 1 μ_N.
- The collective E2 transition strength of the $2^+_{1,\mathrm{MSS}} \rightarrow 0^+_1$ transition is weak. Expected are a few W.u. for the transition strength.

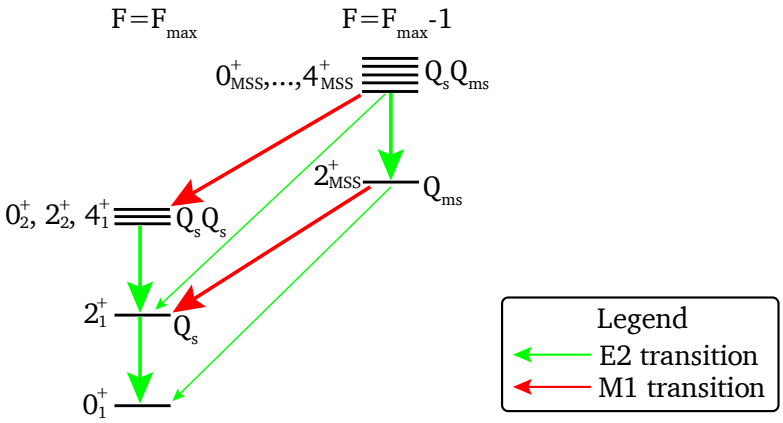

Figure 6: Low lying one- and two-phonon states in the Q-phonon scheme. The strengths of the transitions are indicated by the thickness of the arrows. The 2^+_{MSS} is characterized by a strong M1 transition into the 2^+_1. The figure is based on [57].

2.2.2. Properties of the ^{96}Ru Nucleus

Quadrupole mixed-symmetric states were first observed in the $A \approx 140$ mass region [58]. The nucleus ^{94}Mo turned out to be a textbook example [59,60], initiating the systematic search in the $A \approx 100$ mass region for mixed symmetric states. This led to the discovery of MSSs in the nuclei ^{96}Mo [61], ^{92}Zr [62], ^{94}Zr [63] and ^{96}Ru [47,48].

For the first search for mixed-symmetric states of ^{96}Ru, the 2^+_3 state was populated by Coulomb excitation and the transition strengths were measured. The direct decay to the ground state was weak with $B(E2; 2^+_3 \rightarrow 0^+_1) = 1.6(3)$ W.u, whereas the transition to the first 2^+_1 was strong with a transition strength of $B(M1, 2^+_3 \rightarrow 2^+_1) = 0.78(23)\ \mu_N^2$. This corresponds to the expected behavior from the IBM-2, so that the 2^+_3 state could be identified as the $2^+_{1,\mathrm{MSS}}$ state [47,48]. Furthermore, the 2^+_5 state and the 3^+_2 state were identified as the two-phonon mixed symmetry states $2^+_{2,\mathrm{MSS}}$ and $3^+_{1,\mathrm{MSS}}$ [47]. A study of the even-even $N = 52$ isotones from ^{92}Zr to ^{100}Cd yielded predictions of a restoration of the collective proton-neutron mixed-symmetry structure near mid-shell, providing a quantitative explanation for the pronounced collective mixed-symmetry structures in weakly collective nuclei. This phenomenon, in which protons and neutrons do not contribute equally, is called configurational isospin polarization

(CIP) and was predicted by [64] and experimentally confirmed by [65]. Significant CIP corresponds to a breaking of the F-spin symmetry in IBM-2, leading to a weak M1 strength. At mid-shell, CIP vanishes and rises again as the next shell closure is approached. For ^{96}Ru, which lies with Z=44 protons in the middle between the shell terminations Z=40 and Z=50, a stronger M1 transition is predicted than for the neighboring N=52 even-even isotopes [64]. The trend of M1 strength predicted by CIP for quadrupole states, which becomes maximal for ^{96}Ru, was confirmed in proton scattering experiments and evidence for the characterization of the $3_2^{(-)}$ and 4_2^+ states as one-phonon mixed symmetry states was found [66,67].

Thus, ^{96}Ru with its low-level mixed-symmetric states represents an interesting nuclide for (e,e'γ) experiments. The precise measurement of the branching ratios of the MSS gives in addition of their lifetimes and decay multipolarities information about the transition strengths and thus allows the identification of MSS. At high excitation energies above the neutron separation threshold S_N of 10.7 MeV [68], decays to ^{95}Ru* by emission of neutrons dominate and γ-decays become more difficult to observe. In the GDR region, 99 % neutron decay probability can be expected [69]. This allows studies of the neutron decay channel in the PDR and GDR regions by measuring the γ-decays of the ^{95}Ru*.

Table 2: Key properties of the most dominant states of ^{96}Ru observed in this work. Listed are the excitation energy E_x, half-life $T_{1/2}$, photon energies E_γ of photons emitted in γ-decays and the relative intensities $I(\gamma)$ of the γ-decays. Data taken from [70].

State	E_x (MeV)	$T_{1/2}$ (fs)	E_γ (MeV)	$I(\gamma)$ (%)
0_1^+	0	Stable	Stable	Stable
2_1^+	0.83256 (5)	$2.94 \cdot 10^{+3}$ (6)	0.83255	100
2_3^+	2.28388 (9)	0.15 (5)	1.45131 (12) 2.28378 (22)	100 (11) 7.2 (9)

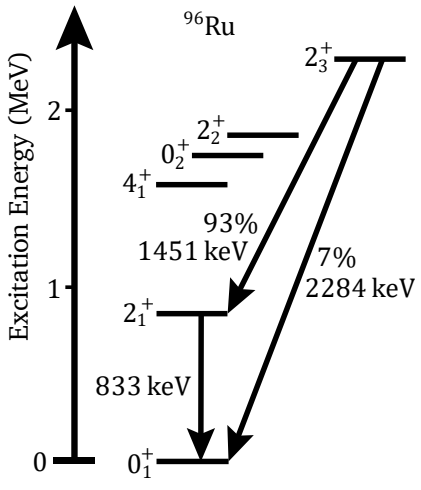

Figure 7: Simplified level scheme of ^{96}Ru. Data taken from [47,67,70].

The measurement of the branching ratios of mixed-symmetric states of ^{96}Ru provides insight into the nuclear processes and serves to characterize the new (e,e'γ) setup by testing the sensitivity to γ-ray branching and weak ground state decays. A listing of some low-lying states of ^{96}Ru and a simplified level scheme are shown in Table 2 and Figure 7.

2.3. (e,e'γ) Formalism

An (e,e'γ) reaction is the inelastic excitation of a nucleus by electron scattering and the subsequent emission of prompt γ-radiation. This section is based on the work of Williamson [22]. Some typos were found and corrected using the description in [71].

Nuclear reactions can be depicted as Feynman diagrams for easier understanding. The Feynman diagrams for the nuclear and bremsstrahlung processes are shown in Figure 8. In the nuclear process (a), the nucleus is excited by the electron and subsequently decays either via intermediate states or directly to the ground state by emission of γ-radiation (b). On the other hand, bremsstrahlung can be produced by the electron after (c) or before the scattering process (d). As can be seen in the Feynman diagrams (Figure 8 (a), (c) and (d)), in these processes the same particles are present before and after the interaction. In the case of a γ-decay to the ground state, the energy of the emitted photon is equal to the energy loss of the electron that excited the nucleus. Similarly, in the case of bremsstrahlung production, the energy loss of the electron is equal to the energy of the bremsstrahlung photon. It has been shown that bremsstrahlung photons are indistinguishable from photons from nuclear decay, thus both processes are coherent [72]. Consequently, the total (e,e'γ) cross section $\sigma_{(e,e'\gamma)}$, given by Equation (2.8), consists of three terms

$$\sigma_{(\mathrm{e,e'\gamma})} = \sigma_{\mathrm{nucl}} + \sigma_{\mathrm{brems}} + \sigma_{\mathrm{inter}}. \tag{2.8}$$

The three terms denote the contributions by photons from nuclear decay σ_{nucl}, bremsstrahlung photons σ_{brems}, and an interference term of the previous two reactions σ_{inter}. The inference term is odd in $E_x - \omega$, where E_x is the excitation energy and ω is the energy of the photon, therefore integration over typical energy resolutions of narrow levels results in the term being zero. For broad resonances such as giant resonances, the interference term may be larger and easier to measure [22]. In the following, the interference term is neglected due to its small effects on narrow states.

As the measured (e,e'γ) cross section is a superposition of the nuclear part, which is more interesting from the point of view of nuclear physics, and the bremsstrahlung, both processes are described in this chapter and their angular distributions are calculated using the example of the 1_2^+ state of ^{12}C. A comparison of the ratio of the differential form factors $(d\sigma_{\mathrm{nucl}}/d\Omega)/(d\sigma_{\mathrm{brems}}/d\Omega)$ will provide information about the conditions under which the nuclear contribution exceeds the bremsstrahlung contribution.

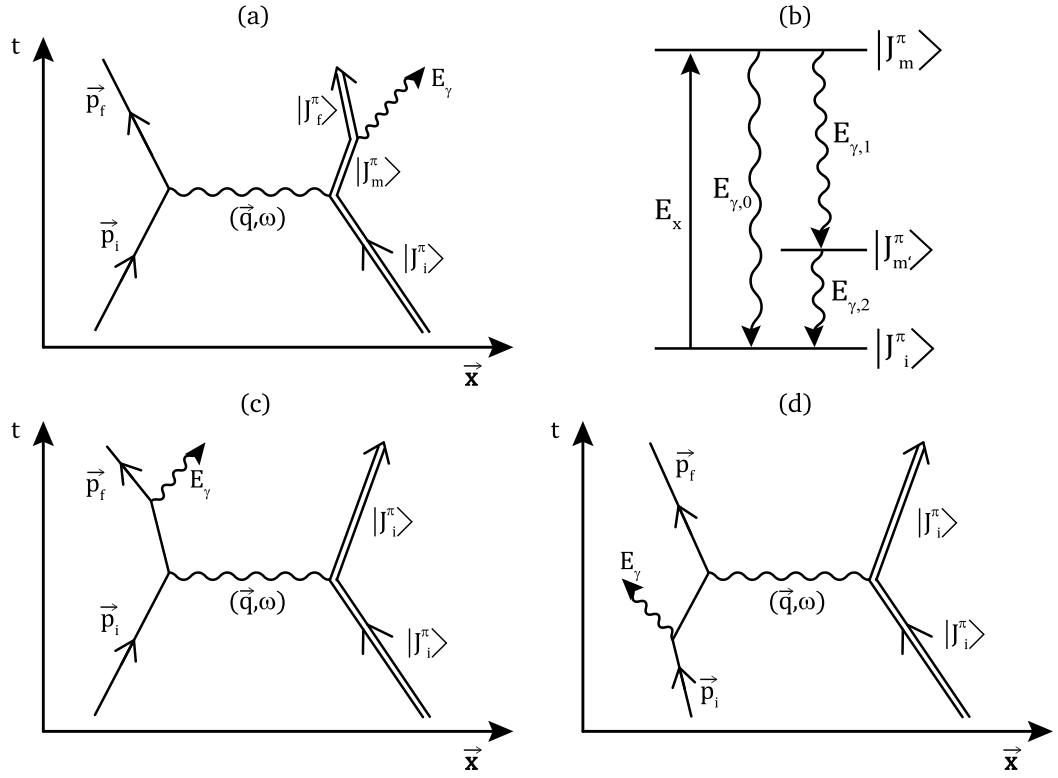

Figure 8: In the inelastic scattering process, a nucleus is excited and subsequently decays to a low-level state or ground state. This is shown in the Feynman diagram (a) and the level scheme (b). The Feynman diagrams for bremsstrahlung processes show the production of bremsstrahlung after (c) and before (d) the scattering process. Since the same particles are entering and leaving the Feynman diagrams, these processes are indistinguishable.

In this chapter, the formalism for describing (e,e'γ) reactions in Plane Wave Born Approximation (PWBA) is presented. The cross section of (e,e'γ) reactions was described in PWBA by Hubbard and Rose for a ground state transition [72] and by Drechsel and Überall for the decay into an excited state [73]. For cross section calculations of heavy nuclei, the effect of the static Coulomb electric field of the nucleus on the wave function of the electron must be considered. This is done in Distorted Wave Born Approximation (DWBA). First DWBA calculations for (e,e'γ) reactions were performed in 1970 [74]. In recent years, there have been advances in DWBA calculations of the cross sections of heavy nuclei [75,76] and the first excited state of ^{12}C has also been calculated [77]. To describe the 1_2^+ state of ^{12}C, which was measured within the scope of this work, PWBA calculations will be used in the remainder of this work. The quantities used in this work are listed in Table 3. Four vectors are denoted by $\tilde{x}$, three vectors by $\vec{x}$ and the magnitude of the three vectors by x.

Table 3: Definitions of the quantities used in this work.

Z	Nuclear charge number
e	Elementary charge
α	Fine structure constant $\alpha = 1/137$
$\hbar c$	Planck's constant times the velocity of light $\hbar c = 197\text{MeV fm}$

J	Spin of the excited state
p_f	Momentum of the scattered electron
p_i	Initial electron momentum
E_i	Initial energy of the electron
E_f	Energy of the scattered electron
Γ_J^{rad}	Partial width for photon decay of the excited state
Γ_J	Total width of the excited state
E_x	Energy of the excited state
ω	Energy loss to the nucleus. Neglecting recoil, this corresponds to the energy of the emitted photon in a ground state transition. $\omega = E_i - E_f$
k	Momentum of the photon
θ	Scattering angle of the electron, the angle between initial and final trajectories of the electron.
q	Momentum transfer $q = \frac{1}{c}\sqrt{4E_i(E_i - E_x)\sin^2(\theta/2) + E_x^2}$
q_{total}	Momentum transfer including energy of the photon $q_{\text{total}} = \lvert\vec{p}_i - \vec{p}_f - \vec{k}\rvert$
F_L	Longitudinal form factor
F_T	Transverse form factor
$C_{m_1,m_2}^{j_1,j_2,j}$	Clebsch-Gordan coefficients for coupling the states with spin $\lvert j_1, m_1 >$ and $\lvert j_2, m_2 >$ to $\lvert j, m >$. Clebsch-Gordan coefficients for which the condition m=m1+m2 is not true have the value 0.
$P_l(x)$	Legendre polynomial
$j_l(x)$	Spherical Bessel function
$\vec{r}$	Position vector
$\rho(\vec{r})$	Transition charge density
$\vec{j}(\vec{r})$	Transition current
$\vec{\mu}(\vec{r})$	Transition magnetization

The relevant vectors and angles for the description of an (e,e'γ) reaction are illustrated in Figure 9. The geometry of the (e,e'γ) process is treated in two planes, the scattering plane and the reaction plane. The scattering plane is defined by the trajectories of the electrons before and after the scattering process, with the momentum transfer vector along the z-axis. The reaction plane is defined by the momentum transfer axis and the direction of the emitted photon.

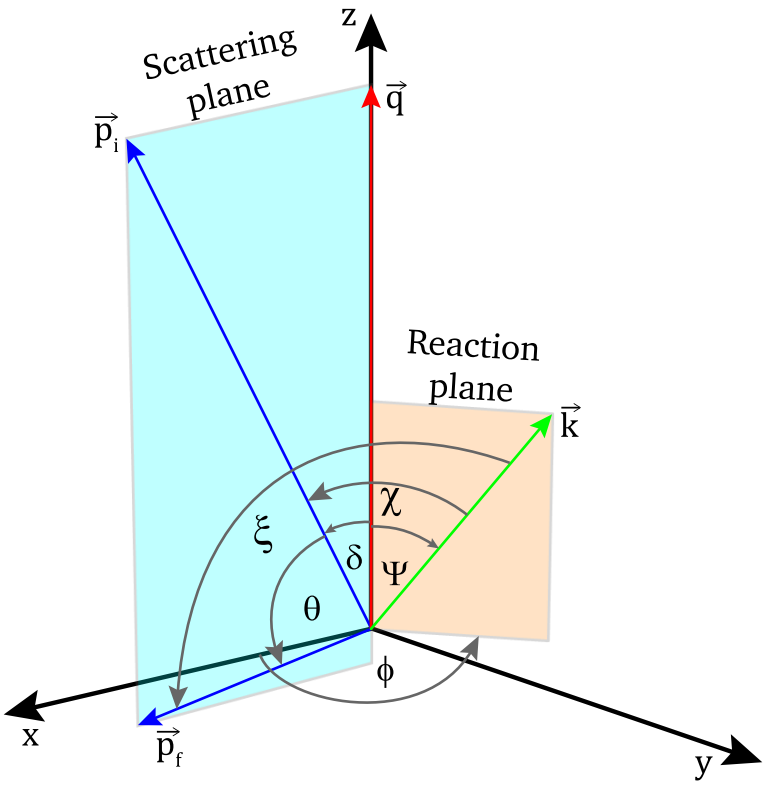

Figure 9: The relevant vectors and angles of the kinematics of an (e,e'γ) reaction are shown. The scattering plane is spanned by the vectors of the electron's momentum $\vec{p}_i$ before and $\vec{p}_f$ after scattering. The coordinate system is aligned so that the scattering plane lies in the x-z-plane and the z-axis is defined by the momentum transfer $\vec{q}$. The vectors of momentum transfer and momentum of the emitted photon, $\vec{k}$, define the reaction plane.

2.4. Nuclear Decay Photons in Electron-γ Coincidence

A general description of the differential cross section of an (e,e'$\gamma_1\gamma_2$...) reaction in which the excited nucleus equilibrates via a cascade of γ-decays is presented in [78]. Special cases in which only one of the γ-rays detects are also discussed therein. In the following, a ground state decay is assumed. The triple differential cross section of an (e,e'γ) reaction for excitation of a nucleus to an isolated state and subsequent decay to a 0_1^+ ground state, neglecting the nuclear recoil, is given by [71]

$$\frac{d^3\sigma}{d\Omega_\gamma d\Omega_e d\omega} = 2\left(\frac{Z\,\alpha\,\hbar c}{4\,\pi}\right)^2 (2J+1)\frac{p_f}{p_i}\frac{\Gamma_J^{\mathrm{rad}}}{\Gamma_J}\frac{\Gamma_J}{(E_x-\omega)^2+\frac{\Gamma_J^2}{4}} \cdot (V_L W_L + V_T W_T + V_I W_I + V_S W_S). \tag{2.9}$$

The factors V contain the kinematics of the reaction, whereas the factors W are the (generalized) form factors [79] and contain the physics information about the nucleus. The indices represent the longitudinal part L, the transverse part T, the interference of the

longitudinal and transverse form factors I, and the spin part S. The kinematic factors are defined by Equations (2.10) – (2.13).

$$V_L = \frac{\left(E_i + E_f\right)^2 - \tilde{q}^2 c^2}{q^4 c^4} \tag{2.10}$$

$$V_T = \frac{2\left(\overrightarrow{p_i} \times \overrightarrow{p_f}\right)^2 + q^2 \tilde{q}^2}{q^2 \tilde{q}^4 c^2} = \frac{2\left(p_i\, p_f \sin(\theta)\right)^2 + q^2 \tilde{q}^2}{q^2 \tilde{q}^4 c^2} \tag{2.11}$$

$$V_I = \frac{4\left(E_i + E_f\right)\left(\vec{k} \times \vec{q}\right)\left(\vec{p}_f \times \vec{p}_i\right)}{\omega\, q^4 \tilde{q}^2 c^2} = \frac{4\left(E_i + E_f\right) p_i\, p_f \sin(\Psi) \sin(\theta) \cos(\Phi)}{q^3 \tilde{q}^2 c^2} \tag{2.12}$$

$$V_S = \frac{2\left(2\left(\left(\vec{k} \times \vec{q}\right)\left(\vec{p}_f \times \vec{p}_i\right)\right)^2 - \left(\vec{k} \times \vec{q}\right)^2 \left(\vec{p}_f \times \vec{p}_i\right)^2\right)}{\omega^2\, q^4\, \tilde{q}^4 c^4} = \frac{2\left(p_i\, p_f \sin(\Psi) \sin(\theta)\right)^2 \cos(2\Phi)}{q^2\, \tilde{q}^4 c^4} \tag{2.13}$$

The Symbol × denotes the antisymmetric three-dimensional vector product. The form factors are defined by Equations (2.14) - (2.17). They depend only on the momentum transfer and the angle between the momentum transfer axis and the direction of the photon.

$$W_L = -|F_L(q)|^2 \cdot \sum_{l=0,2,\ldots} C_{1,-1}^{J,J,l}\, C_{0,0}^{J,J,l}\, P_l(\cos(\Psi)) \tag{2.14}$$

$$W_T = |F_T(q)|^2 \cdot \sum_{l=0,2,\ldots} \left(C_{1,-1}^{J,J,l}\right)^2 P_l(\cos(\Psi)) \tag{2.15}$$

$$W_I = -F_L(q) \cdot F_T(q) \cdot \sum_{l=2,4,\ldots} C_{1,-1}^{J,J,l}\, C_{0,1}^{J,J,l} \left(l(l+1)\right)^{1/2} P_l'(\cos(\Psi)) \tag{2.16}$$

$$W_S = -s(\Pi)\, |F_T(q)|^2 \cdot \sum_{l=2,4,\ldots} C_{1,-1}^{J,J,l}\, C_{1,1}^{J,J,l} \left(\frac{(l-2)!}{(l+1)}\right)^{1/2} P_l''(\cos(\Psi)) \tag{2.17}$$

$P_l'(x)$ and $P_l''(x)$ represent the first and second derivatives of the Legendre polynomials. The function $s(\Pi)$ is 1 for an electric transition ($\Pi = E$) and -1 for a magnetic transition ($\Pi = M$). The longitudinal and transverse form factors for a ground state transition are defined by Equations (2.18) and (2.19) for electric transitions and Equation (2.20) for magnetic transitions:

$$F_L(q) = \frac{1}{Z}\sqrt{\frac{4\pi}{2J+1}} \langle J || M_{LM}(q) || 0 \rangle \tag{2.18}$$

$$F_{T,E}(q) = \frac{1}{Z}\sqrt{\frac{4\pi}{2J+1}} \left(\langle J || T_{LM}^{Ec}(q) || 0 \rangle + \langle J || T_{LM}^{E\mu}(q) || 0 \rangle\right) \tag{2.19}$$

$$F_{T,M}(q) = \frac{1}{Z}\sqrt{\frac{4\pi}{2J+1}} \left(\langle J || T_{LM}^{Mc}(q) || 0 \rangle + \langle J || T_{LM}^{M\mu}(q) || 0 \rangle\right) \tag{2.20}$$

where M_{LM}, $T^{\tau c}_{LM}$ and $T^{\tau \mu}_{LM}$ are multipole operators. The reduced matrix elements are defined by the Wigner-Eckart theorem given by [80]

$$\langle J_m | O_{LM} | J' m' \rangle = C^{J',L,J}_{m',M} \, \langle J || O_L || J' \rangle. \tag{2.21}$$

The multipole operators M_{LM}, $T^{\tau c}_{LM}$ and $T^{\tau \mu}_{LM}$ are given by Equations (2.22) - (2.26). The terms $T^{\tau c}_{LM}$ contain the dependence on the convection current density and the terms $T^{\tau \mu}_{LM}$ contain the dependence on the magnetization density:

$$M_{LM}(q) = \int j_L(qr) Y_{LM}(\hat{r}) \rho(\vec{r}) d^3r \tag{2.22}$$

$$T^{Ec}_{LM}(q) = \frac{1}{q} \int \left(\vec{\nabla} \times j_L(qr) \vec{Y}^M_{LL}(\hat{r}) \right) \cdot \vec{j}(\vec{r}) d^3r \tag{2.23}$$

$$T^{E\mu}_{LM}(q) = q \int \left(j_L(qr) \vec{Y}^M_{LL}(\hat{r}) \right) \cdot \vec{\mu}(\vec{r}) d^3r \tag{2.24}$$

$$T^{M}_{LM}(q) = \int \left(j_L(qr) \vec{Y}^M_{LL}(\hat{r}) \right) \cdot \vec{j}(\vec{r}) d^3r \tag{2.25}$$

$$T^{M}_{LM}(q) = \frac{1}{q} \int \left(\vec{\nabla} \times j_L(qr) \vec{Y}^M_{LL}(\hat{r}) \right) \cdot \vec{\mu}(\vec{r}) d^3r \tag{2.26}$$

where Y_{LM} are spherical harmonics. The vector spherical harmonics are defined by

$$\vec{Y}^M_{LL} = \sum_{M=m+m'} C^{l,1,L}_{m,m'} \; Y_{lm}(\hat{r}) \hat{e}_{m'} \tag{2.27}$$

using the spherical unit vectors $e_{m'}$ with $m' = -1, 0, 1$.

If states are studied whose widths are much narrower than the energy resolution of the measurement instrument, and it is assumed that change of kinematic factors in the range of ω is small, only the Breit-Wigner factor contributes to the integration of Equation (2.9) over ω with the value 2π. Therefore, the double differential cross section can be written as:

$$\frac{d^2\sigma}{d\Omega_\gamma d\Omega_e} = \frac{1}{4\pi} (Z \, \alpha \, \hbar c)^2 (2J+1) \frac{p_f}{p_i} \frac{\Gamma^{\mathrm{rad}}_J}{\Gamma_J} \cdot (V_L W_L + V_T W_T + V_I W_I + V_S W_S) \tag{2.28}$$

For transverse excitations e.g., the 1^+_2 state of ^{12}C, the longitudinal form factor is zero, which simplifies Equation (2.28) to Equation (2.29).

$$\frac{d^2\sigma}{d\Omega_\gamma d\Omega_e} = \frac{1}{4\pi} (Z \, \alpha \, \hbar c)^2 (2J+1) \frac{p_f}{p_i} \frac{\Gamma^{\mathrm{rad}}_J}{\Gamma_J} \cdot (V_T W_T + V_S W_S) \tag{2.29}$$

As an example, the angular distribution of the 1^+_2 state of ^{12}C was calculated using (2.29), assuming a 30 MeV electron beam and a scattering angle of 132.5°, is shown in Figure 10.

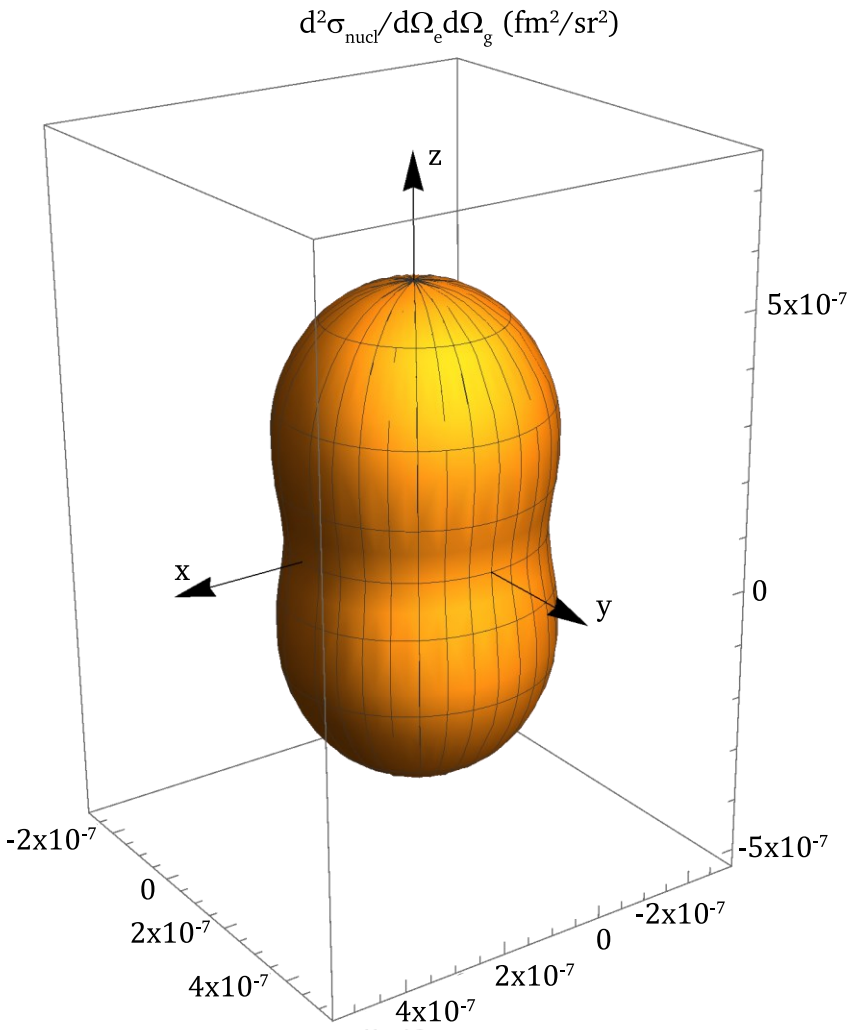

Figure 10: The double differential cross section calculated for the excitation process of the 15.11 MeV state of ^{12}C followed by a γ-decay to the ground state. An energy of the electrons of 30 MeV and a scattering angle of 132.5° were assumed for the calculation.

By integrations of equation (2.28) over the angles ϕ and ψ, the differential effective cross section of conventional electron scattering is obtained, see Equation (2.30) [22]. The γ-decay channel Γ_J^{rad}/Γ_J, which is not determined in conventional electron scattering, was dropped. Here, the loss of information becomes visible.

$$\frac{d\sigma}{d\Omega_e} = (Z\,\alpha\,\hbar c)^2 \frac{p_f}{p_i} \cdot \left(V_L |\mathrm{F_L(q)}|^2 + V_T |\mathrm{F_T(q)}|^2\right) \tag{2.30}$$

For negligible electron rest mass and energy loss $(E_i, E_f \gg m_o\,c^2, E_x)$, the differential cross section is given by:

$$\frac{d\sigma}{d\Omega_e} = \frac{d\sigma_{\mathrm{Mott}}}{d\Omega_e}\left(|\mathrm{F_L(q)}|^2 + \left(\frac{1}{2} + \tan^2\left(\frac{\theta}{2}\right)\right)|\mathrm{F_T(q)}|^2\right). \tag{2.31}$$

The factor $(d\sigma/d\Omega_e)_{\mathrm{Mott}}$ represents the Mott cross section [81], which describes the scattering of a relativistic electron by an infinitely-massive point nucleus with spin zero:

$$\left(\frac{d\sigma}{d\Omega_e}\right)_{\mathrm{Mott}} = \left(\frac{Z\,\alpha\,\hbar c}{2\,E_i}\right)^2 \frac{\cos^2(\theta/2)}{\sin^4(\theta/2)}. \tag{2.32}$$

2.5. Bremsstrahlung

The bremsstrahlung term in the (e,e'γ) cross section can be calculated by the Bethe-Heitler formula [82], which neglects screening by the atomic electrons and the effects due to the finite size of the nucleus. This is fulfilled for light nuclei like ^{12}C, for heavy nuclei like ^{96}Ru corrections are required. The Bethe-Heitler formula is given by:

$$\frac{d^3\sigma}{d\Omega_\gamma d\Omega_e d\omega} = \left(\frac{Z\,\hbar c}{2\pi}\right)^2 \alpha^3 \frac{p_f/p_i}{\omega\left|\vec{q}-\vec{k}\right|^4 c^4} \tag{2.33}$$

$$\cdot\left(\frac{\left|\vec{p}_f\times\vec{k}\right|^2}{\left(\tilde{p}_f\cdot\tilde{k}\right)^2}\left(4E_i^2-\left|\vec{q}-\vec{k}\right|^2c^2\right)+\frac{\left|\vec{p}_i\times\vec{k}\right|^2}{\left(\tilde{p}_i\cdot\tilde{k}\right)^2}\left(4E_f^2-\left|\vec{q}-\vec{k}\right|^2c^2\right)\right.$$

$$-2\frac{\left(\vec{p}_f\times\vec{k}\right)\left(\vec{p}_i\times\vec{k}\right)}{\left(\tilde{p}_f\cdot\tilde{k}\right)\left(\tilde{p}_i\cdot\tilde{k}\right)}\left(4E_iE_f-\left|\vec{q}-\vec{k}\right|^2c^2\right)$$

$$\left.+2\omega^2\frac{\left|\vec{k}\times\vec{q}\right|^2}{\left(\tilde{p}_f\cdot\tilde{k}\right)\left(\tilde{p}_i\cdot\tilde{k}\right)}\right)$$

$$=\left(\frac{Z\,\hbar c}{2\pi}\right)^2\alpha^3\frac{p_f/p_i}{\omega\,q_{\text{total}}^4c^4}$$

$$\cdot\left(\frac{p_f^2\sin^2(\xi)c^4}{\left(E_f-p_f\cos(\xi)c\right)^2}\left(4E_i^2-q_{\text{total}}^2c^2\right)\right.$$

$$+\frac{p_i^2\sin^2(\chi)c^2}{\left(E_i-p_i\cos(\chi)\,c\right)^2}\left(4E_f^2-q_{\text{total}}^2c^2\right)$$

$$-2\frac{p_f\sin(\xi)\;p_i\sin(\chi)c^2}{\left(E_f-p_f\cos(\xi)c\right)\left(E_i-p_i\cos(\chi)c\right)}\left(4E_iE_f-q_{\text{total}}^2c^2\right)$$

$$\left.+2\frac{\left|\vec{k}\times\vec{q}\right|^2c^4}{\left(E_f-p_f\cos(\xi)c\right)\left(E_i-p_i\cos(\chi)c\right)}\right)$$

The four vector products $\tilde{p}_i\cdot\tilde{k}$ and $\tilde{p}_i\cdot\tilde{k}$ in the denominators produce sharp maxima in the bremsstrahlung cross section when the photon is emitted around the direction of the electron before and after the collision, respectively. While the bremsstrahlung has a maximum in a cone around the direction of the electron, a minimum occurs exactly in the direction of motion of the electron. Between the maxima, the cross section decreases by several orders of magnitude and becomes smaller than the contribution from photons produced by the decay of the excited nucleus. These intervals are suitable for the positioning of γ-ray detectors to study photons from the decay of excited nuclei.

A comparison of the nuclear and the bremsstrahlung components of the double differential (e,e'γ) cross section for the 15.11 MeV state of ^{12}C is shown in Figure 11. The two maxima of the differential bremsstrahlung cross section are located at the angles relative to the momentum transfer axis of the incident electron beam and the electrons scattered to the spectrometer. The angular distribution of the nuclear part depends strongly on the multipolarity of the γ-decay. The M1 transition of the excited 1_2^+ of ^{12}C is approximately constant in the scattering plane. At sufficiently large angular distance from the directions of the electron beam and the spectrometer, the contribution by nuclear photons dominates in the γ-ray detectors.

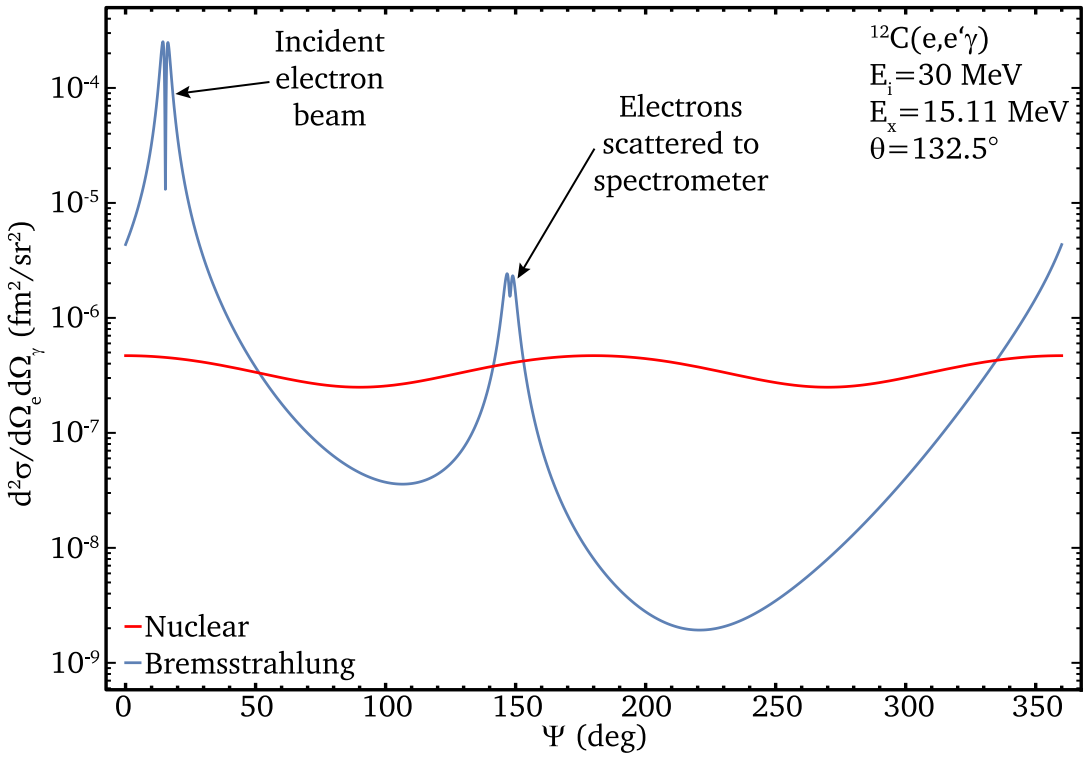

Figure 11: The double differential cross sections in the x-z-plane of the nuclear component of the 15.11 MeV state (blue) and the bremsstrahlung component (red) for electron scattering off ^{12}C are shown. For the bremsstrahlung a relative energy resolution of the electron spectrometer of 10^{-3} was assumed.

3. Experimental Facility

Electron-γ coincidence experiments require a high-quality electron beam and a spectrometer with a large solid angle acceptance for high coincidence count rates at low background rates. The S-DALINAC at the Institute for Nuclear Physics at Technische Universität Darmstadt is an electron accelerator for high resolution electron scattering experiments at low momentum transfer. The large acceptance QCLAM spectrometer was originally developed for coincidence experiments [39]. Therefore, together they provide an ideal framework to create a new (e,e'γ) setup. Both will be described in detail in the next sections.

3.1. S-DALINAC Electron Accelerator

The S-DALINAC (see Figure 12) is a superconducting recirculating continuous-wave electron accelerator [33]. Electrons are generated by a thermionic source and pre-accelerated by an electrostatic field. The chopper pre-buncher section applies a 2.998 GHz time-structure to the electron beam for preparation for further acceleration in the superconducting cavities that are cooled to 2 K and are operated at the same frequency. In the injector section, the electrons are accelerated to energies up to 10 MeV.

After the injector, the electron beam can either be used for bremsstrahlung production and subsequent real-photon scattering experiments at the **D**armstadt **H**igh-**I**ntensity **P**hoton **S**etup (DHIPS) [83] or transported to the main linear accelerator (LINAC) where the electrons gain additional 30 MeV in kinetic energy per passage. In its original setup from 1991 the accelerator had two recirculations to feed the electron beam back to the beginning of the LINAC twice, so that the electrons are accelerated up to three times in the LINAC and reach higher energies. A third recirculation was added in 2015/2016 [84] allowing a maximum electron energy of 130 MeV by accelerating the electrons to 10 MeV in the injector and increasing the energy four times by 30 MeV when using all three recirculations. Depending on the required energy the main accelerator can be used in single-pass mode, single-recirculation mode, or thrice-recirculation mode. An energy-recovering operation mode in which the electrons are recirculated with a phase shift of 180°, transferring the energy previously obtained in the LINAC back to the accelerator, was developed [84] and successfully commissioned in 2017 [85].

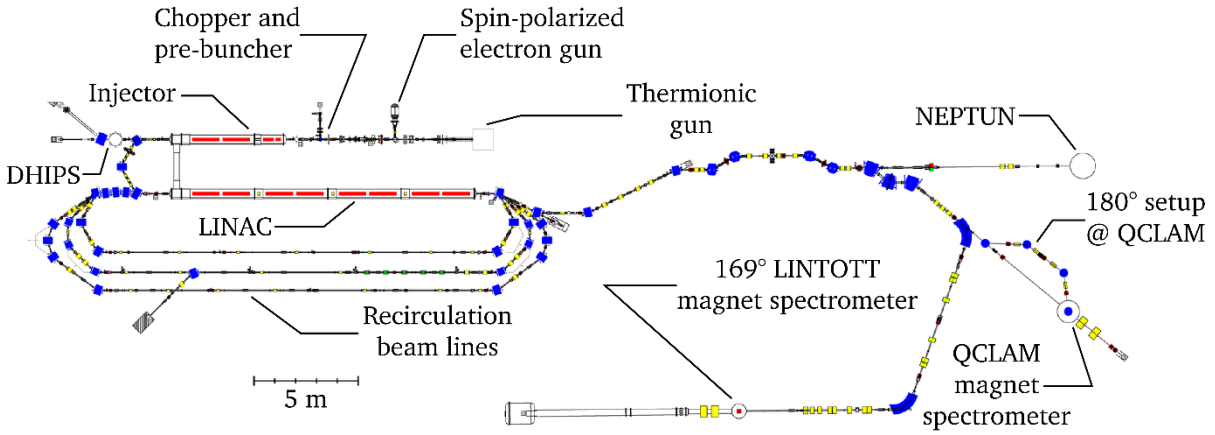

Figure 12: The S-DALINAC consist of a thermionic gun, an injector, and a main accelerator. By using the recirculations, higher electron energies can be achieved, and the accelerator can be operated in energy recovery mode. The electron beam can be transported to different experimental setups: Bremsstrahlung production at DHIPS, (γ,γ'x) at NEPTUN, (e,e') at LINTOTT and (e,e') and (e,e'x) at QCLAM.

After exiting the main LINAC, the electron beam can be transported to the low-energy photon-tagger NEPTUN [86], the high resolution LINTOTT spectrometer [87,88] and the large acceptance QCLAM spectrometer [39].

3.2. High-Energy Scraper System

To further improve beam quality for measurements at the QCLAM, NEPTUN, and Lintott experimental sites, a high-energy scraper system that is depicted in Figure 13 was installed at the S-DALINAC [89]. It consists of two halo scrapers located in chambers 1 and 2 and an energy scraper in between. Halo scrapers are used to block the electron beam's halo that consists of electrons whose distance to the center of the electron beam profile is greater than 5σ [90]. Hence, halo electrons are more likely to hit elements of the beamline resulting in an increased background. The y-halo scraper in chamber 1 and the x-, y-halo scraper in chamber 2 are positioned where the dispersion of the electron beam and thereby its spatial spread is low making the operation of the halo scraper independent of the electron beam's energy width. The designation of the halo scraper is derived from the convention of coordinate systems for description of charged particles in magnetic fields, which defines the direction of motion of the charged particle as the z-axis, the x-axis in the direction of the Lorentz force, and the y-axis perpendicular to the x- and z-axes.

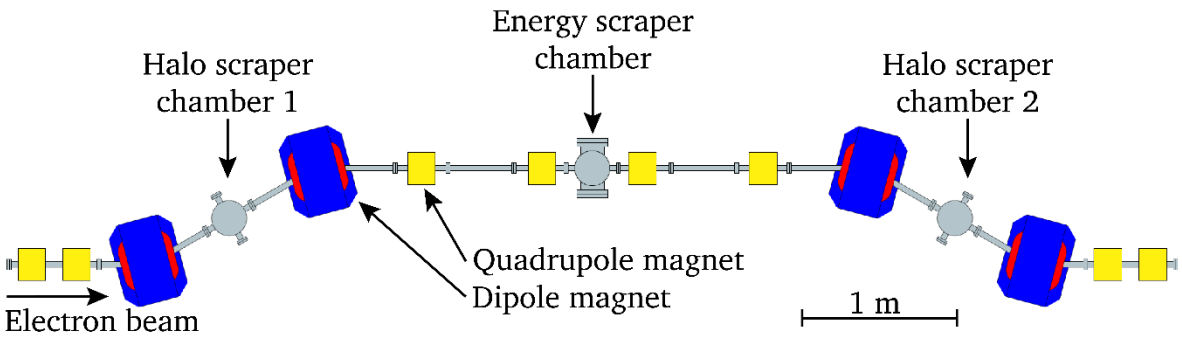

Figure 13: The high-energy scraper system of the S-DALINAC consists of two halo scrapers and an energy scraper. Figure taken from [89].

The purpose of the energy scraper is to improve the energy resolution of the electron beam and thereby increase the energy resolution of the electron spectra measured at the experimental stations. The effect of the energy resolution of the electron beam is discussed in detail in [89]. The dipole magnets in the scraper chicane create a strong dispersion, so that electrons are deflected on trajectories of different radii depending on their energy. At the location of the strongest dispersion is the energy scraper, which consists of two copper blocks that can be moved from both sides towards the center of the electron beam in the x-direction to define an energy interval that is allowed to pass through the scraper. Since only electrons within a defined energy interval can pass through the scraper, also energy fluctuations of the electron accelerator are blocked resulting in a stabilized energy resolution for the experimental setups [89].

The electron beam optimization and stabilization provided by the high-energy scraper is crucial for the reduction of background in (e,e'γ) measurements. Elimination of the beam halo results in a smaller background, which is caused by collisions of halo electrons with elements of the beamline, and the improved energy resolution allows the use of narrow gates on the electron energy during data analysis, reducing the remaining background in measured

spectra. A beam width of $\sigma_x = 0.37 \pm 0.05$ mm and $\sigma_y = 0.10 \pm 0.01$ mm [91] as well as a background rate reduction of 90% and a relative energy resolution of $1.9 \cdot 10^{-4}$ were demonstrated at the Lintott spectrometer with the use of the high-energy scraper system [89].

3.3. QCLAM Electron-Spectrometer

The optimized electron beam from the high-energy scraper section is transported to the experimental site of the QCLAM spectrometer shown in Figure 14, where the electrons impinge on a target inside a scattering chamber. Most of the electron beam passes the target unreacted along the beamline towards the Faraday cup where the beam current is measured. Beam current values between several nanoamperes and microamperes can be recorded. Knowledge of the beam current is important for absolute cross sections measurements. By comparing the measured beam current at the Faraday cup of the QCLAM spectrometer to the beam current emitted by the accelerator, measured by a movable Faraday cup, and the losses on the scraper brackets, information about beam losses that create additional background radiation along the beamline is provided. To improve the transmission between target and Faraday cup and to compensate the angular spread of the electrons, two refocusing quadrupole magnets are used to focus the beam on the Faraday cup.

A small fraction of electrons that impinge on the target are scattered and can enter the spectrometer's opening and thus are transported to the detector system.

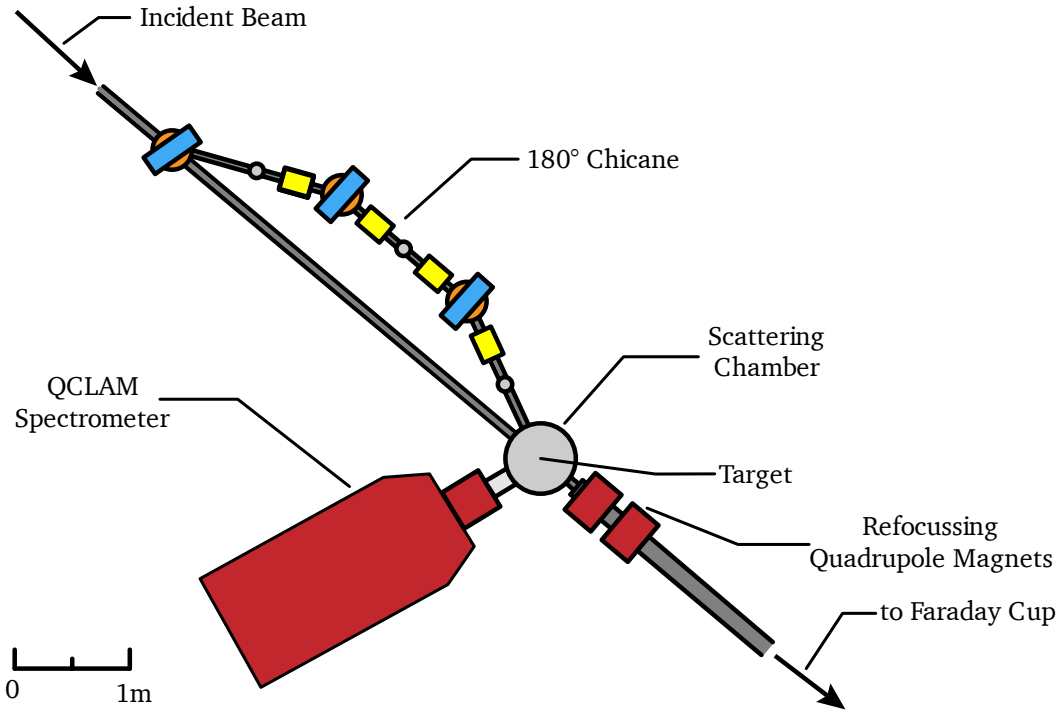

Figure 14: The QCLAM electron spectrometer and its beamline is shown from a top-down perspective. The electron beam from the accelerator is impinging on a target inside the scattering chamber. Most of the electron beam is guided to the Faraday cup. Two large quadrupole magnets refocus the electron beam after the target. Scattered electrons are measured by the QCLAM spectrometer. The 180° chicane in front of the scattering chamber can be used for measurements at a scattering angle of 180°. Taken from [92] and modified.

The QCLAM can be rotated in the horizontal plane around the center of the scattering chamber to measure at different scattering angles. The spectrometer angle corresponds to the

average scattering angle. In the following, the horizontal scattering angle is referred to as the angle between the axis of the incoming electron beam and the projection of the scattered electron on the horizontal plane. The angle between the horizontal plane and the vector of the scattered electron is referred to as the vertical scattering angle. A positive sign of the vertical scattering angle means that the electron was scattered upwards.

The target must be aligned according to the angle of the QCLAM spectrometer as shown in Figure 15. A distinction is made between transmission geometry (a) and reflection geometry (b). In the transmission geometry, all electrons scattered to the spectrometer travel the same path length in the target and suffer similarly large energy losses during traversal. In the reflection geometry, the energy loss of the electrons depends on the location of the scattering process in the target. An electron scattered when entering the target has a shorter path length in the target than an electron scattered just before leaving the target. The energy loss of the electrons is different, resulting in reduced energy resolution depending on the thickness of the target. Therefore, the transmission geometry is preferable. At large spectrometer angles, the transmission geometry becomes impractical because the target would have to be nearly parallel to the electron beam.

The QCLAM spectrometer can be rotated to cover a scattering angle range from 25° to 155° allowing for minimum and maximum accepted scattering angles of 19° and 161° [39]. By using a chicane in front of the scattering chamber and a separating magnet inside the chamber, measurements at a scattering angle of 180° can be performed [93].

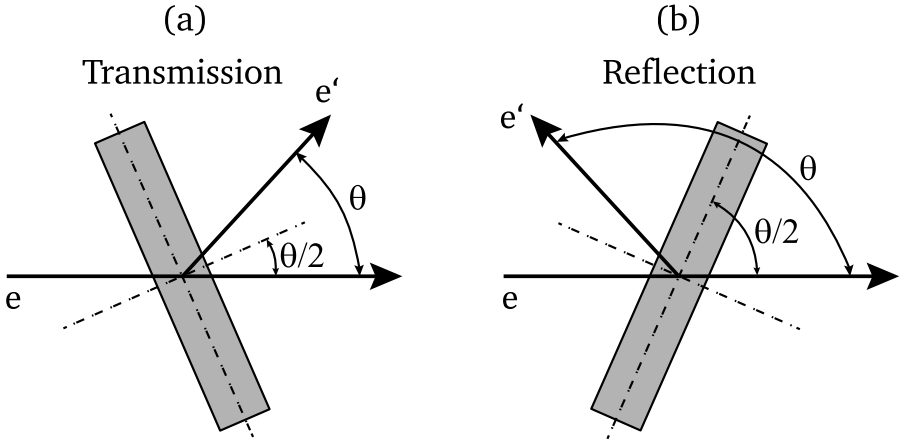

Figure 15: (a): In the transmission geometry, all electrons scattered to the spectrometer travel approximately the same path length in the target. (b): For large scattering angles, the reflection geometry is required. The path length of the electrons in the target depends on the interaction point, which leads to a reduced energy resolution. The figure is based on [87].

The QCLAM spectrometer was built in 1991 and is primary designed for (e,e'x) coincidence experiments [39]. Its large solid angle acceptance of 35 msr, given by the geometry, is essential for the feasibility of coincidence measurements with low cross sections. Therefore, the QCLAM spectrometer is well suited for (e,e'γ) experiment. Measurements indicate that the effective solid angle acceptance of the QCLAM spectrometer is between 25 msr and 30 msr [94]. In addition to the large solid angle acceptance, the spectrometer features a large momentum acceptance of ±10 % and is designed for a maximum electron energy of the reference beam of 200 MeV. The reference beam is defined by the trajectory that enters the spectrometer at the center of its opening perpendicular and leaves the spectrometer at the

center of its exit. The detector system allows for track reconstructions of the trajectory of the electron to achieve an improved relative energy resolution of $3 \cdot 10^{-4}$ [95]. A listing of the key parameters of the QCLAM spectrometer can be found in Table 4.

Table 4: Key parameters of the QCLAM spectrometer. Data taken from [39,95].

Parameter	Value
Maximum momentum	220 MeV/c
Momentum acceptance (rel.)	+/- 10%
Energy resolution (rel.)	$1 \cdot 10^{-4}$
Spectrometer angle interval	25° - 155°
Horizontal angle acceptance	+/- 100 mrad
Vertical angle acceptance	+/- 100 mrad
Solid angle (geometric)	35 msr
Dispersion (dipole magnet)	2.21 cm/%
Maximum current (dipole magnet)	320 A
Maximum current (quadrupole magnet)	225 A

3.3.1. Spectrometer Setup

Since a direct measurement of the energy of ultra-relativistic electrons is not feasible, the energy is determined indirectly by the QCLAM spectrometer, which acts as an electron optical magnet system. Electrons are deflected in the magnetic field of an electron spectrometer according to the Lorentz force on circular paths with radius ρ given by Equation (3.1).

$$B \cdot \rho = p/Q \tag{3.1}$$

B is the strength of the magnetic field, p the momentum and Q the charge of the electron. The momentum information of the electrons is thereby converted via the bending radius into a position information of the of the intersection points of the trajectory with the detector system after leaving the spectrometer magnet. For $p \gg m_e c^2$ the energy of an electron can be approximated to be proportional to its momentum $E \approx pc$, so the energy of the electrons is accessible.

A pure dipole magnet, however, would not provide a focusing effect for electrons entering the electron spectrometer at different angles with the same energy. Therefore, the magnet systems of electron spectrometers contain a quadrupole component to focus electrons of the same energy in one point. The set of all focal points for electrons of different energies is called the focal plane. In the focal plane, the energy can be determined with the greatest accuracy. The strength of the magnetic field determines the energy interval that can be observed in the focal plane. Higher multipole orders such as sextupole components are often used to correct

aberrations in the electron optical magnet systems. The plane in which the electrons are deflected by the dipole magnet is called the dispersive plane. The plane perpendicular to it, in which only minor deflections occur, is accordingly called non-dispersive.

The QCLAM spectrometer, which is shown in Figure 16, consists of two magnets. Electrons that are scattered off the target towards the spectrometer pass at first through a horizontally focusing quadrupole magnet followed by a large deflecting dipole magnet. The quadrupole magnet allows for a huge solid angle acceptance while maintaining the required gap width of 120 mm to 220 mm between the dipole magnet's pole shoes. In addition, the quadrupole has a hexapole component to correct aberrations of the electron optical system consisting of the two magnets. These pole shoes of the dipole magnet are inclined by an angle of 2.54° relative to the dispersive plane adding a quadrupole component, thereby the spectrometers dispersion of 2.21 cm per percent of momentum dispersion is created [39].

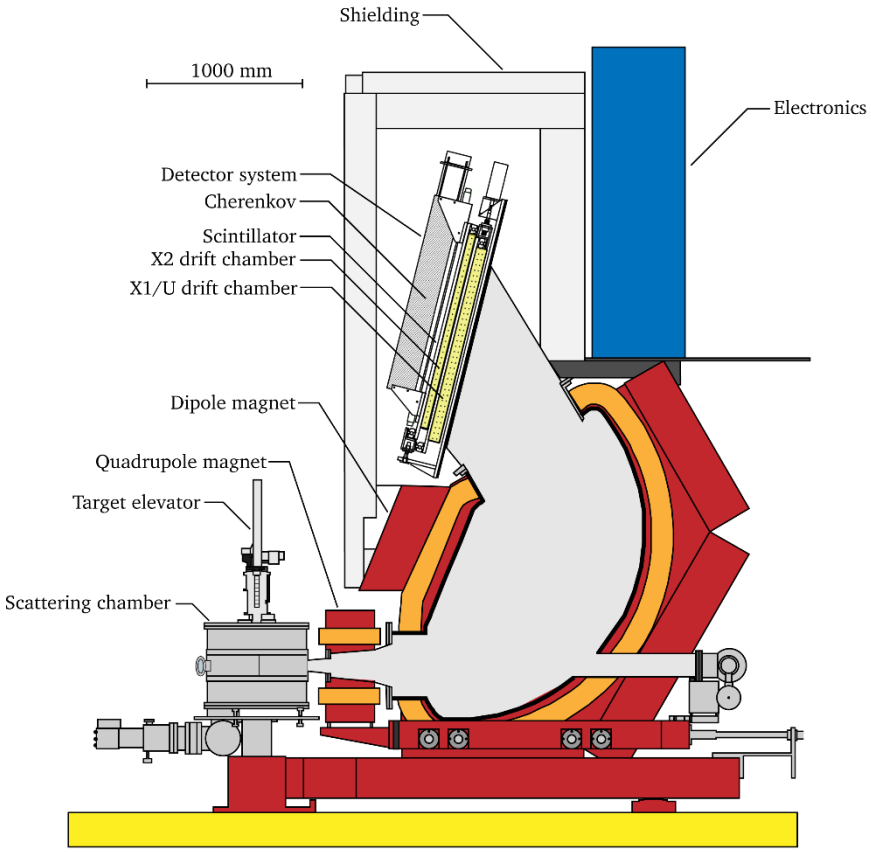

Figure 16: Cross section through the QCLAM spectrometer. The electron beam impinges on the target inside the scattering chamber. Electrons that are scattered off the target can enter the spectrometer and are deflected towards the detector system. Figure based on [96,97].

After the electrons leave the magnets, they enter the detector system through a sealing mylar foil on top of a Kevlar fabric which separates the vacuum inside the spectrometer and in the beamline in the range of 10^{-5} mbar to 10^{-6} mbar from the atmospheric pressure. To protect the detector system from background radiation generated by the electron beam, the detector system is surrounded by a shielding that consists of 50 mm polyethylene with 12.6 % boron oxide, 50 mm pure polyethylene and 100 mm lead [39].

The momentum transfer during a scattering process depends on the electron's energy and scattering angle as can be seen in Table 3. Therefore, to select a particular momentum

transfer either the energy of the electron beam or the angle of the spectrometer must be changed. Since beam-energy tuning can take several days or weeks, it is usually preferred to change the scattering angle of the spectrometer which typically takes a few hours. The QCLAM can be rotated around the scattering chamber on a track to which a scale is attached for reading the spectrometer position, which can be converted into an angle. The angle calibration was recently remeasured in cooperation with Laboratory for Industrial Metrology of the Frankfurt University of Applied Sciences who were previously involved in the alignment of the S-DALINAC [98]. A new position-to-angle calibration was obtained and is used in this work to set the spectrometer to correct scattering angles. Conversions from position to angle and vice versa are given by Equations (3.2) and (3.3). The position-to-scattering-angle conversion is shown in Figure 17.

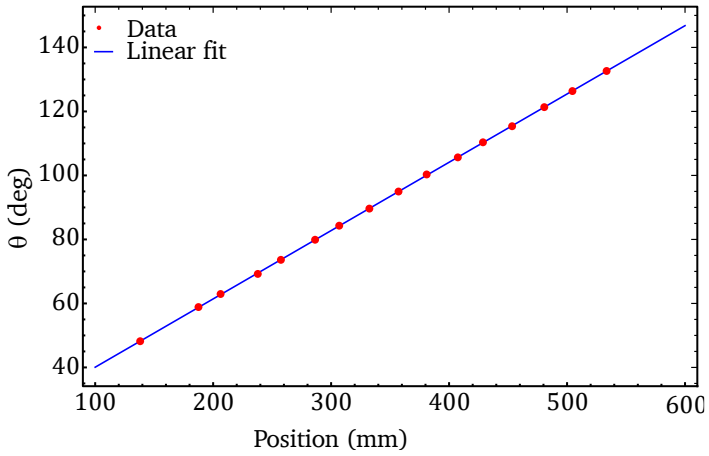

Figure 17: Position-to-angle conversion for the positioning of the QCLAM spectrometer.

$$\theta(x) = 18.7203° + 0.213468°/\text{cm} \cdot x \tag{3.2}$$

$$x(\theta) = -89.10716\ cm + 4.6859\ \text{cm}/° \cdot \theta \tag{3.3}$$

3.3.2. Detector System

The detector system of the QCLAM spectrometer is used to determine the energy of the scattered electrons. The magnets of the QCLAM spectrometer are designed in such a way that the trajectories of electrons with the same momentum but different entrance angles into the spectrometer intersect in the focal plane as it is shown in Figure 18. Due to the electron optical properties of the QCLAM spectrometer, the focal plane is curved and can be approximated by a parabola [39]. Correction of these imaging errors caused by the magnets during the design of the QCLAM would have been costly and time consuming. Therefore, in each measurement campaign calibration measurements are performed to characterize the focal plane and apply corrections to measured data.

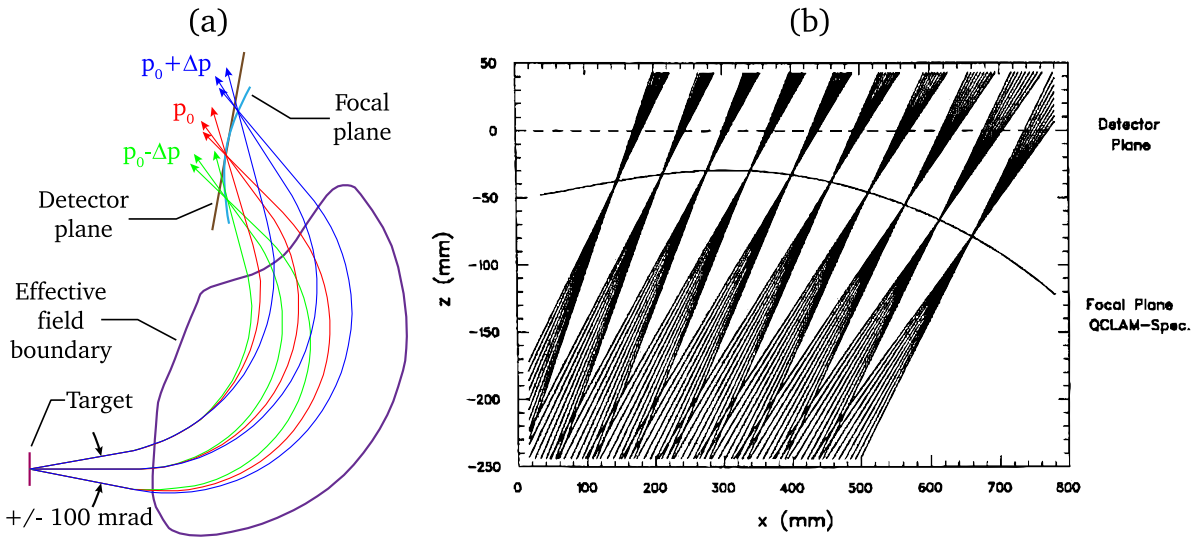

Figure 18: (a): Trajectories of the same energy at different vertical angles are focused by the magnet system in the curved focal plane in front of the detector system. Electrons with lower momentum are deflected stronger in the magnet system so that their focus is shifted downwards. The magnet system is simplified by the effective field boundary of the dipole magnet. Figure (a) is based on [99]. (b): The beams of equal energy have a larger width in the detector system, reducing the energy resolution in the detector system. By measuring the positions and angles of the trajectories in the detector system, it is possible to extrapolate back to the focal plane. Figure (b) taken from [99].

The position and shape of the focal plane depends on the ratio of current settings of the two spectrometer magnets. For 180° scattering experiments, the magnet system of the QCLAM spectrometer is extended by one magnet, resulting in a modified focal plane. Consequently, the focal plane will not be located at the same position for each measurement and differ in shape. Thus, it is required to not only measure the intersection point of the electrons with the detector system, but also reconstruct the full electron trajectories to calculate the intersection points with the focal plane. This is achieved by the detector system of the QCLAM spectrometer that is shown in Figure 19 and consists of three layers of multi wire drift chambers (MWDC), the X1/U double chamber and the X2 chamber and two trigger detectors, a plastic scintillator, and a Cherenkov detector.

By measuring the intersection points of the electrons with each layer of the multi-wire drift chambers, the electron's trajectories can be reconstructed. The X1 and X2 chambers are used to calculate the dispersive coordinate and dispersive angle. The wires of the U chamber are rotated by 26.5° with respect to the wires of the other two chambers. The non-dispersive coordinate and angle are calculated from the measured U coordinate and the information of the other two chambers [100]. By using two drift chambers to calculate dispersive data, the energies are calculated with higher accuracy. Currently, a new drift chamber is under construction, which will have 4 wire planes and will allow for a higher precision reconstruction of the trajectory [101]. The plastic scintillator starts the readout of the chambers, and the Cherenkov detector can be used to further suppress the background by applying a coincidence condition between the signals of both scintillator photomultiplier tubes (PMT) and the signal of the Cherenkov detector.

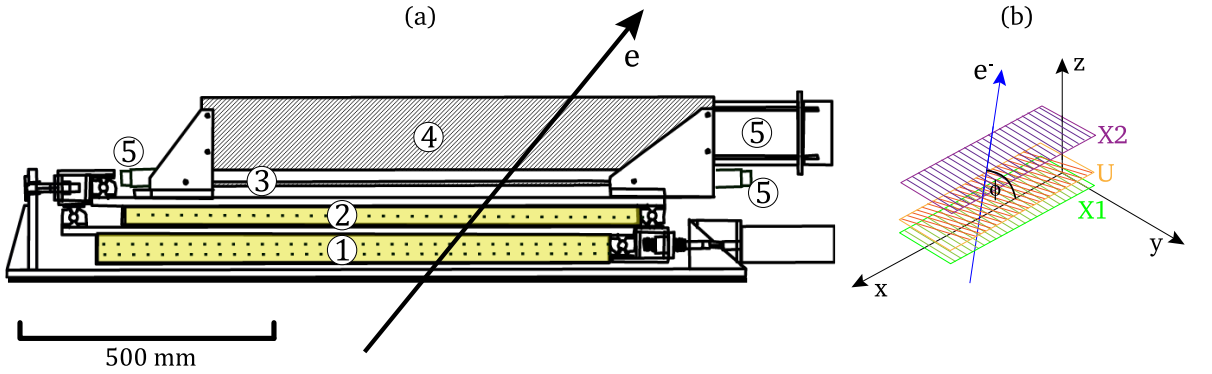

Figure 19: (a): Cross section through the QCLAM detector system consisting of X1/U multi wire drift chamber ①, X2 multi wire drift chamber ②, a plastic scintillator ③, and a Cherenkov detector ④. Photomultiplier tubes ⑤ are attached on both ends of the scintillator and on one end of the Cherenkov detector. An example of an electron trajectory through the detector system is shown. Figure taken from [100] and modified. (b): The schematic diagram shows the trajectory of an electron in the coordinate system of the QCLAM detector system. The non-dispersive y-coordinate is calculated from the X1, X2 and the U multi-wire drift chamber whose wires are rotated by 26.5°.

A multi-wire drift chamber consists of a periodic array of parallel wires between two cathode foils. A high voltage is applied to the anode wires so that an electric field is formed in the volume between the cathode foils. The volume defined by all electric field lines ending in an anode wire is called a drift cell. Figure 20 shows a schematic representation of a section containing four drift cells. The volume between the cathode foils is filled with a gas mixture consisting of a counting gas and a quenching gas. The primary electrons interact along their trajectory with the gas mixture and generate secondary electrons, which are accelerated along the electric field and generate an electron avalanche through collisions with the counting gas. To regulate the electron avalanche and prevent flashovers between the cathode foil and the anode wires, a quenching gas is used. Along their path to the wire, these electrons are accelerated further and generate an electron avalanche, which, in the end, generates an electrical signal at the wires. The mode of operation of a drift cell is the same as that of a Geiger counter [102]. At the QCLAM a gas mixture of 80 % Argon and 20 % Carbon dioxide is used [101]. Three MWDC generations were built for the QCLAM detector system. The first generation [100] has been replaced by the second generation [103], which can operate at a lower field strength between the foils and the wires and reduces the probability of flashovers. The third generation [104] has twice the number of anode wires and allows greater accuracy in reconstructing the trajectories of the electrons. At the time of this work, the second and third generations were operational.

The accuracy of the trajectory reconstruction, and therefore the energy resolution, depends on the accurate knowledge of the intersection points through the three wire planes X1, U and X2. The uncertainty on the calculation of intersection points decreases with increasing number of drift cells hit by the primary electron. On the other hand, the distance that the electrons must travel in the detector system should be small to reduce scattering that would change the primary electron's trajectory. The drift chambers are inclined at an angle of 44° with respect to the reference beam, so that electrons leaving the spectrometer always pass through several drift cells per wire plane [100].

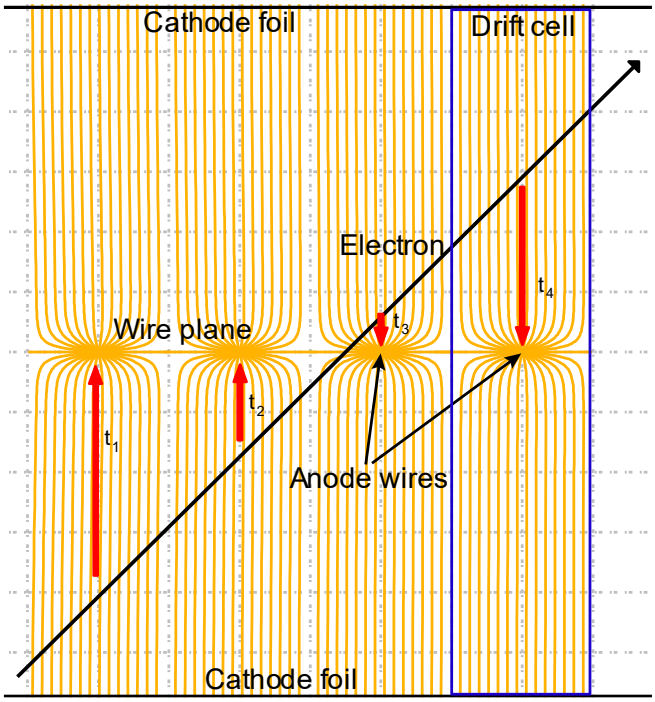

Figure 20: Illustrated are the electric field lines in a third-generation drift chamber. Secondary electrons created by interactions of the primary electron with the gas mixture are accelerated along the field lines towards the anode wires between the cathode foils. A drift cell is defined by all electric field lines that end at the same anode wire. In each drift cell the drift time of the electron avalanche to the anode wires is measured. Figure taken from [97] and modified.

The measurement of the drift times requires a start and stop signal. Plastic scintillators have good time resolution so that the signal from the scintillator is registered before the signal from the anode wires. Therefore, the start signal is created by the scintillator behind the drift chambers and the stop signal is created by the anode wires. The scintillator is read out at both ends by PMTs, so that a position-independent timestamp can be calculated from the average of the signals from the two sides. This is particularly relevant for coincidence experiments, which require a time resolution as good as possible. The time resolution of the QCLAM detector system is 2.2 ns [95].

The ability of the detector system to reconstruct the trajectories of the electrons allows for a calibration of the horizontal and vertical scattering angles by performing and evaluating a sieve slit measurement. For this purpose, a sieve slit is placed at the entrance of the spectrometer so that only electrons at defined angles can enter the spectrometer. Thus, the hole pattern of the sieve slit is projected onto the detector system and the scattering angles of the holes can be assigned to the reconstructed trajectories.

4. Experimental Setup

Within the framework of this thesis, a new detector setup and support structure for the QCLAM measurement station at S-DALINAC was designed. The goal of the new setup is to combine a detector array for (e,e'γ) measurements with the QCLAM spectrometer. For the coincidence measurement of scattered electrons and γ-radiation, γ-ray detectors with excellent time resolution and high efficiency at good energy resolution are required. Other requirements for the setup are modularity and flexibility to adapt the number and the orientation (angle and spacing) of the detectors to the measurement requirements. To achieve these goals, a completely new setup, shown in Figure 21, consisting of the following components was designed:

- Improved beamline ①: A new beamline downstream of the target with additional beam transport elements allows an optimized transport of the electron beam to the target and better focus, resulting in a reduction of beam-induced background.
- Scattering chamber ②: The standard cylindrical scattering chamber of the QCLAM spectrometer is designed for coincidence experiments where small detectors such as silicon detectors are positioned in the scattering chamber [105]. Unfortunately, this is not feasible for large γ-radiation detectors and another, suitable scattering chamber was not available. The new scattering chamber, optimized for (e,e'γ) measurements, reduces background and allows the detectors to be positioned closer to the target.
- Scattering chamber holding structure ③: The new holder allows for precise alignment of the scattering chamber.
- Optimized target elevator ④: The optimized target elevator allows the target to be precisely aligned in the center of the scattering chamber.
- γ-detector housings ⑤: For protection against beam-induced background radiation, the γ-ray detectors are mounted in a lead shielded housing.
- Detector holding structure ⑥: The γ-ray detectors are mounted and aligned in the detector holder.
- Magnetic field shielding ⑦: External magnetic fields influence the signals of the γ-ray detectors used, which may disturb the measured spectrum. To protect the γ-ray detectors from the magnetic field of the quadrupole magnet ⑧ of the QCLAM spectrometer ⑨, a magnetic field shielding was designed.

The components are described in detail in the next sections.

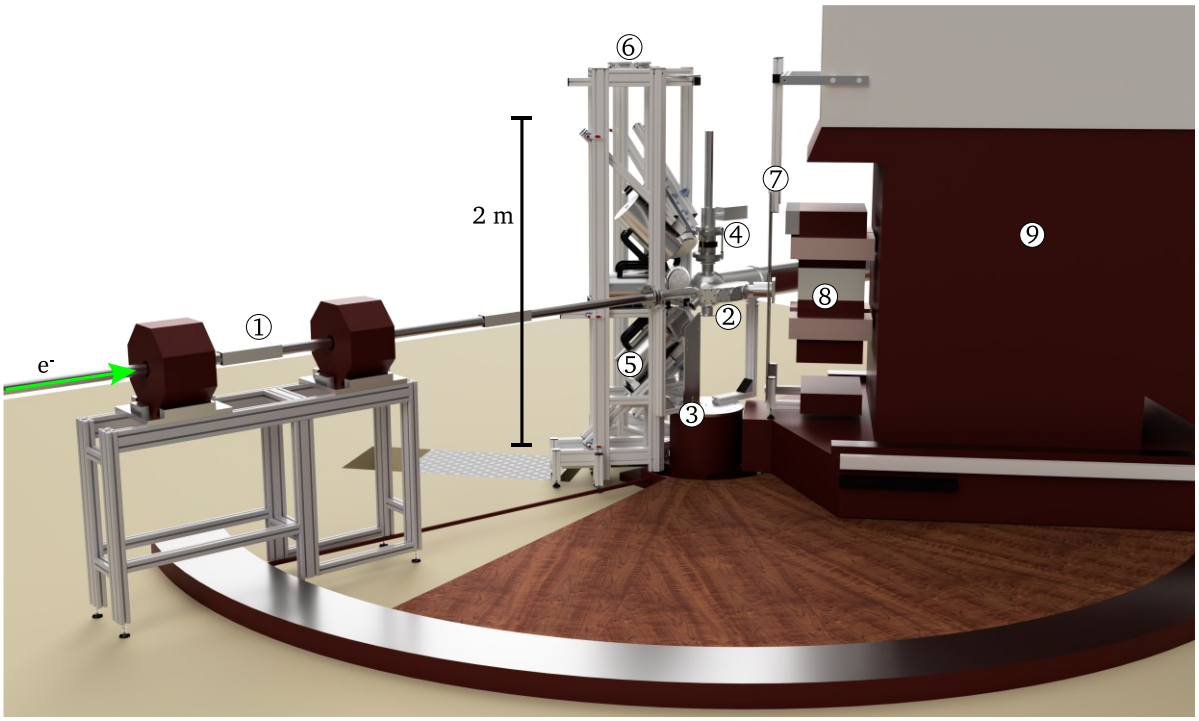

Figure 21: Overview of the new (e,e'γ) experimental setup at the QCLAM spectrometer. ① New beamline, ② (e,e'γ) scattering chamber, ③ scattering chamber holder and target camera, ④ target elevator and target alignment device, ⑤ $LaBr_3$:Ce detectors in housings, ⑥ detector array, ⑦ magnetic field shielding, ⑧ QCLAM quadrupole magnet, ⑨ QCLAM spectrometer. The Figure was created using Autodesk Fusion 360 [106].

4.1. Improved Beamline

A well-focused electron beam positioned at the center of the target is crucial for (e,e'γ) measurements, since the electrons scattered at the beam pipe and other materials along the beamline cause unwanted background radiation. Also, the energy resolution of the measured QCLAM spectra benefits from a better focused electron beam, since the energy resolution is proportional to the size of the beam spot on the target [39].

As there were no beam optimization instruments in the beam line directly in front of the scattering chamber, focusing and positioning the electron beam on the target proved to be difficult in the past. In the original design, the last deflecting element in the beamline upstream of the scattering chamber was the first magnet of the 180° chicane, and a focusing magnet was even further away (see Figure 12). To improve the quality of the electron beam for the planned (e,e'γ) measurements, two quadrupole magnets for better focusing, and two steerers for a better positioning of the electron beam were added to the beamline in front of the scattering chamber.

The new beamline is shown in Figure 22. Two quadrupole magnets of the same model used as the ones in the extraction beamline were mounted on aluminum plates, which are used to align the magnets horizontally in the plane of the S-DALINAC. The plates can be moved along grooves in the aluminum frames of the table in direction of the electron beam. Vertical alignment is achieved by the adjustment of the height of the table, which is set via the adjustable stands. Since quadrupole magnets operate only along the axis through their center without deflection, exact alignment of these magnets was performed using a laser system and the reference points previously set by geodesic measurement of the QCLAM experimental hall.

The table on which the quadrupoles were mounted was manufactured by the company *item Industrietechnik GmbH* [107]. Due to its modular design, the table was adapted to fit the requirements of the measuring station. The table with the heavy magnets was screwed to the floor for better stabilization. Two steerers, which can be moved along the beam pipe, were mounted [108], as shown in Figure 22. The final design of the table and plates was a continuation and optimization of the previous design from 2019 [109].

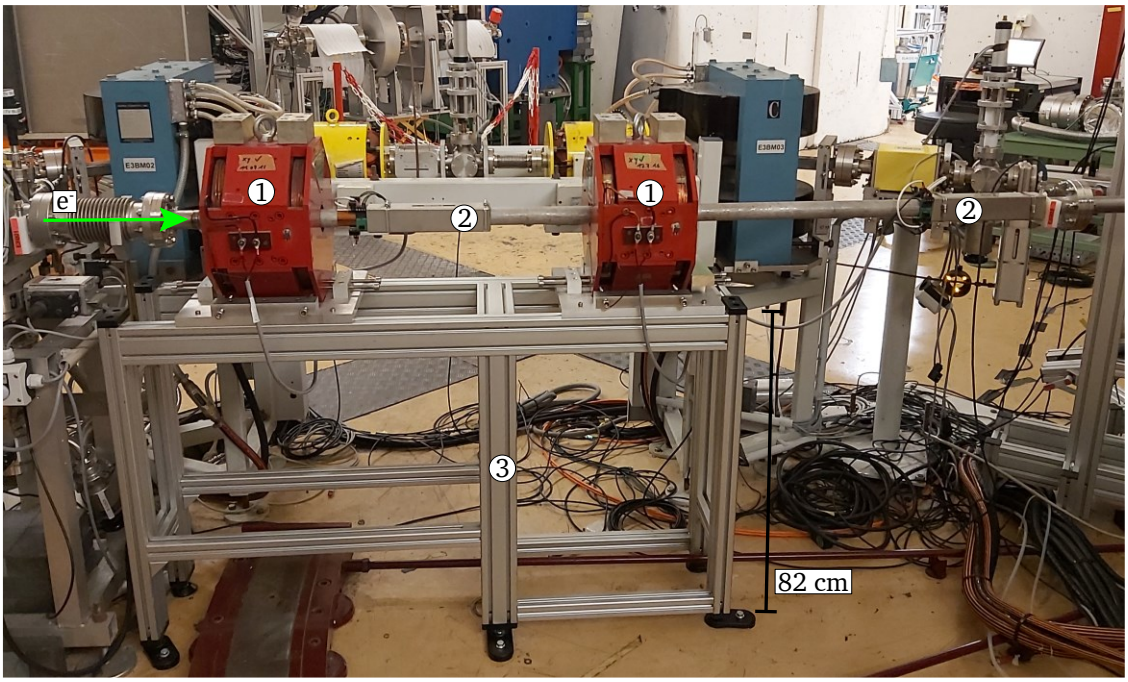

Figure 22: The new beamline built for electron-γ coincidence experiments. It contains newly added quadrupole magnets ① for a better focus of the electron beam on the target and steerers ② for a better alignment of the electron beam. The quadrupole magnets are placed on a dedicated table ③.

The improved beamline can also benefit other inclusive and exclusive electron scattering experiments at scattering angles below 133°. For measurements that require larger scattering angles, like 180° experiments where the QCLAM must be placed at a scattering angle of 155°, mechanical constraints prevent the use of the improved beamline.

4.2. Scattering Chamber

A key component of the experimental setup is the scattering chamber where the electron beam interacts with the target. The QCLAM spectrometer has several scattering chambers designed for different types of experiments with different requirements. The standard multi-purpose cylindrical scattering chamber with a radius of 317 mm [110] is used for inclusive electron scattering experiments, 180° scattering experiments [92,93] and some exclusive scattering experiments. For coincidence experiments, e.g. (e,e'p) measurements [105], particle detectors such as silicon detectors were mounted inside the cylindrical scattering chamber. For (e,e'γ) measurements, this scattering chamber is not suitable. Large volume γ-ray detectors cannot be positioned inside the scattering chamber and due to the 2 cm thick stainless-steel wall, radiation emitted from the target would be strongly attenuated in the wall of the scattering chamber. In addition, the size of the scattering chamber limits the distance of the detectors to the target. Using a smaller scattering chamber allows the detectors to be positioned closer to the target, thus increasing the solid angle with the same number of

detectors. Scattering chambers for measurements on superfluid helium [111] and radioactive ^{14}C [112] have thinner walls but are not suitable because of their geometric limitations. The only existing scattering chamber suitable for (e,e'γ) measurements is the so called ball scattering chamber [113].

4.2.1. Ball Scattering Chamber

The ball scattering chamber that is shown in Figure 23 was designed for (e,e'n) coincidence measurements [113]. This scattering chamber consists of a spherical body with a radius of 122 mm. On both sides beam pipes with standard flanges of a 59 mm diameter (CF-63) are connected for electron beam transport. Two 48 mm standard flanges (KF-50) are welded to the top and bottom of the spherical cavity for mounting the target elevator and a vacuum sensor. A 40 mm standard flange (CF-40) for mounting a window flange at a scattering angle of 150° opposite of the QCLAM port enables beam monitoring by a camera. The scattering chamber has a spectrometer flange at a scattering angle of 47.5°. A second scattering angle at 132.5° can be achieved by rotating the scattering chamber by 180° perpendicular to the electron beam axis. The wall of the scattering chamber is 4 mm thick and is made of stainless-steel [113]. The scattering chamber is attached to the QCLAM via an adapter.

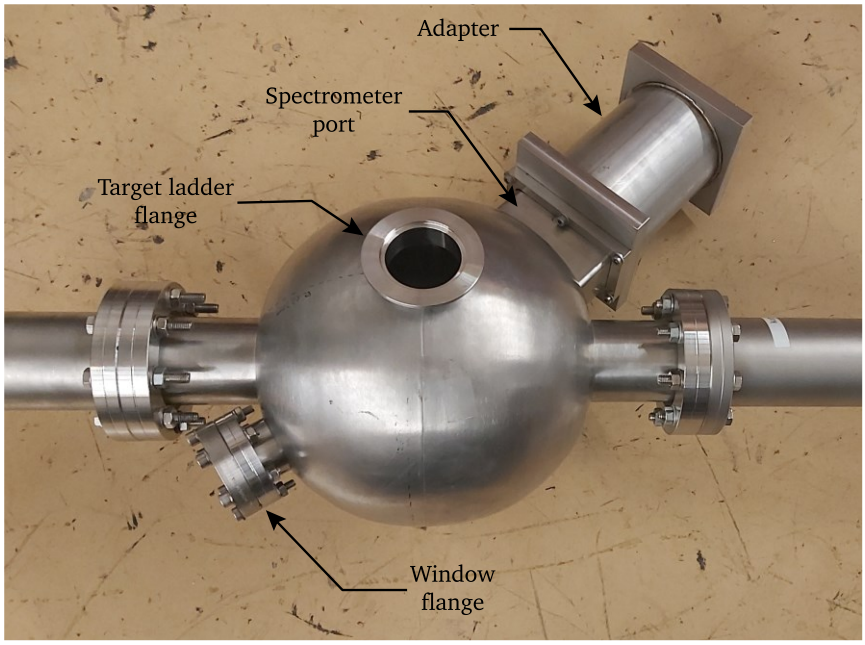

Figure 23: Photo of the ball scattering chamber. It consists of two beam pipe connections on the left and right side of the ball, two flanges for attaching the target elevator and vacuum sensor on top and bottom, a flange to the QCLAM spectrometer and a window flange for beam monitoring. The chamber was designed for (e,e'n) measurements [113].

Despite its smaller size, the ball scattering chamber causes disadvantages for (e,e'γ) measurements. As will be discussed in Chapter 8, the design of the scattering chamber caused a high background rate of 30 kcps [1] per nA during a commissioning measurement. At such high background rates, (e,e'γ) measurements are not feasible. Consequently, the origin of the high background rates had to be identified and eliminated. To identify the background

[1] kcps: kilo counts per second

sources, GEANT4 10.6 [114–116] simulations of the experimental setup were performed, as will be shown in the next section. It was found that the major contribution to the background was caused by the geometry of the ball scattering chamber and its beam pipe. Due to these limitations, a new and scattering chamber design was needed.

In addition, the window flange for the camera limits the positioning of the γ-ray detectors when the QCLAM spectrometer is positioned at a scattering angle of 47.5°, and when the QCLAM is positioned at 132.5°, the camera is exposed to high background radiation which damages the camera chip.

4.2.2. New Scattering Chamber

Due to the limitations of the ball scattering chamber, a new scattering chamber that is optimized for (e,e'γ) measurements was designed and built. In the design of the new scattering chamber, efforts were made to address the limitations of the ball scattering chamber and to make further optimizations with respect to (e,e'γ) measurements.

The requirements for the new scattering chamber are:

- Reduced background rate;
- Additional spectrometer flanges while maintaining the angle interval of 47.5° to 132.5° of the ball scattering chamber to study the momentum transfer dependence of the form factors;
- Window flange for camera at backward direction;
- KF-50 flanges at top and bottom for reuse of vacuum gauges for pressure measurements and the target elevator (see Section 4.4).

For the design of the new scattering chamber, two factors were investigated to reduce the background: the material and the geometry of the scattering chamber. To investigate these factors, detailed GEANT4 simulations of the (e,e'γ) setup including the six $LaBr_3$:Ce detectors, and the scattering chamber were performed

Like the standard scattering chamber of the QCLAM spectrometer, the ball scattering chamber is made of stainless-steel. By using a material with a lower proton number, the background rate can be further reduced. In addition, a simple optimization of the geometry of the scattering chamber is the reduction of the thickness of the material. The minimal thickness depends on the strength of the material. For measurements with an electron beam, the scattering chamber must be evacuated. Thus, the scattering chamber must withstand a pressure of 1 atm. Therefore, the aluminum alloy 3.3535 (AlMg3) is used, that consists of at least 94.35% Al. The second most abundant component is 2.6% - 3.6% Mg. This alloy features high stability and good weldability [117]. Using this alloy, the thickness of the wall could be reduced from 4 mm to 3 mm.

Due to the change to aluminum and the thinner wall of the scattering chamber, less γ-radiation emitted by the target is attenuated by the wall of the scattering chamber, increasing the measured rate of γ-decays of excited target nuclei. Figure 24 shows calculated relative intensities of γ-radiation after passing through different materials of the scattering chamber. The fraction of absorbed radiation in the wall was calculated using the Beer-Lambert law given by

$$I(x,E)/I_0 = \exp(-\mu(E)/\rho\, x). \tag{4.1}$$

Here I_0 and I are the intensities of photons of energy E before and after passing through a material of thickness x with mass attenuation coefficient μ and density ρ. The mass attenuation coefficient of stainless-steel (316L) was taken from [118] and the mass attenuation coefficient for the aluminum alloy was calculated from the mass attenuation coefficients of the different elements of the alloy using [118]

$$\mu(E)/\rho = \sum_i w_i\, (\mu(E)/\rho)_i. \tag{4.2}$$

The mass attenuation coefficients of the elements were taken from [119]. At an energy of 1 MeV, the relative intensity after passing through the material is increased by 15% when 3 mm aluminum alloy is used instead of 4 mm stainless-steel. At an energy of 15 MeV the difference is 8.5%.

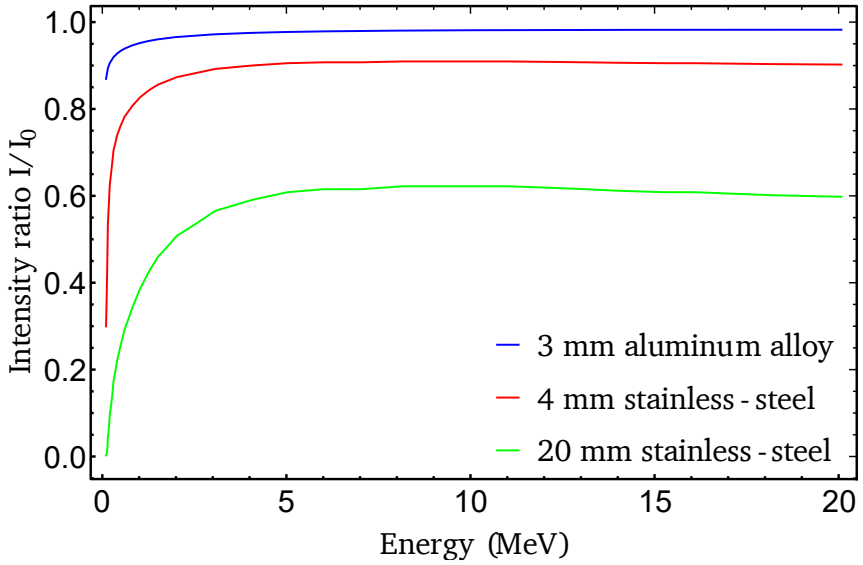

Figure 24: Absorption of γ-radiation after passing through matter as a function of energy. The standard scattering chamber absorbs a substantial part of the radiation due to its thickness of 20 mm. By reducing the wall thickness and using an aluminum alloy, less radiation is absorbed in the new scattering chamber than in the ball scattering chamber.

Further optimizations of the geometry of the new scattering chamber design were done by GEANT4 simulations using the stainless-steel material for better comparability to simulations using the ball scattering chamber. For realistic simulation with sufficient statistics, 10^9 electrons with an energy of 65 MeV were shot at a recreation of the ^{96}Ru target described in Section 8.1. For the simulations, it is assumed that the QCLAM is positioned at an angle of 47.5° and the target is rotated to the corresponding angle of 23.75° for transmission geometry (see section 3.3). Six $LaBr_3$:Ce detectors were placed in two columns at horizontal angles of 90° and 145° and vertical angles of -45°, 0° and 45°. The two detectors in the beam plane are positioned 165 mm and the remaining four detectors 250 mm from the target. For the simulations, the $LaBr_3$:Ce detectors are mounted in the housings (see Section 4.5.2) and a 5 mm lead filter and a 2 mm copper filter in front of each detector is used. This represents the reference geometry (see Figure 25) that will be used for a comparison between the scattering chambers.

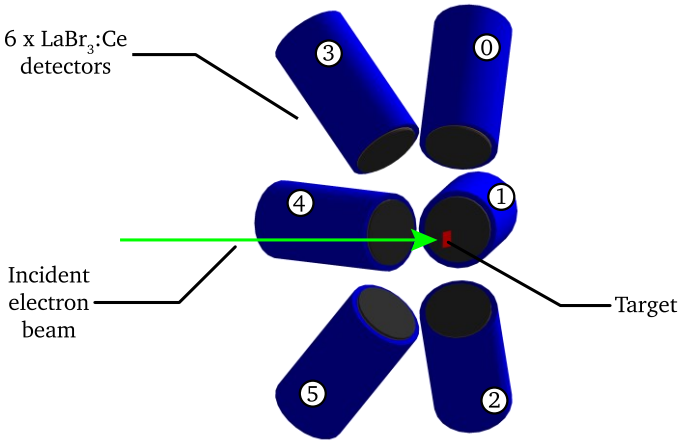

Figure 25 The reference geometry consists of a ^{96}Ru target with ^{197}Au backing surrounded by six $LaBr_3$:Ce detectors.

Simulations have shown that the ball scattering chamber generates the background mainly at the back of the chamber and the adjacent beam pipe, which has an inner diameter of 59 mm. This has been corrected in the design of the new scattering chamber by increasing the inner diameter of the beam pipe to 154 mm. After the optimization of the geometry was completed, the material was changed to aluminum alloy. Figure 26 shows a comparison of the background sources of the reference geometry with ball scattering chamber (a) and the new (e,e'γ) scattering chamber consisting of aluminum alloy (b). The number of interactions projected on the horizontal plane per mm^2 from a top down perspective is shown in (c) for the ball scattering chamber and in (d) for the (e,e'γ) scattering chamber. Both plots use the same color coding. The yellow and red areas upstream of the center of the scattering chamber show areas where the high background radiation originates. The new scattering chamber creates much less background, as can be seen on the green color of the beam pipe. These optimizations reduced the background in the individual $LaBr_3$:Ce detectors by 74% to 90% compared to simulations using the ball scattering chamber. A comparison of the background count rates of the simulations for the different discussed geometries is listed in Table 5.

Table 5: Comparison of count rates obtained by GEANT4 simulations for different scattering chamber designs and materials. Reference: Geometry consisting of target and detectors; Ball chamber: Ball scattering chamber added to reference geometry; Chamber ss: new chamber design made of stainless-steel added to reference geometry; Chamber Al: new chamber design made of aluminum alloy added to reference geometry. For the simulations shown, $5{\cdot}10^9$ electrons were shot at the target. The numbering of the detectors corresponds to the numbering in Figure 25.

Geometry / Material	Detector 0 (kcps/nA)	Detector 1 (kcps/nA)	Detector 2 (kcps/nA)	Detector 3 (kcps/nA)	Detector 4 (kcps/nA)	Detector 5 (kcps/nA)
Reference	5.13±0.08	10.69±0.12	5.13±0.08	1.23±0.04	1.22±0.04	1.23±0.04
Ball chamber	54.0±0.3	53.4±0.3	53.5±0.03	37.6±0.2	21.3±0.2	37.6±0.2
Chamber ss	8.81±0.10	14.0±0.13	8.47±0.10	3.86±0.07	3.87±0.07	3.94±0.07
Chamber Al	5.76±0.08	11.1±0.1	5.65±0.08	1.44±0.04	1.48±0.04	1.52±0.04

The background per detector is only 1.3 to 3.2 times larger when using the new (e,e'γ) scattering chamber compared to the reference geometry without scattering chamber. Consequently, further optimizations on the geometry can only achieve small reductions in the background rate.

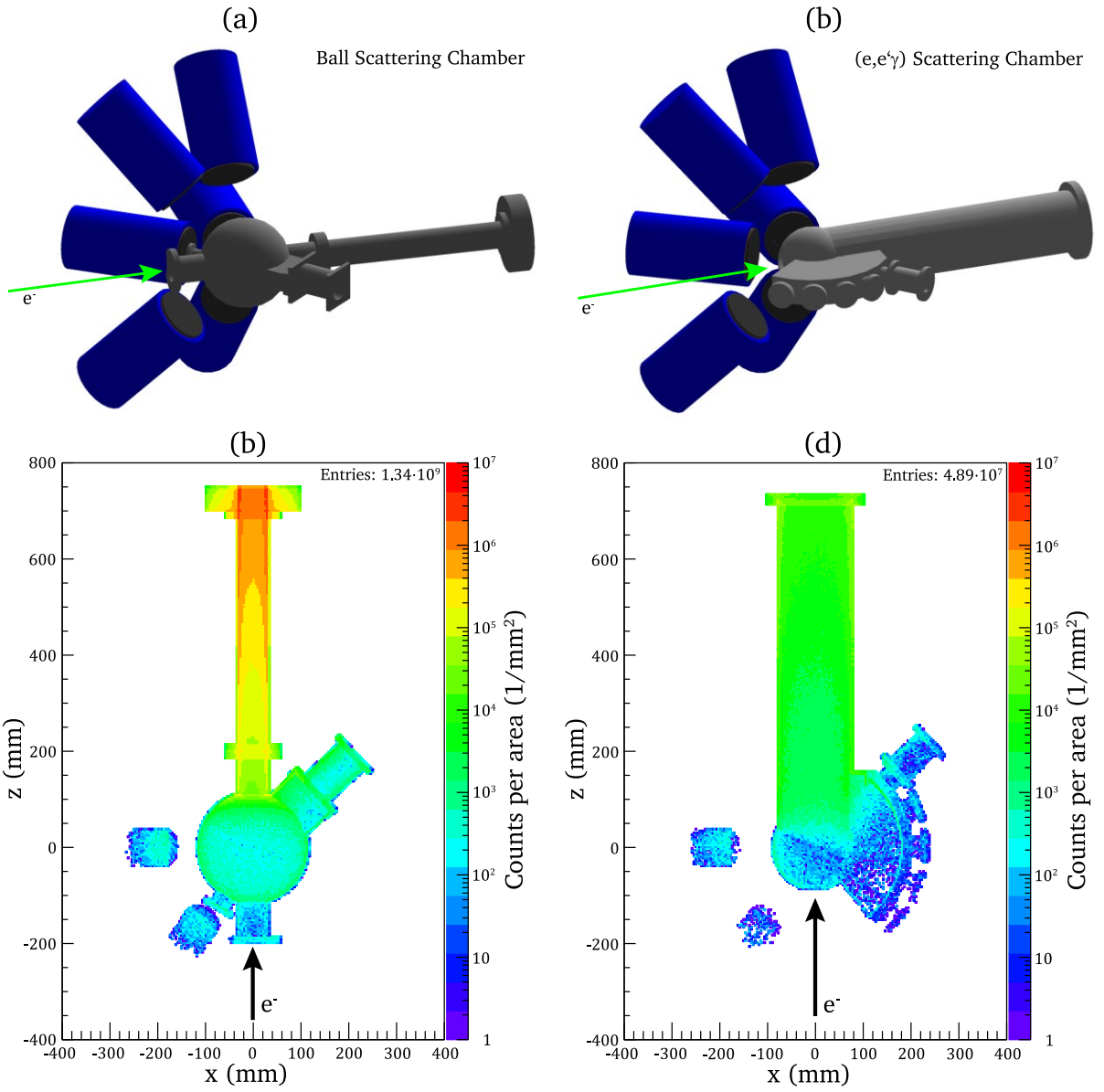

Figure 26: (a): Geometry of the simulation with the ball scattering chamber. (b): Geometry of the simulation with the new (e,e'γ) scattering chamber. (c): GEANT4 Simulation of the ball scattering chamber consisting of stainless-steel. (d): GEANT4 simulation of the new scattering chamber consisting of aluminum alloy. For better visibility, the only component of the $LaBr_3$:Ce detectors plotted are the detector crystals. The lead shielding and housing were suppressed. For the simulations shown, $5 \cdot 10^7$ electrons were shot at the target.

The final model of the new scattering chamber is shown in Figure 27. It consists of a sphere with an inner diameter of 180 mm, to which beam pipes, flanges and an extension box are welded. The beam pipe through which the beam is delivered to the target has an inner diameter of 38.5 mm to leave space for the positioning of the γ-ray detectors. The exit beam tube has a large inner diameter of 154 mm to reduce the background as it was shown by

simulations. Since aluminum is softer than stainless steel, copper gaskets cannot be used as sealing material. Instead, the flanges on both ends of the scattering chamber have grooves for O-rings, which are compatible with the CF-63 and CF-160 flanges in the beamline. For positioning the targets in the electron beam and changing the targets during the measurement campaign, the target elevator, described in section 4.4, is mounted on the upper KF-50 flange of the scattering chamber. Vacuum sensors for monitoring the pressure in the scattering chamber are attached to the lower KF-50 flange. A KF-40 window flange is located 30° below the entrance beam pipe, which is used for beam monitoring by a camera outside of the scattering chamber. At this position, a low background is expected, regardless of the spectrometer angle. The flanges for connecting the scattering chamber to the QCLAM spectrometer are attached to a box, which was welded to the side of the scattering chamber. This allows five spectrometer flanges in the interval from 47.5° to 132.5° in increments of 21.25° with the least possible restriction of the solid angle. The scattering chamber is attached to the spectrometer with a new adapter that is shown in Figure 28. This is necessary to realize five spectrometer angles with a solid angle of 25 msr each, which is close to the effective solid angle acceptance of the QCLAM spectrometer. The new scattering chamber was manufactured by *Kreß GmbH* [120]. A vacuum test performed by the manufacturer showed a leakage rate of $1 \cdot 10^{-6}$ mbar l/s [120].

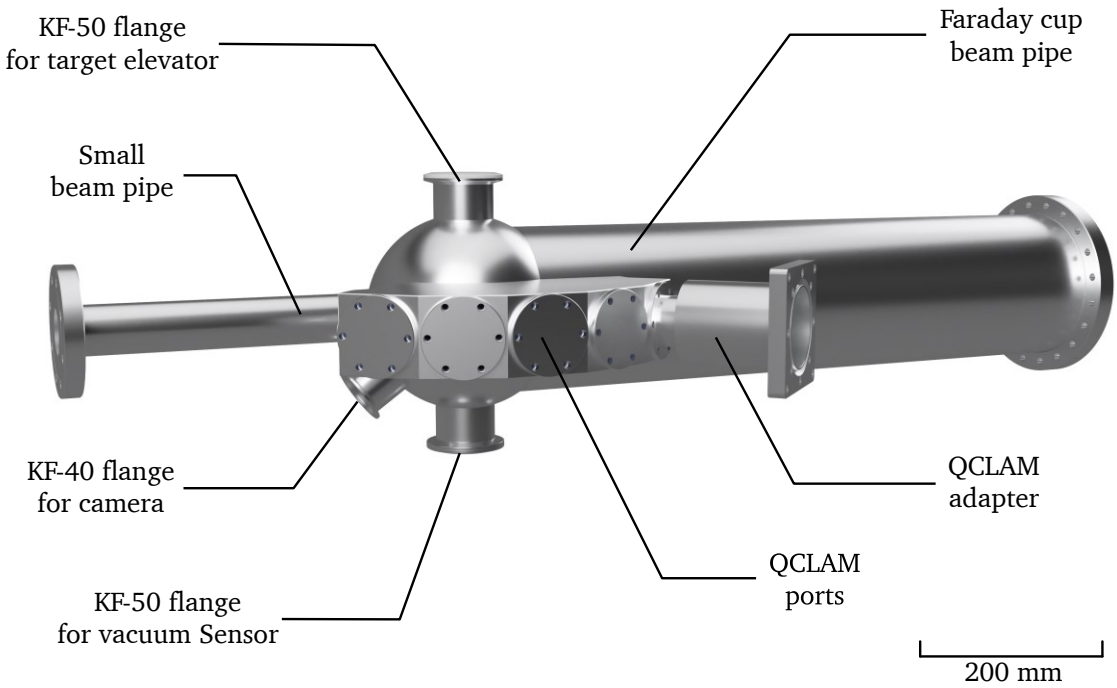

Figure 27 The new scattering chamber has a larger beam pipe behind the target. The QCLAM spectrometer can be flanged to the five side-mounted flanges at angles ranging from 47.5° to 132.5°. Top and bottom flanges are provided for the target ladder elevator and vacuum sensors. The camera flange is located below the small beam tube. The Figure was created using Autodesk Fusion 360 [106].

The scattering chamber is connected to the QCLAM spectrometer using an adapter, which is shown in Figure 28. When the scattering chamber is evacuated and connected to the QCLAM, the air pressure applied externally pushes it to the QCLAM with a force of 172 N. To prevent the scattering chamber from moving towards the QCLAM spectrometer four threaded bolts are clamped between the adapter and the front of the spectrometer.

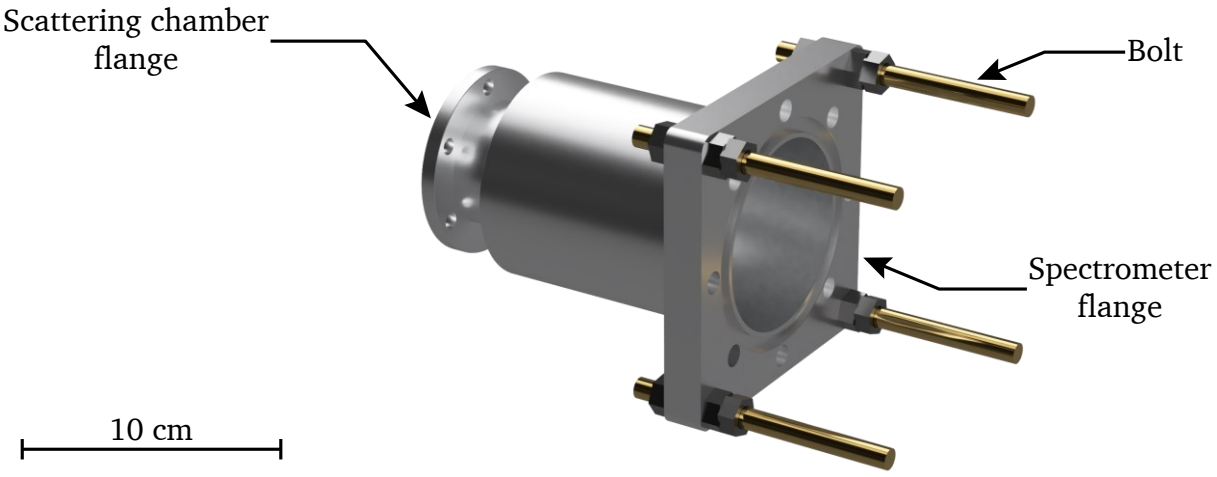

Figure 28: The new adapter of the (e,e'γ) scattering chamber is used to connect the scattering chamber to the QCLAM spectrometer. The adjustment of the distance between scattering chamber and spectrometer is done by the four threaded bolts. The Figure was created using Autodesk Fusion 360 [106].

4.3. Scattering Chamber Holding Structure

The scattering chamber holder is mounted around the center of rotation of the QCLAM spectrometer and is used to position the scattering chamber and detector array. The scattering chamber holder consists of three components, an adapter plate, the support struts with beam tube clamps and a camera device. The complete scattering chamber mount is shown in Figure 29 and technical drawings can be found in Appendix 12.3. Instructions for mounting the scattering chamber holder can be found in Appendix 12.6.

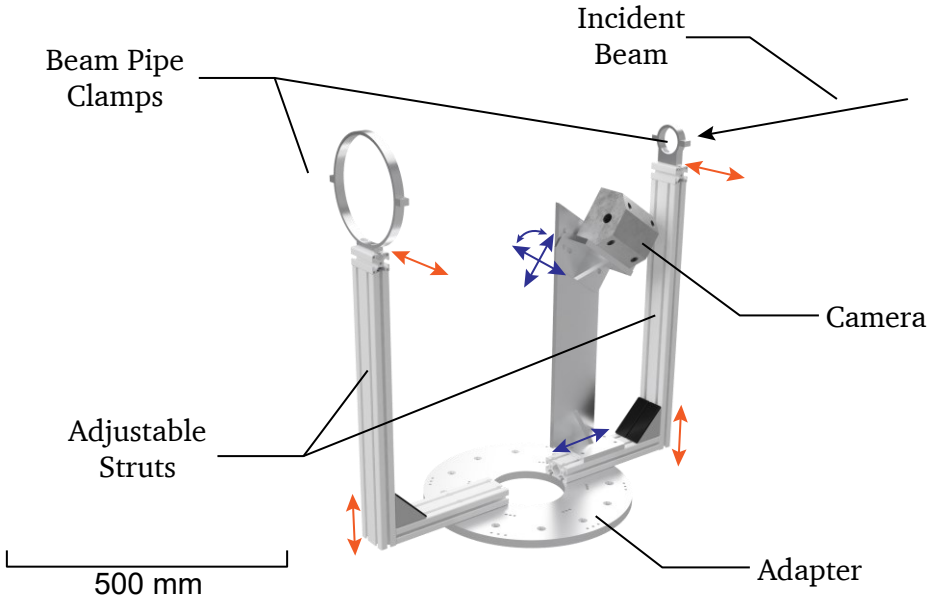

Figure 29: CAD-model of the scattering chamber holding structure. The cylindric panel is mounted on top of the center of rotation of the QCLAM. Height and transverse position can be adjusted to align the scattering chamber. Figure created using Autodesk Fusion 360 [106].

The scattering chamber holder allows exact positioning of the scattering chamber, which is necessary to attach the scattering chamber to the spectrometer and facilitates the alignment of

the targets. The holding struts were manufactured by *item Industrietechnik GmbH* [107] and are attached to the adapter plate. The vertical struts can be moved vertically along the grooves and the beam tube clamps can be moved horizontally along the grooves, allowing alignment transverse to the beam axis. Beam pipe clamps corresponding to the pipes on both scattering chambers have been manufactured so that the clamps can be used for both scattering chambers.

Since the camera flange of the new scattering chamber is mounted 35° below the beam axis, a new camera mount is required. The new camera mount is attached to the grooves of the support struts and can thereby be moved along the beam axis. Two slotted holes allow the height and angle of the camera to be adjusted for optimal alignment with the target. The standard lead housings [121] for protecting the camera chips from background radiation served as a template.

The adapter plate of the scattering chamber holder is mounted to the center of rotation of the QCLAM spectrometer and acts as the central element of the experimental setup to which all other components are connected. The adjustable scattering chamber holding struts and the detector array (see section 4.5.3) are attached to the adapter. The adapter plate consists of an aluminum ring, making the spike that represents the pivot point of the spectrometer accessible for alignment of the entire experimental setup. This is a special feature of the new (e,e'γ) experimental setup and is not directly accessible when using the other scattering chambers. The alignment of the adapter plate is done using two reference lines parallel and perpendicular to the beam axis and the reference markings at the QCLAM setup. Threaded holes were drilled in the plate for mounting and alignment of the scattering chamber holder and the detector array.

The horizontal angles of the γ-ray detectors are determined by the adapter plate of the scattering chamber holder. To find suitable angles, the rate of elastically scattered electrons impinging on the surface of a detector was calculated using the Mott formula (Equation (2.32)) for an estimate of the background. For these calculations, a 100 nA electron beam scattering on the ^{96}Ru target described in section 8.1 was assumed. To simplify the calculations, a constant Mott cross section at the detector surface with diameter 3” and a distance of 165 mm between target and detector was used. Figure 30 shows the calculated rate of elastically scattered electrons impinging the surface of the detector. The rate of elastically scattered electrons decreases with increasing scattering angle by several orders of magnitude due to the angular dependence of the Mott cross section. Therefore, the γ-ray detectors should be positioned at the largest possible scattering angles. Taking geometric constraints into account, the angles 90° and 145° were selected, each with the possibility of moving to 5° smaller or 5° larger angles. The possible angles are listed in Table 6. For possible future applications, for example the measurement of light atomic nuclei where lower backgrounds are expected, additional connectivity has been added at small angles. It should be noted that only elastically scattered electrons were considered, and the actual background will be larger due to further processes. However, this does not change the choice of angles.

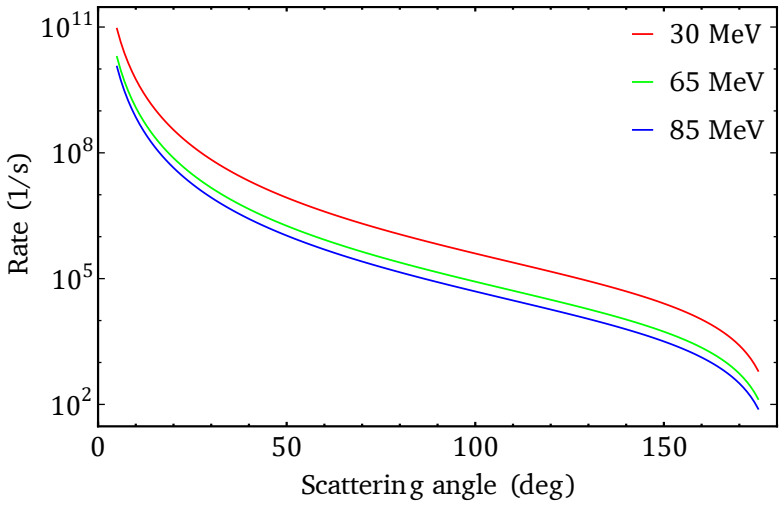

Figure 30: Rate of elastically scattered electrons impinging on a 3" diameter surface at a distance of 165 mm to the target (target and geometry from GEANT4 simulation reference geometry (see section 4.2.2)) per second as a function of scattering angle at a beam current of 100 nA.

Table 6: Listing of angles at which the detector array can be attached to the adapter plate. The angles are divided into groups, and within each group there are three angles with the offsets -5°, 0° and +5°. The angles with negative values are on the side of the QCLAM spectrometer and can only be used with the old, ball scattering chamber.

Group	Angles
1	30°, 35°, 40°
2	85°, 90°, 95°
3	140°, 145°, 150°
4	-40°, -45°, -50°
5	-145°, -155°, -160°

4.4. Target Elevator

On top of the scattering chamber, the target elevator is attached, which allows to move different targets into the electron beam. In addition to the primary measurement target, at least one luminous target (usually BeO) and one empty target location are required for adjusting the electron beam. The target elevator [113] of the ball scattering chamber including the stepper motor type 17HS-240E from *Mclennan* [122] is reused. To control the stepper motor, a new driver of type ST-5-EE [123] from *Applied Motion Products, Inc.* is used. It is configured by the software ST Configurator [124] and operated by the program Q Programmer [125]. Both programs are installed on a dedicated computer inside the experimental hall. It allows the control of the target elevator during the experiment via a remote connection.

During the preparation of the first (e,e'γ) measurement, it was noticed that after mounting the target elevator, the target ladder was not positioned centrally in the scattering chamber and there was no possibility to correct it. Therefore, a new alignment attachment was designed, which is mounted between the scattering chamber and the target elevator. It consists of a

bellow between two flanges and three threaded bolts, that allow to bend the bellow and thereby changing the position of the target. The full target ladder system is shown in Figure 31.

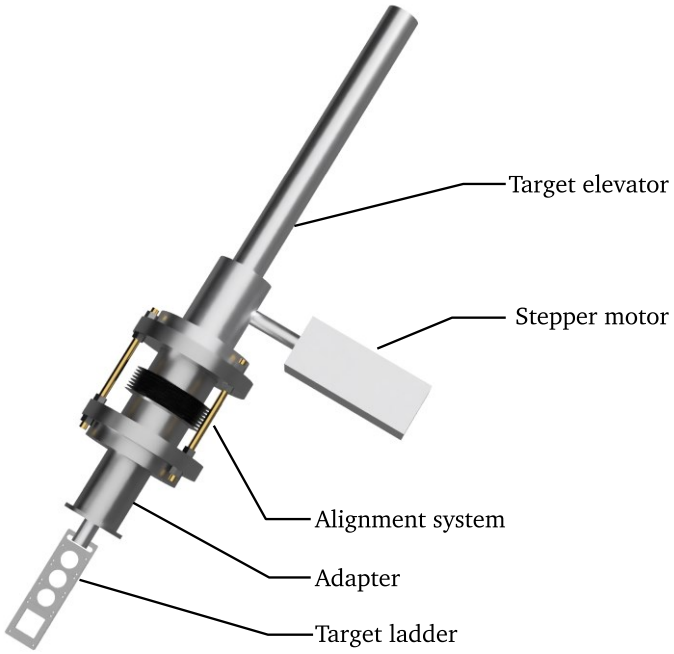

Figure 31: The target elevator system consists of the target elevator, an alignment component, an adapter, and the target ladder. The Figure was created using Autodesk Fusion 360 [106].

For a step-to-path calibration of the target elevator, it was moved repeatedly by a fixed number of steps and the distance covered was measured each time by a sliding caliper. On average, the target ladder moves 1.589(9) mm per 1000 steps. No significant change in position was detected after repeated movements of 80 mm with the target elevator in a horizontal position. Technical drawings of target ladders and target frames are provided in Appendix 12.2.

4.5. γ-ray Detectors and Holding Structure

The detector holding structure is used to position γ-ray detectors around the scattering chamber. The design of the new detector array had to consider the type of γ-ray detectors used, reduction of background radiation and requirements for the mechanical structure. These considerations are discussed in the following subsections.

4.5.1. $LaBr_3$:Ce Detectors

The γ-ray detector array uses $LaBr_3$:Ce detectors of the type Saint-Gobain BrilLanCe®380 [32]. These are inorganic cerium-doped lanthanum bromide scintillation crystals. The first $LaBr_3$:Ce detectors were developed in the early 2000s and consisted of small crystals [126]. In the following years larger crystals were grown and crystals with diameter and length of 3" are typical used. Larger crystals with higher efficiency are available [127]. $LaBr_3$:Ce detectors are characterized by excellent time resolution in combination with good energy resolution and high efficiency compared to other scintillation detectors [128]. These properties make $LaBr_3$:Ce detectors highly suitable for coincidence measurements. In the following the

properties are described in more detail and comparisons between 3"x3" $LaBr_3$:Ce and NaI(Tl) detectors are shown in Figure 32.

- Energy resolution and linearity: $LaBr_3$:Ce scintillators have a high brightness of about 63 photons/keV, leading to a relative energy resolution of 2.9% at 662 keV. In addition, there is a strongly linear response [128]. However, deviations from an ideal linearity are observed when a large energy interval is measured [129].
- Timing properties: $LaBr_3$:Ce crystals have a short scintillation decay time below 30 ns, achieving time resolutions below 1 ns and allowing the detectors to be used at high count rates [130]. Measurements at high count rates have shown that up to 500 kcps the relative energy resolution of the 662 keV line in ^{137}Cs is below 4% and at higher rates, up to 10 Mcps [2], the loss of events caused by pileup effects in the full energy peak can be reduced by applying a pileup correction technique [131].
- Efficiency: Due to the high density of 5.08 g/cm^3, $LaBr_3$:Ce detectors have high full energy peak (FEP) efficiency. At 662 keV, the efficiency of $LaBr_3$:Ce detectors is 118% of the FEP efficiency of NaI(Tl) detectors. At higher energies, the efficiency increases to about 165 % of the efficiency of NaI(Tl) detectors [128].

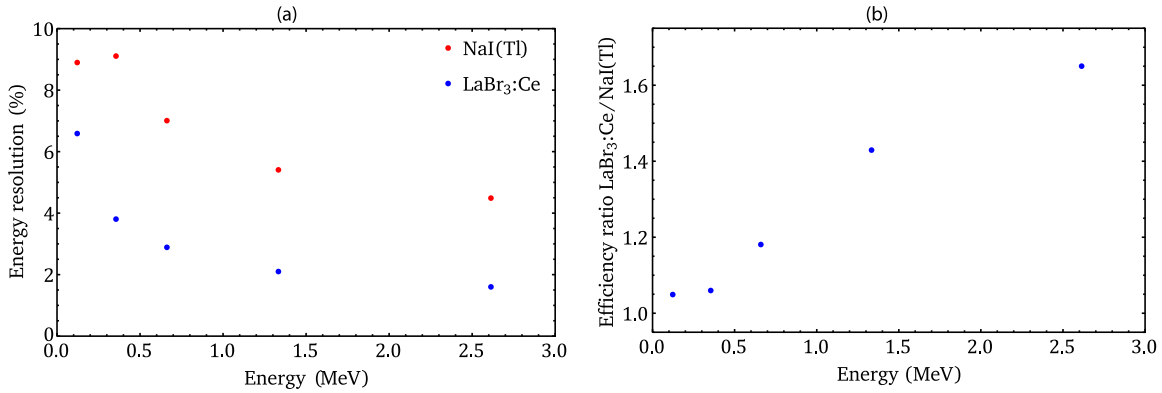

Figure 32: Relative energy resolution of a $LaBr_3$:Ce detector and a NaI(Tl) detector (a) and full energy peak efficiency (b) of a $LaBr_3$:Ce detector with diameter and length 3" relative to a NaI(Tl) detector of the same size. Data taken from [128].

Due to the good time resolution, a narrow time gate can be used to select the events corresponding to the incoming electron beam. The high efficiency of the detector increases the coincident count rate and allows measurements of high-energy photons, for example, in the range of 15 MeV, which is required to measure the γ-decay of giant dipole resonances to the ground state. In addition, the short decay time makes the detectors suitable for measurements at count rates of several 100 kcps.

A characteristic of $LaBr_3$:Ce detectors is their intrinsic activity, which is caused by radioactive isotopes of the detector material (^{138}La, ^{138}Ba and ^{138}Ce) and contaminants (^{227}Ac). ^{138}La decays to 66 % via electron capture to ^{138}Ba and to 34 % via β^- decay to ^{138}Ce. The excited ^{138}Ba nucleus decays to the ground state by emission of a 1.436 MeV photon and a 32 keV X-ray is emitted simultaneously. When both photons deposit their energy inside the detector, a sum peak of 1.468 MeV is measured. The β^- particle emitted in the decay to ^{138}Ce has a

[2] Mcps: mega counts per second

maximum energy of 255 keV and occurs coincident with the ground state decay of ^{138}Ce by emission of a 789 keV photon. The intrinsic background at energies above 1.55 MeV is caused by the alpha decay of ^{227}Ac [128,132]. A typical background spectrum is shown in Figure 33. In coincidence measurements, the intrinsic background can be suppressed.

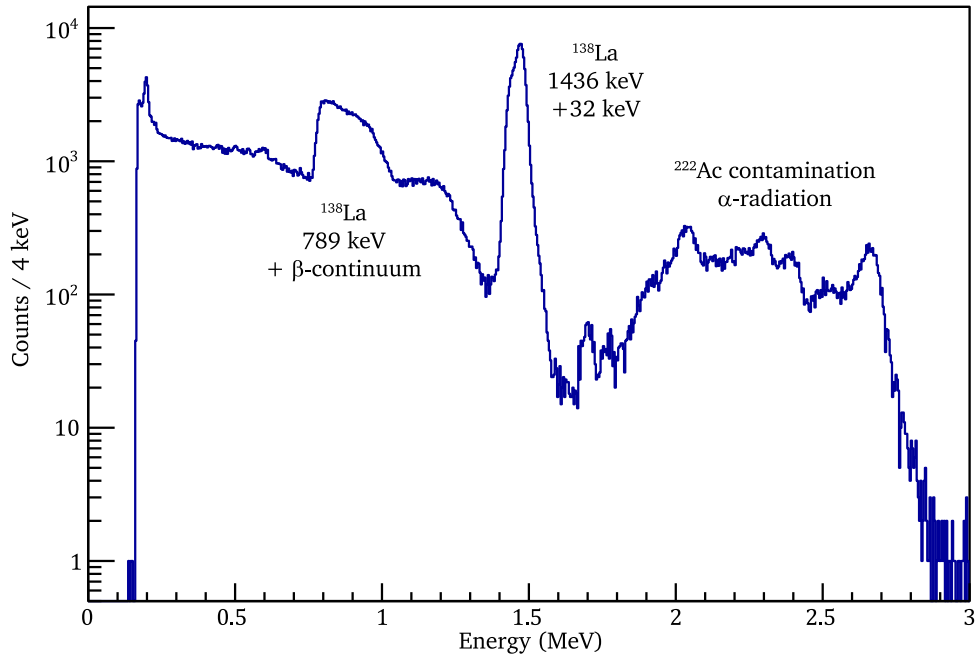

Figure 33: The background spectrum of a $LaBr_3$:Ce detector is dominated by the intrinsic activity of the detector. The measurement duration was 27 minutes with an average rate of accepted events of 318 cps.

The energy deposited in the detector is converted into optical photons, which are converted into electrons by a photocathode. The electrons are accelerated in the electric field of the dynodes of a photomultiplier tube and amplified when they impinge on the dynode in order to get a measurable signal [133]. At the Institute for Nuclear Physics at the TU Darmstadt 17 $LaBr_3$:Ce detectors are available, one of them is shown in Figure 34. They are equipped with *Hamamatsu Photonics K.K.* R6233-100 SEL photomultiplier tubes [134]. Three different voltage dividers are used to distribute the high voltage applied to the detector to the dynodes of the PMT. The detectors are equipped with voltage divider of types E1198-26 from *Hamamatsu Photonics K.K.*, LABRVD designed by the *University of Milano* and an in-house design of the electronics workshop [135]. The high voltage for up to 8 detectors is generated by two *CAEN* Mod. N1470 NIM modules [136] that generate a maximum voltage of 8 kV and a maximum current of 3 mA. The high voltage power supply modules are remote controlled by the manufacturer's software GECO [137] via the dedicated computer inside the experimental hall that is also used to control the target elevator.

Photomultiplier tubes are sensitive to external magnetic fields, which can cause a modification of the trajectories of the electrons in the PMT, and prevent some of them from reaching the next dynode. Thus, the amplitude of the generated signal decreases resulting in a compressed spectrum with reduced energy resolution. Since the detectors are positioned near the quadrupole magnet of the QCLAM spectrometer in the (e,e'γ) experimental setup, a magnetic field shielding was constructed to reduce the influence of the magnetic field (see Section 4.6).

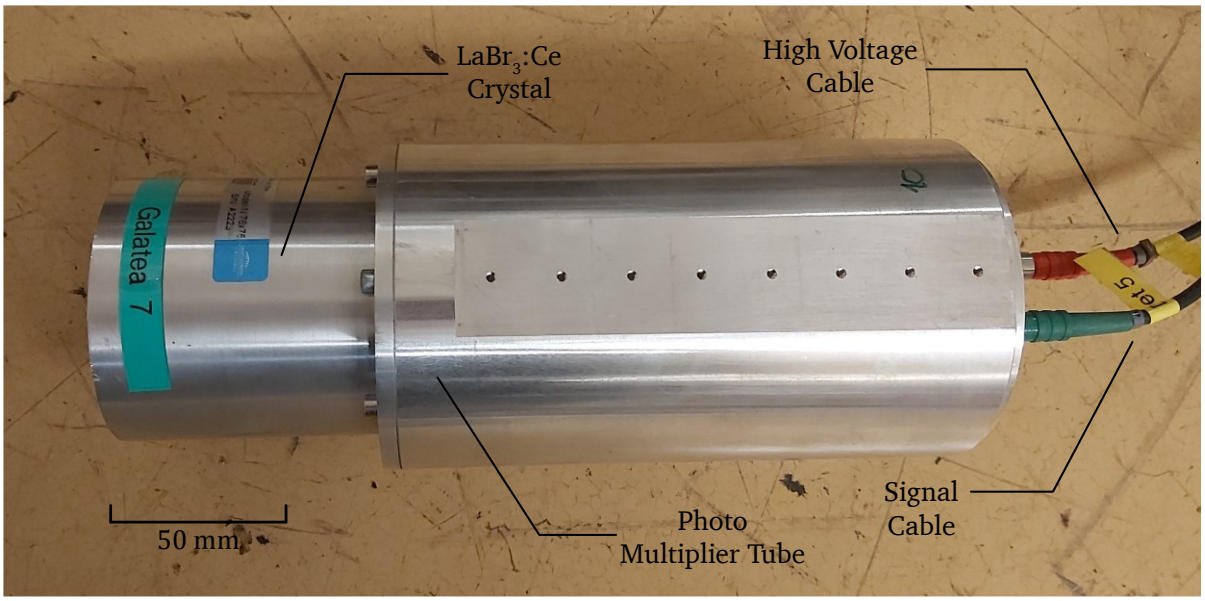

Figure 34: Photo of a $LaBr_3$:Ce detector. The $LaBr_3$:Ce crystal is mounted inside the left part of the detector and the PMT is mounted in the right side.

4.5.2. Detector Housing and Lead Shielding

As high background count rates up to several Mcps are expected in (e,e'γ) measurements, the detectors must be surrounded by shielding material to reduce the background radiation. The $LaBr_3$:Ce crystal and the photomultiplier tube are surrounded by a thin aluminum housing. For better protection against background radiation, an external housing consisting of an aluminum case and a lead shielding was designed and produced [138]. The improved design, shown in Figure 35, used for the new (e,e'γ) setup is built on the previous design, reusing its parts. The crystal is surrounded by a 3 cm lead shielding, while the PMT in the rear area, which contains the photomultiplier tube, is shielded by 2 cm of lead. In the rear of the PMT, two holes are placed in the aluminum case and the lead shielding for the signal and high voltage cables. The aluminum plate and lead shield on the back of the case have two holes, which serve as cable ducts for signal and high voltage cables. Appendix 12.4 contains the technical drawings of the detector housing and the detector sled and Appendix 12.7 contains the instructions for mounting a detector in the housing. The modifications of the design are:

- Two handles have been added to the top of the detector housing to facilitate handling of the detectors, which weigh approximately 40 kg.
- At the bottom of the detector, the housing was flattened, and threaded holes were added. The detector sled, which also includes a handle, allows the detectors to be mounted in the new detector array.
- In addition to the 5 mm lead filters, 2 mm thick copper filters were made. Their purpose is to moderate the X-rays generated in the lead filter.
- For improved alignment of the detectors, spikes that can be attached to the front of the detector housing were produced. The spikes have a length of 265 mm and indicate the axis of the detectors, allowing to point the detector to the center of the target. The technical drawing of the spikes can be found in Appendix 12.8.

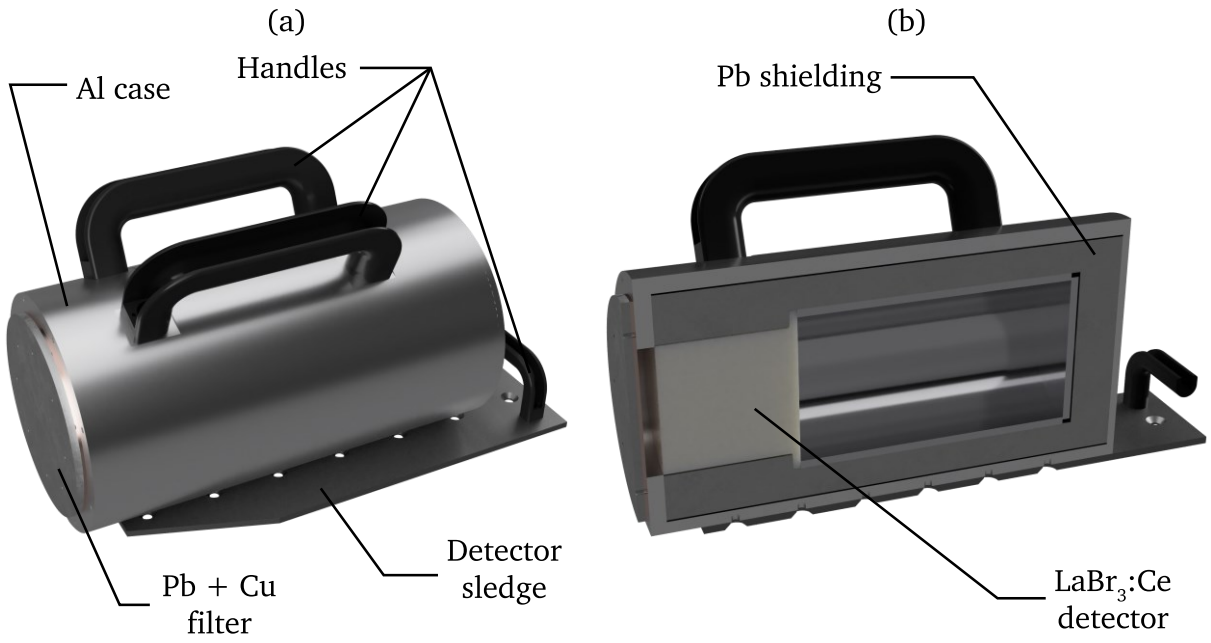

Figure 35 (a): View of the complete detector. The detector is inside the aluminum housing surrounded by lead shielding. Two removable handles are fixed at the top and lead and copper filters can be attached in front of the detector. (b): Cross section through the detector. In the front part of the detector is the scintillation crystal, in the adjacent chamber is the photomultiplier connected. The Figure was created using Autodesk Fusion 360 [106].

The lead shielding integrated in the detector housing protects the detector from radiation incident from the side. A lead shielding in front of the active detector surface also reduces the intensity of γ-radiation emitted from the target. Consequently, a tradeoff must be made between the reduction of background radiation and a low attenuation of γ-radiation emitted from decaying target nuclei. The lead filter reduces the low-energy background while high-energy γ-radiation is affected less. In the lead K_α and K_β radiation are created and would ideally be attenuated before they reach the detector crystal. For this purpose, the thin copper filter is mounted between the lead filter and the crystal to moderate the X-rays created by lead before they reach the detectors. The thickness of the lead filter, and thus the absorption, can be varied by stacking the 5 mm thick lead filters. The ratio of intensities before and after passing through different combinations of filters was calculated using Equation (4.1) and can be seen in Figure 36. The mass attenuation coefficients were taken from [119]. For energies below 1 MeV, the ratio is minimal and thus the attenuation is maximal. The intensity after passing through the filters has a maximum at 4 MeV and slowly decreases thereafter. For the filter configuration 5 mm lead and 2 mm copper, the 511 keV peak dominated in the background is attenuated by 66%, whereas peaks at energies of 2.3 MeV and 15.1 MeV are attenuated by only 29% and 33%, respectively.

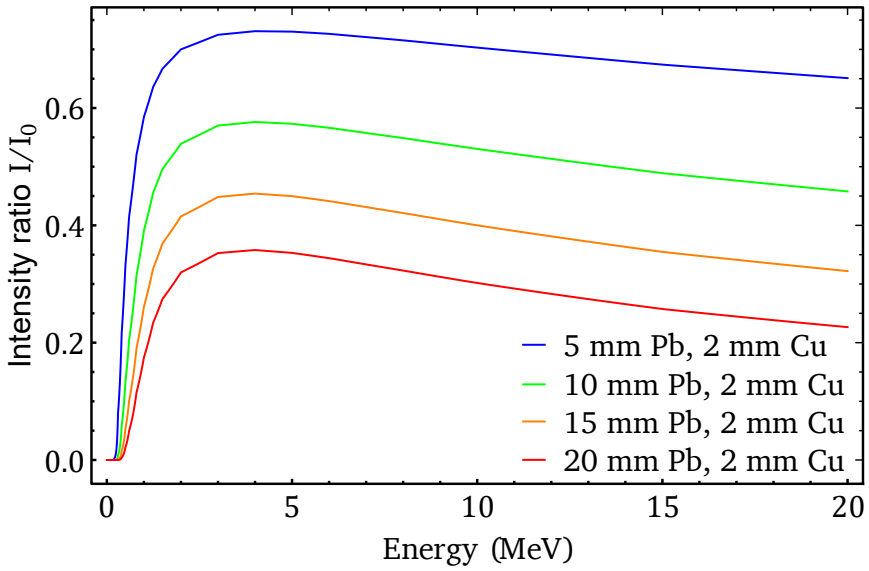

Figure 36: The ratio of outgoing to incoming intensity is shown as a function of photon energy for four filter configurations. Strong absorption at low energies reduces background and count rate in the $LaBr_3$:Ce detectors.

In addition, GEANT4 simulations, for which the results are shown in Figure 37, were performed to evaluate the effect of the filters and to help to determine an appropriate filter thickness for future experiments. For the simulations, a monoenergetic photon source was positioned at the location of the target and a $LaBr_3$:Ce detector was positioned at a distance of 165 mm. Simulations were performed for both scattering chambers and different filter thicknesses with photon energies between 0.1 MeV and 20 MeV. The absolute full energy peak efficiencies were determined in each case.

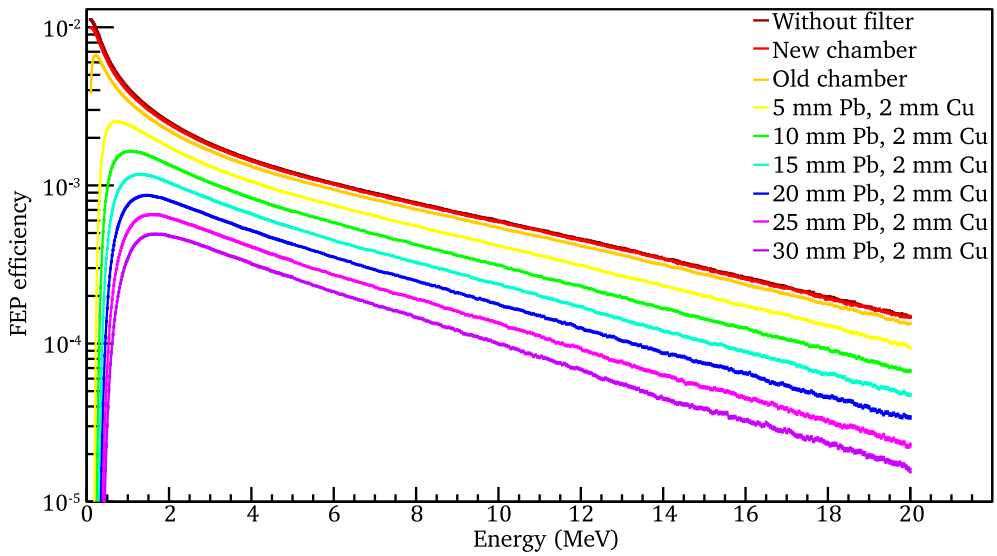

Figure 37: Simulations with monoenergetic photon sources and different combinations of scattering chamber and filters show the reduction of the absolute full energy peak efficiency of a 3"x3" $LaBr_3$:Ce detector at a distance of 165 mm with increasing material thickness. The new (e,e'γ) scattering chamber shows a smaller reduction in efficiency than the old ball scattering chamber. For the simulations with filters, the (e,e'γ) scattering chamber was also used.

The reduction of the full energy peak efficiency when using the new scattering chamber is smaller than the reduction when using the old scattering chamber and can be neglected for

count rate estimations. When the lead filters are used, there is an energy dependent reduction in efficiency of the $LaBr_3$:Ce detectors which is most pronounced at low photon energies, reducing the number of low-energy photons of the experimental background. As the thickness of the lead filter increases, the efficiency decreases, and the maximum efficiency shifts to higher photon energies. From a practical point of view, the minimum photon energies of interest in a measurement should not be below the energy of the maximum efficiency.

The simulated spectra were convoluted with the energy dependent detector resolution taken from [139]. Examples of simulations with photons of energies 1 MeV and 20 MeV are shown in Figure 38. In both cases, attenuation of the full energy peak is evident. Full energy peak efficiencies were calculated using the mass attenuation coefficient of lead and compared to the ones extracted from the simulation. The calculated efficiency consisting of the FEP efficiency and the solid angle, for 1 MeV photons is 0.58 % and the simulated efficiency is 0.61 %. For 20 MeV photons, the calculated and the simulated efficiencies are 0.65 % and 0.66 %, respectively.

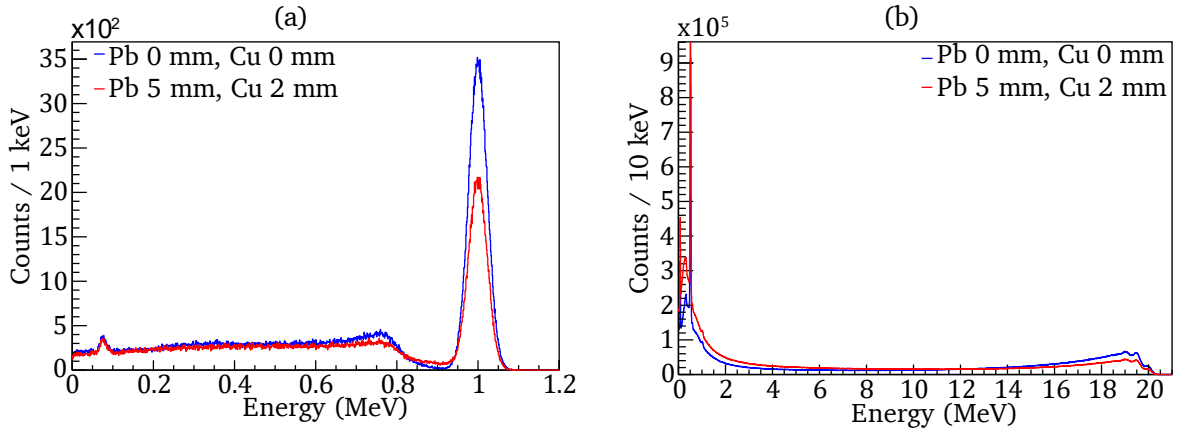

Figure 38: Simulated spectra without filter and with 5 mm lead and 2 mm copper filter. (a): Simulation with monoenergetic photon source of energy 1 MeV. (b): Simulation with monoenergetic photon source of energy 20 MeV. The peak at 75 keV is caused by X-rays generated in the lead housing of the detector.

4.5.3. Detector Holding Structure

The detector array is used to position the detectors around the scattering chamber. The requirements for the detector array are:

- Adjustability: Since the angular distribution of the emitted photons after (e,e'γ) reactions is not isotropic and depends on the transition of interest and the momentum transfer axis, it is required to adjust the horizontal and vertical angles of the detectors.
- Stability: Due to the heavy weight of the lead shielding of the detectors, the detector holder must be sufficiently stable and secured against falling over.
- Modularity: A modular design is needed, which can be expanded/adapted for future measurements.
- Experimental conditions: Due to the high experimental background in electron scattering experiments, the detectors must be positioned primarily at backward angles.

These requirements were considered in the design of the new detector array that is shown in Figure 39. It consists of two towers that are fixed to the adapter plate of the scattering chamber holder, thus setting the horizontal scattering angles of the towers. The distance to

the center of rotation of the spectrometer is set with the angular alignment struts on the detector towers. Three detectors can be installed per tower, one above the other, with design values of the vertical scattering angles of -45°, 0° and 45°. For the adjustment of the experimental setup, the vertical angles can be tuned. The rails on which the detectors are mounted are adjustable in height and angle. To adjust the distance to the target and thereby the solid angle of the detectors, the detector sledges can be moved along the rails. To provide sufficient stability, aluminum profiles manufactured by *item Industrietechnik GmbH* [107] were used in the construction of the detector array. For further stabilization and increased resistance to overturning, the center of gravity is shifted downward by lead weights at the lower end of the towers and the towers are connected to each other on the top side. Instructions for connecting the detector towers to the adapter plate of the scattering chamber holder can be found in Appendix 12.8.

The modular design allows the detector array to be expanded to include additional towers and detectors. For an increased number of detectors per tower, tapered detector housings could be designed, and the use of silicon photomultipliers would allow the use of compact detector housings with reduced weight and easier handling.

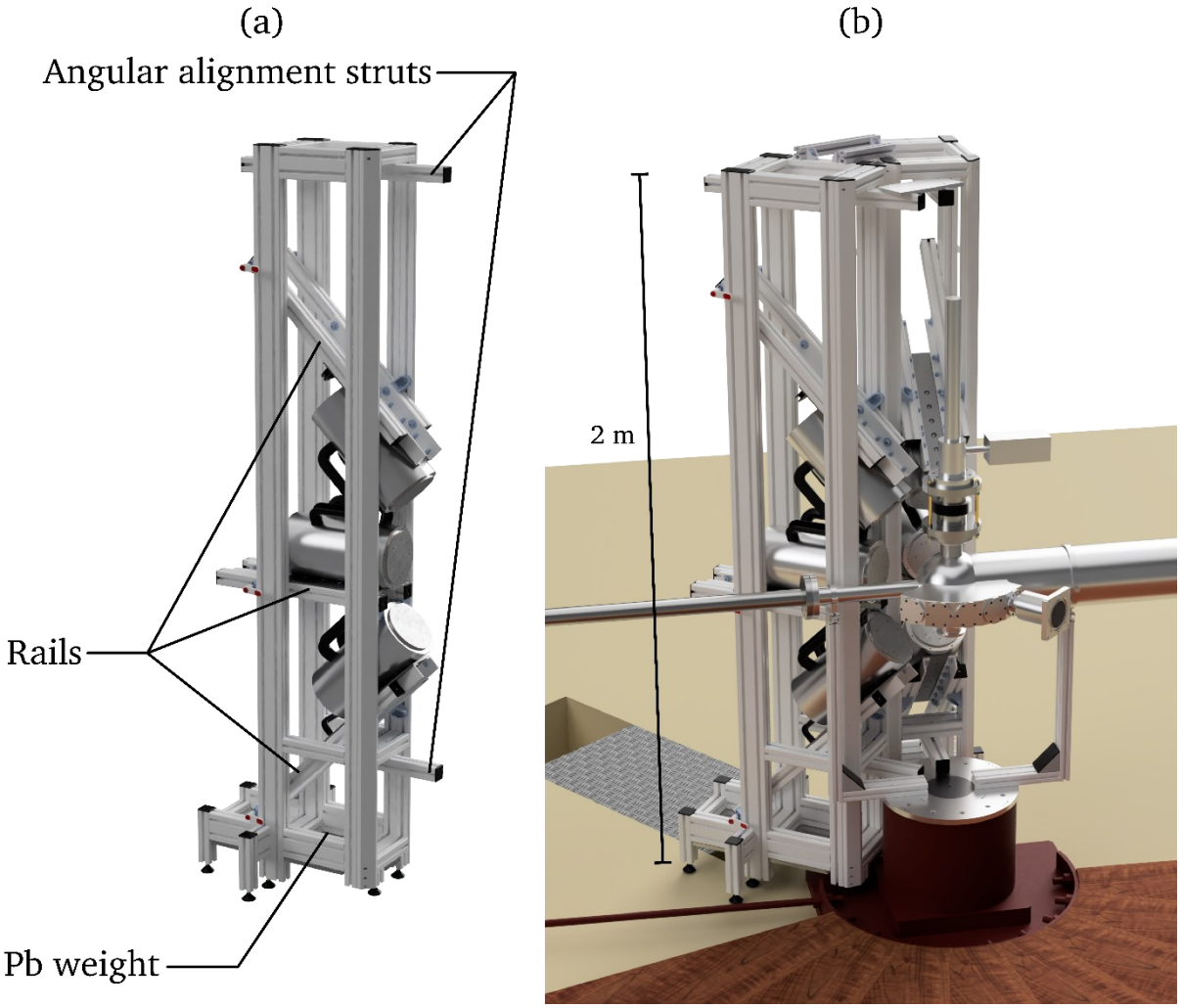

Figure 39: (a): One tower of the detector array contains three $LaBr_3$:Ce detectors, their angles and distances are adjusted by use of the rails. (b): The detector array consists of two towers that are attached to the adapter plate of the scattering chamber holder. The Figure was created using Autodesk Fusion 360 [106].

4.6. Magnetic Field Shielding

The detectors are mounted inside the detector holding structure near the QCLAM quadrupole magnet, which generates a magnetic field with far-reaching field components. In a PMT, electrons are accelerated by an electric field and when they hit a dynode, they release further electrons which are accelerated to the next dynode. In this way an amplification is achieved. However, electrons can be deflected by an external magnetic field and do not reach the next dynode, thus the amplification is decreased. As a result, the signal of the photomultiplier tube in the pulse height spectrum is shifted to smaller channels and the energy resolution is reduced.

To estimate the effect of an external magnetic field on the energy resolution and the peak positions in pulse height spectra, measurements were performed using a ^{22}Na source and a permanent magnet. The strength of the magnetic field was varied by the distance between the detector and the magnet. For this measurement, an *ORTEC* EASY-MCA multi-channel analyzer was used. The evaluation of the measurement showed that the signal amplitude of the detector was not suitable for the input range of the module, resulting in signals with a large amplitude not being processed correctly. The full energy peak of the 1.275 MeV photons of the ^{22}Na source was affected by this in measurements with a weak magnetic field, so the 511 keV peak was used for the analysis. Figure 40 shows the relative shift of the 511 keV peak and the energy resolution as a function of magnetic field strength measured by a Hall effect sensor. Small field strengths of 0.5 mT shift the peak position by about 48 %. While the effect on the energy resolution is smaller, at 0.5 mT the resolution decreases from 3.8 % to 4.1 %. Due to different magnetic field geometries and absolute values, these findings cannot be applied quantitatively to the effect of the quadrupole magnet, but qualitative conclusions are possible.

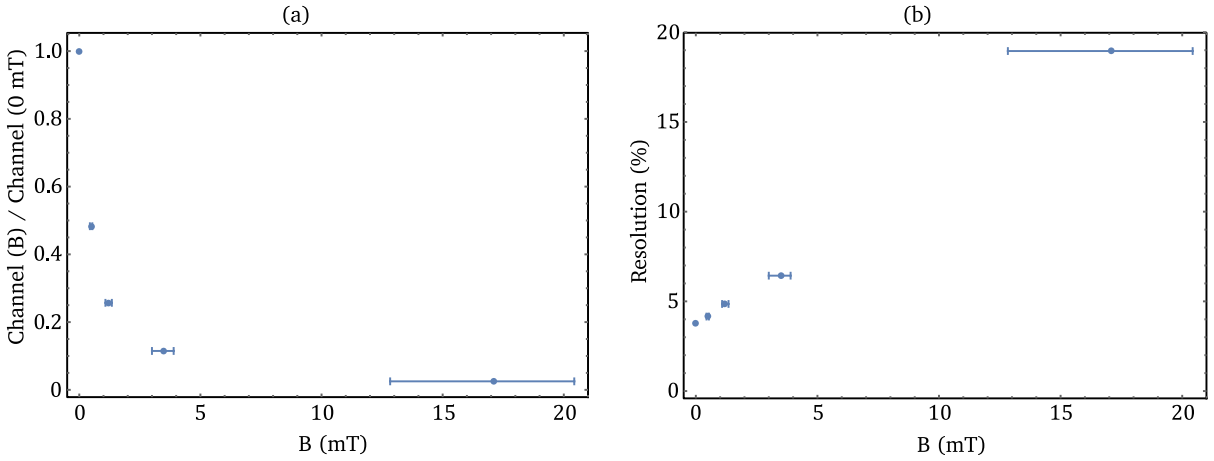

Figure 40: The effects of an external magnetic field on the position (a) and resolution (b) of the 511 keV peak of a ^{22}Na source measurement are shown. A $LaBr_3$:Ce detector with photomultiplier tube and a permanent magnet were used for the measurement. The magnetic field strength at the surface of the detector was varied by the distance between the detector and the permanent magnet.

During the preparations for the beam time in November 2019 (see Chapter 7), measurements on the effect of the magnetic field of the QCLAM to the γ-ray detectors were performed. Based on an electron energy to QCLAM dipole conversion factor of 1.4 A/MeV [140] and a current ratio between quadrupole and dipole of 1.15 to 1.35 [95], this corresponds to electron energies of 119 MeV to 140 MeV. Due to the linearity of the material [39] of the QCLAM

magnets, these values can be scaled to match other electron energies. Figure 41 compares a spectrum without external magnetic field to a spectrum with external magnetic field of several mT. Without the external magnetic field, the spectrum of the intrinsic activity of the $LaBr_3$:Ce detector shows the expected structures (a). With external magnetic field, the electrons in the PMT are deflected and a part does not reach the next dynode. Therefore, the amplitude of the detector signal decreases and is interpreted by the analysis software as a low energy signal, so that the spectrum is compressed towards zero (b). Additionally, the lower amplitude of the detector signals reduces the energy resolution. A beam energy of 35 MeV was expected for the beam time, the current of 55 A for the dipole magnet and 82.5 A for the quadrupole magnet were chosen for this test. This magnetic field setting is already sufficient to render the spectrum unusable. As the current of the magnets is proportional to the energy of the electron beam, stronger effects are to be expected at higher beam energies.

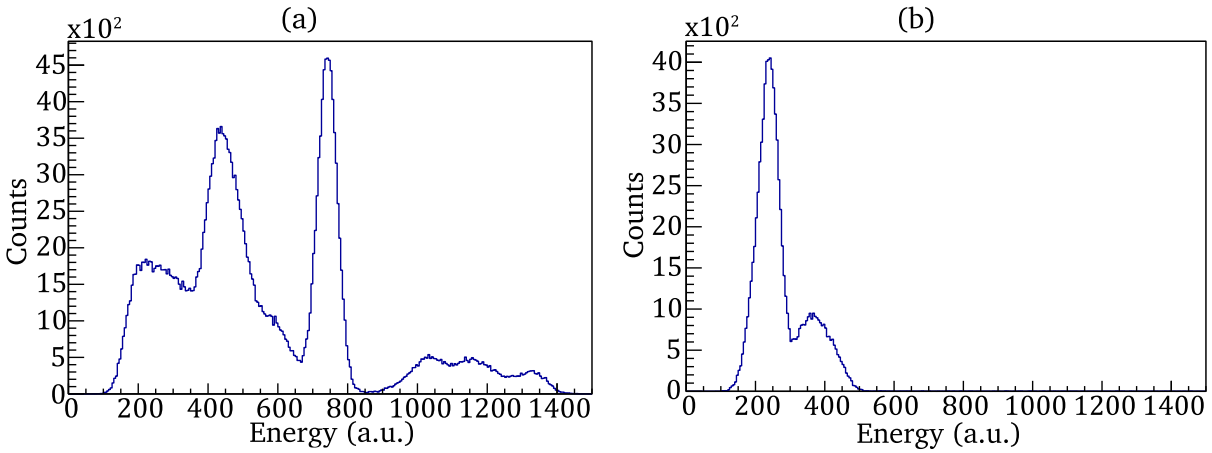

Figure 41: (a): Spectrum of intrinsic activity of a $LaBr_3$:Ce detector without external magnetic field. (b). Spectrum of the intrinsic activity of a $LaBr_3$:Ce detector with a current of 55 A at the dipole magnet and 82.5 A at the quadrupole magnet.

To investigate the expected effect of the quadrupole magnet on the $LaBr_3$:Ce detectors, simulations were performed using CST Studio Suite 2020 [141] to determine the magnetic field strength at the surfaces of the $LaBr_3$:Ce detectors. CST Studio Suite calculates the resulting magnetic field distribution based on the geometry of a magnet. An existing CST project of the QCLAM quadrupole [140] was used for the simulations. Figure 42 shows an example of the geometry used for the CST simulations. The quadrupole magnet of the QCLAM spectrometer is positioned at a scattering angle of 47.5°. In the center of the magnet a volume with the material property vacuum is added to achieve a locally refined mesh for improved accuracy of the simulation. The two components of the magnetic field shielding are placed in front of the quadrupole and on the side of a detector tower. The cutouts on the sides of the magnetic field shielding are necessary due to the geometric constraints caused by the beam pipe. The six $LaBr_3$:Ce detectors are represented by cylinders in two rows representing the two detector towers at 90° and 145° on the other side of the beam tube at a distance of 250 mm from the target at the vertical angles of -45°, 0° and 45°. The origin of the coordinate system is at the location of the target, with the *z*-axis indicating the direction of the incident electron beam. Since good agreement between simulated and measured values of the magnetic field strength has already been demonstrated [140], additional measurements at the positions of

the detectors were not necessary. All simulations were performed with the maximum current of the QCLAM quadrupole magnet of 225 A.

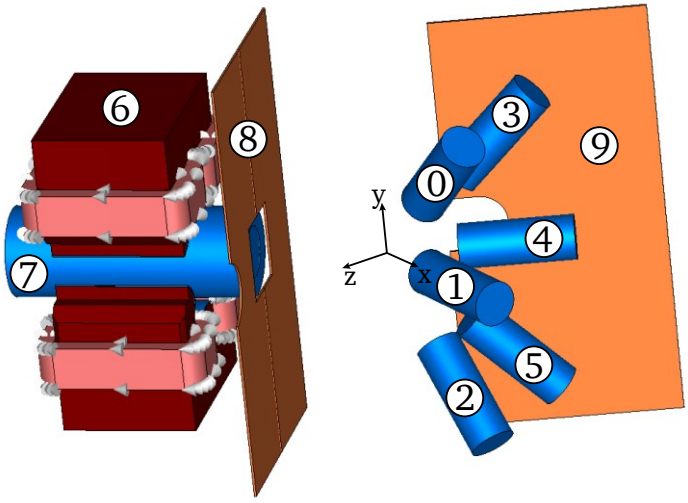

Figure 42: A simplified geometry of the measurement setup was used for the CST simulations. The geometry contains six $LaBr_3$:Ce detectors (⓪ - ⑤), the QCLAM quadrupole magnet ⑥, a vacuum volume for a locally refined mesh for improved accuracy of the simulation ⑦ and the two stages of the magnetic field shielding in front of the quadrupole ⑧ and on the side of a tower ⑨. The coordinate systems origin is placed at the position of the target with the z-axis indicating the electron beam direction. Figure created using CST Studio Suite [141].

The simulations showed a maximum magnetic field strength of 2.5 mT at the surfaces of the detector housings. Figure 40 shows that significant effects on the position and resolution of the $LaBr_3$:Ce detectors can be expected at this magnetic field strength. Based on this, a magnetic field shielding was designed to reduce the strength of the magnetic field at the positions of the detectors. The magnetic field shielding must be suitable for all spectrometer angles between 47.5° and 132.5°, which is why a two-stage magnetic field shield was designed. The first stage of magnetic field shielding consists of a 5 mm thick iron plate in front of the quadrupole magnet, which reduces the magnetic field strength towards the scattering chamber, the second stage consists of a 5 mm thick iron plate at the side of a detector tower. The technical drawings of the magnetic field shielding are included in Appendix 12.5

To investigate the reduction of the magnetic field caused by the magnetic field shielding, a series of simulations were performed with and without the shielding. The results of the simulations can be seen in Figure 43 and Table 7. Due to the larger distance between the detectors and the quadrupole magnet, the magnetic field strengths are smaller at the spectrometer angle of 47.5° than at 132.5°. Simulations using a spectrometer angle of 132.5° showed a reduction of the maximum magnetic field strength from 2.4 mT to 0.32 mT when both shieldings are used, reducing the impact on the spectra to an acceptable level. The QCLAM quadrupole magnet has a neutral fifth pole shoe in the lower half of the magnet, resulting in different magnetic field strengths at the upper and lower detectors.

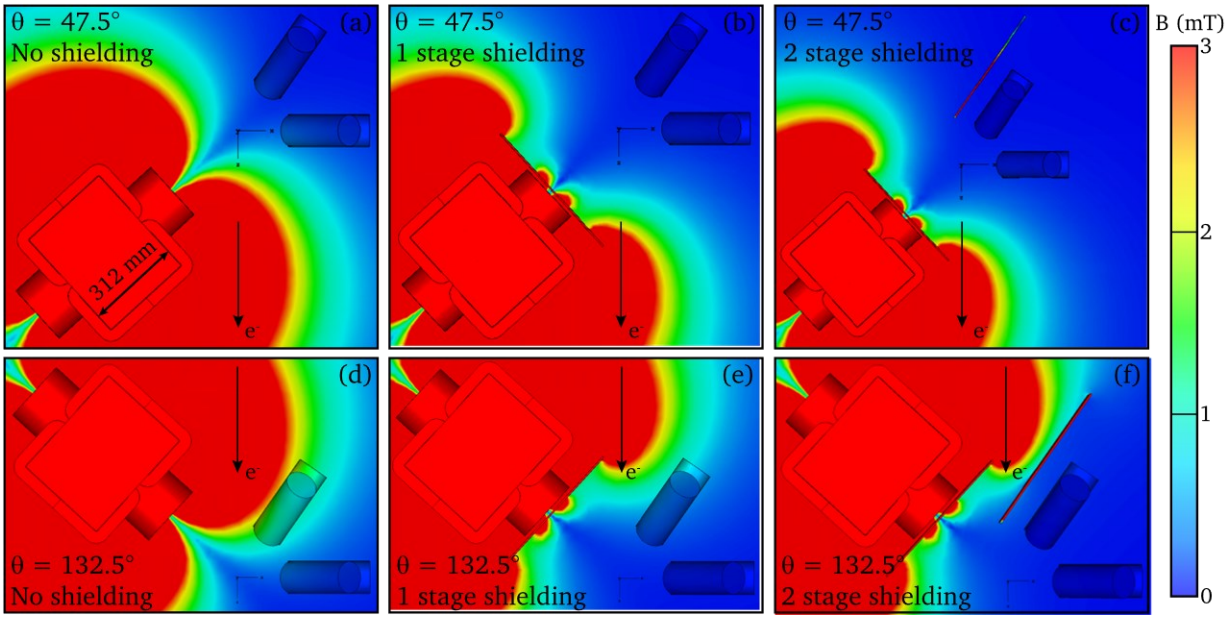

Figure 43: The results of CST simulations of the magnetic field distribution of the QCLAM quadrupole magnet show the effect of the magnetic field shielding. Simulations were performed for the spectrometer angle 47.5° without shielding (a), with one stage shielding (b) and with two stage shielding (c) and at 132.5° without shielding (d), with one stage shielding (e) and with two stage shielding (f). The Figure was created using CST Studio Suite [141].

Table 7: Maximum magnetic field values at the surface of the detector casings for the spectrometer angles 47.5° and 132.5° with no magnetic field shielding, with shielding at the quadrupole magnet, and with shielding at the quadrupole magnet and besides the tower at 132.5°. The positions of the detectors can be taken from Figure 42. The use of the magnetic field shielding reduces the magnetic field strength approximately by one order of magnitude. The asymmetry between the upper and lower detectors is due to the fifth pole of the quadrupole magnet.

Setup	$B_{max,0}$ (mT)	$B_{max,1}$ (mT)	$B_{max,2}$ (mT)	$B_{max,3}$ (mT)	$B_{max,4}$ (mT)	$B_{max,5}$ (mT)
47.5°, no shielding	0.44	0.47	0.70	0.24	0.25	0.46
47.5°, 1 stage shielding	0.13	0.19	0.27	0.041	0.11	0.19
47.5°, 2 stage shielding	0.13	0.19	0.26	0.030	0.096	0.19
132.5°, no shielding	0.43	0.46	0.70	2.1	2.4	2.4
132.5°, 1 stage shielding	0.10	0.17	0.25	0.56	0.97	0.87
132.5°, 2 stage shielding	0.040	0.10	0.16	0.060	0.22	0.32

Measurements were performed with the single-stage magnetic field shielding at the spectrometer angle of 47.5°. The current of the quadrupole magnet was increased from 0 A to 200 A in steps of 50 A. The changes in position and energy resolution of the 1.332 MeV peak of a ^{60}Co source are shown in Figures 44 and 45 respectively.

Labels (a), (b), and (c) correspond to detectors in the tower at 90° and labels (d), (e), and (f) correspond to detectors in the tower at 145°. The vertical angles for (a) and (d) are 45°, for (b) and (e) 0°, and for (c) and (f) -45°. To investigate the effects of the magnetic field, polynomials of first order were fitted to the data and for better comparability the slope was

normalized with the offset. The parameters of the polynomials are listed in Table 8. Subfigures (a), (c), (d), and (e) show the expected effect that the positions of the peaks are shifted to smaller energy values with increasing magnetic field strength. However, (b) and (f) show an opposite behavior. The detectors from plots (b) and (e) show a smaller effect than the detectors at the top and bottom because they are closer to the axis through the quadrupole magnet, where the magnetic field strength of an ideal quadrupole magnet becomes zero. For (c) - (f) the energy resolution shows no significant change, whereas (a) and (b) show a slope with different relative sign. Depending on the position of the detector relative to the spectrometer, the spectra are being affected even with magnetic field shielding in place. Due to the remaining magnetic field strength with the magnetic field shielding in place, it is recommended to perform an energy calibration of the $LaBr_3$:Ce detectors after each change of the magnetic field. In addition, the change of the magnetic field of the quadrupole magnet caused by the shielding affects the trajectories of the electrons inside the QCLAM spectrometer, so a new sieve slit measurement is recommended to calibrate the scattering angles.

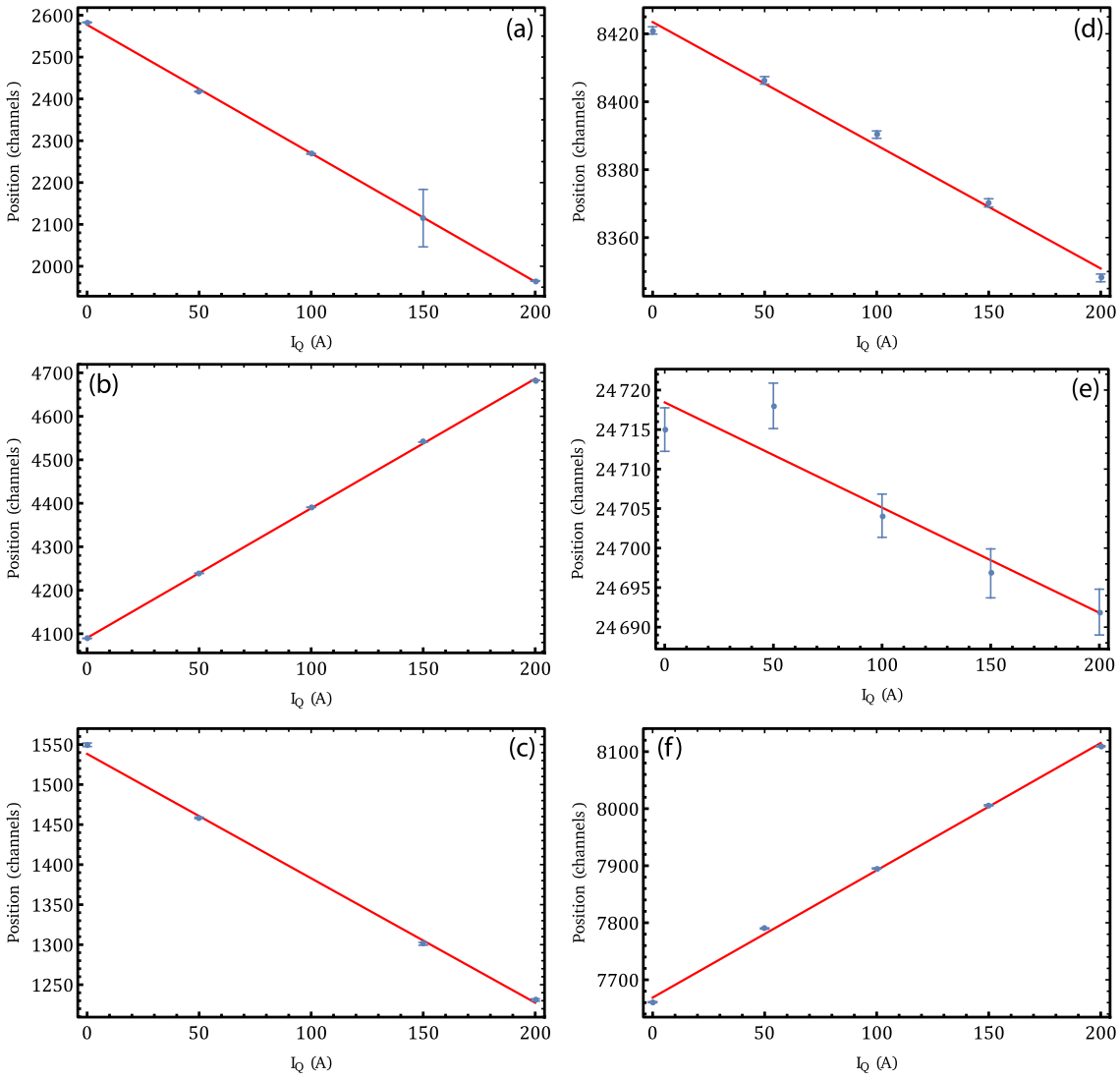

Figure 44: The position changes of the 1.332 MeV peak (blue dots) in the spectra of the six $LaBr_3$:Ce detectors as a function of the current strength of the QCLAM quadrupole magnet are shown. Linear fits (red lines) were used to approximate the position changes of the peak. The data point at 100 A in (c) could not be used.

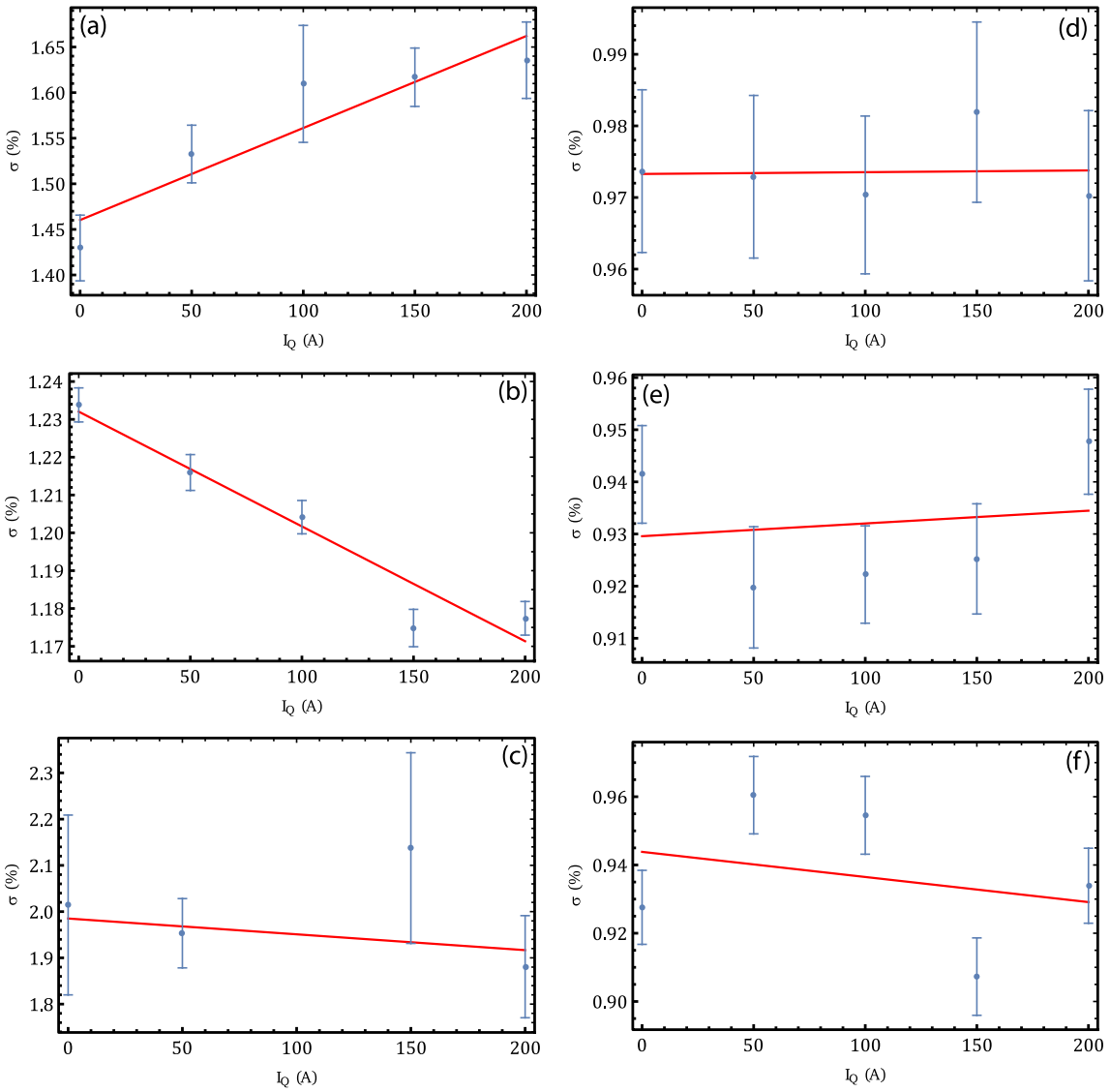

Figure 45: Effects of the external magnetic field generated by the quadrupole magnet of the QCLAM spectrometer on the energy resolution of the 1.332 MeV peak (blue dots) in the spectra of the six $LaBr_3$:Ce detectors as a function of the current of the QCLAM quadrupole magnet. Linear fits (red lines) were used to approximate the dependence of the energy resolution on the current of the quadrupole magnet. The data point at 100 A in (c) could not be used.

The usage of silicon photomultipliers instead of photomultiplier tubes might be an alternative, as silicon photomultiplier are not sensitive to magnetic fields [142]. Silicon photomultipliers should be considered for future optimization of the experimental setup.

A new setup for (e,e'γ) measurements was designed. The improved beamline allows better transport of the electron beam to the target and can be used for inclusive and exclusive electron scattering experiments at spectrometer angles below 133°. For (e,e'γ) measurements a dedicated scattering chamber with focus on background reduction was designed. The γ-ray detectors are fixed in the new detector holder and aligned to the target. Now the setup is complete and the readout of the detector signals, which is described in the next chapter, must be done.

Table 8: Parameter of fits of first order polynomials to the data from Figures 44 and 45. The slope from Figure 44 was normalized with the offset.

Label	Position offset (ch)	Position slope (ch/A)	Relative slope slope/offset (1/A)	σ offset (%)	σ slope (%/A)
(a)	2577 (4)	-3.07 (3)	-1.19 (1) 10^{-3}	1.46 (2)	10 (1) 10^{-2}
(b)	4091 (2)	2.98 (2)	7.28 (5) 10^{-4}	1.232 (6)	30 (5) 10^{-5}
(c)	1538 (5)	-1.55 (5)	1.01 (3) 10^{-3}	1.99 (7)	3 (6) 10^{-4}
(d)	8423 (2)	-0.36 (2)	4.3 (2) 10^{-5}	0.973 (4)	2 (33) 10^{-6}
(e)	24718 (3)	-0.13 (3)	5 (1) 10^{-6}	0.92 (1)	2 (8) 10^{-5}
(f)	7668 (6)	2.23 (5)	2.91 (7) 10^{-4}	0.94 (2)	7 (15) 10^{-5}

5. Electronics and Data Acquisition

Another key element of the (e,e'γ) setup are the electronics and the data acquisitions, which process and record events in the QCLAM detector system and the $LaBr_3$:Ce detectors. In this work, a new system for data acquisition of the signals from the $LaBr_3$:Ce detectors was developed and combined with the existing QCLAM data acquisition [95] to produce a coincidence data acquisition. In this chapter, the existing electronics and data acquisition of the QCLAM spectrometer are presented at first. Then, the electronics and data acquisition of the newly developed system for processing the signals from the $LaBr_3$:Ce detectors is introduced. At the end of the chapter, the combined system for processing coincident events detected by the QCLAM and $LaBr_3$:Ce is described.

5.1. QCLAM Electronics and Data Acquisition

In the past, (e,e'x) coincidence experiments have been performed on the QCLAM spectrometer [38,143] using the initial DAQ of the QCLAM spectrometer [100]. In 2018, a new data acquisition for the QCLAM spectrometer was put into operation, which supports the use of an extended detector system with a higher number of anode wires in the drift chambers. In the development of the new data acquisition, the possibility to extend it for coincidence experiments was anticipated [95]. The QCLAM data acquisition system utilizes commercially available VME [144] and NIM [145] standards. Both standards are widely used in nuclear physics and a plethora of commercially available modules exist.

When an electron passes through the detector system of the QCLAM spectrometer (see Section 3.3.1), it generates signals at the wires of the MWDCs. These are amplified by the preamplifier boards, which are attached to the sides of the MWDCs and routed to time to digital converter (TDC) VME modules of type VFB6 by ELB Bonn [146]. Each wire of the drift chambers is connected to an input channel of the TDCs. The TDC modules measure the drift times of the drift cells but require a reference signal for the relative time measurement. This is realized by the fast scintillation detector behind the drift chambers. The scintillator has PMTs at both ends, whose signals are passed through a constant fraction discriminator (CFD) to create a logic signal, so that the timing information of the signal does not depend on the amplitude. These signals are split and distributed to the TDC modules and the trigger logic of the QCLAM data acquisition system [95].

The trigger logic uses predefined criteria to decide whether an event is classified as valid and whether the trigger for processing the event should be generated. The validity of a signal is determined by the QCLAM trigger logic from the signals of the trigger detectors, namely the scintillator (2 PMTs) and the Cherenkov detector (1 PMT). The signals from the trigger detectors are linked to an AND logic module that allows to enable coincidence conditions between them. For example, an event may be considered valid if either the lower or upper PMT of the scintillator has generated a signal. The best suppression of background events, i.e., events not generated by an electron that has traversed the entire detector system, is achieved by the coincidence condition of the three PMT signals of scintillator and Cherenkov detectors. A schematic diagram of the QCLAM detector system and electronics is shown in Figure 46.

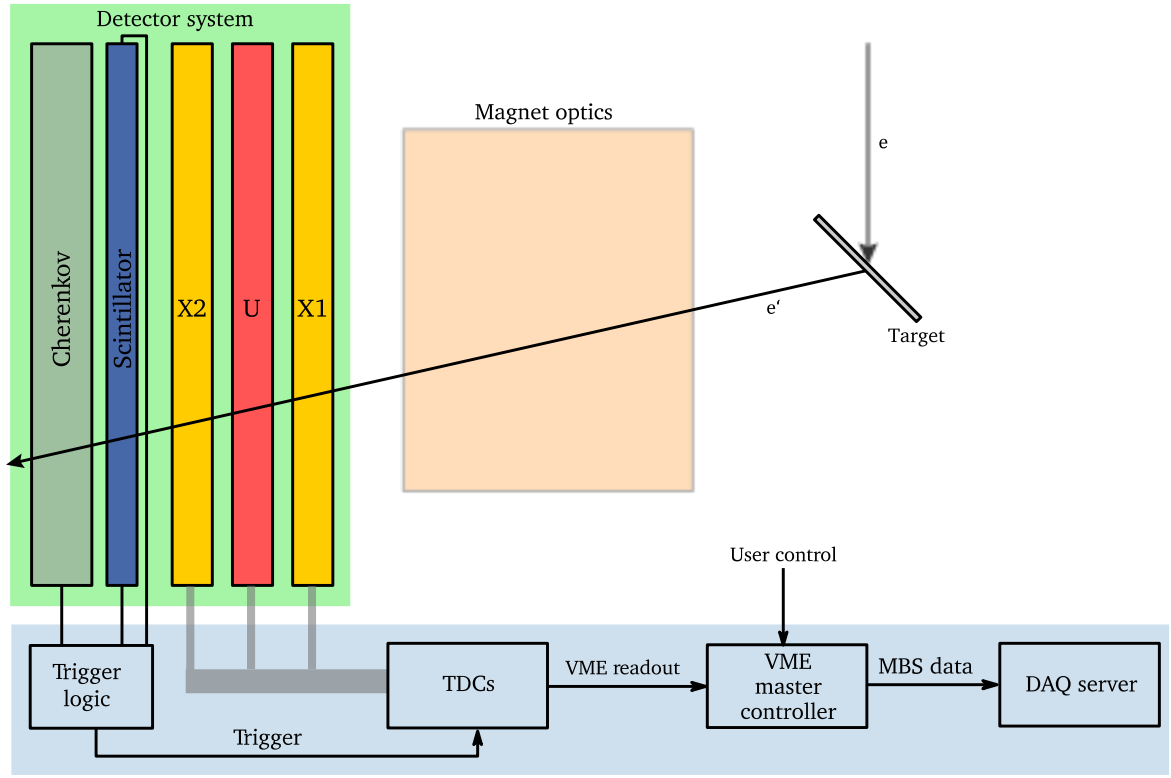

Figure 46: After the scattered electron is deflected in the magnetic field of the QCLAM spectrometer, it passes through the detector system. From the signals of the Cherenkov and scintillation detectors the trigger is generated, which is used for the measurement of the drift times of the MWDCs in the TDC modules. A delayed trigger starts the readout process of the master controller, which reads the data from the TDC modules and stores them on a server. Figure taken from [95] and modified.

Since the drift times in the drift cells of the MWDCs are up to 260 ns long [100], it is necessary to delay the QCLAM trigger until events of the MWDCs are processed by the TDC modules. After that, the QCLAM trigger starts the readout process of the master controller, which reads data from the TDC modules and writes it to a server. In addition, the QCLAM trigger generates a timestamp, i.e., information about the time for each TDC event. Timestamps can be used, for example, to calculate the duration of a measurement, the average rate, and the time interval between successive events. The accuracy of a timestamp depends on the time resolution of the detector system and the electronics. The digital trigger logic of the QCLAM spectrometer operates at a frequency of 125 MHz, hence the time resolution of the trigger is 8 ns. However, the timestamp is stored with a time resolution of 1 µs.

Depending on the design and use of the data acquisition system, it may be necessary to introduce an additional coincidence criterion. Reasons for this are for example coincidence measurements, where only events with simultaneous detections of two or more particles in different detector systems are accepted, or usage of a dead time lock. Dead time describes the time interval in which a system is not able to process newly arriving events. A dead time lock is used to suppress the generation of a trigger when the system is not ready to process events. The total dead time consists of the dead time of the detector system and the dead time of the electronics and data recording. The dead time of the drift cells is given by the drift time. The dead time of the electronics and data acquisition results from the time in which the electronics is blocked for processing a signal. An additional dead time occurs at high event

rates, when the data rate of the recorded events, which must be written to the server, becomes too large and new events cannot be stored. This dead time starts about 500 ns after the QCLAM trigger is generated and continues until the DAQ readout process is complete, which takes about 100 μs. To bridge the gap between the dead times of the drift cells and the QCLAM DAQ, an artificial dead time of 560 ns was introduced. Thus the dead time of a QCLAM event is at least 560 ns and, if this event starts a readout process, the dead time lasts until the readout process is completed [95].

Due to the total dead time of a system, the number of accepted events N_{acc} is less than or equal to the number of real events N_{raw}. For small event rates, N_{acc} is approximately N_{raw}. As the event rate increases, the discrepancy between N_{acc} and N_{raw} increases. The maximum data acquisition rate of the QCLAM spectrometer is 5 kcps in standard mode and 12 kcps in asynchronous mode [95].

The QCLAM data acquisition [95] is based on the Multi-Branch System (MBS) [147] developed by GSI [148]. This system is used at the Institute of Nuclear Physics at TU Darmstadt, for example, at the QCLAM and Lintott spectrometers. MBS is a general purpose data acquisition system used in over 200 systems worldwide [149], thus experience with this system is available in the field of experimental nuclear physics. The master controller module used for the new data acquisition is a CES RIO4 [150] running the LynxOS operating system [151]. Configuration and readout of the VME modules are defined in a f_user.c file, which is the user readout interface of the MBS system. The data acquisition software is written in the programming language C. To provide the required trigger processing and dead time locking, a GSI TRIVA7 trigger module [152] and a GSI VULOM 4B dead time locker and trigger priority encoder module [153] are used.

5.2. $LaBr_3$:Ce Electronics and Data Acquisition

The basis for the new $LaBr_3$:Ce data acquisition (LaBr DAQ) was an existing simple framework [154] that has been extended and improved to fit the needs of (e,e'γ) coincidence measurements.

Experimental conditions, such as high radiation background, must be considered for the development of the data acquisition. Due to high expected background rates of more than 100 kcps per γ-detector in electron scattering measurements, it is impractical to record all γ-events. For this reason, it is beneficial to use a hardware trigger that is only generated if a γ is detected in coincidence with a scattered electron, thereby data rate and dead time are reduced. For calibration measurements of the $LaBr_3$:Ce detectors, there must be the possibility to switch off the coincidence condition in order to perform measurements with radioactive sources in singles mode.

A narrow gate on the time difference between electron and γ time information further reduces the rate of accepted events which demonstrates the importance of a good time resolution. The following requirements are specified for the new electronics and data acquisition:

- The system must be able to operate in stand-alone mode, but with the option to accept an external trigger for coincidence mode
- Possibility to switch between coincident and singles modes via software during beam time operation

- Support for a minimum of six $LaBr_3$:Ce detectors with an option to add more detectors
- Total time resolution of the $LaBr_3$:Ce detectors and the electronics below 2 ns so that the time resolution of the coincidence system is approximately given by the time resolution of the QCLAM spectrometer
- For ease of use, the new LaBr DAQ should be operated in analogous way to QCLAM DAQ
- Optional recording of signal shapes for subsequent pileup correction (see Section 6.1.2).

5.2.1. LaBr Electronics

The electronics of the new system for reading out the $LaBr_3$:Ce detectors use the VME and NIM standards, as do the electronics of the QCLAM spectrometer. The system shown in Figure 47 consists of a NIM crate and a VME crate, which contain the electronic modules.

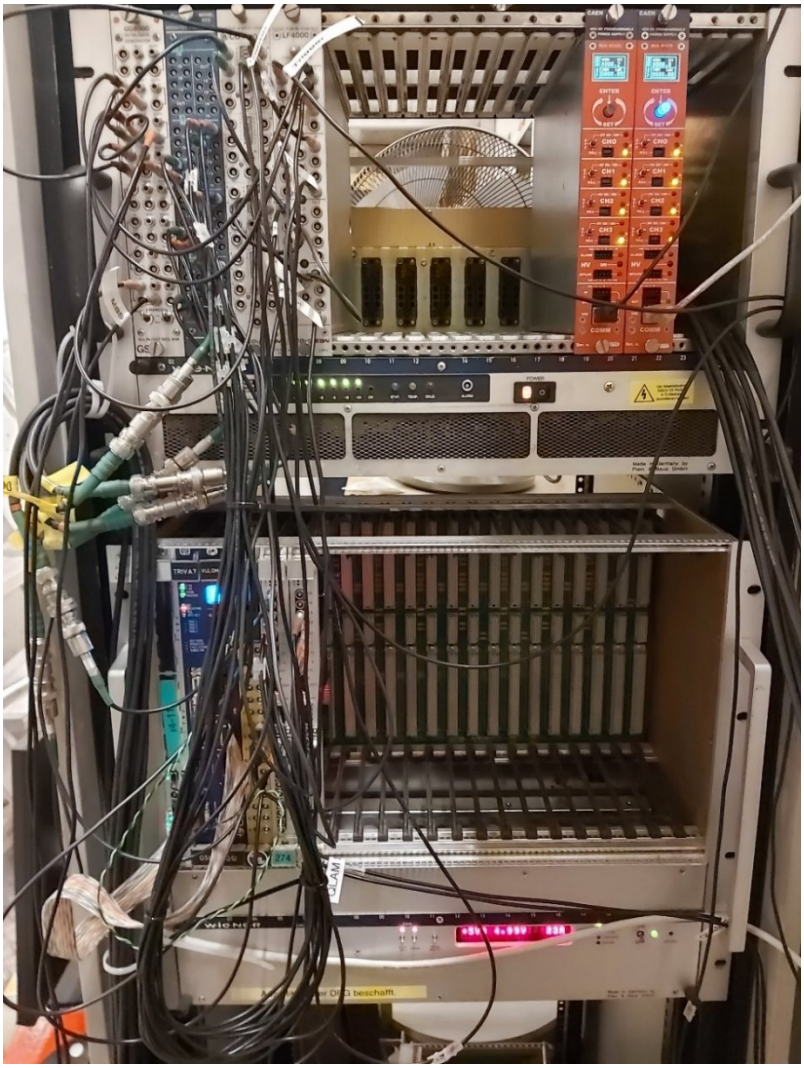

Figure 47: The LaBr data acquisition consists of a NIM (top) and a VME (bottom) crate. The NIM crate contains the linear fan in/fan out module for duplication of the detector signals, a gate generator to generate the coincidence gate, a coincidence module, a logic fan in/fan out and two high voltage modules. The VME Crate contains a RIO4, a TRIVA7 and a VULOM4B for the MBS system. The ENV3 module converts the rectangular signal into an ECL signal which is sent to the TRIVA7 to start the readout process. The two SIS3316 modules process signals from the $LaBr_3$:Ce detectors, with the right module generating the LaBr trigger which is sent to the QCLAM spectrometer and the left SIS3316 module stores accepted detector signals.

The NIM crate contains the following modules (left to right):

- GSI GG8000 Octal Gate Generator: Gate Generators generate an output signal with adjustable length and delay on an incoming logic signal, which can be used to open a gate.
- LeCroy Model 628 Linear Fan In/Fan Out module: A linear fan in/fan out module copies the incoming signal to multiple outputs. These modules can be used to duplicate the signal of a detector without affecting the waveform too significantly.
- CO4010 Coincidence Module: Coincidence modules output a signal when the incoming signals match the logic set previously. For example, a coincidence of at least 2 of the four incoming signals can be required.
- Logic Fan In / Fan Out LF4000: Logical fan in / fan out modules duplicates incoming logical signals and allows them to be distributed to several other modules.
- 2x Caen N1470 high voltage (HV) power supplies [136]: HV generate a high voltage which is needed, for example, to operate detectors.

The VME crate contains the following modules (left to right):

- GSI trigger system modules: RIO4, TRIVA7 and Vulom4B.
- ENV3: This module converts an incoming logical signal into a differential signal and vice versa. Differential signals are required by the GSI trigger system.
- 2x SIS3316: The SIS3316 module is an analog to digital converter (ADC) and is used to digitize signals from detectors for further processing. The module performs calculations and determines for example the uncalibrated energy and the timestamp of a signal.

5.2.2. The SIS3316 Module

Signals from the detectors are processed by SIS3316 digitizers from Struck Innovative Systems [155]. The SIS3316 modules are 16 channel ADCs operated at a sample rate of 250 MHz so that in steps of 4 ns the amplitudes at all inputs are digitized with an accuracy of 14 bit. The input range of the module can be set to 2 V or 5 V with maximum amplitudes between -5 V and 5 V. A higher resolution is achieved if the 2 V setting is used. The module provides the possibility to record for each event the digitized voltage amplitude at the input channel during an adjustable time interval to obtain additional information of the signal shape and, for example, to separate overlapping signals. In the following the stored voltage amplitudes of an event are called trace. The operation of the SIS3316 modules is configurated by a master controller, which can communicate with the SIS3316 module via the backplate of the VME Crate. The 16 channels are divided into groups of four, some module settings can be set per channel and others per group. Therefore, the groups have been assigned tasks. The module has two internal memory banks where the data of accepted events can be stored. This allows one memory bank to be read while the other is being written to, resulting in a reduced dead time.

Each of the 16 input channels has an internal trigger generation, for which a moving average window (MAW) with 10 samples gap time and 5 samples peaking time is used. The operating mode of the MAW is shown in Figure 48. The trigger logic is armed when the threshold of a channel is exceeded. When the moving average falls below 50 % of the maximum value, the

internal channel trigger pulse is generated which corresponds to a functionality analogous to a constant fraction discriminator [155].

The module has three further groups of inputs and outputs, namely Trigger-In and Trigger-Out, User-In and User-Out, and Clock-In and Clock-Out. The Trigger-In connector allows the use of an external trigger or gate, making the module suitable for use in coincidence data acquisition. Trigger out can be used to distribute the internal triggers of the channels to other modules. User-In and User-Out are configurable ports. The User-Out port can be used, for example, to output a signal when the amount of data in the active memory bank exceeds a threshold (Address Threshold). Clock-In and Clock-Out are used to synchronize multiple SIS3316 modules.

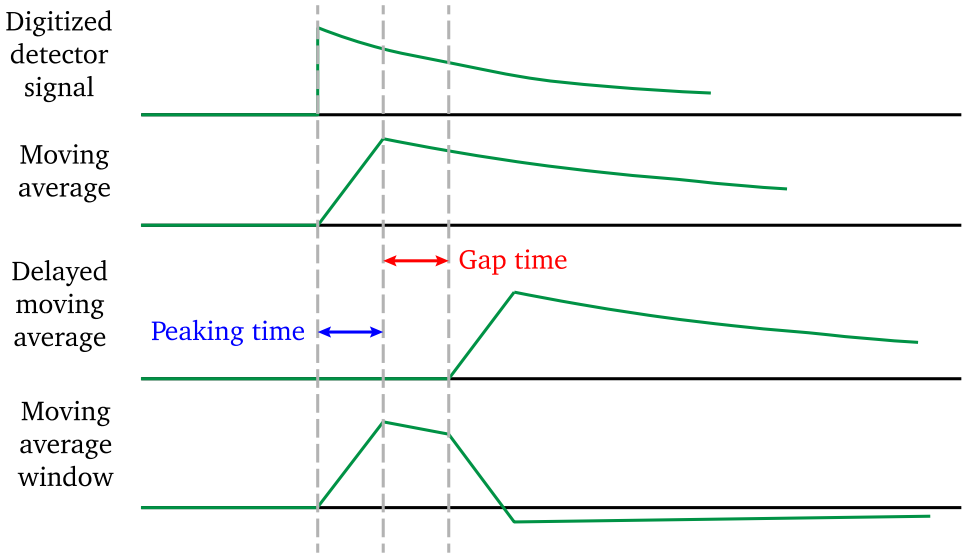

Figure 48: The moving average window, which is used by the SIS3316 module to generate trigger signals, is calculated from the difference of the moving average and the delayed moving average. The moving average is the ADC signal integrated over the peaking time and the delayed moving average is additionally delayed by the gap time. Figure based on [155].

The module's time resolution has an accuracy of 4 ns due to the internal 250 MHz clock. If the CFD mode is used, the maximum value of the moving average window MAW_C and the values before (MAW_B) and after (MAW_A) the internal channel trigger is generated are saved in addition to the 48-bit timestamp $t_{48\text{-bit}}$. This allows the calculation of a corrected timestamp by using the linear interpolation

$$t_{corr} = 4\ \text{ns}\left(t_{48-bit} - \frac{\text{MAW}_C/2 - \text{MAW}_B}{\text{MAW}_B - \text{MAW}_A}\right). \tag{5.1}$$

to improve the time resolution [155]. Using this linear interpolation, a FWHM time resolution of 165 ps was obtained in a test measurement with a square wave signal from a pulse generator. Measurements with a ^{60}Co source between two $LaBr_3$:Ce detectors provide a time resolution of 0.9 ns.

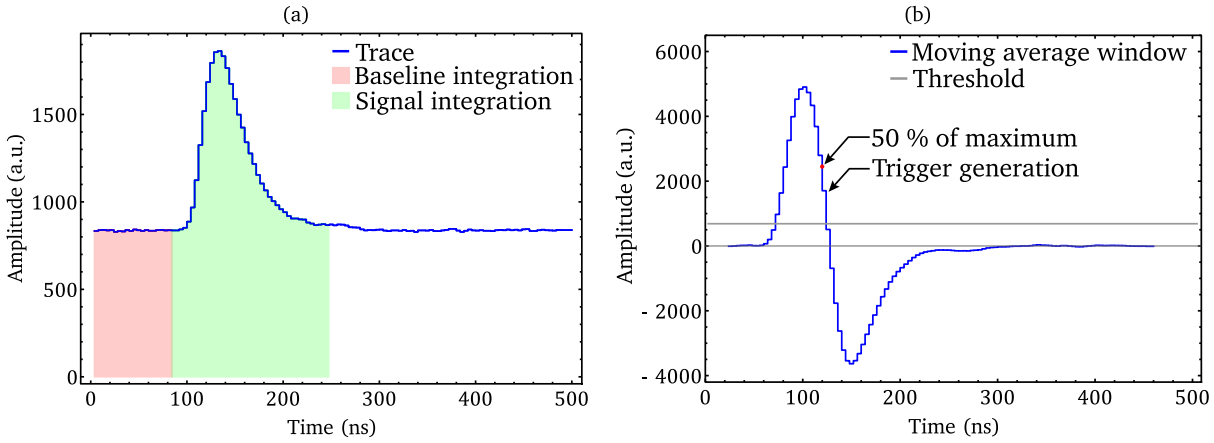

Figure 49: (a): Trace of a $LaBr_3$:Ce detector. The input signal has a negative voltage amplitude, which is inverted by the module. The area integrated by the first accumulator gate is shown in red. This is used to correct the offset of the baseline. The area of signal and baseline is shown in green. By subtracting the red area from the green area using interval length weighting, the area of the signal is obtained. This provides the uncalibrated energy value. (b): The moving average window shown was calculated from the trace shown on the left. An amplitude above the threshold value arms the trigger logic. An internal trigger signal is generated when the amplitude drops to 50 % of the maximum value. By linear interpolation between the two samples before and after the generation of the trigger pulse, a corrected timestamp can be calculated with a time resolution much better than the sampling rate of 4 ns.

For determination of the energy value of an event, two accumulator gates are used which integrate the voltage amplitudes of the incoming signal at specified intervals relative to the time of trigger pulse generation. An example of the accumulator gates and trigger pulse generation is shown in Figure 49. An accumulator gate with a length of 80 ns immediately before the signal (red) and an accumulator gate of 160 ns length (green) are used to obtain the area of the baseline $A_{baseline}$ and the area of the signal plus the corresponding baseline $A_{baseline+signal}$, respectively. The uncalibrated energy value E_{raw} is calculated during data analysis by

$$E_{raw} = A_{baseline+signal} - 2 \cdot A_{baseline}. \tag{5.2}$$

Alternatively, the energy value can be calculated by the maximum amplitude of the MAW. Using the accumulator gates to determine the energy gave a better energy resolution, which is why this method is used.

With increasing count rate, pileups occur increasingly. Time intervals between successive detector signals become smaller than the length of a signal resulting in an overlap of multiple signals. This results in the DAQ registering these overlapping signals as a single signal, thus assigning incorrect energy and time information to this event. The probability of N pileups occurring at a count rate n in the time interval τ assuming a Poisson distribution is given by

$$P(N,n) = \frac{(n\tau)^N e^{-n\tau}}{N!}. \tag{5.3}$$

1-$P(0,n)$ is the probability of the occurrence of a pileup event. It has been demonstrated that at count rates below 500 kcps pileups can be neglected [131]. The signal length of the $LaBr_3$:Ce detectors is about 160 ns. Thus, at a rate of 500 kcps 7.7 % of all events are expected to be pileups.

To reduce the effects of pileups, the count rates should be limited to less than 500 kcps during the measurements. If this is not feasible, a pileup correction technique must be applied. The SIS3316 module allows to record the trace of each event. In steps of 4 ns the amplitude of each $LaBr_3$:Ce event is stored during an interval length of 124 samples. Pileup correction is performed during data analysis as described in Section 6.1.2.

Each of the 16 input channels has six statistic counters, which are used for determination of dead time and raw/accepted count rates.

- Raw: Counts each event that exceeds the threshold. This is the real number of events with corresponding amplitudes that are produced by the detector.
- Accepted: Counts all events that start the readout process for the corresponding channel.
- Dead time: Counts events that are within the dead time of the module.
- Pileup: Counts pileups and repileups. The time interval for pileups must be set by the user in the configuration of the data acquisition. Based on the signal shapes, the time interval for repileup and pileup were set to 60 and 40 samples.
- Veto: Counts events while the gate for the channel is not open.
- High energy: Counts events with a MAW amplitude above the high energy threshold and are therefore rejected. This is only used to count the signals of the external 10 MHz clock by setting the high energy threshold to 0 for the channel of the external clock. This prevents signals of the clock from creating data rate that would influence performance of other channels.

The dead time of the module's sample logic consists of the dead time of the hit/event storage logic of each channel $t_{\text{event active}}$ and the dead time t_{swap} when swapping memory banks. Since memory banks are swapped after processing of an event has been completed, the total dead time of the swap lies between t_{swap} and $t_{\text{swap}} + t_{\text{event active}}$. The bank swapping dead time t_{swap} has a constant value of 144 ns. The event dead time of each channel depends on the channels settings and what data is stored [155]. As an example, a case is considered in which events are stored on channels 0-2 without a trace and signals are stored on channels 8 to 15 with a trace of 124 samples. For channels 0, 1 and 2, $t_{\text{event active}}$ is 600 ns and for channels 8-15 the dead time is 1236 ns.

To keep the dead time low, it is recommended to use a mode where both memory banks of the SIS3316 module are used. The module switches between these two memory banks whenever a readout process is started so that in parallel to the readout of one memory bank data can be stored on the other bank.

5.2.3. Signal Processing

The LaBr DAQ system can be used in singles mode to read out $LaBr_3$:Ce detectors, or integrated into a system for coincidence measurements by incorporating an external trigger. The processing of the signals in the electronic modules varies due to the different requirements.

In both cases, the high voltage needed for the PMTs of the $LaBr_3$:Ce detectors is generated by two four channel Caen N1470 HV power supplies. The high voltage modules can be remotely controlled via a computer in the experimental hall running the manufacturers control software GECO [137]. $LaBr_3$:Ce detectors are operated at voltages between 700 V and 1000 V.

The electronics for use as a stand-alone system is shown in Figure 50. The signals from the $LaBr_3$:Ce detectors are passed through the linear fan in / fan out to the input channels of the SIS3316 module, where the signals from the detectors are processed and stored in the active memory bank. The internal trigger is routed to the Trigger-Out as LaBr trigger and starts the readout process of the data. A dead time interlock is not required in this operating mode. Events arriving at the electronics during the dead time are not saved. For time measurement, e.g., for calculation of count rates, an external 10 MHz clock is connected to one of the inputs of the SIS3316 module.

The MBS trigger is converted to a differential signal by the ENV3 module and then registered by the TRIVA7 trigger module. MBS starts reading data from the first SIS3316 module via the VME bus and sends the data via a network connection to a server where data are written to a list-mode format (LMD) file.

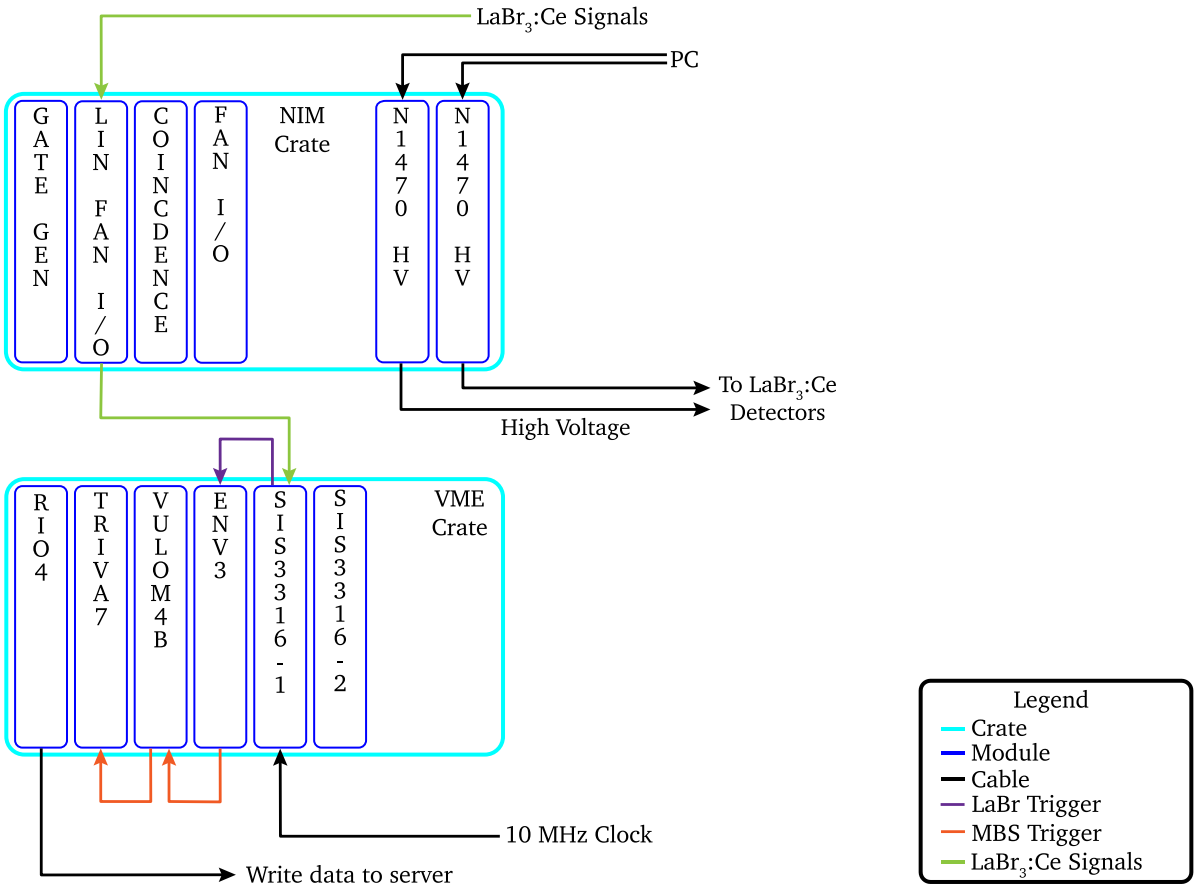

Figure 50: For the operation of the electronics in stand-alone mode for processing the signals of the $LaBr_3$:Ce detectors only a part of the electronics is needed. The signals of the $LaBr_3$:Ce detectors are processed by the SIS3316 module and the internal trigger of the module is output as LaBr trigger and triggers the readout of the MBS trigger system.

The wiring of the electronics for integration into a system for coincidence measurements is shown in simplified form in Figure 51. A detailed map of all modules and cables is shown in Appendix 12.10. The signals from the $LaBr_3$:Ce detectors are duplicated by the linear fan in/fan out module and distributed to the inputs of two SIS3316 modules where the corresponding input channels of each detector signal have the same configuration and threshold settings. In the first SIS3316 module (from here on referred to as SIS3316-1), which is used for actual data recording, the signals are delayed by an internal delay to wait

for the external trigger. The sole purpose of the second SIS3316 module (from here on referred to as SIS3316-2) is the generation of the LaBr trigger when in any $LaBr_3$:Ce detector channel a signal exceeds the threshold. This corresponds to the use of a CFD for each detector, where the threshold can be set remotely in the DAQ software for each channel individually. Both modules use the same thresholds so that a signal that created a LaBr trigger in one module is also processed by the other module. The LaBr trigger of 20 ns length is sent to the external trigger logic where the coincidence trigger is crated if both detector systems, the $LaBr_3$:Ce detectors and the external detector detected events simultaneously. The coincidence trigger is routed to the LaBr electronics as an external trigger. The external trigger is passed from the logic fan in / fan out module to the gate generator, where it generates a gate for the trigger-in input of the SIS3316-1 module. The previously delayed signals from the $LaBr_3$:Ce detectors are now inside the gate and are processed by the SIS3316-1 and stored in its internal memory.

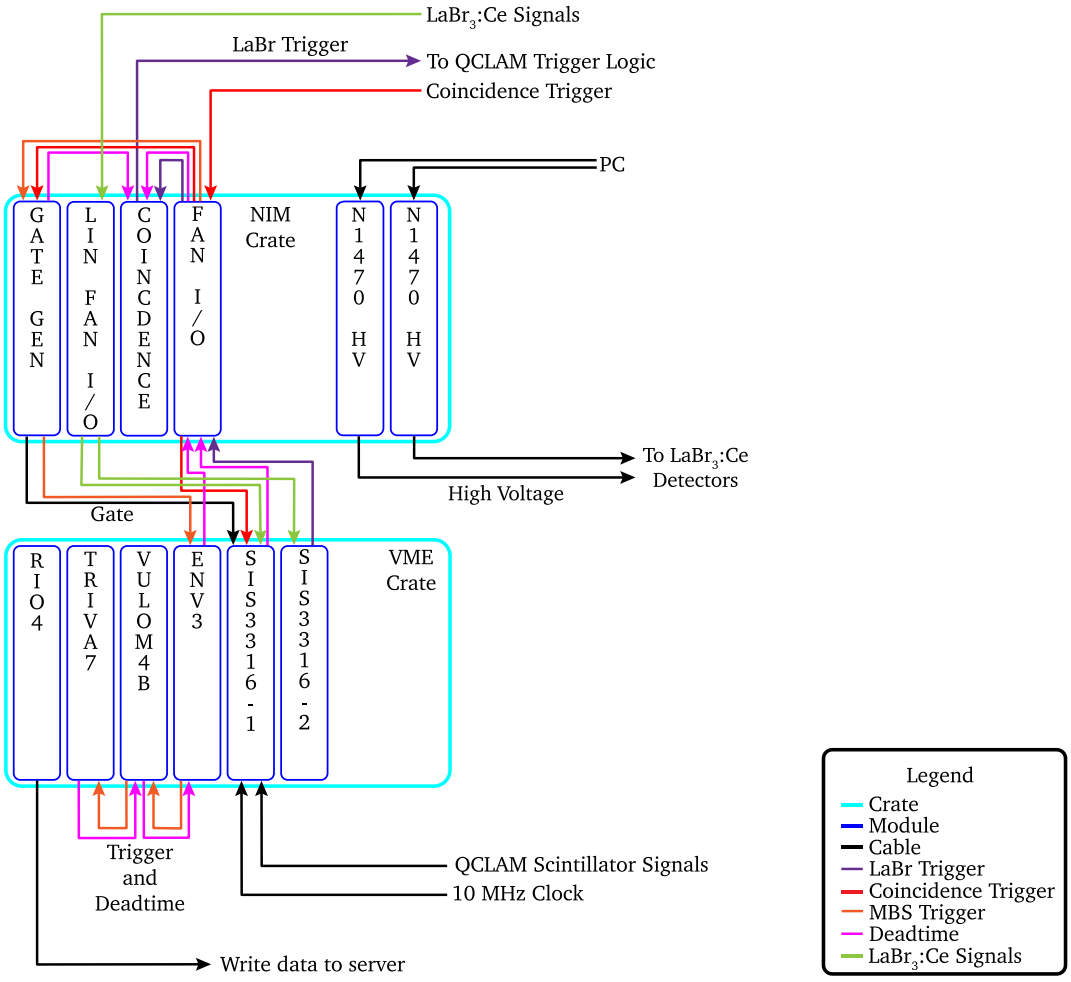

Figure 51: Shown is the working principle of the LaBr data acquisition. It consists of a NIM and VME crate in which the respective modules are installed. Signals from the $LaBr_3$:Ce detectors generate the LaBr trigger, which is routed to the QCLAM. If an electron is detected coincident at the QCLAM, the LaBr-QCLAM trigger is distributed to the LaBr data acquisition, which opens a gate for the delayed $LaBr_3$:Ce signals and starts the readout process.

Depending on the configuration, the MBS trigger for starting the readout process can be generated either from the coincidence trigger or when the address threshold of the SIS3316-1 is exceeded.

For integration into a coincidence measurement system, a dead time lock is required to prevent a LaBr trigger from being sent to the external trigger logic while the LaBr electronics are not ready to process the event. The total dead time is composed of the dead time of the SIS3316-1 module, the dead time of the readout process and an artificial dead time for bridging. These dead times are sent as a logical signal to the coincidence module, where they are linked to a logical And. If one of these dead times is present, the LaBr trigger is suppressed and not sent to the external trigger logic.

5.2.4. LaBr DAQ

The goal of combining the LaBr DAQ with the QCLAM DAQ into one system for coincidence measurements on the QCLAM spectrometer was considered in the development of the LaBr DAQ for two reasons. Existing experience with the QCLAM DAQ can be used for work on the LaBr DAQ and the operation of the two DAQs is analogous, making it easy to use.

The LaBr DAQ features three operating modes that can be set in the data acquisitions software:

- Singles mode: In singles mode, no external gate is used, and all events (besides during dead time) are accepted. This mode is intended for calibration and efficiency measurements of the $LaBr_3$:Ce detectors, as the maximum data rate is limited.
- Single coincidence mode: In single coincidence mode, the external DAQ is self-triggering and produces singles data, for example, like in (e,e') measurements. The external trigger signal is sent to the LaBr DAQ and opens a gate for the internal trigger signals created by the signals from the $LaBr_3$:Ce detectors. This mode is a simple implementation of a coincidence condition and can be used at low count rates (e.g., measurements on light nuclei like ^{12}C). A robust algorithm to merge the data can fix single missing timestamps of the coincidence trigger that were not recorded due to dead time of the LaBr data acquisition. The advantage is that the external DAQ also produces singles spectra and peaks in a spectrum become visible quickly.
- Double coincidence mode: Only events from the external DAQ and LaBr DAQ are accepted if both DAQs have generated a trigger simultaneously. Dead time locks in both data acquisitions ensure that events are only recorded when both systems are ready. Thereby every external trigger generates a timestamp in both data acquisitions.

Analog to the QCLAM DAQ the configuration of the SIS3316 modules is done in the "f_user.c" file of MBS. To avoid that MBS must be recompiled every time small changes are made, the most important settings of the SIS3316 modules are stored in three text files, which are read in when MBS is started. The three text files contain general settings of the module (e.g. singles/coincidence mode and address threshold), settings for each channel (e.g. thresholds and internal delays) and settings for each group of channels (e.g. length of traces and accumulator gates).

The inputs of the SIS3316 modules must be configured for the properties of the incoming signals. Since with the 2 V range a better resolution is achieved when digitizing the voltage amplitudes, this setting is used. Using the 2 V range, photon energies up to 20 MeV can be measured with typical high voltages at the PMTs used in the $LaBr_3$:Ce detectors. Since the signals from the $LaBr_3$:Ce detectors and the external trigger have negative amplitudes, an offset is used to cover the interval between -1.9 V and 0.1 V. The external 10 MHz clock uses positive voltage amplitudes and therefore this channel covers a positive range. To prevent the

signals of the clock from being stored by the SIS3316-1 module and thus significantly increasing the dead time, the high energy threshold of this channel was set to 0, so that all signals with an amplitude greater than 0 are suppressed but counted by the scaler of the channel as high energy suppressed events.

The data stored in the SIS3316-1 module are stored on a server by the master controller after generation of the MBS trigger started the readout process. The data structure is specified by the modules used. For the SIS3316 modules there are two readout modes, namely event data and statistics data. The event data contains all stored information about the detected events. The statistics data contains the data of the statistics counter of the SIS3316 module. The event data structure, which is shown in Figure 52, contains the following information:

- Raw timestamp: 48-bit timestamp in units of the internal clock's cycles. If the module is operated in 250 MHz mode, one cycle corresponds to 4 ns. After 13 days an overflow occurs. This is not relevant for merging of the data from both data acquisitions since only time differences are considered.
- Channel: Channel ID for identification of the input channel.
- Format: Used for module identification in case multiple modules are used.
- Accumulator gates: The two accumulator gates store the integrated values of the baseline and signal plus baseline, from which the uncalibrated energy value is calculated.
- MAW data: A corrected timestamp is calculated from the maximum amplitude (MAW_A) and the values before (MAW_B) and after (MAW_C) the generation of the trigger pulse.
- Energy values: Values obtained from energy filter. This was not used because a better resolution was achieved by the usage of accumulator gates.
- Pileup or repileup: In case of a pileup or repileup this flag is set to 1. The integrated pileup detection uses the same threshold as the internal trigger, consequently the sensitivity of the pileup detection depends on this setting. A more powerful detection of pileups is the pileup correction during offline analysis.
- Trace: Recorded signal shape of the event.

Once per second the readout of events from the 16 input channels is followed by a readout of the statistical counter, which is used for example for determination of dead time and count rates. Since the module does not provide a timestamp for the readout process, an external 10 MHz clock is connected to one of the module's input channels. This allows to calculate the time since the previous readout from the number of detected pulses of the clock. In order not to produce unnecessary data, the high energy threshold of this channel was set to 0, so the signals are counted but not processed. Since the external clock is the only element in the data acquisition that generates signals with a positive voltage amplitude, the polarity of this channel must be inverted.

Since no timestamp is generated by the data acquisition during the statistics counter readout process, an external 10 MHz clock is used to calculate the time elapsed since the previous readout process and thus the rates for each counter can be determined from the difference between the counter values divided by the time difference. The statistics counters are read out by the data acquisition if at least one second has passed since the previous statistics counter readout and a MBS trigger is received. By limiting the number of statistics counter readouts, data rate and thereby dead time is reduced.

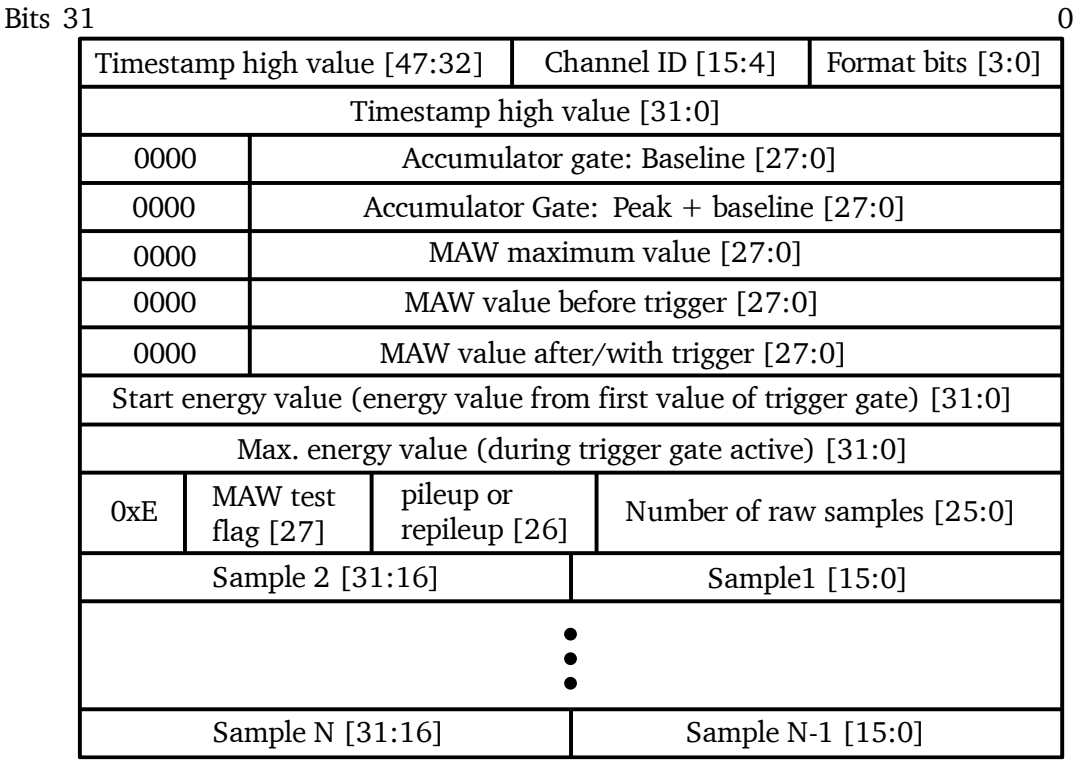

Figure 52: Data structure of an event in the LaBr data acquisition. The size of an event depends on the number of samples of the trace. The memory size for an event without trace is 40 bytes, with a trace of 124 samples the size is 288 bytes. This figure is based on [155].

Since the high energy threshold has been set to 0 for the channel of the external 10 MHz clock, the high energy trigger counter must be used to determine the elapsed time since the previous statistics counter readout. Measurements showed irregularities in the statistics counters, causing incorrect values to be stored. This error also occurred with other modules of the same type [156,157]. One solution is to reset the counters after each event, so that they only have to count up to 1 [156]. However, this solution is not practical. The cause of the problem is probably a faulty bit in the data word [156]. Since the error was only observed in the raw counter, its value is not used in the evaluation of the data and instead the sum of the other five trigger counters is used as correct value of the raw counter. The data structure of a trigger counter readout is shown in Figure 53. The four groups of measuring inputs are read out successively, whereby the individual channels within a group are read out one after another.

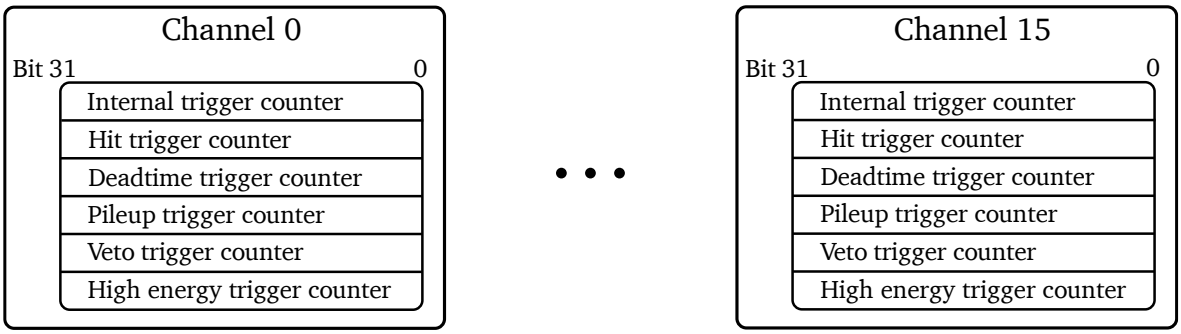

Figure 53: The data structure of a trigger counter readout process is shown. The size of a trigger counter readout is 384 bytes. This figure is based on [155].

Analogous to the dead time interlock of the QCLAM electronics, the LaBr electronics uses an artificial dead time to bridge the dead time of the SIS3316 module and the beginning of the dead time of the readout process of the LaBr DAQ. The dead time interlock is explained in the next section using the example of the dead time interlock for use of the LaBr DAQ in coincidence with the QCLAM DAQ.

An important factor of the dead time is the data transfer rate from the SIS3316 module to the server via the backplate of the VME crate. If the limit of the data transfer rate is exceeded, data is stored faster in the SIS3316 module than it can be copied from MBS to the server. Therefore, the memory of the SIS3316 module is filled and events cannot be stored. If both memory banks are used and the limit of the data rate is not exceeded, the dead time of the SIS3316 module is negligible. The dead time starts to increase strongly near the data rate limit. By using block transfer mode, the maximum data rate of the VMEbus is 40 MB/s [144]. The minimal and maximal size of a coincidence event are given, in addition to the three QCLAM signals, if at least in one and a maximum of all six $LaBr_3$:Ce detectors a signal was recorded. An event without trace has a size of 40 bytes with the settings of the data acquisition and an event with a 124 samples long trace has a size of 288 bytes. This results in a minimum size of 408 bytes and a maximum size of 1848 bytes for a coincidence event in the LaBr DAQ. The length of the traces thus influences the dead time.

The total dead time of the LaBr data acquisition was measured by using Poisson distributed pulse generator signals to multiple channels of the SIS3316. This represents an upper limit of the dead time, since in a measurement with a radioactive source or with electron beam not all detectors always generate a signal simultaneously. The effects of the length of the traces and number of detectors are shown in Figure 54. The dead time of the LaBr DAQ is close to zero until the limit of the data rate is reached. Then the dead time starts to increase rapidly. By reducing the stored samples of the trace, the rate at which the dead time starts to increase rapidly is shifted to higher rates. Similarly, reducing the number of channels while keeping the length of the trace constant leads to a reduction in the data rate and allows higher accepted rates. When using 500 ns long traces for six channels, the dead time starts to strongly increase at a rate of 6 kcps. This is approximately the maximum trigger rate at which measurements were made on the QCLAM. This makes the LaBr DAQ suitable for the planned experimental setup consisting of six $LaBr_3$:Ce detectors for use in the coincidence DAQ for (e,e'γ) measurements.

If an upgrade of the LaBr DAQ leads to a major increase in the required data rate or dead time, the DAQ can be expanded to transfer data to the server via the gigabit ethernet port at the front plate of the SIS3316 module. In this case, data is not sent via the VMEbus, thus bypassing this bottleneck [155].

LaBr data acquisition was successfully used to read out the $LaBr_3$:Ce detectors in singles mode and in coincidence mode in the measurements described in Chapters 7 to 9. Other uses of LaBr data acquisition included detector test measurements with silicon photomultipliers [158] and testing pulsed beam operation at the S-DALINAC, where the length of the bunches was measured [159].

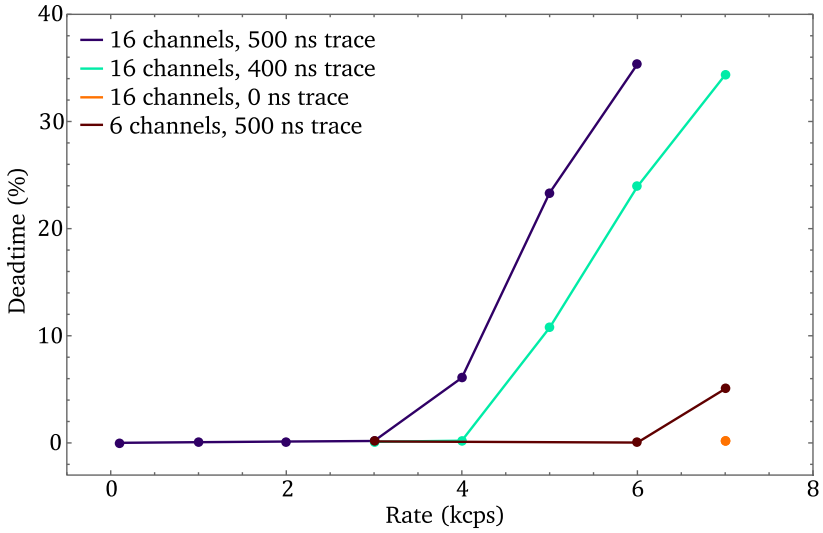

Figure 54: The dead time of the LaBr DAQ is primarily determined by the data rate and the associated dead time.

5.3. Coincidence Data Acquisition

The new developed DAQ for (e,e'γ) coincidence measurements at the QCLAM spectrometer consists of two independent DAQs: the existing DAQ of the QCLAM spectrometer and the newly developed LaBr DAQ for the γ-ray detectors. The concept of the combined (e,e'γ) coincidence DAQ is shown in Figure 55. The design of the coincidence DAQ follows the idea for extending QCLAM DAQ for coincidence measurements from [95].

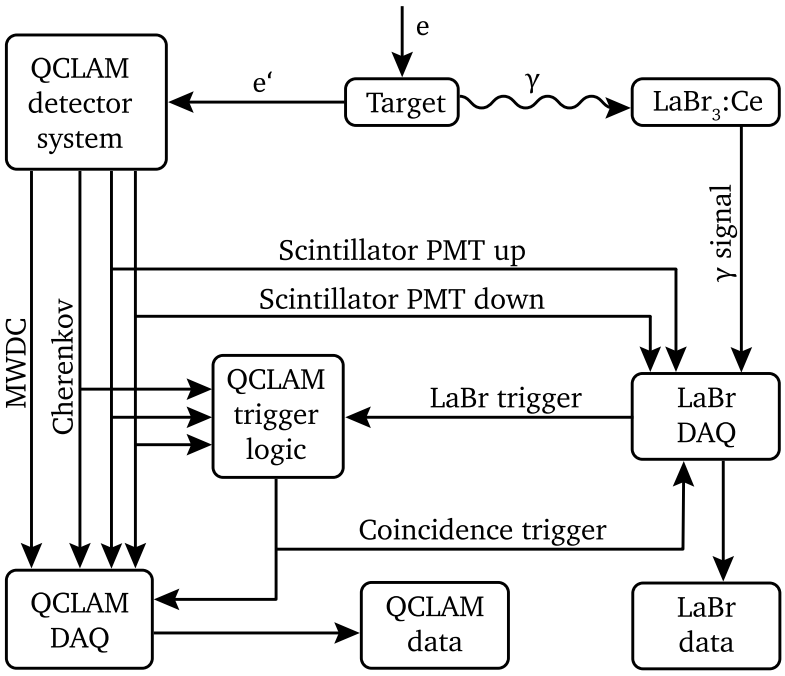

Figure 55: Schematic diagram of the (e,e'γ) coincidence data acquisition. In the QCLAM trigger logic, a QCLAM-LaBr trigger is generates from the LaBr trigger and the signals from the QCLAM trigger detector system and starts the readout process in both data acquisitions. The LaBr DAQ and the QCLAM DAQ store the measured data in their own files.

Inelastic scattering processes occur when the electron beam hits the target, exciting the nucleus and scattering the electron. Electrons scattered to the QCLAM spectrometer are

detected by the QCLAM detector system which creates the QCLAM trigger. To create coincidence of both, the QCLAM trigger and the LaBr trigger, the QCLAM trigger must be delayed by 465 ns to wait for the slower LaBr trigger. Immediately after the scattering process, the excited nucleus decays by emission of γ-radiation. When detected, these photons generate a signal in the $LaBr_3$:Ce detectors that are connected to the input channels of the LaBr data acquisition. If a signal from a $LaBr_3$:Ce detector is detected, the LaBr trigger is generated and routed to the QCLAM DAQ, and the signal is delayed by 736 ns to wait for the LaBr-QCLAM coincidence trigger. If both, the delayed QCLAM trigger and the LaBr trigger are simultaneously detected by the QCLAM trigger logic, the LaBr-QCLAM coincidence trigger is generated and distributed to both DAQs. The LaBr-QCLAM trigger causes the QCLAM DAQ to store the event data of the MWDC in the TDC modules. In the LaBr DAQ the LaBr-QCLAM coincidence trigger opens a 100 ns long gate for the previously delayed $LaBr_3$:Ce signal. A timestamp with an accuracy of 8 ns is added to the event by the LaBr-QCLAM trigger. In addition to the QCLAM trigger, the signals of the two PMTs of the QCLAM scintillator are also routed to the LaBr DAQ to calculate a timestamp with a higher accuracy. Both data acquisitions work independently and generate their own files, QCLAM files contain data of the scattered electrons and have the same data structure as files recorded in (e,e') reactions [95] and LaBr files contain data from the $LaBr_3$:Ce detectors and timestamps from the QCLAM trigger detectors. The advantage of using two independent data acquisitions is the ability to use the LaBr DAQ at other measurement facilities and, for example, to run the DAQ in a lab for testing.

The assignment of the channels of both SIS3316 modules is listed in Table 9. The first group (channels 0-3) processes the signals of the QCLAM data acquisition and the external clock, the second group (channels 4-7) serves as additional scalers for dead time measurement and the third and fourth groups (channels 8-15) are used for processing γ-signals.

Table 9: Overview of the configuration of the 16 channels of both SIS3316 modules. The first eight channels are reserved for signals from the QCLAM spectrometer, an external clock and scaler. The remaining eight channels are reserved for γ-ray detectors.

Channel	SIS3316-1	SIS3316-2
0	QCLAM trigger	-
1	QCLAM scintillator PMT down	-
2	QCLAM scintillator PMT up	-
3	External 10 MHz clock	-
4	LaBr trigger (raw)	-
5	LaBr trigger (accepted)	-
6 - 7	Scaler (reserved)	-
8 - 15	Detectors	Detectors

The format of the LMD filenames generated by the LaBr data acquisition follows the format of the QCLAM filenames [95] to provide an uniform naming scheme. The file names consist of

an identifier for the data acquisition ('labr'/'q'), the run ID and a file ID. When a new run is started, the run ID is incremented, and the file ID is set to the value 0. The file ID is incremented when the file size limit is reached, and MBS automatically creates a new file. As a result, a different number of files can be created for each MBS system during a run. By simultaneously controlling the three MBS systems of the (e,e'γ) data acquisition using the provided scripts, a uniform run numbering is ensured. Examples for the file names:

- labr_012_3456.lmd (File of LaBr data acquisition.)
- q_c0_012_4567.lmd (File of first crate in QCLAM data acquisition.)
- q_c1_012_5678.lmd (File of second crate in QCLAM data acquisition.)

Since the clocks of the LaBr DAQ and the QCLAM DAQ are not synchronized and the only connections between the two data acquisitions are the LaBr trigger signal, the signals from both photomultiplier tubes of the QCLAM scintillator and the LaBr-QCLAM coincidence trigger the mapping of events in the LaBr DAQ files and the QCLAM DAQ files. The LaBr-QCLAM coincidence trigger generates a timestamp that is used to map QCLAM data to $LaBr_3$:Ce data by matching the trigger patterns saved in the recorded data of both data acquisitions. A trigger pattern is defined as the information of the time differences of successive trigger events. These time differences have approximately the same value in both data acquisitions, whereas absolute timestamps have an arbitrary offset. Since the internal clocks of both data acquisitions are not synchronized, there is no fixed offset between the absolute values of the timestamps of both data acquisitions. The principle of trigger pattern matching is shown in Figure 56. After the associated trigger patterns are found, the information from the scattered electrons can be combined with the information from the γ to form a coincidence event. The calculation of the time difference between the detected electrons and γ-rays is calculated from the data of the LaBr DAQ, which stores the timestamps with higher accuracy. The LaBr-QCLAM trigger is not suitable for the calculation of the time difference due to the time resolution of 8 ns. Instead, the timestamps created by the signals from the PMTs of the QCLAM scintillator in the LaBr DAQ are used. The timestamps of the scintillator PMTs depend on the distance between the PMTs of the scintillator and the intersection point of the scattered electron in the QCLAM detector system. This is corrected by using the mean value of the timestamps of the lower and upper PMTs of the scintillator, making the timing information independent of the location in the detector system.

For an estimation of the time resolution and a test of the coincidence condition for a real (e,e'γ) coincidence measurement, a $LaBr_3$:Ce detector was positioned next to the QCLAM scintillator and a ^{60}Co source was fixed between the detectors. The achieved time resolution using a threshold of 1.1 MeV to suppress Compton scattered events in data evaluation of the $LaBr_3$:Ce detectors was 4.3 ns. Since the data acquisition of the QCLAM spectrometer does not store energy information of the trigger detectors, this result is still affected by Compton scattered photons. The measured value therefore represents an upper limit.

Depending on the settings in the data acquisition software, either each coincidence event is read out individually (single-event readout), or events are accumulated in the internal memory of the module until it is full and starts the readout process (multi-event readout). Since a higher number of readouts leads to a higher dead time, the multi-event readout mode is to be preferred.

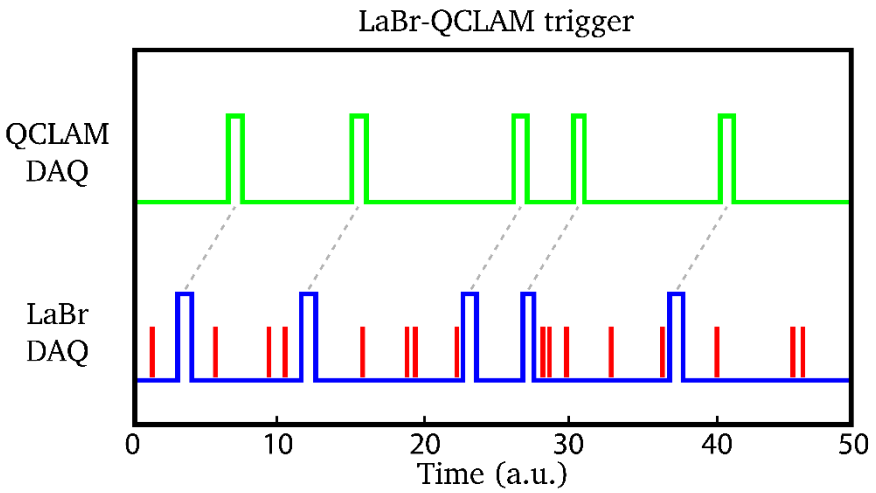

Figure 56: Synchronization of the two independent DAQs by matching the trigger patterns. The dashed line indicates the mapping of the LaBr QCLAM trigger timestamps in the QCLAM DAQ (green) to the timestamps in the LaBr DAQ (blue). The red dashes represent the γ-events.

In the single-event readout mode, all events belonging to a single coincidence event are read out by generating the MBS trigger of the LaBr DAQ at the trigger output of the SIS3316-1 module and the dead time lock is blocking the creation of further LaBr trigger until the readout process is finished. This is realized by having the LaBr-QCLAM trigger create an artificial dead time that is extended from the MBS dead time to the end of the readout process. LaBr triggers generated between the LaBr trigger which started the readout process, and the beginning of the artificial dead time are sent to the QCLAM DAQ but suppressed there by the artificial dead time of the QCLAM DAQ. The dead time interlock of the single-event readout mode is illustrated in Figure 57.

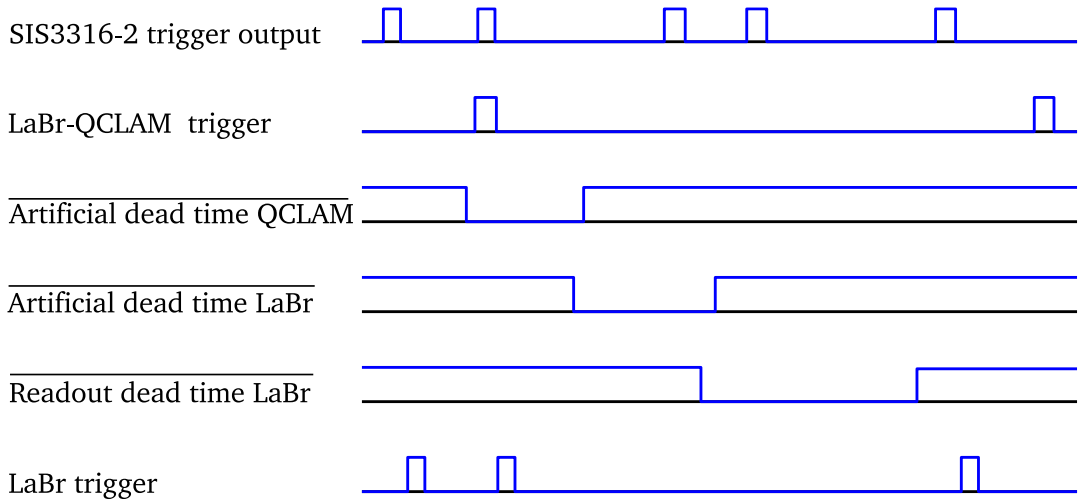

Figure 57: Shown is the logic of the dead time lock of the LaBr data acquisition. A coincidence signal is created from the trigger output of the SIS3316-2 module, the inverted artificial dead time and the inverted readout dead time to ensure that a trigger signal is only send to the QCLAM spectrometer if the LaBr data acquisition is ready to process an event. The artificial dead time LaBr is generated to bridge the time between the input of the LaBr-QCLAM coincidence trigger and the readout dead time. Analogously, there is an artificial dead time in the QCLAM data acquisition which overlaps with the artificial dead time of the LaBr data acquisition. The lines above the name of a signal indicate that it is an inverted signal.

In the multi-event mode both memory banks of the SIS3316-1 module are used to reduce the number of time-consuming readout processes. If the occupied memory of the active memory bank of the SIS3316-1 exceeds the address threshold, the MBS trigger to start the readout process is generated at the user output. At the beginning of the readout process, the system switches between the memory banks of the SIS3316-1 module and the readout process of the full memory bank begins. While the data is read out from the now inactive memory bank, the now active memory bank is filled with event data. Dead time is present in the multi-event readout mode when the active memory bank is full and waiting for the change of the memory banks. At high trigger rates, the second memory bank can be filled before the readout process of the first memory bank is completed. Then there is a sharp increase in the dead time.

The single-event readout mode is simple and can be beneficial for testing but the advantage of having two memory banks is lost. The use of the address threshold allows higher count rates by simultaneously writing and reading data from both memory banks and is recommended for coincidence measurements. The operation of the dead time lock of the coincidence data acquisition and the two readout modes is shown in Figure 59. An overview of the timeline of the processing of the signals can be found in Appendix 12.11.

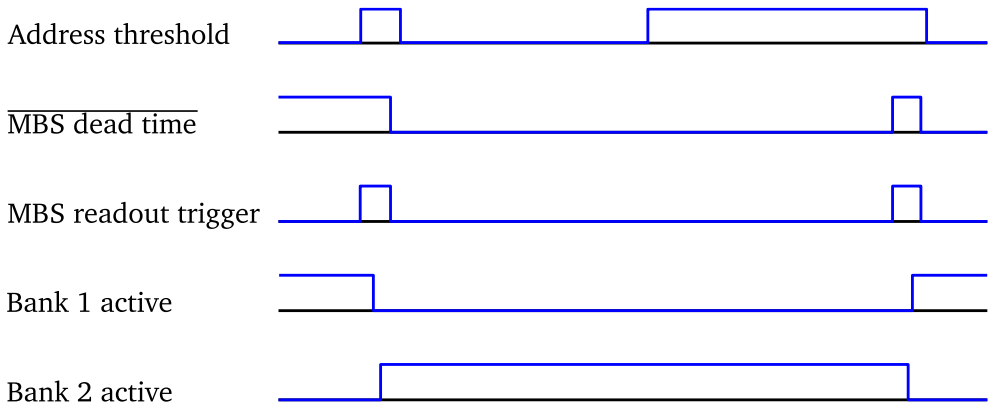

Figure 58: Illustration of the MBS trigger generation using the address threshold. At the beginning, the address threshold is not exceeded and therefore it has the value zero. Since MBS is not busy with a read process at that moment, the inverted MBS dead time outputs a signal. If the memory occupancy exceeds the address threshold, the coincidence of the address threshold and the inverted MBS dead time generates the MBS trigger to start the readout process which generates the MBS dead time and changes the active memory bank of the module. While one memory bank is read out, the other one is written to and thus the effective dead time is minimized. If the second memory bank is filled during the present MBS dead time, an address threshold signal is output, and a new MBS trigger is generated at the end of the MBS dead time.

Nuclear physics measurements at accelerator facilities typically take several weeks. During this time, the experiment must be continuously monitored, and measurements must be controlled by an operator. Since not all personnel is familiar with each experimental setup, a facilitated and consistent operation of the coincidence DAQ is required. Instead of controlling each DAQ individually and directly via MBS, scripts were written in the Python 3 programming language, which control the three MBS systems (two MBS systems of the QCLAM DAQ and one MBS system of the LaBr DAQ). An overview of the scripts can be found in Appendix 12.11.

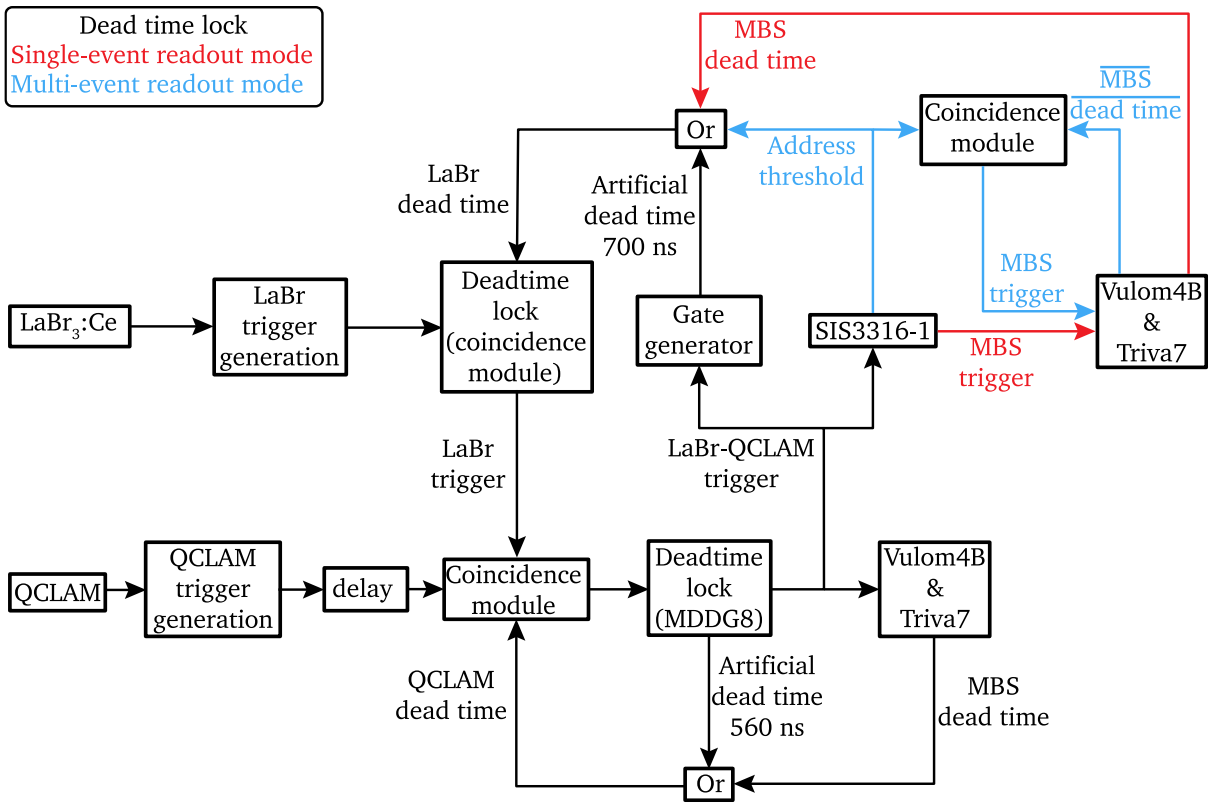

Figure 59: Shown is the dead time locker logic of the (e,e'γ) data acquisition. Two readout modes with different dead time locks are available. Red: If each event is read out individually, the MBS dead time is used for the dead time of the read-out process. Blue: If events are accumulated in the memory of the module until it is full, the readout dead time is given by the address threshold of the SIS3316 module.

Despite the focus on combination with the QCLAM DAQ, the LaBr DAQ can be connected to other DAQs that stores timestamps of trigger signals and provides access to its trigger. Since no synchronization of the timestamps is required, only the trigger cables must be disconnected from the old external DAQ and reconnected to the new external DAQ. The only required adjustments to the LaBr data acquisition is the optimization of internal delays and the modification of the input data structure expected by the analysis software (see Chapter 6).

An early version of the LaBr DAQ was used parasitically for a first test in 2017 during an (e,e') measurement at the Lintott spectrometer where the basic operation could be demonstrated. After successfully merging the data from the Lintott DAQ and the LaBr DAQ, in the following years, the new LaBr DAQ was connected to the QCLAM spectrometer and another parasitic test and an (e,e'γ) commissioning experiment on ^{12}C were performed. Adaption of the new LaBr DAQ to the QCLAM DAQ required little effort due to the concept as an independent operatable DAQ and the synchronization by trigger pattern matching. During the development of the combined coincidence DAQ, improvements were also made to the QCLAM DAQ [160], which will benefit future inclusive and exclusive electron scattering measurements.

A simple test of the full (e,e'γ) setup before starting an experiment is to use cosmic showers hitting the QCLAM detector system and at least one of the $LaBr_3$:Ce detectors simultaneously. It should be noted that the time resolution is reduced to 8.2 ns due to different directions from which cosmic showers originate and the time difference between QCLAM and $LaBr_3$:Ce detector is shifted by about -20 ns due to the time-of-flight of the cosmic rays and the absence of the time-of-flight of an electron in the QCLAM spectrometer.

6. Analysis software

For the processing and the evaluation of raw data produced by the LaBr data acquisition and by the coincidence data acquisition, a new set of analysis software tools was developed. The analysis software is based on the ROOT 6.20 framework [161], which is widely used in data evaluation of nuclear physics measurements and is written in the C++ programming language. It has been built in a modular way so that each part can be executed independently, for example to process only the data of the $LaBr_3$:Ce detectors. An illustration of the concept of (e,e'γ) analysis software is shown in Figure 60. It can be divided into three categories: analysis of $LaBr_3$:Ce data, analysis of QCLAM data, and analysis of combined LaBr-QCLAM coincidence data. To analyze the data of a coincidence measurement, the data from the LaBr and QCLAM data acquisitions must first be processed independently and can then be merged. Apart from the QCLAMon [95] for processing the QCLAM data and parts of the Unpacker, the software was developed within the scope of this work.

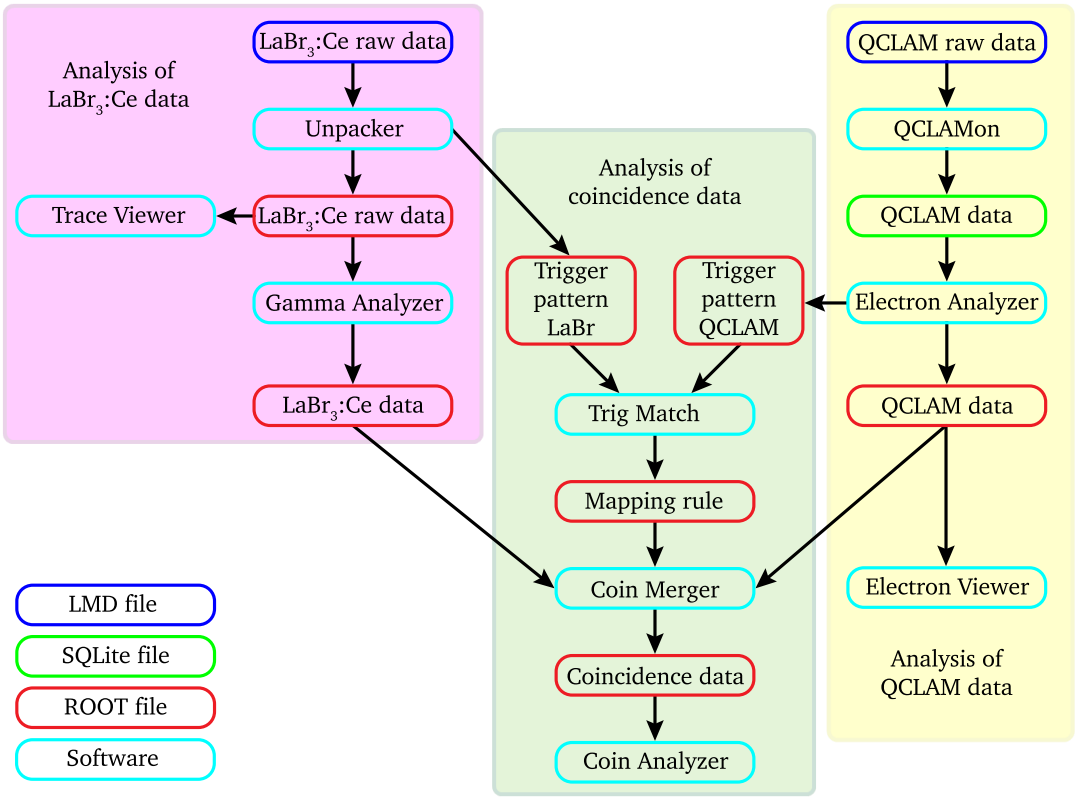

Figure 60: The modular structure of the analysis software. Software parts are shown in light blue and datablocks are color coded according to its formats (blue: LMD data: green: SQLite, red: ROOT). The analysis of the $LaBr_3$:Ce data (pink area) and the analysis of the QCLAM data (yellow area) are performed separately. After that, the analysis of the coincidence data (green area) begins. A mapping rule for the data from both data acquisitions is created by matching trigger patterns. Subsequently, data from the QCLAM spectrometer and the $LaBr_3$:Ce detectors are merged and the coincident data are analyzed.

The merging of the LaBr and QCLAM files is done in three steps. In the first step, raw data of both data acquisitions are unpacked and analyzed independently. For the LaBr data, this is done by the Unpacker and the Gamma Analyzer. QCLAM data are analyzed by QCLAMon and the Electron Analyzer. Trace Viewer and Electron Viewer can optionally be used for additional analysis of the data. The second step is the merging process of the LaBr and QCLAM data. Trig Match generates a mapping rule from the trigger patterns and creates the mapping of the

LaBr and QCLAM events. Subsequently, the LaBr and QCLAM data are combined by Coin Merger into a coincidence data set using the mapping rule. In the third step, the files containing the coincident data are read by the Coin Analyzer where histograms of the coincident events are generated.

Analogous to the operation of the data acquisition, Python3 scripts are available for the analysis software for easier operation. The data structures of the output files of Unpacker, Gamma Analyzer, Electron Analyzer, Trig Match, and Coin Merger can be found in Appendix 12.13 to 12.17.

6.1. Unpacker

Data acquisitions generate raw data in a binary file format, which needs to be transformed into more easily understandable data for analysis tools like ROOT. The UCESB (unpack and check every single bit) tool [162] is used to unpack the raw data from the LaBr DAQ. Unpacking the raw data represents the first step in the analysis of recorded LaBr data.

6.1.1. The UCESB Unpacker

UCESB is a generic unpacker for event-based data, e.g. recorded during nuclear physics experiments. In UCESB, the data structure of the raw data is specified in the form of a C structure-like format. The support of user generated code allows to add functions for additional calculations in the different levels of the unpacker [162]. UCESB and the user functions are written in the C++ programming language. The UCESB unpacker is able to read files from a hard drive or receive data from a stream server [162], which makes it suitable for the processing of offline and online data.

For offline and online applications, a correspondingly adapted version of the unpacker was created in the scope of this work based on an existing UCESB version. The basis for the unpacker of the (e,e'γ) analysis software was an customized UCESB version, which contained a predefined data structure of a SIS3316 module, to save data in a ROOT file [154]. The offline unpacker instance processes and converts raw data into ROOT data and the second (more basic) online unpacker instance can be used for online monitoring of count rates of all $LaBr_3$:Ce detectors, QCLAM trigger rates, and dead time.

Data of the individual MBS readout processes of the LaBr DAQ are unpacked one after the other. For each readout process first the event data and then, if available, the statistics counter data of the SIS3316 module are unpacked. Processing of the event data is done by looping over all subevents by calling the appropriate member functions to interpret the data of the input buffer. The data is placed by the unpacker in a data structure which resembles the SIS3316 data structure. In each level of the unpacking and processing stage, user functions that contain user-defined code can be executed. User generated code can be used to perform first calculations that need to be executed only once during the entire data analysis. Placing these calculations in the unpacker is more efficient since the unpacker usually is executed once while other analysis steps for a data set are performed multiple times.

For higher versatility and control over the data, the existing unpacker version has been expanded within this work. The extensions of the user code are:

- Ability to unpack traces of all events.

- Optional pileup correction technique for reconstruction of overlapping subevents.
- Calculation of corrected timestamps (see Section 5.2.2) to achieve time resolutions better than 4 ns.
- Calculation of mean timestamp of QCLAM scintillator signals.
- Option to define QCLAM timestamps in LaBr DAQ as LaBr-QCLAM trigger, PMT down of QCLAM scintillator, PMT up of QCLAM scintillator or the mean of the two scintillator signals.
- Evaluation of the statistics counters including calculation of dead time and count rates.
- Calculation of raw energy from the accumulator gates.
- Sorting of events from all channels and improved output file format.
- Generation of trigger pattern file.

The definition of the QCLAM timestamp in the LaBr DAQ and the usage of the pileup correction technique are handled by command line options. It was found that the best time resolution is obtained by using the average of the PMTs, which can be attributed to its independence on the position of interaction of the electron within the QCLAM scintillator.

After the raw data file is processed, the data is written to two ROOT files. The first file contains the for each of the input channels of the SIS3316 module an individual ROOT tree containing the unpacked event data and a ROOT tree containing the QCLAM timestamps in the LaBr DAQ. The second file contains the trigger pattern in the form of the time difference of successive coincidence triggers. These are used for the creation of the mapping rule for the evaluation of a coincidence measurement in one of the following analysis steps. The output file can be opened directly within ROOT or by the Gamma Analyzer, which automatically generates spectra.

6.1.2. Pileup Correction

(e,e'γ) coincidence measurements are accompanied by a high beam-induced background, which dominates the count rate in the $LaBr_3$:Ce detectors. As the count rate increases, the average time difference between two events decreases and becomes shorter than the pulse length of the detector signal. Consequently, signals overlap in time and measured signals become distorted. This effect is usually known as pileup. It causes a loss of time and energy resolution and full energy peak efficiency. To avoid interference of signals, an upper limit of the count rate defined by the data acquisition performance can be specified. Due to the correlation between background and beam current, this results in an upper limit for the beam current and would thus lead to a reduced rate of true coincidences. By using a pileup correction technique, the initial signals are reconstructed from the measured signal and resolution and efficiency are restored.

A study has shown that $LaBr_3$:Ce detectors can be operated with conventional methods at rates up to 500 kcps without significant reduction of resolution and efficiency [163]. It must be taken into account that these detector signals decayed faster and returned to the baseline level already after 80 ns, whereas the detectors of the (e,e'γ) experimental setup reach the baseline only after 160 ns. A possible reason for this difference is the PMT type that is used. Since commissioning experiments of the new setup at the S-DALINAC measured rates above 500 kcps up to several Mcps (see Chapter 8), an optimized setup for background reduction and a pileup correction for handling higher rates were developed in parallel.

There are different existing approaches to correct for pileups, including an analytical approach [163] and a least squares fitting method [164]. The analytical method is rather efficient but requires a pulse shape that is independent of the amplitude. The number of overlapping events is determined using a moving average window. Since for measurements over a large energy interval, from a few hundred keV up to 15 MeV, changes in the pulse shape occur, this method cannot be used in the present work and a fitting method was chosen instead. The pileup correction is implemented in the user code of the UCESB unpacker and executed after all data are unpacked und before the output file is created. It utilizes a ROOT internal fit algorithm and the ROOT internal multi-threading support, which is necessary for a good performance and allows a pileup correction during the measurements.

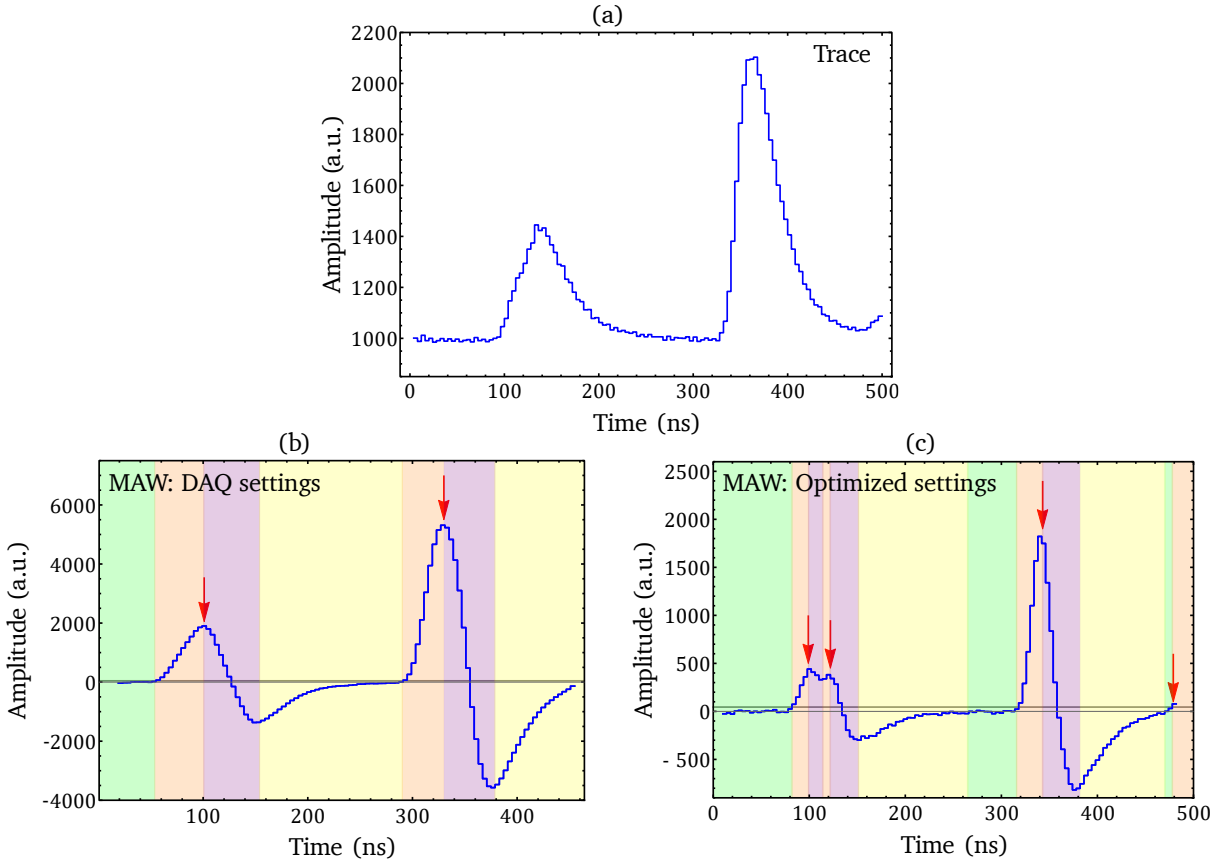

Figure 61: (a) The pileup correction is demonstrated using a trace of an event from the ^{12}C commissioning experiment (see Chapter 7). At t=100 ns, two pulses with a time difference smaller than the decay time of a detector signal overlap. A third pulse is located at t=330 ns, which is followed by a fourth signal shortly before it reaches the baseline. (b): MAW using settings of the LaBr DAQ during data recording. The stages of the pileup correction algorithm are color coded to indicate the active category. Green: baseline, orange: rising edge, purple: falling edge, yellow: minimum to baseline. Due to the large peaking time and gap time only two subevents are detected. (c): Optimized MAW with increased sensitivity to pileups.

The pileup correction of each event is divided into two steps. In the first step, shown in Figure 61, the number of subevents, i.e. the number of $LaBr_3$:Ce signals in the recorded trace of an event, is determined. In the second step a curve fitting of the individual subevents to the recorded trace is performed, which determines the energies and timestamps of each subevent. Analogous to the generation of internal triggers and pileup detection of the SIS3316 module, the detection of the number of subevents of a trace is done by means of a moving average window (see Section 5.2.2), which is configured to be more sensitive to events with small amplitudes. The optimized setting of the MAW (peaking time: 3 samples, gap time: 0

samples), used in (c), already ensures an increased sensitivity to pileups compared to the settings defined in the DAQ for internal trigger generation. Sensitivity was further improved by a subdivision of the trace into stages of four categories, that are color coded in Figure 61: In the first category (green), detection takes place when the amplitude of the MAW exceeds a threshold. This corresponds to the procedure used in [163]. After the threshold is exceeded, the second category (orange) becomes active, in which pileups are searched by checking for changes of the slope of the rising edge. If the maximum is reached and the amplitude decreases, the third category (purple) begins and analogous to the second category, pileups are detected based on changes of the slope of the falling edge. The fourth phase (yellow) begins when the minimum of the MAW is reached and ends when the baseline is reached.

To achieve accurate results, precise knowledge of the pulse shape is required for fitting of the subevents to the trace. This is achieved by fitting a model function without fixed parameters to a measured pulse shape. To determine the signal shape with higher accuracy, many traces were averaged for reduction of statistical fluctuations. The best results were obtained using an empirical approach given by

$$s_n(x) = A_n \left(g_{asym,exp,n}(x) + \sum_{j=1}^{3} g_{asym,n,i,j}(x) \right) \tag{6.1}$$

consisting of a superposition of an asymmetric Gaussian with exponential tail

$$g_{asym,exp,n}(x) = \begin{cases} a_0 \, e^{-\frac{(x-x_{0,n})^2}{\overline{\sigma}_{0,l}}} & , x \le x_0 \\ a_0 \, e^{-\frac{(x-x_{0,n})^2}{\overline{\sigma}_{0,r}}} & , x > x_0, x \le x_0 + \eta \\ \dfrac{c3}{(c4 + x - x_{0,n})^{\gamma}} & , x > x_0 + \eta \end{cases} \tag{6.2}$$

and three asymmetric Gaussians

$$g_{asym,n,i,j}(x) = a_j \begin{cases} e^{-\frac{(x-x_j-x_{0,n})^2}{\overline{\sigma}_{j,l}}} & , x \le x_0 \\ e^{-\frac{(x-x_j-x_{0,n})^2}{\overline{\sigma}_{j,r}}} & , x > x_0 \end{cases}, \tag{6.3}$$

using minimization of the residual as the criterion. The fit determines the values of the parameters that define the shape, so that for the pileup correction a model function with fixed parameters can be used.

The resulting model function has only two free parameters per subevent, namely the amplitude A_n and a position $x_{0,n}$, which provide the energy value and time offset of the subevents. After fitting the reference signal, the amplitudes a_j, the shifts relative to the asymmetric Gaussian with exponential decay x_j, the squared widths $\overline{\sigma} = 2\sigma^2$ of the left and right half Gaussians with $\sigma_{j,l}$ and $\sigma_{j,r}$ of the asymmetric Gaussians and the parameters of the exponential decay $c3$, $c4$, γ and η have been uniquely defined. The index j with $j \in [0,3]$ labels the Gaussian curves and the index n corresponds to the number of the subevent of the

trace. For pileup correction, the following formula is fitted to the trace so that energy values and time offsets of each subevent are obtained:

$$f(x) = \sum_{n=1}^{N} s_n(x) + b. \tag{6.4}$$

N is the total number of subevents in the trace. The additional fit parameter b describes the offset of the baseline. Attempts to apply this model function, which was optimized using low energy events, to large energies caused huge deviations between model and measured trace. It was found that the pulse shape depends on the amplitude. Therefore, a linear combination of pulse shapes obtained at low and high energies are used to describe signals of arbitrary amplitudes introducing a third fit parameter l per subevent:

$$\tilde{f}(x) = A'_n \left(l\, s_{low,n}(x) + (1 - l)\, s_{high,n}(x) \right). \tag{6.5}$$

The parameter l is limited to values between 0 and 1 and its start value is determined based on the start value of the amplitude of the subevent. The amplitudes A_n of the model functions for low and high energies were normalized to 1 for this purpose, so that the parameter l does not influence the resulting amplitude. The energy of a subevent is now given by the new amplitude A'_n. The final model function for pileup correction is described by

$$h(x) = \sum_{n=1}^{N} \tilde{f}(x) + b. \tag{6.6}$$

A ^{56}Co source measurement was used to determine the parameters of the model function at low energies. The low count rate of 843 cps, together with the pileup suppression by the new pileup detection algorithm guaranteed that the recorded traces corresponded to single events. A gate was placed on the 511 keV peak created by the annihilation of the positron emitted during the β^+-decay of ^{56}Co with a relative width of 6.8%. This way, 28,000 traces were recorded and averaged, and the shape defining parameters were determined by a fit. Parameters of the high energy model function $s_{high,n}$ were optimized for a photon energy of 15 MeV. Photons emitted from radioactive sources usually have energies up to a few MeV. Energies up to about 10 MeV can be obtained, for example, from (γ,n) reactions (e.g. 8.55 MeV in ^{35}Cl(n,γ)^{36}Cl [165]). Higher photon energies can be achieved in beam operation at accelerator facilities as bremsstrahlung photons and photons from the decay of excited states are created. Since a (e,e'γ) measurement with a ^{12}C target was already performed at the QCLAM spectrometer in the context of this thesis (see Chapter 7), these data were used. A gate with a relative width of 8% at an energy of 15 MeV was used to select high energy bremsstrahlung photons. For the fit of the model function at high energies, 14 traces were averaged. The suppression of pileups was done manually because the automatic detection was less reliable for subevents whose amplitudes differed strongly. Since the relative statistical fluctuations are smaller for large amplitudes, the small number of 14 traces was sufficient. To achieve the best possible results, it is recommended to optimize the signal shape for each detector for the evaluation of each measurement independently, as significant differences in signal shape were found between different detectors. Examples of fitted parameters are listed in Appendix 12.18.

Figure 62 shows example signals of energies 511 keV and 15 MeV and the fitted signal shapes. A fit of the low photon energy signal shape to a 511 keV photon (a) results in a residual, defined as the difference of the measured trace and the fitted model function, fluctuating around zero (c). The signal shape of a 15 MeV photon (b) cannot be described by the previously determined low energy signal shape (red) shown in (a). Therefore, a new set of fit parameters must be determined (green). The residual shows that the high energy signal shape gives a better result than the low energy signal shape (d). Nevertheless, a structure can be seen in the residual of the signal shape for large photon energies, indicating an incomplete description of the true signal shape.

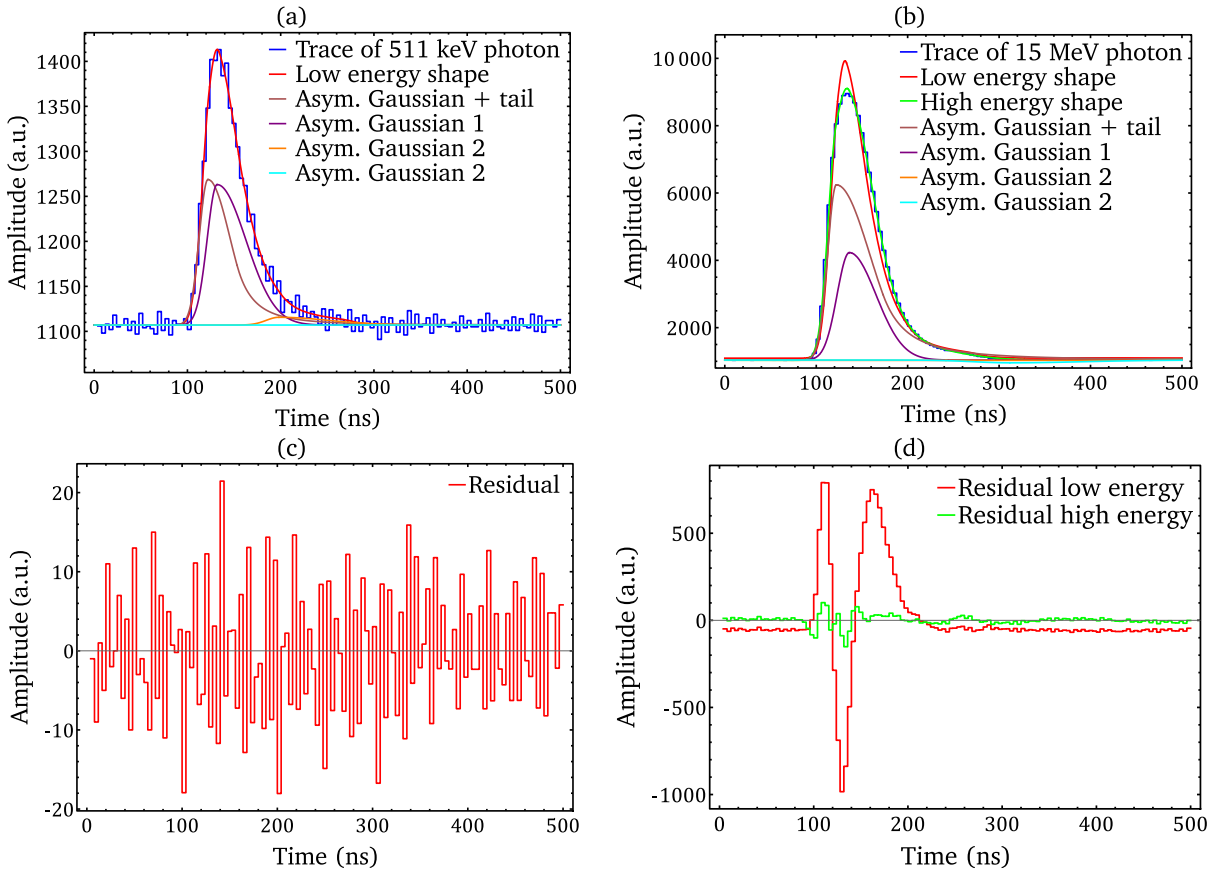

Figure 62: (a): Pulse shape of a 511 keV event. The low energy model function is fitted to the trace. (c): The residual at low energy shows no structure and fluctuates around the baseline. (b): Pulse shape of a 15 MeV event. The low and high energy model functions were separately fitted to the trace. (d): Residual of the model functions for low energy shows a distinct structure and offset from the baseline. The residual for the model function at high energies shows a small structure and it fluctuates around the baseline.

After the parameters defining the signal shape are fixed, the parametrizations from Equation (6.6) can be fitted to signals of arbitrary amplitudes to determine energy and time offset for each subevent of the trace. Figure 63 shows an example of pileup correction where four subevents of a trace were reconstructed. The first two subevents (orange and green) of approximately the same amplitude are processed by the accumulator gates as one event with summed area. Without the new pileup correction algorithm, subevents 1 and 2 would have been processed as one event with the summed area and subevents 3 and 4 would not have been registered. In addition, the pileup correction assigns an individual timestamp to each subevent, whereas without the pileup correction a single timestamp would have been generated for the trace. The fourth subevent is truncated at the end of the trace and therefore

provides unreliable values for energy and timestamp, but fitting its amplitude improves the fitted baseline. Another possible use of the pileup correction is, for example, the reconstruction of events below the threshold of the LaBr DAQ to check the energy calibration.

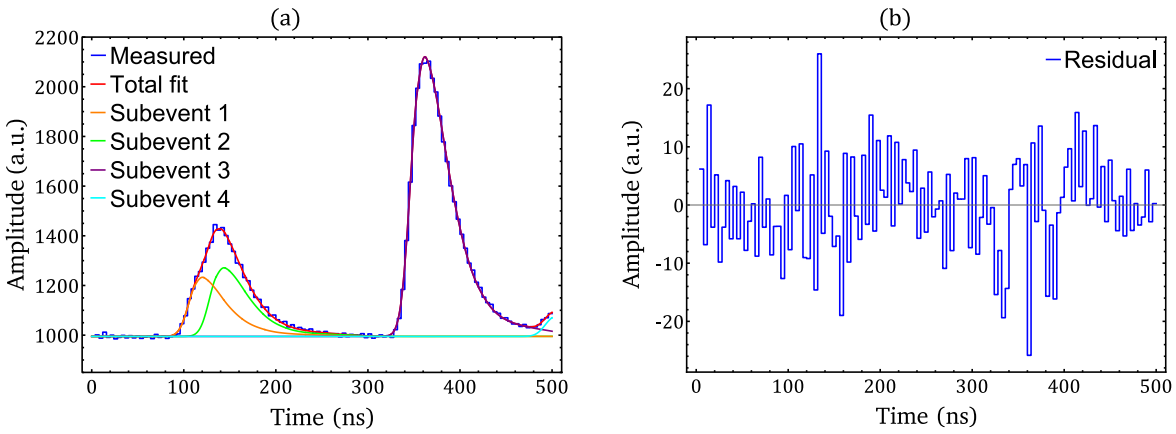

Figure 63: (a): Demonstration of the pileup correction using the trace from Figure 61 as an example. The total function (red) is the sum of the four individual pulse shapes (orange, green, purple and cyan). (b): Residual from curve fitting.

The pileup correction was tested using simulated traces as well as data from the commissioning beamtime in 2019 (see Chapter 7). During these measurements, count rates in the order of 1 Mcps were measured so that the pileup correction can be tested. For the next test of the pileup correction algorithm, simulated traces were generated, and spectra were generated with and without the pileup correction applied. For this purpose, traces containing two subevents were generated. To make the simulation more realistic, random noise (σ=3 a.u.) was added to the simulated traces and its amplitude was convoluted according to the resolution of 3.2 % for an 511 keV photon and 0.7 % for a 15 MeV photon given by [139]. The first subevent corresponds to an energy of 15 MeV and represents the photon emitted from the atomic nucleus. The second subevent represents a randomly distributed 511 keV background event. The 15 MeV subevent is randomly distributed around the position 118 ns by 4 ns, which is the uncorrected time resolution of the SIS3316 module. To simulate the varying time difference between the two subevents, the 511 keV subevent was shifted from left to right through the simulated traces in steps of 0.04 ns. For an increase in statistics, this process is repeated multiple times.

Figure 64 shows the results of this test. If the pileup correction algorithm is not used (red histogram), the overlap of the 511 keV subevent with the accumulator gates affects the calculation of the energy value of the event. If the 511 keV subevents overlaps with the baseline accumulator gate, up to twice the energy of the 511 keV subevent is subtracted since this accumulator gate is half the size of the accumulator gate of the energy signal (see Figure 49). Hence, the integrated area is subtracted twice. If both subevents overlap, the maximum energy is the sum of the two subevents. By using the pileup correction (green histogram), the true spectrum can be reconstructed to a large extent and the peak at 511 keV is recovered. By using the accumulator gates, i.e. no pileup correction, the peak area decreases to 74 % of the peak area of the real 15 MeV events. Applying the pileup correction, the peak area is increased to 95 %, 5 % of the simulated 15 MeV subevents could not be reconstructed with the correct energy. At energies below 100 keV, there is an accumulation of subevents, which is

due to the large number of subevents detected. An excess of subevents of 36 % was detected, which are negligible for the 15 MeV peak because of their low amplitudes.

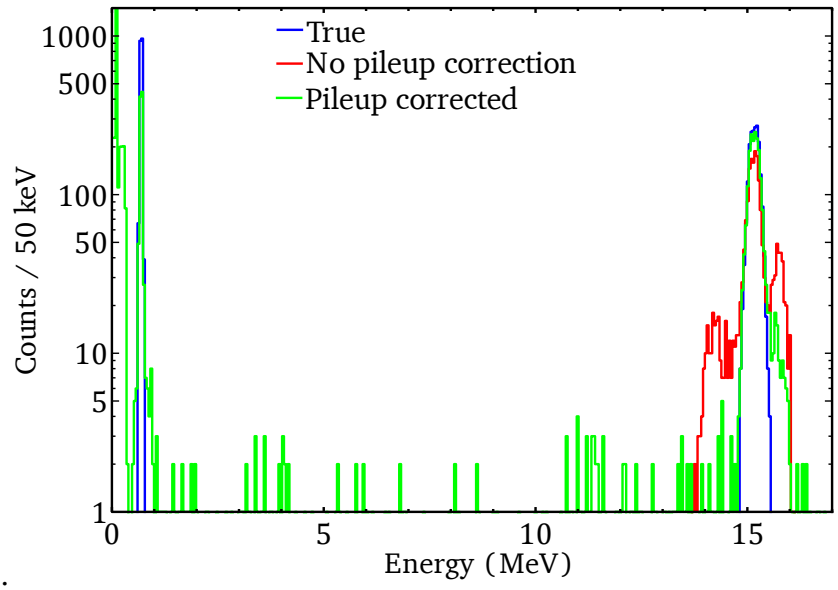

Figure 64: Spectra calculated from simulated traces consisting of a 15 MeV subevent and a background subevent of energy 511 keV. Blue: True energies of both subevents that were used to generate the simulated traces. Red: Energy values obtained by using accumulator gates. If both subevents are on top of each other, the energies are added. If the 511 keV subevent is in the accumulator gate, which determines the baseline, twice the area of the 511 keV subevent is subtracted from the 15.1 MeV subevent. Green: Pileup correction is able to reconstruct most overlapping subevents.

The reconstruction efficiency of the pileup correction was tested using simulated traces. As a measure of efficiency, the ratio of successful reconstructions of both simulated subevents to the number of traces is used. Figure 65 shows the dependence of the reconstruction efficiency for two 511 keV subevents as a function of the time difference between them (a) and the efficiency for a 15 MeV and a 511 keV subevent (b). As in the previous simulated spectra, the position of one subevent was fixed at 120 ns and the second subevent was shifted stepwise from left to right to investigate the influence of the time difference between both subevents. For (b), the position of the 15 MeV subevents was fixed. Due to the increased sensitivity of the pileup detection, tails of subevents that are positioned at the edge of the trace are detected, resulting in the reconstruction of events up to 70 ns before the start of the trace and 12 ns after the end of the trace. The efficiency is 100 % unless the time interval between the two subevents becomes too small, in which case the efficiency drops to zero within 8 ns. The time interval in which the efficiency drops to zero depends on the ratio of the amplitudes of the two subevents, since a comparatively small amplitude of a pileup is more difficult to detect from irregularities in the slope of the trace. If two 511 keV traces are used, the time interval is 40 ns long and in case a 15 MeV and a 511 keV trace are used, the length of the interval is 120 ns.

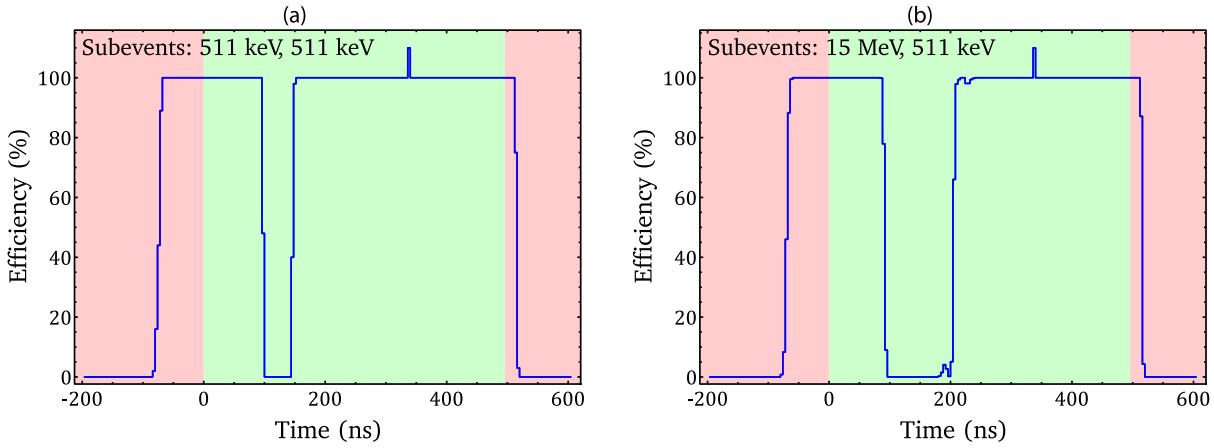

Figure 65: The x-axis indicates the time relative to the beginning of the measured trace (green area), the red areas are not recorded. (a): Reconstruction efficiency for two 511 keV subevents. The pileup correction algorithm is able to detect subevents outside the trace but with decreasing time difference between real signal (t=120 ns) and background signal the efficiency decreases to 0% for about 40 ns. (b): Reconstruction efficiency for a 15 MeV subevent an a 511 keV subevent. Because of the factor 30 in amplitude between both subevents, the gap where the reconstruction efficiency drops to 0 is increased to 120 ns. The bin with efficiency greater than 100% occurs at the same location in both figures and may be a binning artifact.

An example of the pileup correction applied to a measured γ-ray spectrum with a raw count rate of 1 Mcps is shown in Figure 66. Subfigure (a) shows the spectrum of a $LaBr_3$:Ce detector with and without pileup correction. By using the pileup correction, events above and below the threshold were reconstructed. The peak at 70 keV in the reconstructed spectrum is probably caused by X-rays produced in the lead shielding of the $LaBr_3$:Ce detectors. Since the trace is 500 ns long, events outside the 100 ns coincidence gate are also reconstructed. This could provide increased statistics for background investigations, e.g., X-rays for energy calibration. Subfigure (b) shows the corresponding time difference spectrum.

Application of the pileup correction increases the number of events above the threshold of 400 keV by 60%, and the counts in the 511 keV peak are increased by 89%. The energy resolution of the spectrum without pileup correction is 32(1) keV and matches the energy resolution of 32(1) keV of the spectrum with pileup correction. The FWHM time resolution without pileup correction is 6.1(7) ns and does not significantly differ from the time resolution with pileup correction of 5.4 (6) ns. The pileup correction increases the number of usable events without negative impact on energy and time resolution.

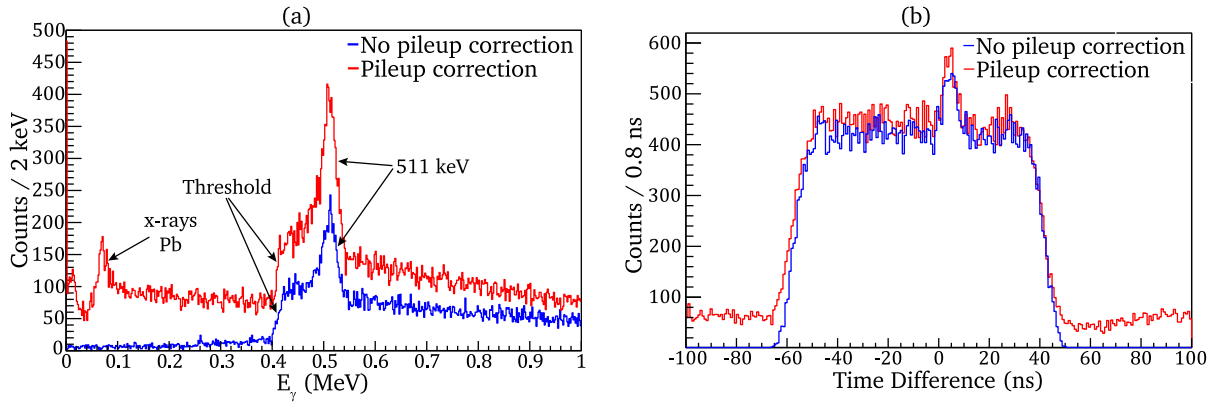

Figure 66: (a): Energy spectra with and without pileup correction. (b): Time difference spectra with and without pileup correction.

The functionality of the pileup correction was demonstrated by simulations and measurements. Additional events were reconstructed with negligible effects on energy and time resolution. However, simulations showed that the pileup detection algorithm of the pileup correction is too sensitive and detects too many subevents in a trace. This should be investigated further before the pileup correction can be used to evaluate a measurement. Another possible optimization concerns the model function for high energy events, where the residual shows a structure.

6.2. Gamma Analyzer and Trace Viewer

The unpacked raw data contains all information but must be further processed and sorted for analysis. This task is performed by the Gamma Analyzer, which is suited for the evaluation of data from the LaBr DAQ alone, e.g., for calibration measurements and optimization of data acquisition parameters, and is used as an intermediate step in the analysis of coincidence experiment. Since the same trigger signal generates a timestamps in the LaBr DAQ and the QCLAM DAQ, the timestamps of the $LaBr_3$:Ce events can be mapped to the timestamps of the LaBr-QCLAM trigger in the Gamma Analyzer. When the QCLAM and LaBr files are merged (see Section 6.4), only the associated electron information needs to be mapped to the events of the Gamma Analyzer output files. In addition, the time differences between the QCLAM event and the $LaBr_3$:Ce event can be displayed in the Gamma Analyzer. A development related to the Gamma Analyzer is the Trace Viewer, which starting from the raw data allows to visualize the traces and to optimize the settings of the data acquisition. Trace Viewer was also used as a test environment for the pileup correction. Gamma Analyzer and Trace Viewer are based on the ROOT framework.

After the unpacked raw data has been read in by the Gamma Analyzer, the singles and coincidence analyses of the Gamma Analyzer are performed in sequence. The singles analysis runs through the ROOT trees of the SIS3316 input channels one after the other and generates energy spectra of all channels. Since the raw data does not contain an assignment of the $LaBr_3$:Ce events to the time information of the QCLAM trigger, a loop is performed for each channel per QCLAM trigger timestamp to search for events which timestamp differs from the QCLAM trigger timestamp by a maximum of 500 ns. These events are considered coincident and are stored in a new ROOT tree and written to a file. The analysis of the coincident data generates a coincident energy spectrum and a time difference spectrum for each channel. In addition to the two analysis steps, raw and accepted rates as well as other statistics such as the number of subevents in a trace are displayed for each channel.

The coincident data is stored in a ROOT tree in a file. For each coincident event, there is a timestamp of the coincident trigger and at least one $LaBr_3$:Ce event whose information is stored in a standard C++ vector. If a pileup correction is used, there is at least one subevent for each $LaBr_3$:Ce event, which are again stored inside a vector.

6.3. Electron Analyzer and Electron Viewer

The raw data from the QCLAM data acquisition are unpacked by QCLAMon and all corrections such as correction of aberration and scattering angle calibration are applied to generate final electron spectra [95]. The electron data are stored by QCLAMon in an SQLite database [166] that contains a list of the QCLAM events and corresponding information like timestamps, coordinates, and angles of the electron at the detector system. Since the SQLite

file format is uncommon in nuclear physics applications, the primary task of the Electron Analyzer is the conversion of the QCLAMon output files from SQLite to ROOT files. This is required for merging the coincident data from both data acquisitions. The Electron Analyzer generates two output files: the converted SQLite file and a file containing the trigger patterns of the coincidence trigger in the QCLAM data acquisition. The latter is required for the Trig Match analysis step for matching the trigger patterns of the QCLAM trigger in both data acquisitions. In addition to the file format conversion, the Electron Analyzer is used for initial analysis steps: correction of aberration, correction of shifts of peaks between runs, energy calibration, and application of the time-of-flight correction.

The Electron Analyzer can be used for inclusive and exclusive electron scattering measurements at the QCLAM. Since the LaBr data acquisition was used for an initial test of merging electron data and $LaBr_3$:Ce data at the Lintott spectrometer, a template for the structure of the SQLite database of the Lintott data acquisition is provided in the source code as well, so that the Electron Analyzer could also be used for evaluation of Lintott data. Electron Viewer is a tool optimized for summing and evaluating pure electron data of the Electron Analyzer output files and was already used for a limited time during an electron scattering experiment at a scattering angle of 180° [167].

Due to different trajectories of the electrons inside the QCLAM spectrometer, the time-of-flight of the electrons from the target to the detector system varies. For inclusive electron scattering experiments, this effect does not matter. For coincidence experiments on the other hand, a precise determination of the timing of the scattered electron is crucial.

Based on the geometry, it is assumed that the non-dispersive coordinate, y, and the non-dispersive angle have a negligible effect on the time-of-flight. In this case, the time-of-flight can be expressed by a polynomial approach

$$t_{tof}(x, \phi) = b_1 + b_2\, x + b_3\, \phi + b_4\, \phi^2 + b_5\, x\, \phi. \tag{6.7}$$

This is an empirical approach that has been used in the past for time-of-flight correction of QCLAM data [99]. Here, b_i stands for the parameters of the polynomial, x for the dispersive coordinate and ϕ for the dispersive angle in the detector system. To test the validity of the empirical approach, the trajectories of electrons with five different vertical scattering angles and nine different energies were calculated within the angular and momentum acceptance of the QCLAM spectrometer in a simulated magnetic field using CST Studio Suite [141]. The simulated trajectories are shown in Figure 67. The simulation was performed using a previously created geometry of the QCLAM magnet system [140].

To perform the time-of-flight correction, Equation (6.7) is fitted to the positions and angles of the electrons in the detector system to determine the values of parameter b_i. Figure 68 shows the time-of-flight before and after time-of-flight correction. Without the correction the time-of-flight is uniformly spread between 10 ns and 15 ns. After the correction a constant time-of-flight is obtained with a resolution of 0.1 ns FWHM. Given that the time resolution of the QCLAM spectrometer detector system is 2 ns, the empirical approach is suitable to be used in the evaluation of (e,e'γ) coincidence measurements. The parameters for the time-of-flight correction obtained from the simulation are listed in Table 10.

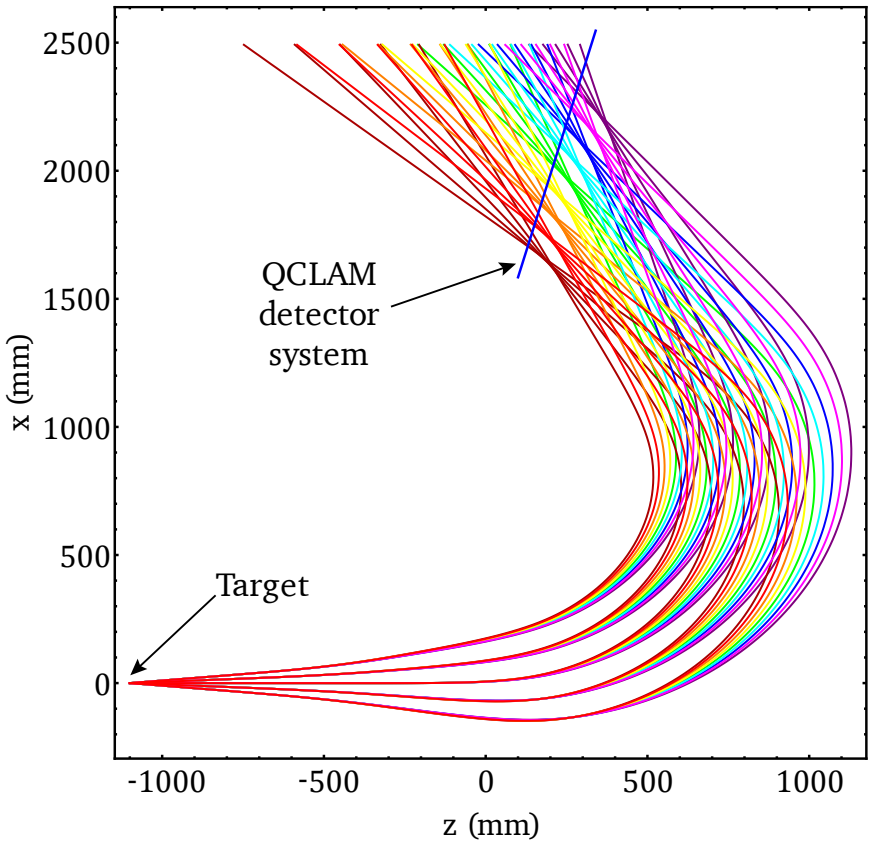

Figure 67: Trajectories of electrons with nine different energies and five different vertical scattering angles were simulated with CST Studio Suite [141]. Trajectories of the same energy are color coded identically and intersect in the focal plane in front of the detector system. The simulation was performed using a previously created geometry of the QCLAM magnet system [140].

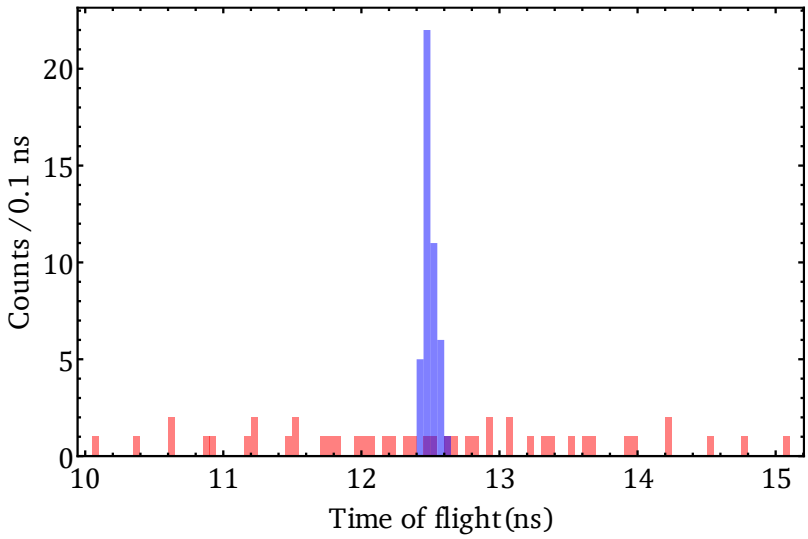

Figure 68: Without correction, the simulated time-of-flight of the electrons is 10 ns to 15 ns (red). By applying the time-of-flight correction, the time-of-flight distribution forms a sharp peak (blue).

Table 10: The parameters of the time-of-flight correction given by Equation (6.7) were obtained by a fit to simulated electron trajectories. If no correction from measured data is available, these parameters can be used.

Parameter	Value
b_1	10.13 ns
b_2	$-3.678 \cdot 10^{-3}$ ns/mm
b_3	$7.055 \cdot 10^{-2}$ ns/deg
b_4	$9.512 \cdot 10^{-4}$ ns/deg^2
b_5	$-4.481 \cdot 10^{-5}$ ns/(mm deg)

Since the time information of both particles of the exclusive measurements are required for this determination of the correction parameter, it cannot be performed by the QCLAMon or the Electron Analyzer. But the application of the correction requires only the fixed correction parameter and the position and angle of the trajectory of the electron inside the QCLAM detector system, which are provided by the QCLAM data.

The Electron Analyzer is a tool for analyzing QCLAM data and provides the required functions. Using the two output files of the Electron Analyzer and the output files of the unpacker and Gamma Analyzer, the data of an (e,e'γ) measurement can be combined into a coincidence data set.

6.4. Trig Match

Before the data from both data acquisitions can be merged, a mapping rule that assigns the corresponding LaBr event to each QCLAM event must be created. For this purpose, the dedicated software Trig Match was developed. It reads the files containing the time differences of consecutive coincidence triggers, produced by the unpacker and the Electron Analyzer, and searches for matching patterns. From this, the mapping rule is generated and stored in a file.

Random matches of the trigger patterns may lead to a wrong mapping. To prevent this, a sufficiently large minimum number of consecutive matches must be defined. Tests with a minimum of 5 to 1000 matches achieved good results. In addition, the maximum allowed time difference between the successive triggers in both DAQs should be kept low. In early tests a maximum allowed time difference of 150 ns was used. Due to a change in time resolution of the QCLAM timestamps, the maximum allowed time differences was increased to 30 µs. For future experiments, the time resolution of the QCLAM timestamp should be optimized to use an upper limit of 150 ns again.

To search for matching trigger patterns, the LaBr and QCLAM data are labeled file 1 and file 2. For each element in file 1, the algorithm searches by looping over all elements in file 2 for an element that differs in value by less than a predefined maximum time difference from the element in file 1. If no match is found, the next element in file 1 is searched for a match in file 2 until either a match is found or all elements in file 1 have been run through. If a match is found, a counter is incremented by one and the next element from file 1 is compared to the next element from file 2. The counter is incremented with each new match until either the

end of file 1 or file 2 is reached or no match is found. If the value of the counter is then greater than the threshold for the required minimum number of matches, these events are classified as related and their indices relative to the first entry in the file form the mapping rule and are stored in a ROOT tree. Then the counter is set to zero to search for the next match. The algorithm continues in this way until the end of file 1 or file 2 is reached. By requiring a minimum number of matches, the probability of random matches is greatly reduced. If there is no match for individual events due to an error in a file, for example, these events are skipped but subsequent events can be matched, minimizing the loss of events.

If data is written to a file by the LaBr data acquisition, before the QCLAM data acquisition is ready to write data to a file, loops over all the elements in file 2 for the first n' elements of file 1 are performed, which is time consuming if there are a large number N of events in file 2. This is optimized by swapping the mapping of the LaBr and QCLAM files as file 1 and file 2 if after 20 tries no match was found. Now the QCLAM file is labeled file 1 and a match to the first element is found in the first loop over all elements in file 2. Figure 69 illustrates this optimization. If a run consists of multiple files there is a time window between the closing and opening of the files during which no data can be saved. By saving the index N' of the file not having reached the end, the search for matching trigger patterns can continue at this point.

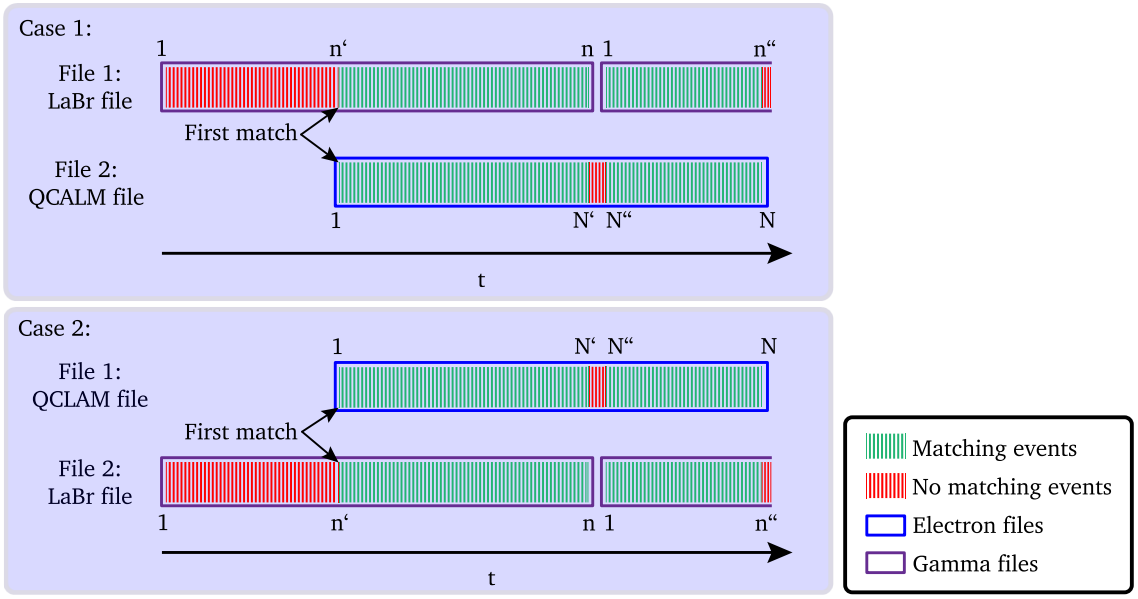

Figure 69: The files of both data acquisitions containing the time pattern of the coincidence trigger are labeled as file 1 and file 2, respectively. If there is no match in file 2 for the first elements in file 1, the labels are swapped, and a match is found. Thus, matches of events with indices n' to n in the first file of the LaBr data acquisition are assigned to events 1 to N' of the QCLAM data acquisition. For the second file of the LaBr data acquisition the corresponding events 1 to n'' are assigned to the events N'' to N' of the QCLAM data acquisition.

A first test of this matching algorithm was performed in 2017 during a parasitic measurement at the Lintott spectrometer, where data from the Lintott spectrometer and an early version of the LaBr data acquisition were successfully merged. In the following year, a parasitic test was performed at QCLAM with difficulties in finding matching trigger patterns. A detailed examination of the trigger patterns led to the findings shown in Figure 70.

- Multi-hit event: At high trigger rates, the QCLAM spectrometer writes multiple events in one read out process to a file but creates only one timestamp for all events in this readout.

- Split multi-hit event: The distribution of these events to the previous or subsequent timestamp was not consistent and resulted in splitting these multi-hit events.
- Delayed readout: In some cases, the timestamp of the QCLAM data acquisition was delayed. This was caused by the order of the QCLAM readout process, where the timestamp was created at the end of the readout process and therefore depended on the duration of the readout process. Creating the timestamp at the beginning of the readout process solved this problem [160].
- Missing LaBr/QCLAM event: In few cases, one of the data acquisition systems did not register an event and did not generate a timestamp.

The correction of these effects was done by summing successive time differences until a match, indicated by the dotted lines in Figure 70, is found. If the summed number of QCLAM events is equal to the number of summed coincidence timestamps in the LaBr DAQ, i.e., no event was lost, the QCLAM events without an individual timestamp can be mapped to a timestamp of the coincidence trigger in the LaBr data acquisition. By using the dead time lock, as explained in Section 5.3, it can be ensured that only one event is contained in each readout process. For the future, the implementation of a timestamp for each event instead of each readout process is recommended.

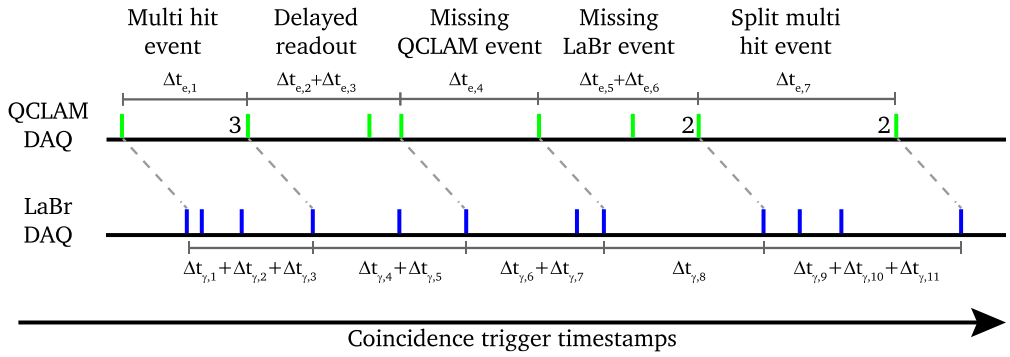

Figure 70: Due to the errors presented, the trigger patterns of the coincidence trigger differ in the two data acquisitions. The numbers next to a timestamp indicate the number of associated events. If only one event is included, the number was not shown for a better overview. The correction is done by summing several time differences.

Since the clocks of the two data acquisitions are not synchronized another effect occurs: the offset of the timestamps is not constant, but changes in first order proportional to the elapsed time. This affects the time differences of successive coincidence triggers and can lead to deviations larger than the maximum allowed time difference at low rates, e.g., when the electron beam is lost, and the detectors are triggered by background radiation. Therefore, a correction of the QCLAM timestamp is performed using

$$\Delta t_{trig,corr} = \Delta t_{trig}\,(1 + a). \tag{6.8}$$

The time difference Δt_{trig} is the difference of the timestamps of both DAQs created by the QCLAM trigger, the parameter a is the rate, at which the timestamps run apart. This parameter is determined by a fit to measured data.

Figure 71 shows an example of a successful matching. The matching trigger patterns of the two data acquisitions are shown in (a). The exact speed at which the clocks of the two data acquisitions run apart varies between measurements. In the example shown, the value

determined by the fit in (b) is $4.98837 +/- 6.4 \cdot 10^{-12}$ ms/s so that without correction the maximum allowed time difference is exceeded after less than a second without trigger. If random matches occur, this becomes visible in the plot of the running apart time differences. Since random matches do not have a fixed time relation to other matches, this results in jumps in the otherwise constant slope. The residual of the measured and fitted data shown in (b) is plotted in (c). The periodic time structure is caused by accuracy of the electronics, which generates the QCLAM timestamp.

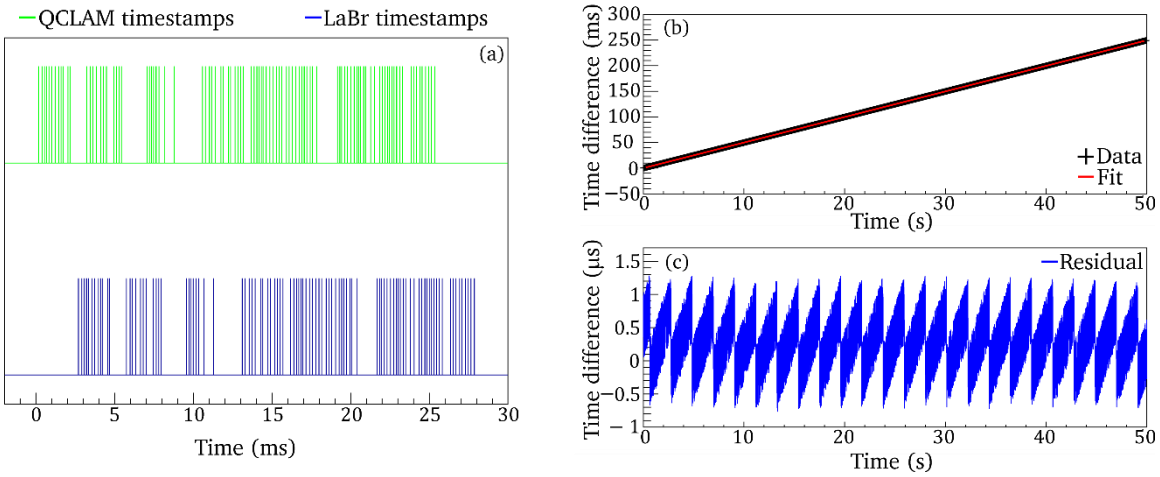

Figure 71: (a): Shown are the first 100 matching coincidence triggers. The offset was adjusted for the display. (b): Plot of time difference between QCLAM and LaBr data acquisitions plotted against measurement time. The fitted slope is shown in red. (c): In the residual of the fit, the time resolution with which the QCLAM electronics generates the timestamps is visible.

The problems in assigning the events from both data acquisitions was solved by optimizing the readout process and the new dead time interlock. Thus, a rule for merging can be created from the trigger pattern files. This rule is used by Coin Merger to combine the data from the individual DAQs to a coincidence data set, as will be described in the next section.

6.5. Coin Merger and Coin Analyzer

Coin Merger reads the output files containing the event data from Gamma Analyzer and Electron Analyzer and the created mapping rule from Trig Match and creates a coincident event based on the entries in the mapping rule, which contains the corresponding data of the QCLAM event and the events of the $LaBr_3$:Ce detectors. Depending on whether one or more $LaBr_3$:Ce detectors have registered an event coincident with the QCLAM, the coincident event contains the data of at least one but at most all $LaBr_3$:Ce detectors. The coincident events are stored in a ROOT file and can be read by the Coin Analyzer for evaluation.

The Coin Analyzer is used for visualization and evaluation of the coincident data. In a configuration file any number of gates can be set to the excitation energy and the γ-ray-energy, from which spectra are automatically generated when running the Coin Analyzer. In addition, parameters for the automatically executed background subtraction are defined, which is described in Section 7.6. In addition, the Coin Analyzer contains functions for determining the correction parameters for optimizing the time difference, namely the time-of-flight correction and the correction of the time effect between the electron timestamp and the

γ-timestamp, which is described in Section 7.4. The correction functions and the automatic background subtraction ensure that the Coin Analyzer is easy to use.

This completes the preparation of the data beginning at the events of the individual DAQs to the combined coincidence event and the evaluation of the measurement can begin. For this purpose, further tools of the Coincidence Analyzer are available, such as automatic generation of histograms with gates on the excitation or γ-ray-energy, which can be defined in a text document. Alternatively, histograms and the ROOT tree can be exported for further analysis with other software.

7. Commissioning Measurement on ^{12}C

The first dedicated commissioning of an early version of the (e,e'γ) experimental setup was performed using a ^{12}C target. The ^{12}C nucleus has been selected for the test because of the strong M1 transition of the 1_2^+ state at 15.1 MeV and the low background that is expected because of its low mass number. This nuclide was also studied in the first (e,e'γ) coincidence experiment [22] making it an ideal benchmark. The goal of this commissioning was to measure the excitation and coincident γ-decay of the 1_2^+ state at 15.11 MeV to demonstrate the feasibility of (e,e'γ) measurements at the S-DALINAC. In addition, the 2_1^+ state of ^{12}C at 4.4 MeV was measured, and an additional test was performed to investigate the GDR in ^{96}Zr. Findings from this measurement were the basis for improvements to the (e,e'γ) setup.

7.1. Experimental Setup

The first version of the (e,e'γ) experimental setup, shown in Figure 72, consisted of three $LaBr_3$:Ce detectors, the ball scattering chamber ③, and a magnetic field shielding ④ consisting of iron plates attached to each other. In addition to the magnetic field shielding, μ-metal was used where gaps were formed. For protection against background radiation, the detectors were mounted in the first version of the new detector housings consisting of an aluminum housing with an integrated lead shielding. Detector 0 was positioned downstream from the target below the beam pipe, detector 1 in a lead castle ① and detector 2 ② next to the QCLAM quadrupole magnet ⑤. The positions of the detectors are listed in Table 11. For this measurement, drift chambers from two different generations were used, the second-generation X1/U double chamber [103] and the third-generation X2 chamber. The high voltage applied to the drift chambers was 6100 V for the X1/U double chamber and 5600 V for the X2 chamber. The QCLAM spectrometer was rotated to a scattering angle of 132.5°.

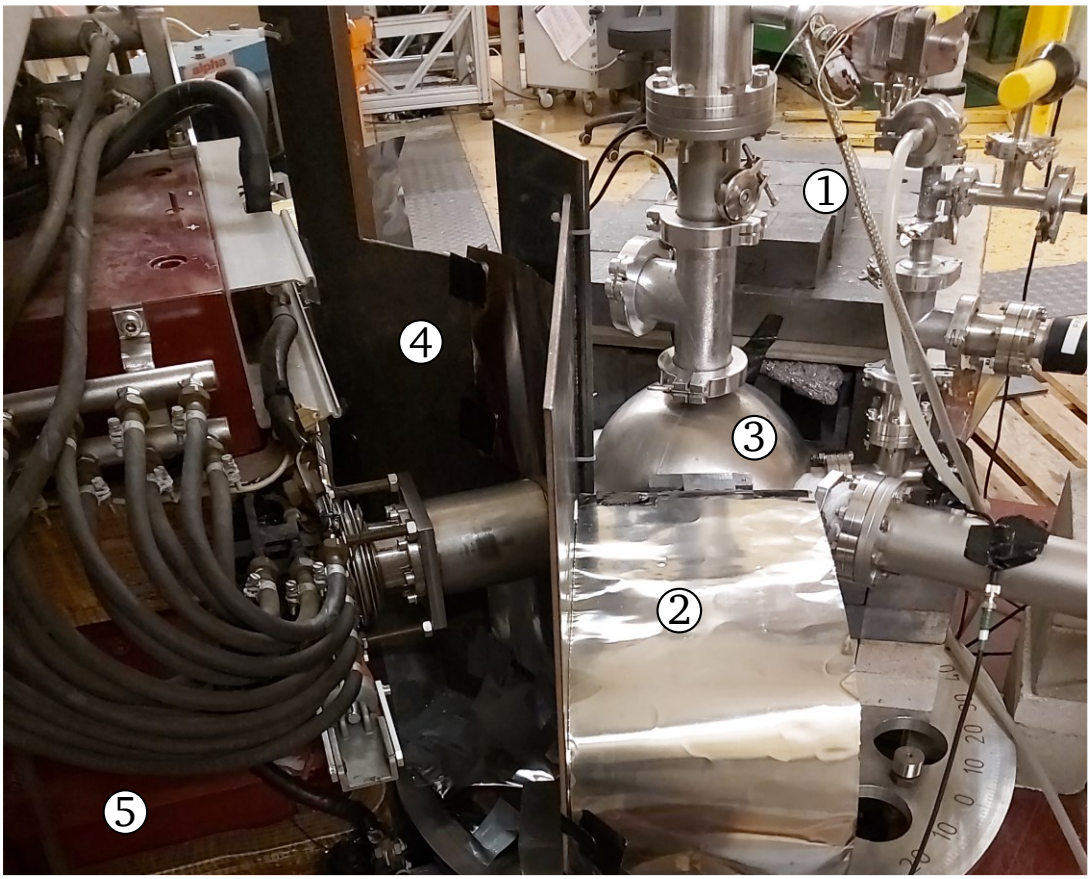

Figure 72: Early version of the experimental setup. Three $LaBr_3$:Ce detectors were used, one was installed inside a lead castle ①, the second was set up close to the spectrometer and had to be shielded by additional µ-metal ②, and the third detector was fixed under the beam pipe in front of the scattering chamber but is not visible in the photo. For this measurement the ball scattering chamber ③ was used, the beam pipe on the right side of the photo is pointing towards the Faraday Cup. The first version of the magnetic field shielding ④ consisted of iron plates placed between the scattering chamber and the QCLAM quadrupole magnet ⑤.

Table 11: The positions of the three $LaBr_3$:Ce detectors are listed. Detector 0 was placed below the beam pipe entering the scattering chamber, detector 1 was positioned next to the QCLAM Spectrometer and detector 2 was inside the lead castle. The column distance indicates the distance between the target and the front of the $LaBr_3$:Ce detectors.

Detector	Distance (mm)	Angle horizontal (deg)	Angle vertical (deg)
0	168	180	45
1	230	108	0
2	153	60	0

The four targets used at the beginning of the measurement campaign are shown in Figure 73. A 1 mg/cm^2 ^{197}Au target was used for optimization and to check the energy resolution. The position and size of the electron beam on the target were optimized using a BeO target, which glows at the point of impact of the electrons and thus enables visualization of the electron beam. Efficiency calibration measurements of the detector system of the QCLAM spectrometer were performed using a 10.1 mg/cm^2 ^{208}Pb target.

The low momentum transfer at a beam energy of 30 MeV and the small scattering angle of 47.5° resulted in a low form factor (see Figure 1) and thereby a low count rate. This made it necessary to position the QCLAM spectrometer at 132.5° to increase the momentum transfer for the commissioning experiment to achieve higher count rates. At this angle, the target had to be positioned in reflection geometry. The steep angle between the target and the electron beam increased the effective thickness of the target. Moreover, in the reflection geometry, the path length and thus the energy loss of scattered electrons in the target depends on the interaction point. Both effects reduce the energy resolution, which made it necessary to replace the 99 mg/cm^2 ^{12}C target used at the beginning of the measurement by a 10 mg/cm^2 thick ^{12}C target. For the measurement of GDR of ^{96}Zr, a 10 mg/cm^2 ^{96}Zr target was attached to the target ladder.

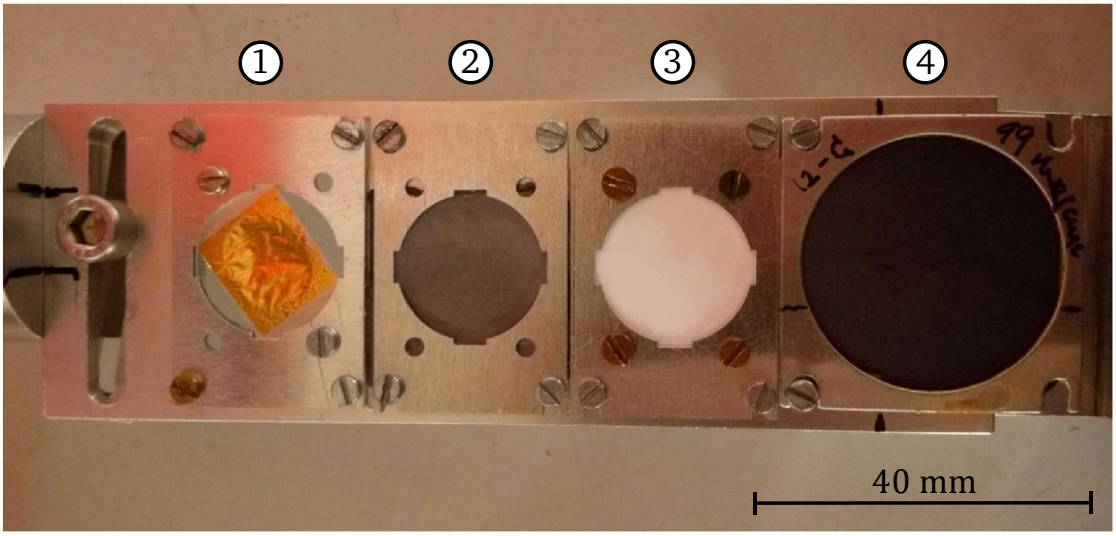

Figure 73: Four targets were mounted on the target ladder. The 1 mg/cm^2 ^{197}Au target ① is used to optimize the energy resolution. The 10.1 mg/cm^2 ^{208}Pb target ② is used for the efficiency measurement of the QCLAM spectrometer. A BeO target ③ is used for the optimization of the electron beam. At the beginning of the measurement campaign, a 99 mg/cm^2 ^{12}C target was used, which was replaced by a 10 mg/cm^2 ^{12}C target during the measurement.

7.2. Experimental Conditions

The first (e,e'γ) commissioning at S-DALINAC took place in 2019 from November 12th to December 13th. The energy of the electron beam was 30 MeV, and the maximum electron beam current was around 1 µA. Due to the limited cooling capacity of the S-DALINAC at that time, continuous beam operation could not be maintained during the measurements and had to be interrupted for several hours every day. The magnetic field settings used in the measurements of the 2_1^+ and 1_2^+ states of ^{12}C, the GDR of ^{96}Zr, and the calibration measurements of the efficiency and aberration of the QCLAM spectrometer are listed in Table 12. During the ^{12}C measurements, the trigger rate of the QCLAM detector system was up to 170 cps, and during the ^{96}Zr measurement, the trigger rate increased to 1500 cps. To correct for the change in peak positions in the spectra of the $LaBr_3$:Ce detectors, a five-minute measurement of the background lines was performed after each hour of electron beam measurement time.

Energy and efficiency calibration measurements of the three $LaBr_3$:Ce detectors were performed using ^{60}Co and ^{56}Co sources. The ^{56}Co measurements were also used for the energy

calibration at low γ-energies. For energy calibration at high photon energies, a $^{35}Cl(n,\gamma)^{36}Cl$ measurement was done using an Am/Be neutron source.

Table 12: Magnetic field settings of the measurements. The magnetic field of the QCLAM spectrometer is controlled by the current of the dipole and quadrupole magnets. The measurement for correction of the abberation of the spectrometer was done by moving the elastic line with four magnetic field settings to different positions in the detector system.

Measurement	I_{Dipole} (A)	$I_{Quadrupole}$ (A)
^{12}C, 2_1^+	36	45
^{12}C, 1_2^+	22.3	27.88
^{96}Zr, GDR	23.2	28.75
^{96}Zr Aberration	42 43.8 45.6 49.2	52.5 54.25 57 61.5
^{208}Pb Efficiency	18.5	23.13

7.3. Energy Calibration

Energy calibration measurements of the QCLAM spectrometer must be conducted with an electron beam on a calibration target. For the ^{12}C measurements, the measurement target also served as the calibration target. In the $LaBr_3$:Ce detectors, however, the spectrum is dominated by the electron beam related background, so that only the 511 keV peak can be seen in the singles spectra. Therefore, calibration measurements with radioactive sources were performed before and after the electron beam measurement. In the following sections the energy calibrations of the QCLAM and $LaBr_3$:Ce spectra are described.

7.3.1. Electron Optical Corrections of QCLAM Data

Before the energy calibration of the QCLAM data can be performed, the imaging properties of the spectrometer, which cause the focal plane to be curved as described in Section 3.3.1, must be corrected. By applying this correction, the energy resolution is significantly improved.

A measure of the energy of the electrons is the dispersive coordinate x in the detector system, which has a dependence on the remaining measured coordinates and angles in the detector system due to the electron optical imaging properties of the spectrometer [39]. The aim of the correction is the mapping of the measured data to a corrected coordinate x_{corr}. An approach often used is to correct for the dependence of the dispersive coordinate x and the dispersive angle ϕ using the polynomial

$$x_{corr}(\phi_{corr}) = \sum_{i,j} a_{ij}\, x^i\, \phi_{corr}^j \tag{7.1}$$

neglecting the much weaker dependencies from non-dispersive coordinates and angles. In the first step, the dependence of the dispersive angle from the dispersive coordinate, is extracted using

$$\phi(x) = a + b \cdot x. \tag{7.2}$$

This correction simplifies handling of the dispersive angle and application of gates, but Equation (7.1) can also be applied when the uncorrected dispersive angle is used. Figure 74 shows $x - \phi$ plots of a ^{208}Pb measurement before and after correction of the angle ϕ by the linear approach

$$\phi_{corr}(x) = \phi - \phi(x). \tag{7.3}$$

The parameters of the correction of the angle ϕ are listed in Table 13. Due to electron-optical imaging properties, a measured nuclear state, e.g., the elastic line, is represented by a curved line so that a wide distribution and thereby a low energy resolution is obtained when the $x - \phi$ plot is projected onto the x axis.

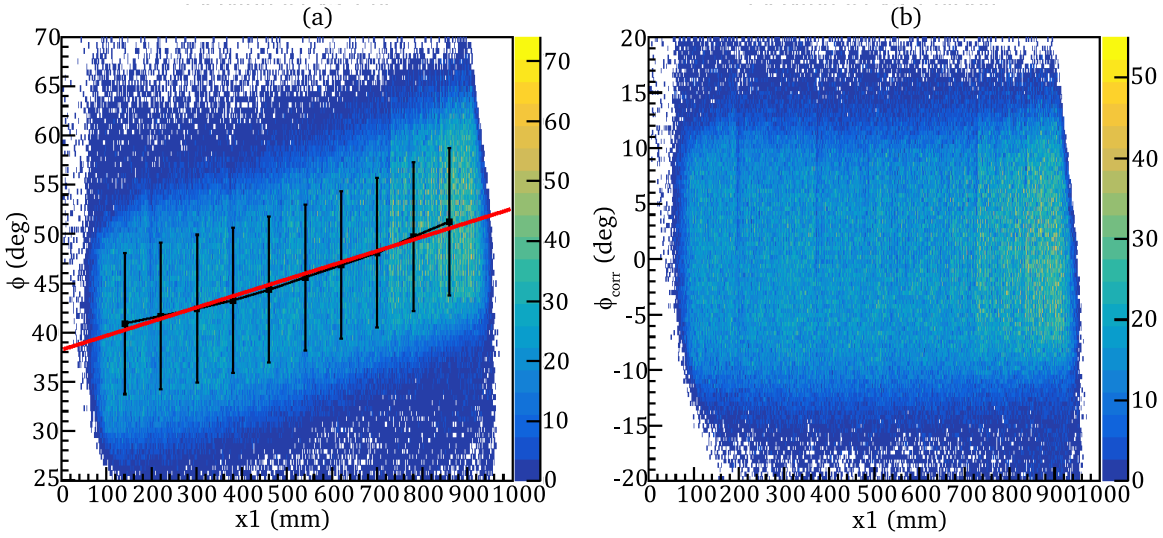

Figure 74: (a): $x - \phi$ plot of a white spectrum obtained in a ^{208}Pb measurement. The histogram was cut into slices, each slice was projected onto the ϕ axis and whose mean value was determined. A straight line (red) was fitted to the values obtained in this way. (b): $x - \phi$ plot after correction of the angle ϕ.

Table 13: Parameters for correcting the mean x dependence of the angle ϕ using equation (7.2).

Parameter	Value
a	38(7)°
b	8.2(12) 10^{-2} ° / mm

The parameters a_{ij} of the correction of the dispersive coordinate shown in Equation (7.1) are obtained by a multidimensional fit to multiple measured elastic lines of ^{96}Zr, which were moved across the focal plane by changing the current and thus the magnetic field of the dipole to four different values in the range of 42 A to 49.2 A, while keeping the quadrupole-to-dipole ratio constant at 1.25. The (x, ϕ) tuples required for the fit were obtained by cutting the $x - \phi$ plots along the ϕ axis in slices and fitting the electron scattering peak shape to each slice. For the corresponding x_{corr} value to which each elastic line is to be mapped, the

intersection of the curve with $\phi_{corr}(x) = 10°$ was calculated so that a uniform criterion is used for each magnetic field setting. Figure 75 shows an elastic line before and after correction for aberration using the parameters from Table 14.

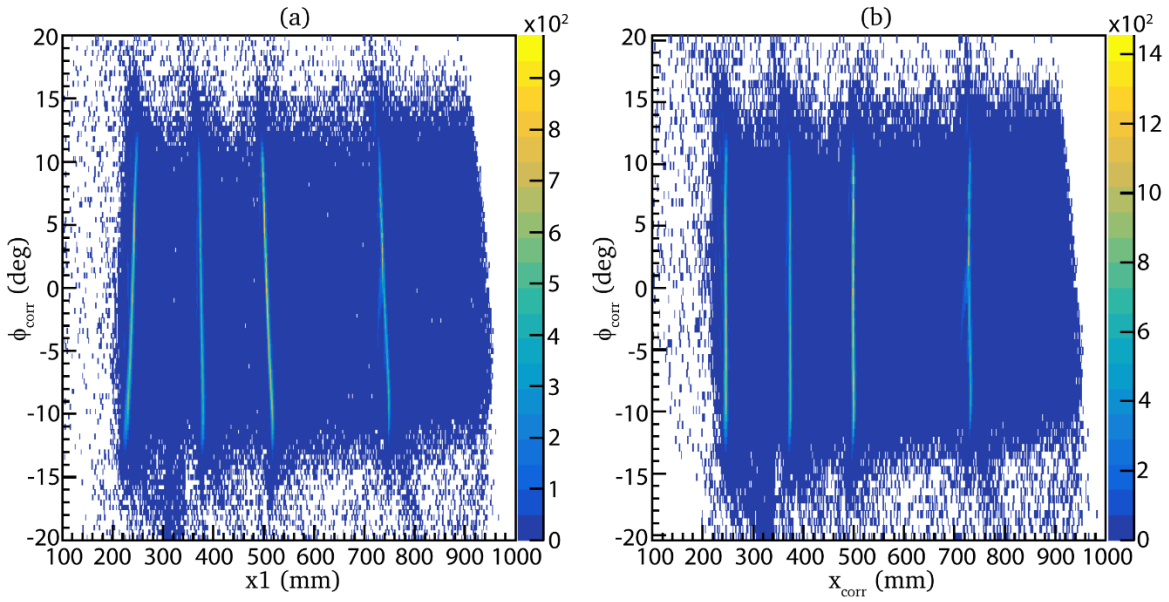

Figure 75: (a): Before the correction, the elastic lines from the four measurements shown in the $x - \phi_{corr}$ plot are curved because of the aberration of the electron spectrometer. (b): After correction of the aberration, the lines representing elastic scattering at different magnetic field settings are straight vertical lines.

Table 14: Listed are the parameters for the correction of the electron optical aberrations of the QCLAM spectrometer according to Equation (7.1).

i	j	a_{ij}
0	0	5.77 10^{1} (4) mm
1	0	8.74·10^{-1} (23)
2	0	1.13·10^{-4} (3) / mm
0	1	6.45 (5) mm / °
0	2	5.8·10^{-2} (6) mm / °²
1	1	1.38 10^{-2} (3) / °
2	1	-1·10^{-5} (40) / mm°
1	2	-8.8·10^{-5} (38) / °²
2	2	1.5 10^{-7} (5) / mm°²

Figure 76 shows the projections of the $x - \phi$ plots before (red) and after (blue) correction for the x-coordinate. The correction transforms the broad distributions of the elastic lines into peak-shaped structures, which already shows a significant improvement of the energy resolution. The x_{corr} values are used as the value of the uncalibrated energy in the further analysis of the QCLAM data.

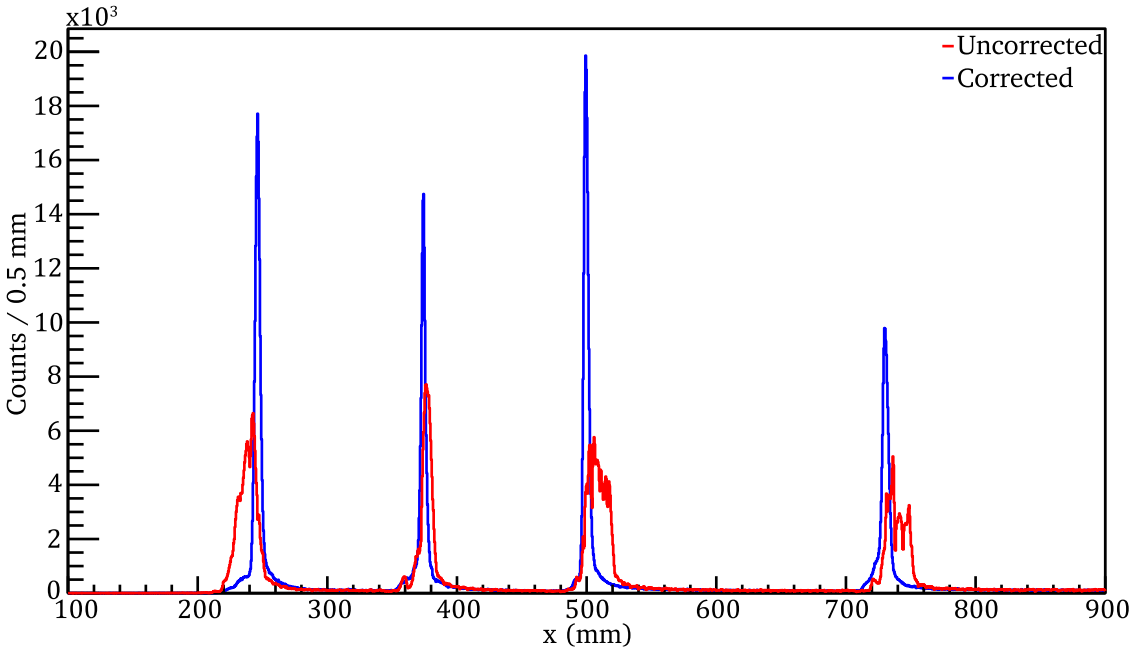

Figure 76: The spectrum of the elastic lines without correction shows broad distributions. After correction for aberration, the elastic lines form narrow peaks.

7.3.2. Energy Calibration of QCLAM Data

For further optimization of the energy resolution in the summed spectra of all runs of the measurement campaign, shifts resulting in a shift of the peak positions between the individual runs are corrected by an offset, which is determined for each run individually. Figure 77 shows the shifts for the measurements of the 2_1^+ state and the 1_2^+ state of ^{12}C. The peak shape of the peaks in the energy spectrum of the scattered electrons is described by the phenomenological parametrization

$$f(x) = \begin{cases} c_1/(\sqrt{2\pi}\,\sigma_1)\exp[-(x-x_0)^2/(2\sigma_1^2)] & ,x < x_0 \\ c_2/(\sqrt{2\pi}\,\sigma_2)\exp[-(x-x_0)^2/(2\sigma_2^2)] & ,x \geq x_0 \wedge x < x_0 + \eta\sigma_2 \\ c_3/(c_4 + x - x_0)^\delta & ,x \geq x_0 + \eta\sigma_2 \end{cases}, \tag{7.4}$$

which consists of two half Gaussian curves and followed by an exponential decay to describe the radiative tail [168,169]. The parameters σ_1 and σ_2 are the widths of the two half Gaussians, x_0 is the position of the maximum, the parameters c_1, c_2 and c_3 are scaling factors, c_4 and δ are parameters of the exponential decay and η determines the beginning of the exponential decay. To fulfill the continuity of $f(x)$ in Equation (7.4) between the different intervals, the following conditions must be fulfilled:

$$\sigma_2 = \sigma_1\, c_2/c_1 \tag{7.5}$$

$$c_4 = -(\eta^2 - \delta)\sigma_2/\eta \tag{7.6}$$

$$c_3 = c_2 \exp[-\eta^2/2](\eta\,\sigma_2 + c_4)^\delta/(\sqrt{2\pi}\,\sigma_2) \tag{7.7}$$

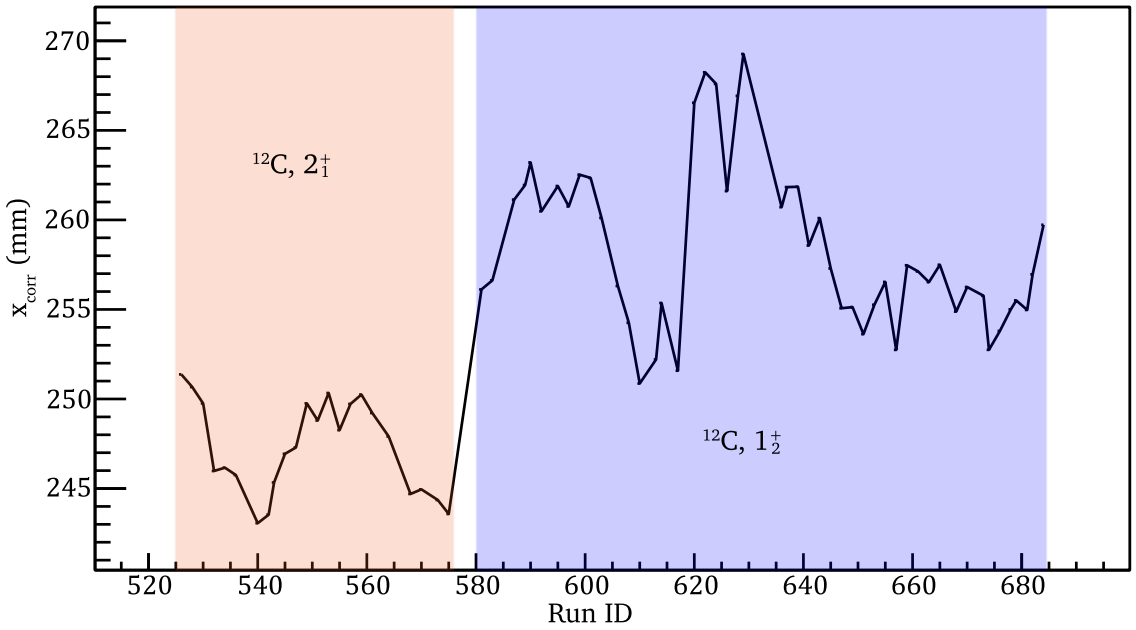

Figure 77: During the measurement campaign the position of the peaks in the QCLAM detector system changes. This is caused, for example, by fluctuations in the magnetic field strength, beam energy and (vertical) position of the electron beam on the target. For the ^{96}Zr measurements, the shifts could not be determined since there are no visible peaks in the spectrum.

The energy calibration of the QCLAM spectrometer was performed in previous measurements using a third-order polynomial [99]. However, since only two peaks in the acceptance of the QCLAM spectrometer were visible in the ^{12}C(e,e'γ) measurements, the energy calibration is performed according to a first-order polynomial

$$E(x_{corr}) = a + b \cdot x_{corr}. \tag{7.8}$$

During the measurement of the 2_1^+ state of ^{12}C, the states listed in Table 15 were in the momentum acceptance of the spectrometer. This resulted in the values $a = 2.298(16)$ MeV and $b = 8.558(27)\ 10^{-3}$ MeV/mm for the parameters of the energy calibration. The energy calibrated excitation spectrum is shown in Figure 78. The energy resolution of the 2_1^+ state is 41 keV FWHM.

Table 15: The listed states and their fitted positions were used for the energy calibration of the excitation spectra of the measurement of the 2_1^+ state of ^{12}C. Energy values taken from [43].

State	Energy (MeV)	Position (mm)
2_1^+	4.43982(21)	250.2(12)
0_2^+	7.65407(19)	625.8(3.6)

For the energy calibration of the measurement of the 1_2^+ of ^{12}C, the states listed in Table 16 were used, resulting in the values $a = 13.68(14)$ MeV and $b = 5.493(48)\ 10^{-3}$ MeV/mm. The energy calibrated excitation spectrum is shown in Figure 79. The energy resolution of the 1_2^+ state is 40 keV FWHM.

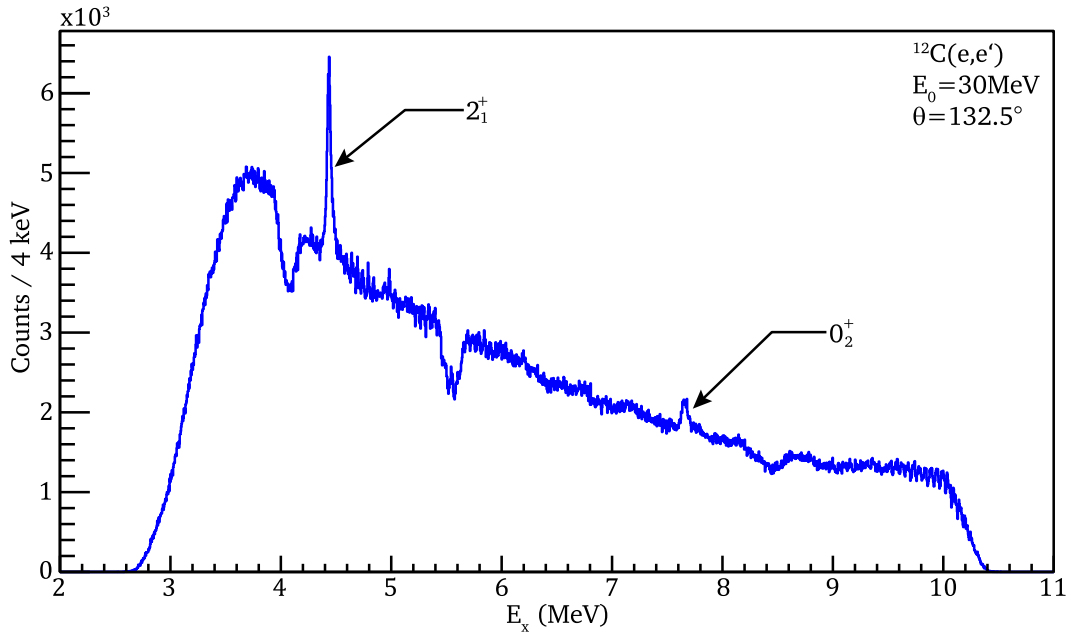

Figure 78: In the excitation spectrum of the measurement of the 2_1^+ state of ^{12}C, two states can be seen, the 2_1^+ state and the 0_2^+ state. The background of the spectrum is dominated by the radiative tail of the elastic line from the ^{12}C target. The structures in the background are due to the lack of efficiency calibration.

Table 16: The listed states and their fitted positions in the detector system were used for energy calibration. Energy values taken from [43].

State	Energy (MeV)	Position (mm)
1_2^+	15.110 (3)	259.97(4)
2_3^+	16.1060 (8)	441.3(3)

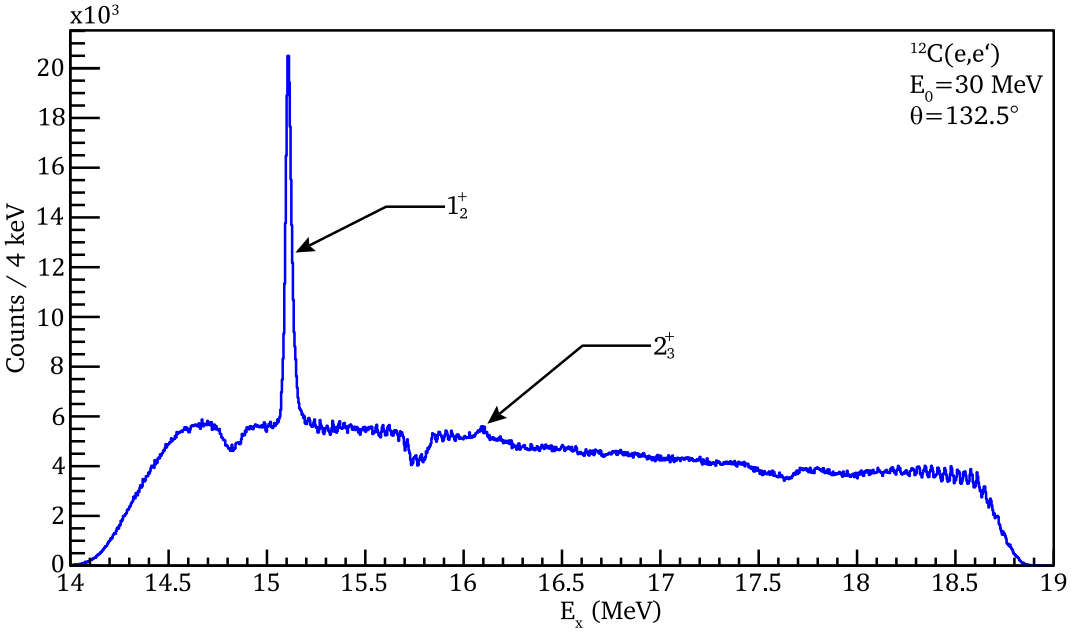

Figure 79: Two states are visible in the excitation spectrum of ^{12}C in the range between 14.5 MeV and 18.5 MeV, the 1_2^+ state and the 2_3^+ state. Due to the high excitation energy, the background due to the radiative tail of the elastic line is smaller and shallower than in the measurement of the 2_1^+.

7.3.3. $LaBr_3$:Ce Energy Calibration

The energy calibration of the $LaBr_3$:Ce detectors is performed with radioactive sources. By using a ^{56}Co source, see measured spectrum in Figure 80, an interval between 0.85 MeV and 3.5 MeV is covered for the energy calibration at low energies. Since the 2_1^+ state and the 1_2^+ state of ^{12}C emit photons of energies up to 15 MeV, the energy calibration must be extrapolated over a large range if using a ^{56}Co source only. Therefore, an additional measurement was performed using a $^{35}Cl(n,\gamma)^{36}Cl$ reaction that emits photons with energies up to 8.58 MeV. The setup is shown in Figure 81. The scattering chamber was dismounted, and canisters filled with salt (NaCl) water were placed around an Am/Be neutron source. The water serves as a mediator and the neutron capture is performed on the dissolved chlorine. The corresponding γ-ray spectrum of a $LaBr_3$:Ce detector is shown in Figure 82.

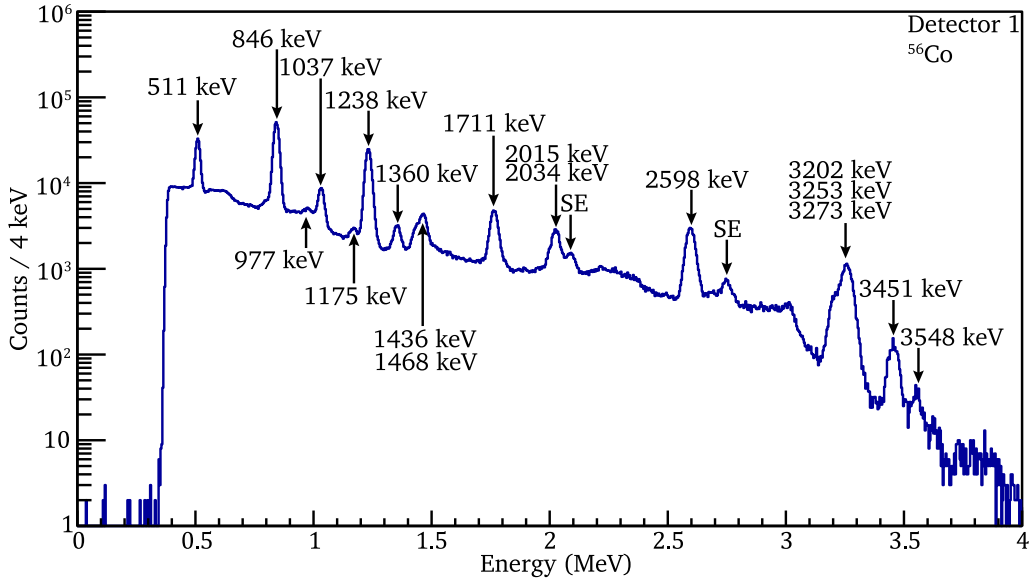

Figure 80: The spectrum of a ^{56}Co source covers γ-ray energies in the range between 0.85 MeV and 3.5 MeV.

By using both, the ^{56}Co and $^{35}Cl(n,\gamma)^{36}Cl$ measurements, an interval from 0.85 MeV to 8.6 MeV is covered. $LaBr_3$:Ce detectors show a small deviation from the linear relation between ADC channel and energy of the photons [139]. For better extrapolation to a photon energy of 15.1 MeV, correction for this deviation using higher orders was omitted and a linear energy calibration function was used. The parameters of the energy calibration are listed in Table 17.

Figure 81: For energy calibration using a $^{35}Cl(n,\gamma)^{36}Cl$ reaction, the scattering chamber was removed and a neutron Am/Be source surrounded by salt (NaCl) water canisters was placed in front of the detectors.

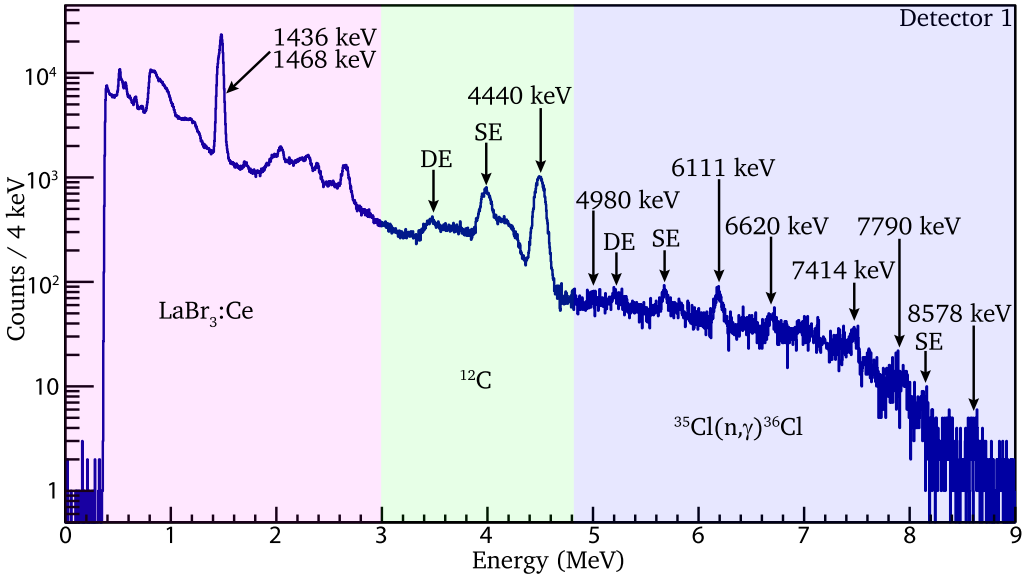

Figure 82: The spectrum of the $^{35}Cl(n,\gamma)^{36}Cl$ measurement with an Am/Be source is composed of three parts. At energies below 3 MeV, the spectrum is dominated by the intrinsic activity of the $LaBr_3$:Ce crystal. At intermediate energies between 3 MeV and 5 MeV, the spectrum is dominated by the 2_1^+ state of ^{12}C and its single and double escape peaks. Since ^{12}C is a product of the Am/Be source, the associated peaks in the spectrum are broadened due to the Doppler shift. At energies above 5 MeV, the peaks of $^{35}Cl(n,\gamma)^{36}Cl$ are visible. Data taken from [170].

Table 17: Listed are the energy calibration parameters of the three $LaBr_3$:Ce detectors.

	Detector 0	Detector 1	Detector 2
Offset (MeV)	$-7.5(10) \cdot 10^{-3}$	$6.3(78) \cdot 10^{-3}$	$9.0(15) \cdot 10^{-3}$
Slope (Mev/ch)	$1.0298(2) \cdot 10^{-4}$	$1.5444(3) \cdot 10^{-4}$	$1.3198(4) \cdot 10^{-4}$

The energy resolution of γ-ray detectors depends on the energy of the photons and the detection mechanism and can be described by several approaches such as polynomials and a square root function [129] given by

$$\mathrm{FWHM}(E) = \sqrt{a + b \cdot E}. \tag{7.9}$$

This function is used because an extrapolation up to 15.1 MeV is required and a polynomial approach would result in larger deviations. The fitted parameters are listed in Table 18. Figure 83 shows the energy-dependent resolution of the detector at 110°. For the fit, the Doppler broadened data point at 4.4 MeV and the correlated single and double escape peaks of the ^{12}C were not used. The detector has a relative energy resolution of 1.2% at 4.4 MeV and a relative energy resolution of 0.66% at 15.1 MeV.

Table 18: Listed are the parameters describing the energy dependence of the FWHM energy resolution according to Equation (7.9).

	Detector 0	Detector 1	Detector 2
a (keV²)	36(29)	138.8(63)	235(39)
b (keV)	0.679(28)	0.6406(72)	0.522(35)

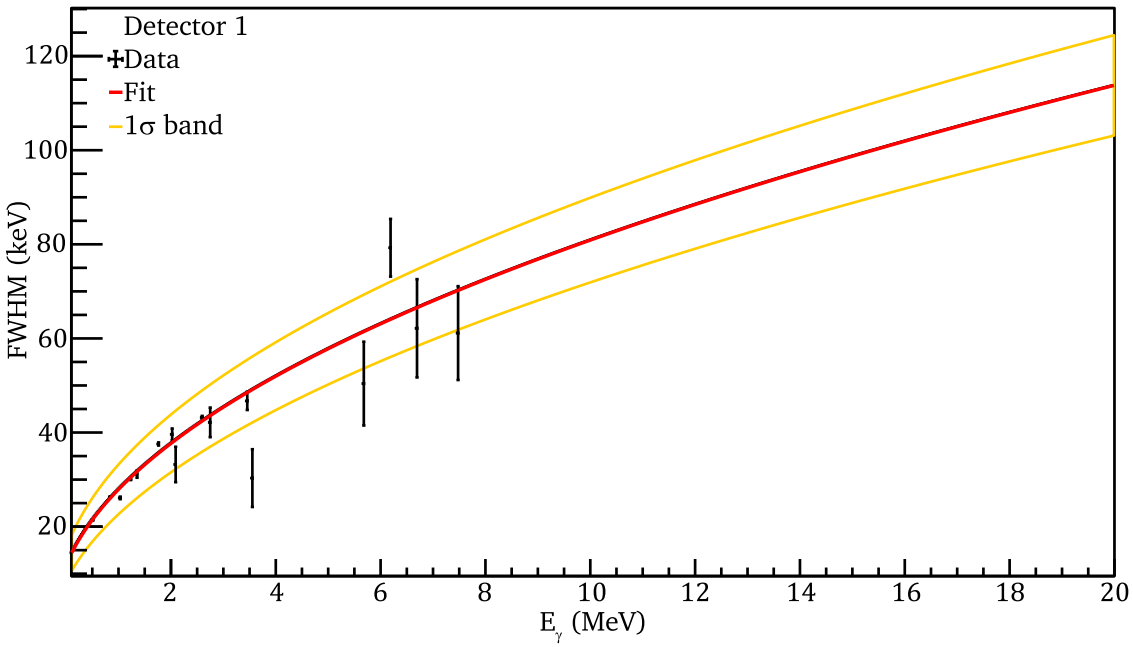

Figure 83: The energy resolution of a $LaBr_3$:Ce detector depends on the energy of the photons to be detected. The red line was fitted to the measurement points and the two yellow lines indicate the 1-σ interval. The peaks of the ^{12}C are Doppler broadened, thus these resolutions where not used.

During the measurement campaign, shifts in the gain of the detectors arise, which must be corrected individually for each run. For this purpose, the electron-positron annihilation peak was used and a scaling factor was determined to shift this peak exactly to 511 keV. Figure 84 shows scaling factors for the three $LaBr_3$:Ce detectors for all runs.

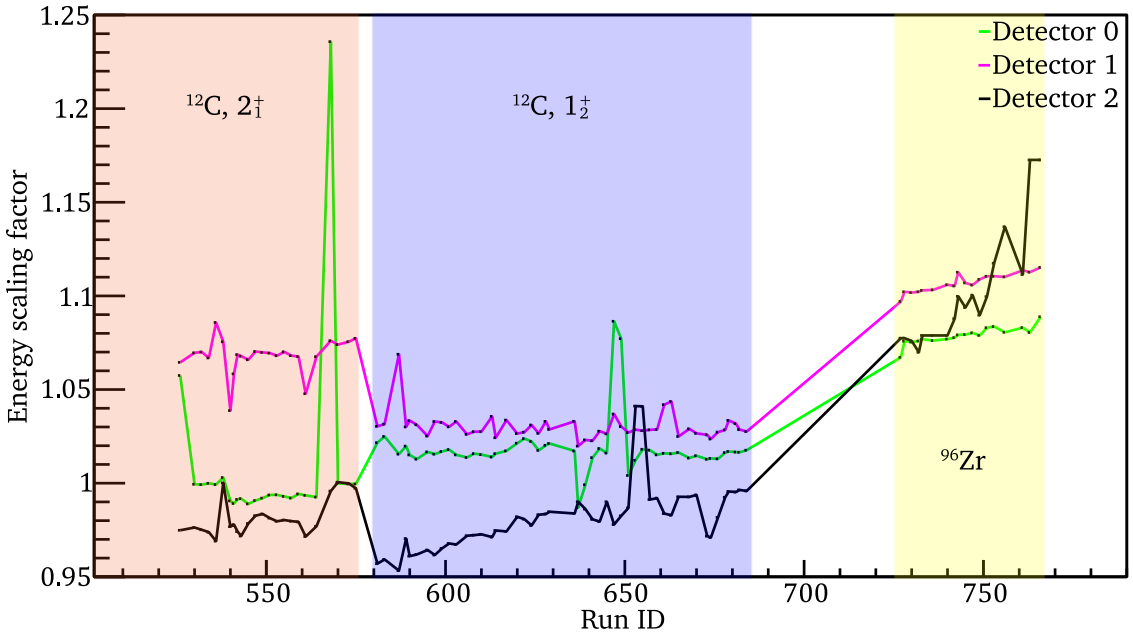

Figure 84: The deviations of the individual runs from the energy calibration obtained from source measurements are corrected by scaling factors, which are determined by fits to the 511 keV peak. The individual measurements are color coded: 2_1^+ state of ^{12}C (orange), 1_2^+ state of ^{12}C (blue), ^{96}Zr (yellow).

In addition to the shift in peak positions between runs, there was a correlation between the count rate of the $LaBr_3$:Ce detectors and the position of the peaks, which is shown in Figure 85. The position of the 511 keV peak in channels was plotted versus the average count rate of the run. A more detailed investigation of the rate dependence is described in Section 9.3.2 by performing measurements at well-defined count rates. It can be assumed that the rate dependence of the measurement campaign in 2019 was partially corrected by correcting for shifts in peak position. The linear fit provides a slope of 0.52 (2) channels/kcps for detector 1 for the 511 keV peak, corresponding to a total drift of 33 keV.

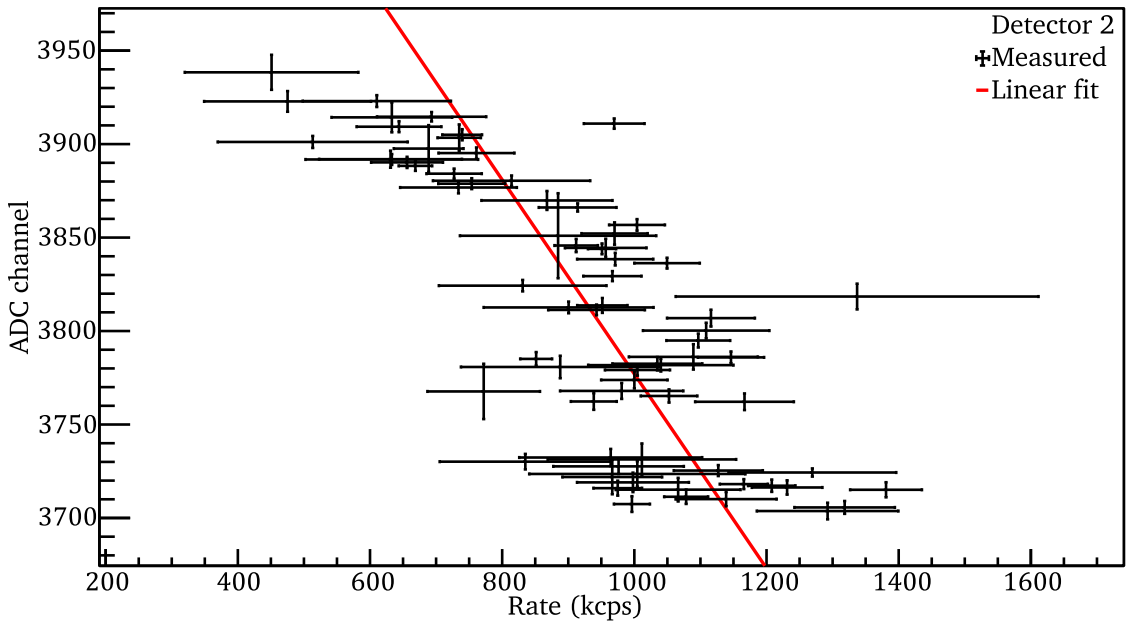

Figure 85: A correlation between the count rate of the detectors and the position of the 511 keV peak in the γ-ray spectra is observed. The rates of the ^{12}C measurements were used.

Another effect that should be studied in more detail in the future is the shift to smaller peak positions over the period of the entire measurement campaign, which is shown in Figure 86. In the left region the magnetic field of the QCLAM spectrometer was set for the measurement of the 2_1^+ state of ^{12}C. From Run ID 580 on, the 1_2^+ state of ^{12}C and ^{96}Zr were measured, for which similar magnetic field settings were used. In this interval, a shift as a function of Run ID to smaller ADC channels is observed.

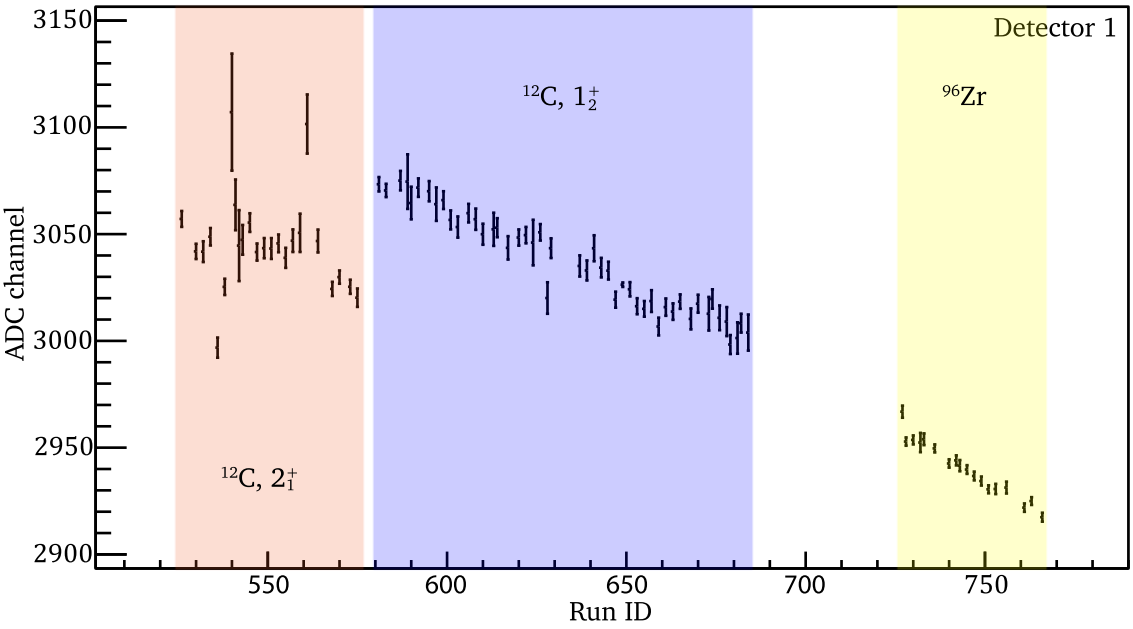

Figure 86: Detector 1 shows a continuous shift in the position of the 511 keV peak over the period of the entire measurement campaign.

7.4. Time Resolution

The power of coincidence experiments lies in the ability to use gates on simultaneously detected events in different detector systems to reduce the background due to uncorrelated events in time. Coincident events form a peak in a histogram of the time differences of the timestamps from the detector systems, whereas uncorrelated events form a flat background. The width of the peak decreases with improved time resolution allowing the use of a narrow gate, thus truncating a larger fraction of the background. The time difference is defined by

$$\Delta t = t_e - t_\gamma \tag{7.10}$$

as the difference of the timestamp of the detected electron t_e and the detected γ-ray t_γ. The measured time difference depends not only on the time at which the particles hit the detector, but also on the properties of the setup, which reduce the time resolution. These effects can be corrected with sufficient knowledge of the individual events. During the first electron-γ coincidence experiment at S-DALINAC, two effects were observed that lead to a reduced time resolution, the time-of-flight of electrons inside the QCLAM spectrometer and an energy dependent offset of the $LaBr_3$:Ce detectors.

The time-of-flight depends on the trajectories before entering the spectrometer and the energies of the electrons. To correct the time-of-flight of the electrons, the method described in Section 6.3 was used, where the time-of-flight was obtained from a simulation. Because of the low statistics and low x-dependence of the coincident events, since there is only one peak in the acceptance of the spectrometer for which coincident photons are expected, no correction is made using the measured data, but the correction from the simulation is used instead.

$$\Delta t_{corr,tof} = \Delta t - t_{tof} \tag{7.11}$$

After correcting the time-of-flight (see Equation (7.11)), it has been observed that the corrected time difference $\Delta t_{corr,tof}$ has a dependence on the photon energy. A possible cause for this effect is the generation of the triggers in the $LaBr_3$:Ce data acquisition, which is described in Section 5.2.2. The timing of the generation of the trigger pulse depends on the waveform, which depends on the amplitude and thus on the energy as described in Section 6.1.2. An examination of the effect reveals a linear relationship as shown in Equation (6.5). The correction is done according to

$$t_{te} = a + b \cdot E_\gamma. \tag{7.12}$$

Figure 87 shows the effect using the time difference between the detector at 110° and the QCLAM spectrometer. For the determination of the correction parameters from Equation (7.12), in the first step the interval between 1 MeV and 15 MeV is divided into 14 intervals, each 1 MeV wide, which are projected onto the time difference axis. The position of the time difference peak is determined by the fit of a Gaussian curve on a linear background. In the second step, Equation (7.12) is fitted to the obtained pairs of values. The correction parameters are listed in Table 19. The effect is about 0.13 ns to 0.16 ns per MeV for all detectors, resulting in a difference of about 2.1 ns for an energy interval of 15 MeV. The corrected time resolution is given by

$$\Delta t_{corr} = \Delta t_{corr,tof} - t_{te}. \tag{7.13}$$

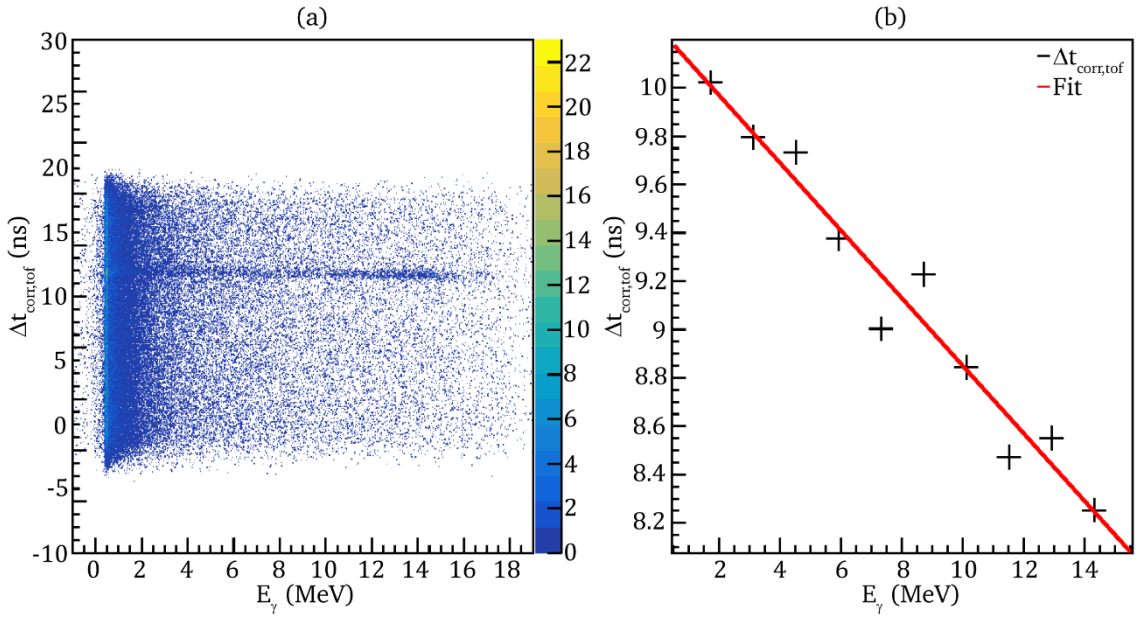

Figure 87: (a): The time-of-flight corrected time difference of detector 1 obtained in the measurement of the 1_1^+ state of ^{12}C shows a dependence on the energy of the detected photons. (b): This effect is corrected by a fit of Equation (7.12) to the position of the time difference peak at different photon energies.

Table 19: The listed parameters are used to correct the photon energy dependence of the time-of-flight corrected time difference.

	Detector 0	Detector 1	Detector 2
a (ns)	4.52(10)	$1.025(9) \cdot 10^1$	2.040(70)
b (ns/MeV)	$-1.31(11) \cdot 10^{-1}$	$-1.399(11) \cdot 10^{-1}$	$-1.571(7) \cdot 10^{-1}$

The corrections to the measured time difference improved the time resolution from 5.1 ns to 3.1 ns FWHM. A comparison between the uncorrected (red) and corrected (blue) time differences is shown in Figure 88. In the plot of the time difference between the detector at 60° and the QCLAM spectrometer, a second coincidence peak with an offset of 11.3 ns was observed. This second coincidence peak was not observed in the measurement of the 2_1^+ state of ^{12}C, suggesting a correlation with the excitation energy.

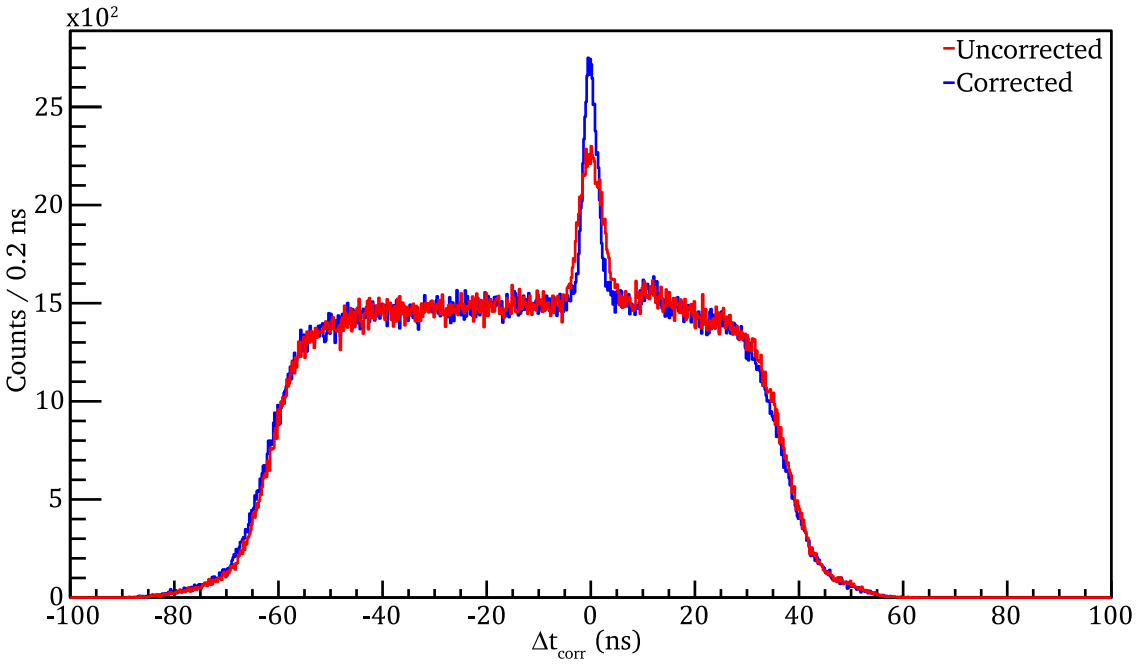

Figure 88: Comparison of time resolution of the measurement of the 1_2^+ state of ^{12}C before (red) and after correction (blue). The time resolution was improved from 5.1 ns to 3.1 ns.

Figure 89 shows a comparison between the time difference histograms of the individual detectors for the measurements of the 2_1^+ state (a) and the 1_2^+ state of ^{12}C (b). The second time difference peak appears only during the measurement of the 1_2^+ state of ^{12}C, which suggests a connection with the excitation energy, since for this measurement the magnetic field of the QCLAM spectrometer was changed. Therefore, backscattering behind the target can also be excluded. In addition, the second time difference peak was only observed in detector 2.

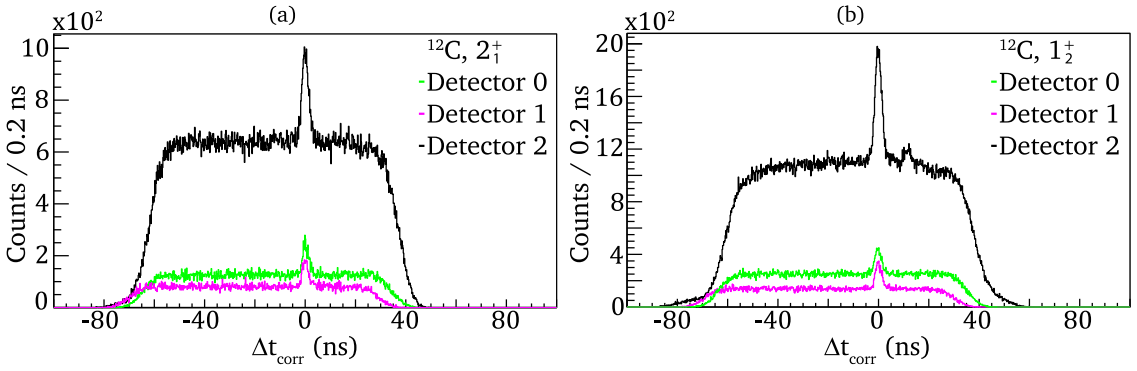

Figure 89: (a): The time difference plots of the measurement of the 1_2^+ state of ^{12}C of the three $LaBr_3$:Ce detectors show a coincidence peak at Δt_{corr} = 0 ns. Detector 2 shows a second peak at Δt_{corr} = 11.3 ns. (b): The second coincidence peak is not visible in the time difference plots of the measurement of the 2_1^+ state of ^{12}C.

7.5. Efficiency Calibration

Efficiency calibrations of energy spectra are essential for measurements of absolute quantities and relative measurements, in which a state is measured relative to a state known with high accuracy. In the QCLAM spectrometer, the efficiency depends on the piercing point and the angle of the electron at the detector system, and on the status of the drift chamber wires, i.e.

applied high voltage and gas mixture influence the efficiency [101]. Therefore, high voltage and gas mixture must be kept constant during a measurement. The efficiency of $LaBr_3$:Ce detectors, like all γ-ray detectors, is energy dependent due to the interaction of photons with the detector material. With higher photon energy, the probability of deposition of the total photon energy inside the detector crystal decreases and the probability of a Compton scattered photon leaving the detector increases. Above 1.022 MeV the probability of electron-positron pair production and subsequent escape of one or both 511 keV photons increases. Both effects cause a reduction of the full energy peak efficiency.

7.5.1. QCLAM Efficiency Calibration

The efficiency of the QCLAM detector system is determined by measuring a so-called white spectrum, where it can be assumed that all energies and angles of the detected electrons are uniformly distributed. The measurement of a white spectrum is accomplished by a magnetic field setting of the spectrometer, which limits the momentum acceptance to events with high excitation energies, where no pronounced structures exist. This results in a flat excitation spectrum. For the efficiency measurement, a ^{208}Pb target was used at beam currents between 100 nA and 500 nA and excitation energies above 18 MeV.

Normalized spectra of the individual runs of the efficiency at different electron beam intensities (a) and the full statistics (b) are shown in Figure 90. The data showed a correlation between beam current and efficiency, which is lower in the new QCLAMon version from Feb. 2022. For a beam current of 500 nA, a small dependence is evident in the range between 550 mm and 700 mm.

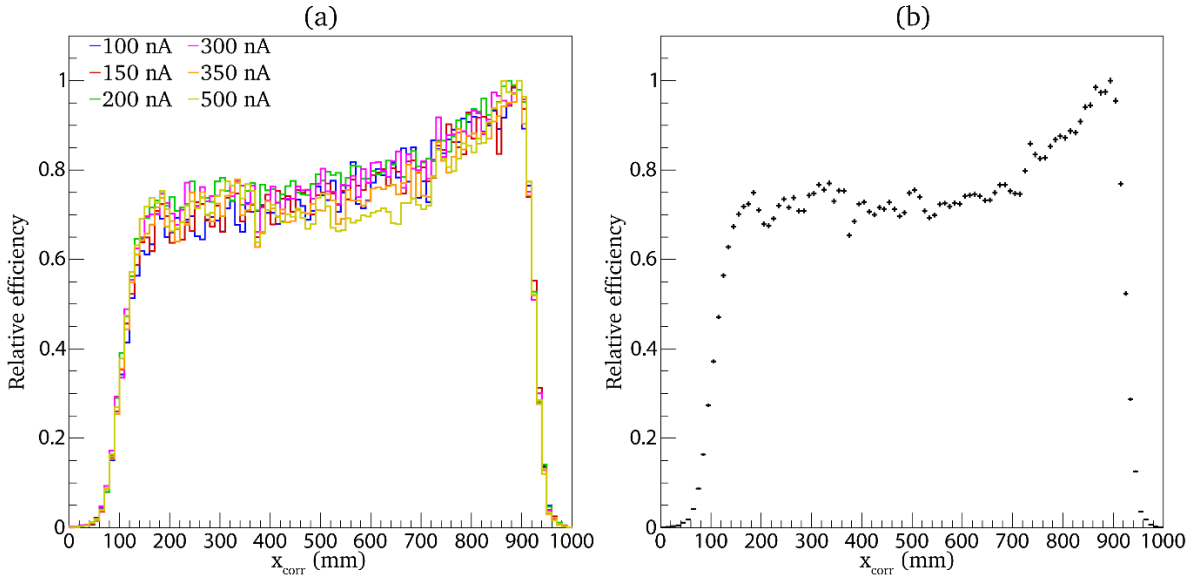

Figure 90: (a): The efficiency measurements at beam currents between 100 nA and 500 nA. For each measurement, the spectrum was normalized to the content of the maximum bin. As the beam current increases, the relative efficiency at the center of the detector system decreases. (b): The total efficiency spectrum.

By applying the efficiency correction to the spectrum of the measurement of the 1_2^+ state of ^{12}C, the efficiency corrected spectrum is not perfectly flat in between excited states, as can be seen in Figure 91, suggesting insufficient reliability of the efficiency correction. To investigate the beam current dependence of the relative efficiency correction, the six efficiency correction measurements were divided into three efficiency corrections - a correction with two runs

between 100 nA and 150 nA, a correction with four runs between 100 nA and 300 nA, and a correction using all runs between 100 nA and 500 nA. The efficiency correction using the four runs follows the efficiency correction from all runs in the range between 15 MeV and 15.7 MeV. In the range between 15.7 MeV and 18.5 MeV, the efficiency correction from the four runs follows the course of the efficiency correction at small beam currents, which illustrates the qualitative difference between the efficiency measurements at low and high beam currents.

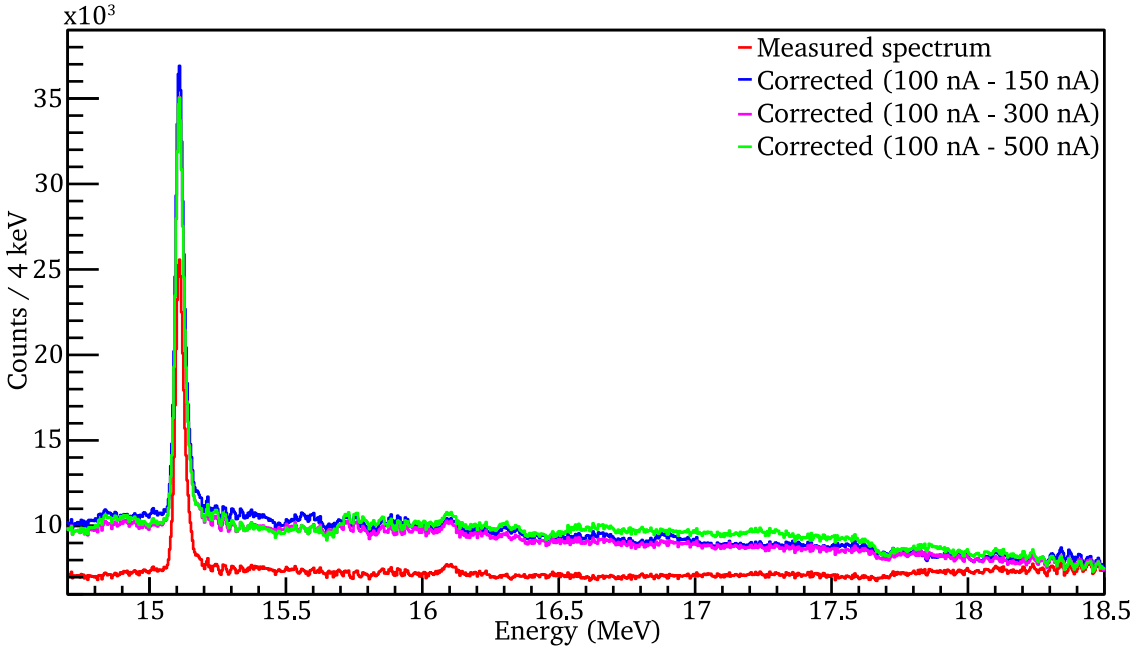

Figure 91: A comparison between the measured spectrum and efficiency-corrected spectra shows several structures in the efficiency-corrected spectra, which indicate an insufficient reliability of the relative efficiency correction. Furthermore, a dependence of the efficiency correction on the beam current is shown.

7.5.2. $LaBr_3$:Ce Efficiency Calibration

The full energy peak efficiency of the $LaBr_3$:Ce detectors is energy dependent and can be determined with radioactive sources for discrete energies. The efficiency can be determined relatively for states with known intensities and absolutely for known activities of the sources. In the case of a γ-decay cascade, the efficiency can be determined absolutely using a coincidence condition without knowledge of the activity of the source by using gates on the energies of the cascade. The latter method was used for the efficiency calibration of the three $LaBr_3$:Ce detectors with a ^{60}Co source, which emits two coincident photons of energies 1.173 MeV and 1.332 MeV [171]. The angular correlation between the two γ-rays, which enclose the angle α, is given by

$$W(\alpha) = 1 + 0.125\cos^2(\alpha) + 0.0417\cos^4(\alpha) \tag{7.14}$$

[172] and was corrected during evaluation. The simulated efficiencies of the $LaBr_3$:Ce detectors were fitted to the measured efficiencies from Table 20 as shown in Figure 92.

Table 20: The absolute full energy peak efficiencies were determined for the $LaBr_3$:Ce detectors for the energies of the γ-decay cascade of ^{60}Co.

Energy (MeV)	Detector 0 Efficiency	Detector 1 Efficiency	Detector 2 Efficiency
1.173	$4.64(24) \cdot 10^{-4}$	$1.22(19) \cdot 10^{-3}$	$3.26(39) \cdot 10^{-4}$
1.332	$5.06(86) \cdot 10^{-4}$	$1.26(24) \cdot 10^{-3}$	$3.68(30) \cdot 10^{-4}$

Due to the different thicknesses of the lead filters in front of the detectors, the efficiency of detector 1 peaks at lower energy and the efficiency is larger despite the larger distance to the target.

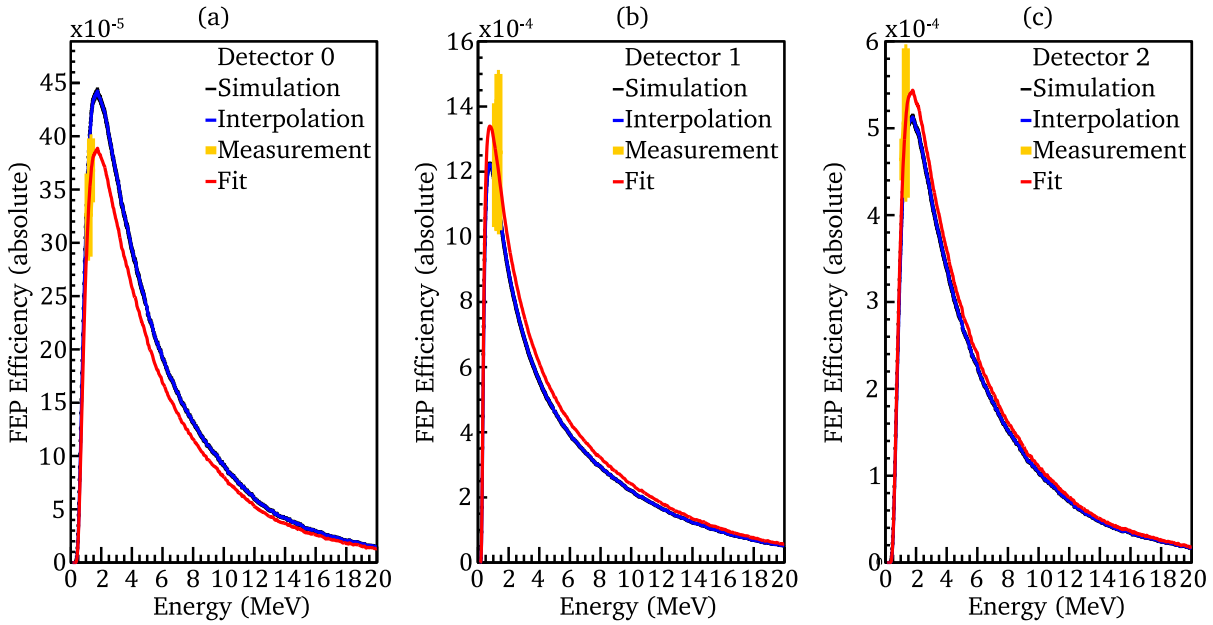

Figure 92: The shape of the absolute efficiency of detector 0 (a), detector 1 (b) and detector 2 (c) as a function of energy is obtained by GEANT4 simulations (blue) and scaled to measured efficiencies (red). The simulation is represented by an interpolating line connecting the simulated efficiencies at discrete energies, so that the simulation can be used for arbitrary energies.

7.6. Background Subtraction

Measured data contains true coincidences and random coincidences, which form a constant background in the time difference plot. Consequently, spectra with a gate on the time difference peak contain true coincidences and background events. To subtract the background, gates are placed next to the time difference peak, as shown in Figure 93, so that spectra generated using the gates contain only background.

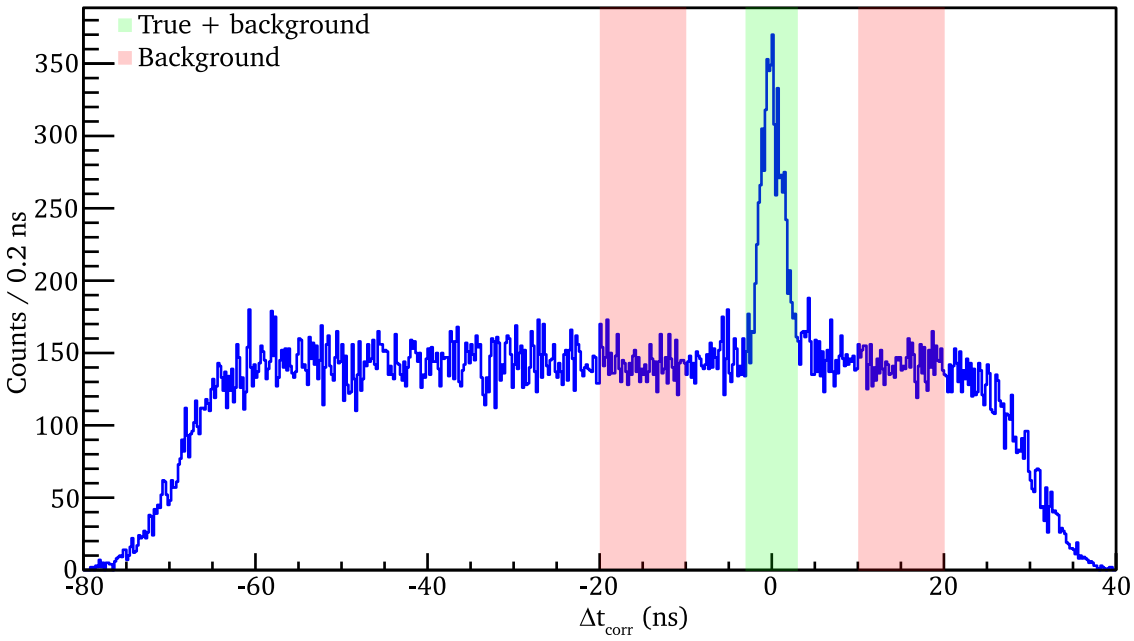

Figure 93: Gates on the time peak (green) contain true coincidences and random coincidences. By using gates next to the time peak (red), pure background spectra are obtained, which are used for background subtraction.

The background subtraction is demonstrated in Figure 94 using the measurement of the 1_2^+ state of ^{12}C. To compensate for the different widths of the gates, the pure background spectrum is scaled by the ratio of the width of the gate on the coincidence peaks to the sum of the width of the gates next to the coincidence peaks before background subtraction. It should be noted that a time-correlated background such as bremsstrahlung cannot be subtracted by this method.

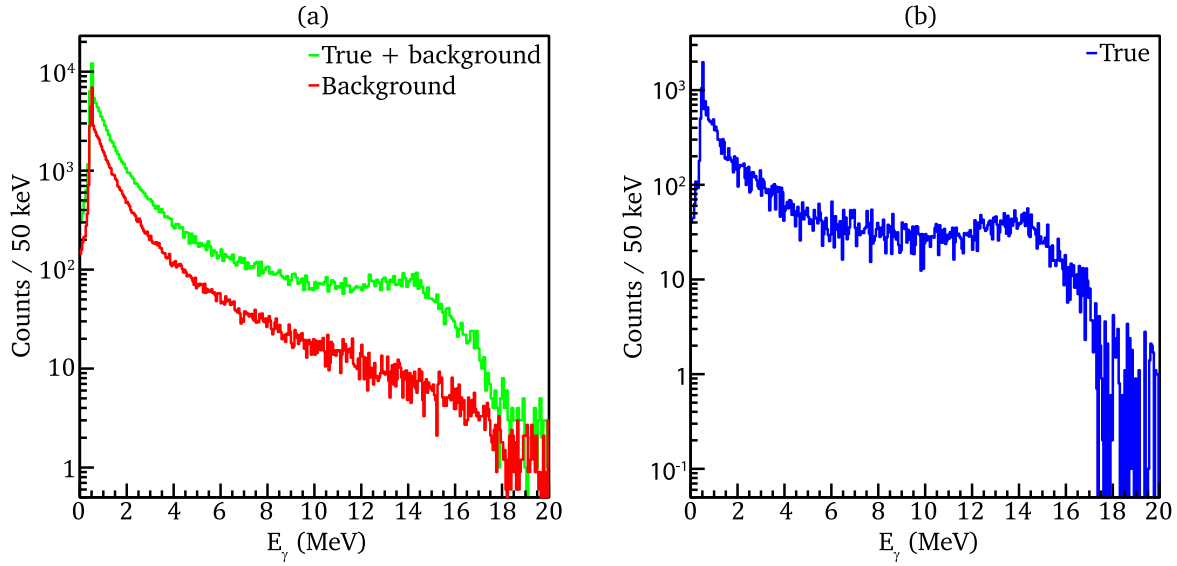

Figure 94: The summed γ-ray spectra of the measurement of the 1_2^+ state of ^{12}C of the three detectors are shown. (a): Using a gate on the time peak and gates to the left and right of the time peak, spectra are obtained for the background subtraction containing the true events plus background (green) and pure background (red). (b): By subtracting the pure background spectrum from the spectrum containing true coincidences and random coincidences, a background corrected spectrum is obtained.

7.7. Analysis

In this section, the results of the three measurements of the measurement campaign are described in succession, namely the measurements of the 2_1^+ and 1_2^+ states of ^{12}C and the measurement in the region of the GDR in ^{96}Zr. The ^{12}C measurements represented a first test of the new experimental setup in which isolated states are excited and subsequently decay directly to the ground state. In contrast, the ^{96}Zr measurement excited a broad resonance, the giant dipole resonance (GDR), which is interpreted as a collective oscillation of the protons against the neutrons. The GDR decays approximately by 99% via neutron emission and by 1% via γ-decay [69]. Data on the γ-decay of the GDR in Sn isotopes indicate comparable intensities for the decays to the ground state and the first excited 2^+ [173].

7.7.1. Measurement of the 2_1^+ state of ^{12}C

The 2_1^+ state with an excitation energy of 4.44 MeV is the first excited state of ^{12}C and consequently can only decay directly to the ground state, so that the excitation energy corresponds to the energy of the coincidently measured photons. In the $E_x - E_\gamma$ matrix shown in Figure 95, the 2_1^+ state can be identified due to the full energy peak at $E_x = E_\gamma = 4.44$ MeV and the detector response leading to a vertical line. Superimposed on the measured state is bremsstrahlung, which is indicated by the line along $E_x = E_\gamma$ and the corresponding detector response, since the energy of the bremsstrahlung photons corresponds to the energy loss of the scattered electrons. An energy dependence can be seen in the bremsstrahlung, so that the intensity of the bremsstrahlung decreases with increasing photon energy. The 0_2^+ state with excitation energy 7.654 MeV decays approximately by 100% via alpha decay, so no coincident photons from the decay of the 0_2^+ state could be measured in this measurement campaign, consequently this state is not present in the coincident data.

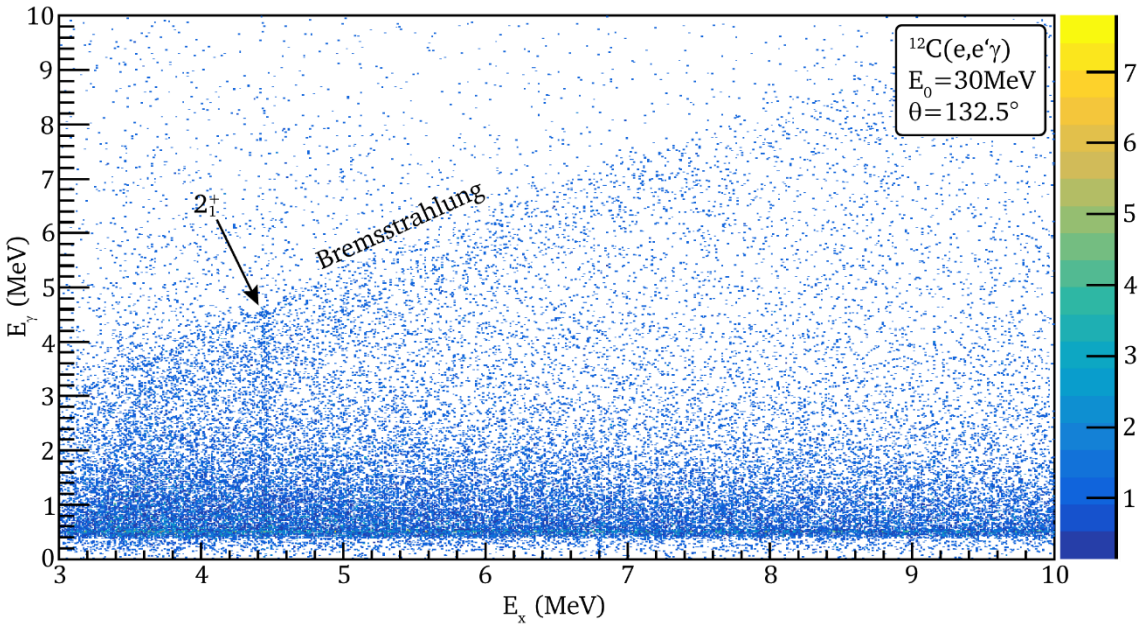

Figure 95: The background subtracted $E_x - E_\gamma$ matrix shows the excitation and subsequent γ-decay of the 2_1^+ state of ^{12}C at an excitation energy of 4.4 MeV and a continuous coincident bremsstrahlung background.

A comparison of the γ-ray spectra with a gate on the excitation energy on the 2_1^+ state to gate on lower and higher energies shows an increased number of counts in Figure 96.

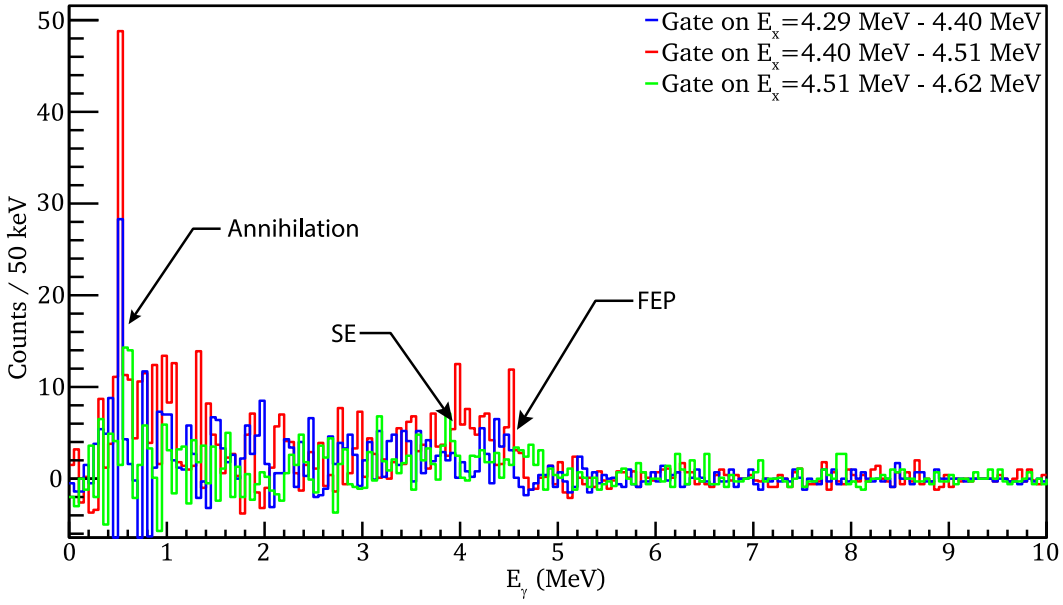

Figure 96: A gate on the excitation energy of the 2_1^+ state of ^{12}C (red) shows a higher number of counts than gates at smaller and larger energies (blue and green) on the pure bremsstrahlung background.

7.7.2. Measurement of the 1_2^+ state of ^{12}C

For the measurement of the 1_2^+ state of ^{12}C, the magnetic field of the QCLAM spectrometer was tuned to cover the excitation energy range between 14 MeV and 19 MeV for the given energy of the electron beam of 30 MeV. The intensity of bremsstrahlung at such high energy losses of the scattered electrons is significantly lower than for the measurement of the 2_1^+ state, resulting in less background from bremsstrahlung in the matrix as shown in Figure 97. The 1_2^+ state decays by 95.9% via γ-decay, of which 90% decays directly to the ground state. The 2_3^+ state with the excitation energy of 16.106 MeV, which was used for the energy calibration of the QCLAM spectrometer, decays to 99.3% via alpha decays and is consequently not visible in the coincident data.

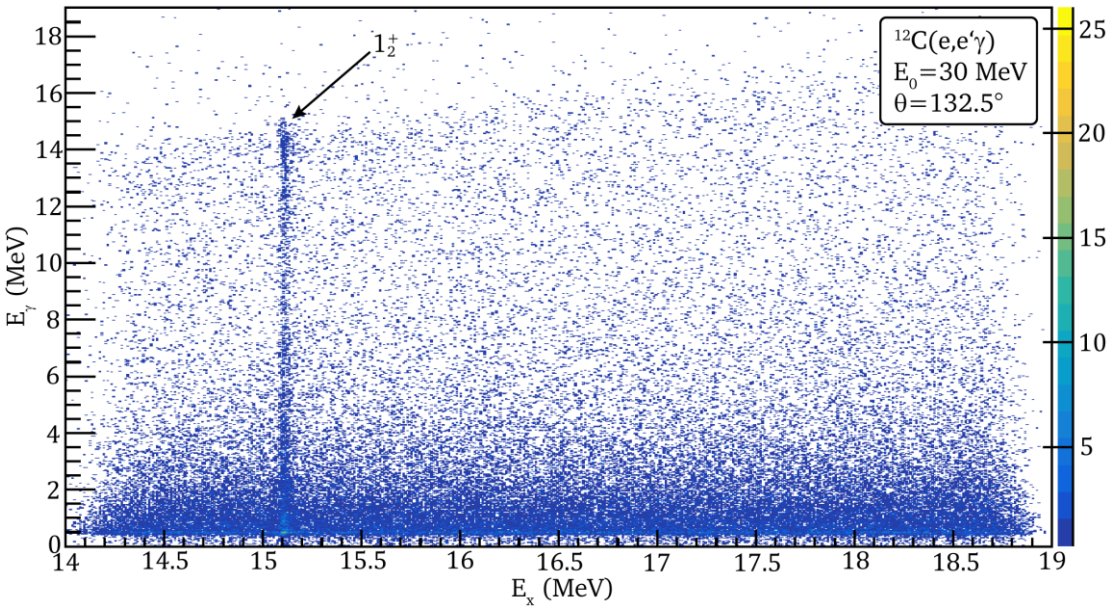

Figure 97: In the background subtracted $E_x - E_\gamma$ matrix, the 1_2^+ state of ^{12}C is on a low background caused by to bremsstrahlung.

Figure 98 shows a comparison of the measured γ-ray-spectrum with a GEANT4 simulation. The measured spectrum (blue) was obtained using a gate on the excitation energy of the 1_2^+ state of ^{12}C and shows the γ-decay to the ground state. For the simulation, a point-like photon source was placed at the location of the target isotropically emitting 15.1 MeV photons. The simulated spectrum (red) was scaled to the number of measured events between 1 MeV and 16 MeV. Due to the low-energy threshold of 400 keV for reduction of the rate of accepted events in the measurement, deviations between the measured and simulated spectra occur below this threshold. An upper threshold was not used since the intensity of the radiation background decreases exponentially. Pronounced full energy peaks and single and double escape peaks are not expected in the measured spectrum due to the low statistics and inaccuracies of the energy calibration. Despite this, there is a clear agreement between the measured and simulated spectra.

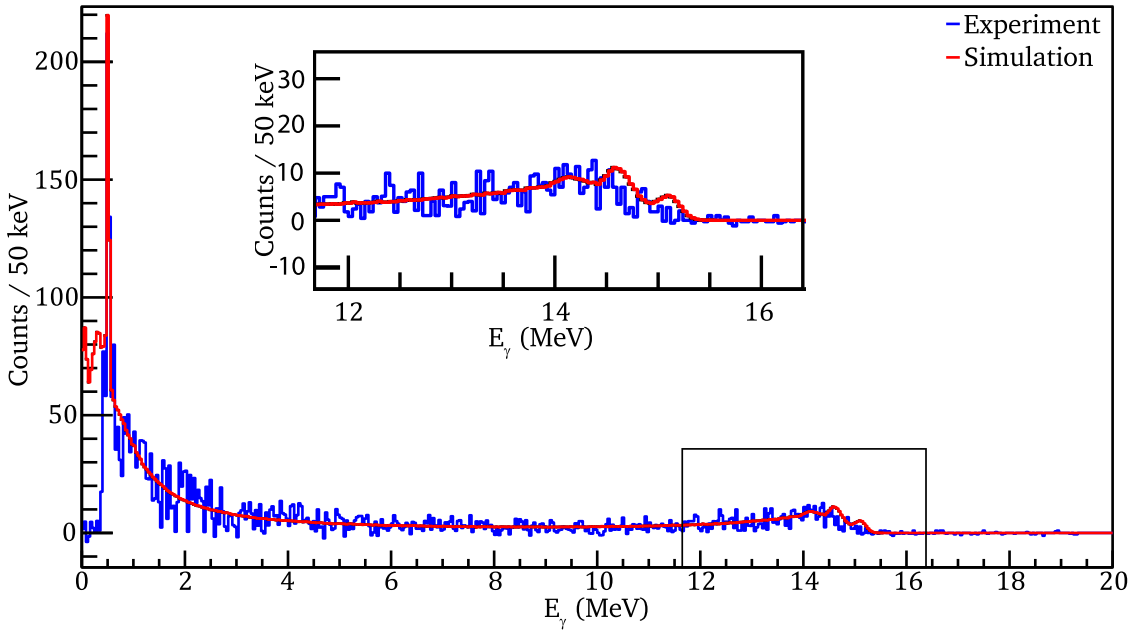

Figure 98: The comparison of a simulated spectrum using a monoenergetic 15.11 MeV photon source shows good agreement with the measured spectrum when a gate is used on the 1_2^+ state of ^{12}C.

7.7.3. ^{96}Zr GDR

For the ^{96}Zr measurement, a magnetic field setting close to the setting used for the measurement of the 1_2^+ state of ^{12}C was applied, so a similar excitation energy interval was measured. Therefore, the energy calibration from the ^{12}C measurement was used for the ^{96}Zr measurement. As can be seen in Figure 99, a flat excitation spectrum is observed in the ^{96}Zr measurement. A broad hump-like distribution as expected for the GDR was not observed.

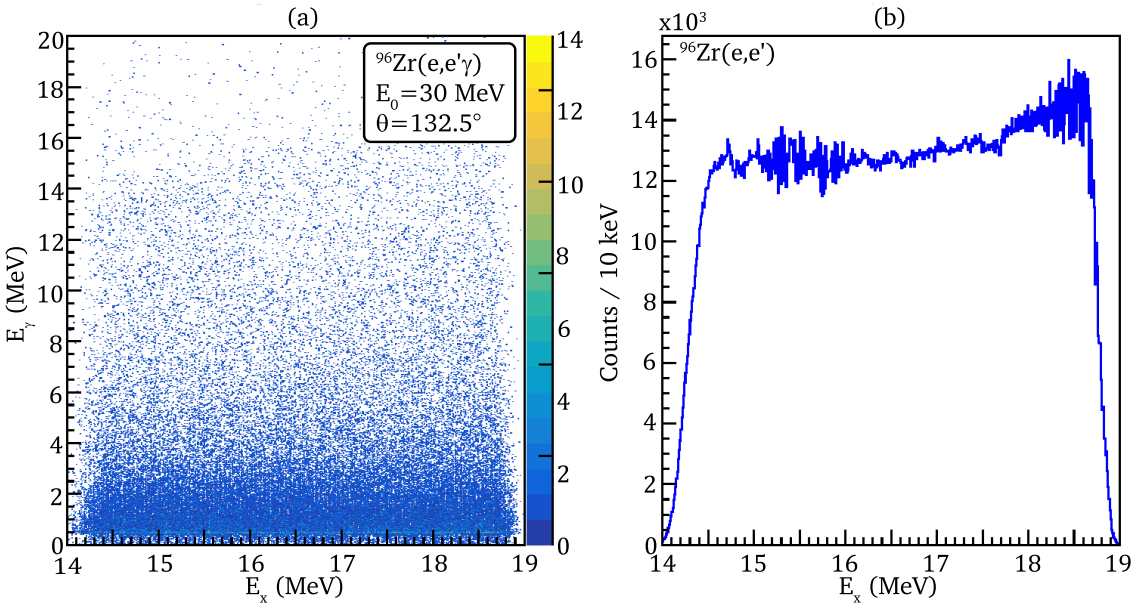

Figure 99: (a): The background subtracted $E_x - E_\gamma$ matrix of the ^{96}Zr measurement shows no distinct structures. (b): The excitation spectrum of the ^{96}Zr measurement is flat.

The GDR decays by 99% via neutron emission and by 1% via γ-decay. Consequently, the excited ^{96}Zr decays with high probability to ^{95}Zr and with low probability high energy photons from the γ-decay of the GDR to the ground state or low-lying excited states of ^{96}Zr. Figure 100 shows the corresponding γ-ray-spectrum. At the photon energy of 1.6 MeV, a peak can be seen which could be due to the decay of low energy excited states in ^{95}Zr to the ground state after the neutron decay of the excited ^{96}Zr. In ^{95}Zr, there are three excited states between 1.6 MeV and 1.7 MeV [174].

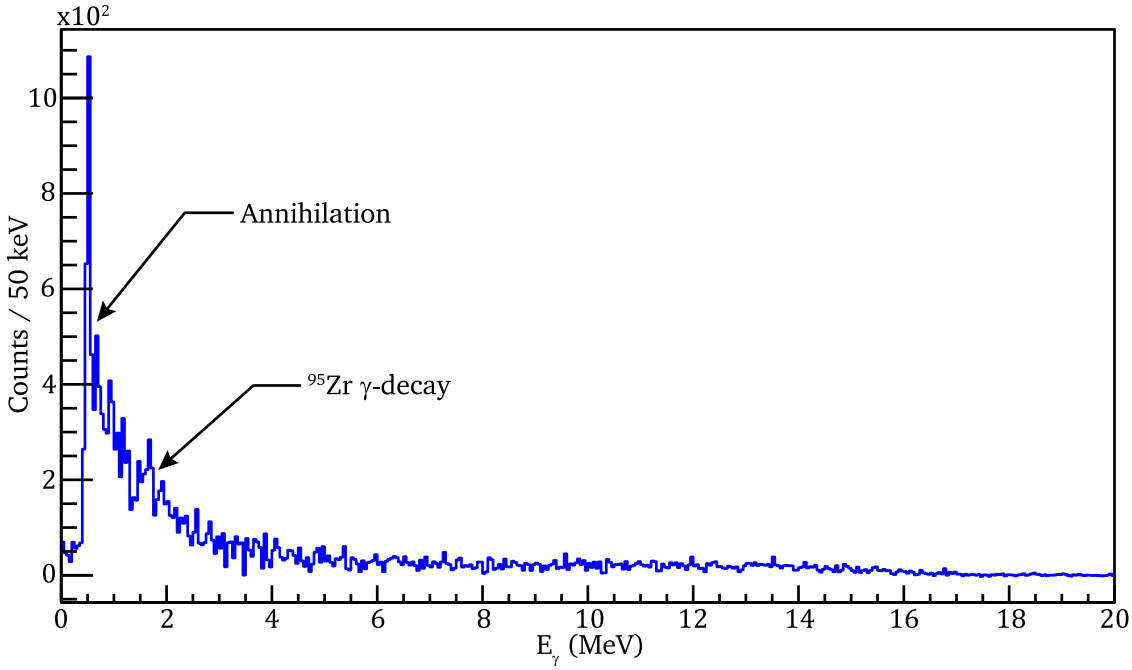

Figure 100: In the γ-spectrum of the ^{96}Zr measurement, a structure can be seen at 1.6 MeV, which could originate from the decay of low excited states in ^{95}Zr after the neutron decay of ^{96}Zr.

In this experimental campaign, which is the first test experiment of the new (e,e'γ) setup, excitation and decay of the 2_1^+ and 1_2^+ states of ^{12}C were successfully measured and the operation of the new setup was demonstrated. The measurement of the GDR in ^{96}Zr shows structure at low γ-energies, but a longer measurement is required to measure the γ-decay of the GDR.

7.8. Results

For the measurement of the 1_2^+ state of ^{12}C, the counts in the γ-ray detectors were determined in the interval from 4 MeV to 16 MeV using a 150 keV wide gate on the excitation energy of the state. The coincident bremsstrahlung background was estimated and subtracted by gating at smaller and larger excitation energies next to the peak, like it is depicted in Figure 96. The obtained counts were efficiency corrected for better comparability to PWBA calculations (see Chapter 2).

Figure 101 shows the calculated double differential cross section and the scaled data. A comparison of the three detectors with the calculated angular distribution is listed in Table 21, the measured angular distribution of the 1_2^+ state is similar to the PWBA calculations. Detector 2, which was positioned at a scattering angle of 60° and accordingly had the highest background count rate, deviates from the calculated angular distribution. Possibly, the background was overestimated and too large a value was subtracted. The dipole pattern of the M1 transition was observed.

Due to the limited measurement time, the statistics of the 2_1^+ measurement was insufficient for evaluation of the angular distribution.

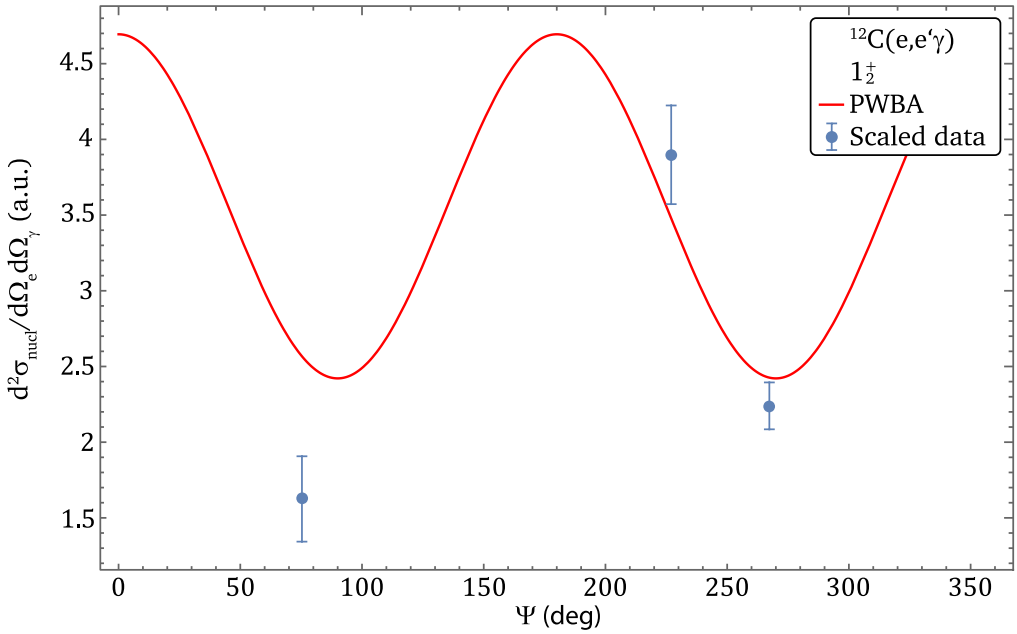

Figure 101: The measured counts in the $LaBr_3$:Ce detectors (blue dots) were scaled to the calculated angular distribution of the dipole pattern of the 1_2^+ state of ^{12}C (red line).

Table 21: Comparison of the calculated double differential cross sections of the 1_2^+ state of ^{12}C with the scaled counts in the $LaBr_3$:Ce detectors from the first commissioning experiment (see Chapter 7). The angles Ψ and Φ correspond to the angles in the coordinate system introduced in Figure 9.

Detector	Ψ (deg)	Φ (deg)	Calculated $\frac{d^2\sigma}{d\Omega_e\, d\Omega_\gamma}$ (a.u.)	Scaled counts
0	227.0	-75.2	3.4	3.9(3)
1	267.3	0	2.4	2.2(2)
2	75.3	0	2.6	1.6(3)

8. Test Experiment with ^{96}Ru

For the second experiment, a more advanced setup was used. The measurement was performed on a ^{96}Ru target to characterize the setup for targets with larger nuclear charge numbers. The acquired data was used for optimizations of the setup.

8.1. Setup

For the second commissioning experiment, the new setup (see Chapter 4) including the magnetic field shielding and the detector array consisting of two towers positioned at horizontal scattering angles of 90° and 135° angles each with three $LaBr_3$:Ce detectors was used, increasing the number of detectors from three to six. The vertical angles of the detectors were -45°, 0° and 45° relative to the horizontal plane and the distances of their surface to the target were 154 mm to 245 mm. The exact positioning of the detectors and filter configurations are listed in Table 22. As in the previous beam time (see Chapter 7), the existing ball scattering chamber was used. The setup is shown in Figure 102. To increase the reaction rate, the QCLAM spectrometer was positioned at the scattering angle of 47.5°.

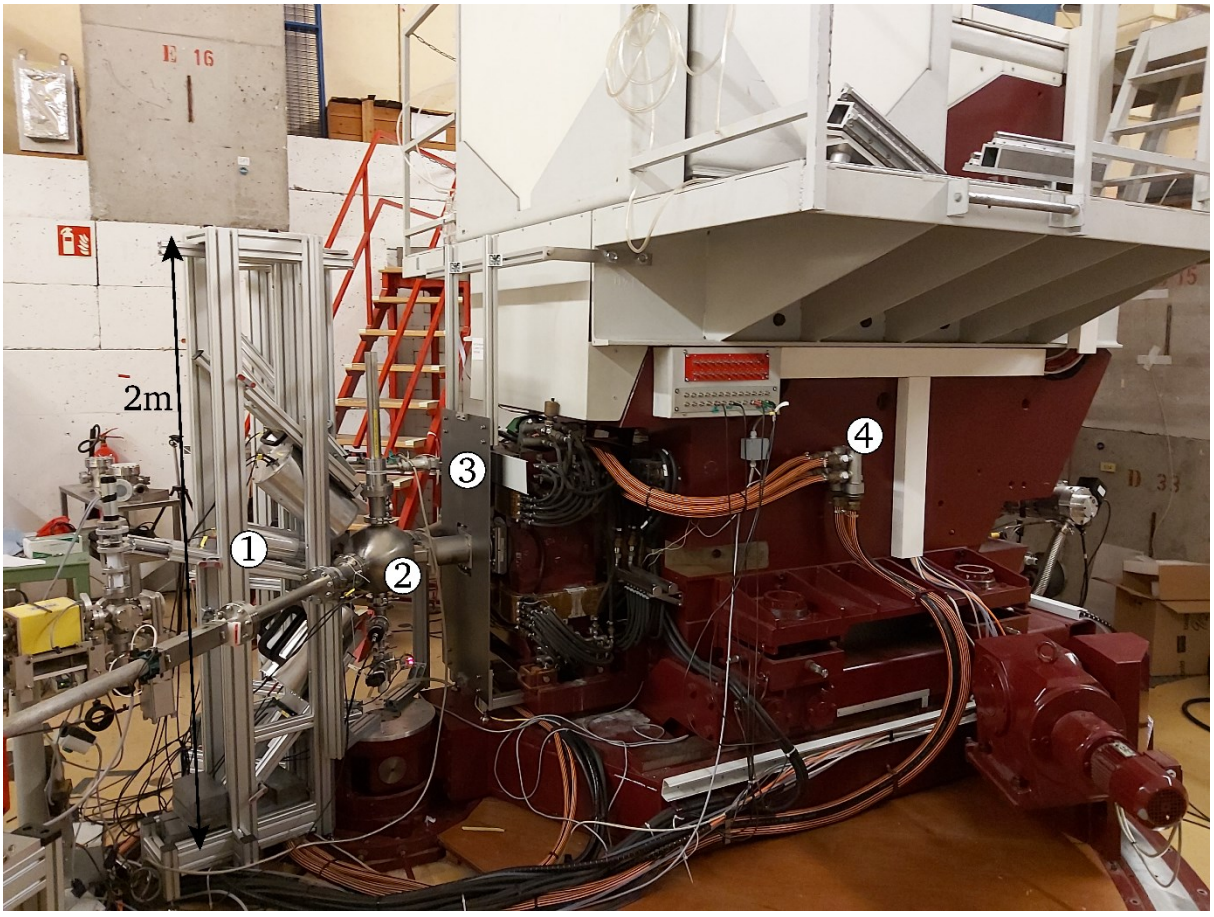

Figure 102: The experimental setup, used during the second commissioning experiment, includes the new detector towers ①, the ball scattering chamber ②, and the magnetic field shielding ③. The QCLAM spectrometer ④ was positioned at a scattering angle of 47.5°.

A 1 cm thick plastic scintillator was positioned in front of detector 5 to test its function as a veto detector for events generated by scattered electrons as it was already investigated in [175].

Table 22: The positions and angles relative to the target in the horizontal plane and the filter configurations are listed. The filter thicknesses were 5 mm for the lead filter and 2 mm for the copper filter.

Detector	Distance (mm)	Angle horizontal (deg)	Angle vertical (deg)	Filter
0	250	90	45(1)	Cu
1	160	90	0(1)	Cu
2	268	90	-45(1)	Cu + Pb
3	204	135	45(1)	Cu
4	245	135	15(1)	No housing
5	197	135	-46(1)	Cu

Two of the three target slots on the target ladder shown in Figure 103 were equipped with the ^{96}Ru and BeO targets, and the last slot was kept free for beam optimizations. The ^{96}Ru target consists of a circular ^{96}Ru disk of 5 mm diameter and an areal density of 28 mg/cm^2 between two gold foils of areal densities of 3.9 mg/cm^2 and 9.7 mg/cm^2 [176]. Due to the thickness of the gold backing, an 80% increase in background rate due to elastic electron scattering is expected. The BeO target is used for optimizing the electron beam on the target.

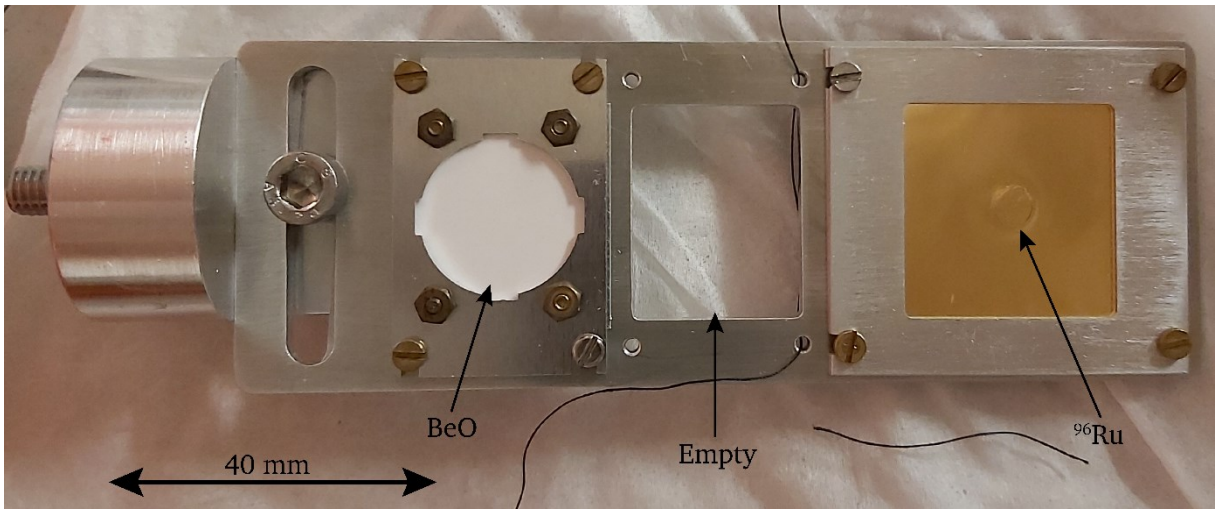

Figure 103: The ^{96}Ru target and a BeO target were mounted on the target ladder. The middle target slot was kept free to optimize the electron beam.

8.2. Measurement

The measurement including the optimization of the 65 MeV electron beam was performed between November 13th, 2020 and November 17th, 2020. Due to the high count rates of several Mcps in the $LaBr_3$:Ce detectors, the beam current had to be limited to 4 nA. Coincidence measurements with the ^{96}Ru target could not be performed in the short measurement campaign, but data on background count rates in the $LaBr_3$:Ce detectors could be obtained. The measured high background count rates of the $LaBr_3$:Ce detectors complicates the performance of (e,e'γ) coincidence experiments due to the higher probability of pileups

and thus perturbed spectra. Two options were explored to enable future measurements. The analysis software was extended to include the pileup correction described in Section 6.1.2, which allows the perturbation of the spectra to be corrected. The second approach was to identify the sources of the high background count rates by comparing GEANT4 simulations with measured count rates. This led to the design of the new (e,e'γ) scattering chamber described in Section 4.2.2.

8.3. Simulation

A high background count rate during (e,e'γ) measurements increases the difficulty for observation of nuclear reactions, since the peak-to-background ratio becomes smaller. Furthermore, at count rates above 500 kcps in $LaBr_3$:Ce detectors, pileup correction techniques are needed to correct for distortions of the measured spectrum [163]. To identify the background sources, GEANT4 simulations were performed. Results of the simulations were used for optimization of the experimental setup resulting in a reduced background count rate. Subsequently, further simulations were performed to characterize the setup and for planning future experiments.

8.4. Simulations of the Measurement 2020

For the simulation of the experimental setup, a simplified geometry of the (e,e'γ) measurement site at the QCLAM spectrometer was replicated in GEANT4, which is shown in Figure 104. The simulations were performed using the *nutr* package [177]. To compare the results of the simulation with the measurement, parameters and geometry corresponding to the experiment were used. For the simulations, the ^{96}Ru target (see Section 8.1) was used and the six $LaBr_3$:Ce detectors were positioned according to Table 22. The first step was to investigate which components contribute significantly to the background. It was started with a simulation consisting of the six $LaBr_3$:Ce detectors and the ^{96}Ru target on which a simulated electron beam consisting of 10^9 electrons impinged. Several simulations were performed extending the geometry step by step, starting with a bare simulation with the target and the detectors only and adding consecutively the scattering chamber and other geometry upstream of the target. The geometry of the Faraday Cup was taken from an existing simulation [178].

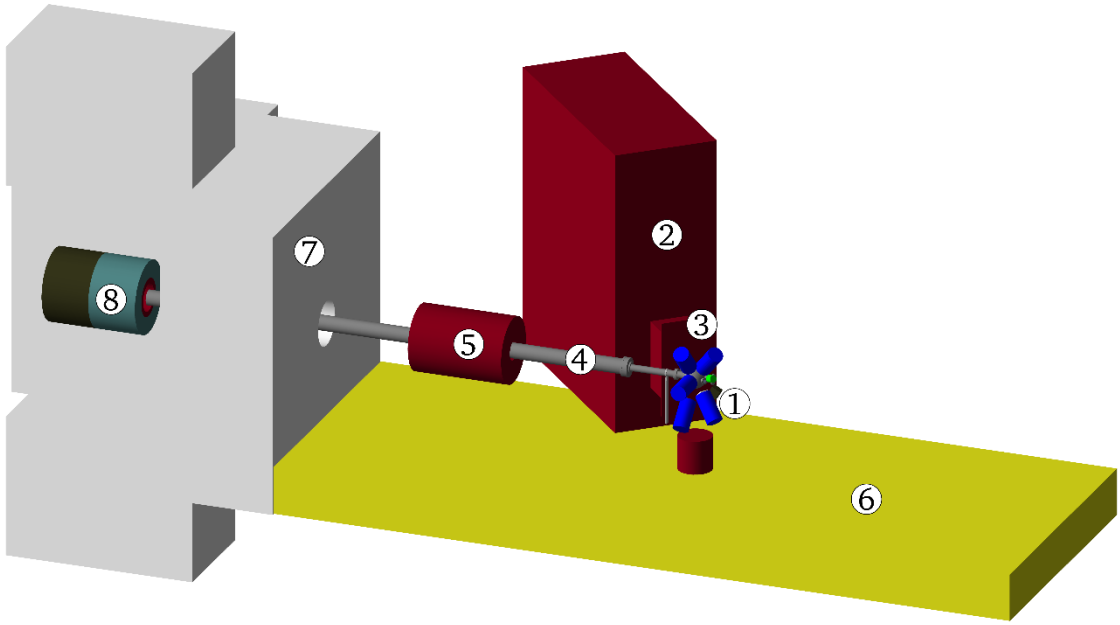

Figure 104: The replicated geometry of the QCLAM measurement setup includes the six $LaBr_3$:Ce detectors around the target including target guide in the scattering chamber ①, the QCLAM spectrometer ② with magnetic field shielding ③, the Faraday Cup beamline ④, the refocusing quadrupoles ⑤, the floor ⑥, the concrete wall ⑦ and the Faraday Cup ⑧. For a better overview, one wall on the side of the Faraday Cup has been removed.

The results of all simulations are shown in Figure 105. The background count rate of the six $LaBr_3$:Ce detectors increases by a factor of 8.1 when the ball scattering chamber is added to the target, and by a factor of 29 compared to the simulation with target only when the beam tube of the scattering chamber is added. This increase in background is caused by electrons of the beam hitting the opening of the scattering chamber towards the Faraday Cup and the beam pipe in combination with the use of stainless steel for the scattering chamber material. Thereby, background radiation in forward direction, such as elastically scattered electrons, is re-scattered and interacting in the material of the scattering chamber creating additional background. Using the full geometry leads to a further increase of 25 % compared to simulations with scattering chamber and its beam pipe. Removing the detector housing and its integrated lead shielding increases the count rate in the $LaBr_3$:Ce detectors by a factor of 3.2, so the use of the lead shielding is recommended for future experiments. The background count rate in the detector without lead shielding increased strongly when the lead shielding of the other detectors was removed. This detector had a greater distance to the target than the detector next to it and was protected by the lead shielding of the adjacent detector from background radiation originating downstream. Due to the small effect of the Faraday Cup on the background in the $LaBr_3$:Ce detectors and the considerably longer simulation time, the Faraday Cup is omitted for the following simulations.

To quantify the quality of the simulations, the simulated rates of the six $LaBr_3$:Ce detectors are compared with the measured rates of the 2020 measurement campaign in Table 23. For better comparability, the rates are normalized to a beam current of 1 nA. The uncertainty of the measured rates per nA is composed of the statistical uncertainty and a systematic uncertainty from the measurement of the beam current. The uncertainty of the simulation contains only the statistical uncertainty.

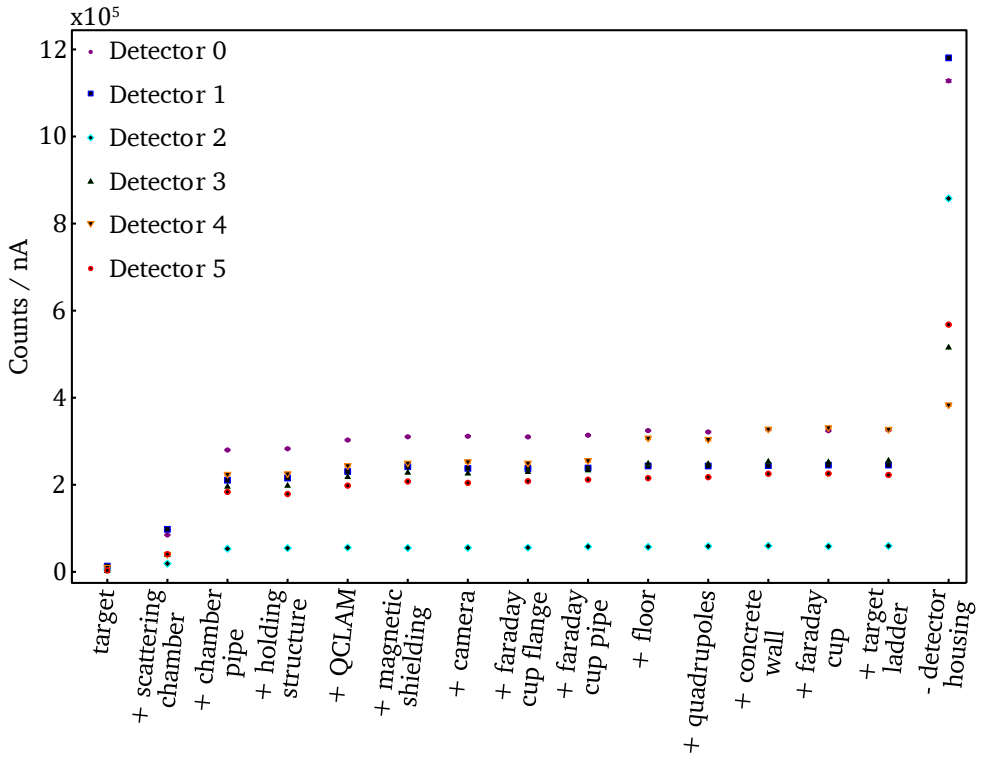

Figure 105: By expanding the geometry step by step, the effect of individual components on the background is investigated in the six $LaBr_3$:Ce detectors. The background is primarily caused by the ball scattering chamber and its beam tube, further geometry leads to minor increases. If the lead shieldings of the detectors are removed, the background increases strongly.

Table 23: The simulated rates of the six $LaBr_3$:Ce detectors are compatible with the measured rates. A discrepancy between the ratios of detectors 0 to 2 and 3 to 5 is evident.

Detector	Normalized rate (measured) (kcps/nA)	Normalized rate (simulated) (kcps/nA)	Ratio measured / simulated
0	40 (10)	62.0 (6)	0.65 (16)
1	32 (8)	51.9 (6)	0.62 (15)
2	21 (5)	31.5 (4)	0.67 (16)
3	44 (11)	47.1 (5)	0.93 (23)
4	47 (12)	48.2 (5)	0.98 (25)
5	45 (11)	41.4 (5)	1.09 (26)

The magnitude of the simulated rates is in very good agreement with the measured rates. However, the ratio of the measured rates and simulated rates of the detectors 0 to 2 in the tower at 90° differ from the ratio of the detectors 3 to 5 in the tower at 145°. This difference could be caused by an incomplete reconstruction of the actual geometry or the electron beam. Since all massive elements upstream from the target were reconstructed and added to the simulation, background radiation that is originated upstream from the target is not simulated. But as the measured count rate of detector 4, which was mounted without lead shielding, has

similar count rates as detectors 3 and 5 below and above it, as in the simulations, it can be assumed that the background originating upstream from the target was low. Another reason could be the electron beam, which passes through the center of the beam tube in the simulation. If the actual electron beam was tilted, a larger part of the scattered beam would hit the components downstream of the target. The quality of the simulation was sufficient to identify the ball scattering chamber as the primary background source. These findings helped in the design of the new (e,e'γ) scattering chamber, minimizing the background in the $LaBr_3$:Ce detectors (see Section 4.2.2).

8.5. Simulations of the Optimized Setup

The simulations for identifying possible background sources were repeated with the newly developed (e,e'γ) scattering chamber instead of the ball scattering chamber. The geometry used corresponds to the geometry of the first production run, which is listed in Table 24 in Section 9.1. Figure 106 shows that by adding the new (e,e'γ) scattering chamber the background increases by 13%, which is 25 times lower than using the old scattering chamber. There is a 73% jump in the simulated background when adding the Faraday Cup beam tube. The increase in background in the three detectors in the tower at 145° is 4.2 times greater than the increase in the detectors in the tower at 90° and is a consequence of the larger active area of the detectors in the Faraday Cup direction, since most of the background occurs behind the target. Adding further components to the setup leads to small effects on the background. The Faraday Cup is therefore not used for the following simulations. If the lead shields of the detectors are removed, the count rate of the detectors increases by a factor of 16, so the use of the lead shield is recommended even when using the new scattering chamber.

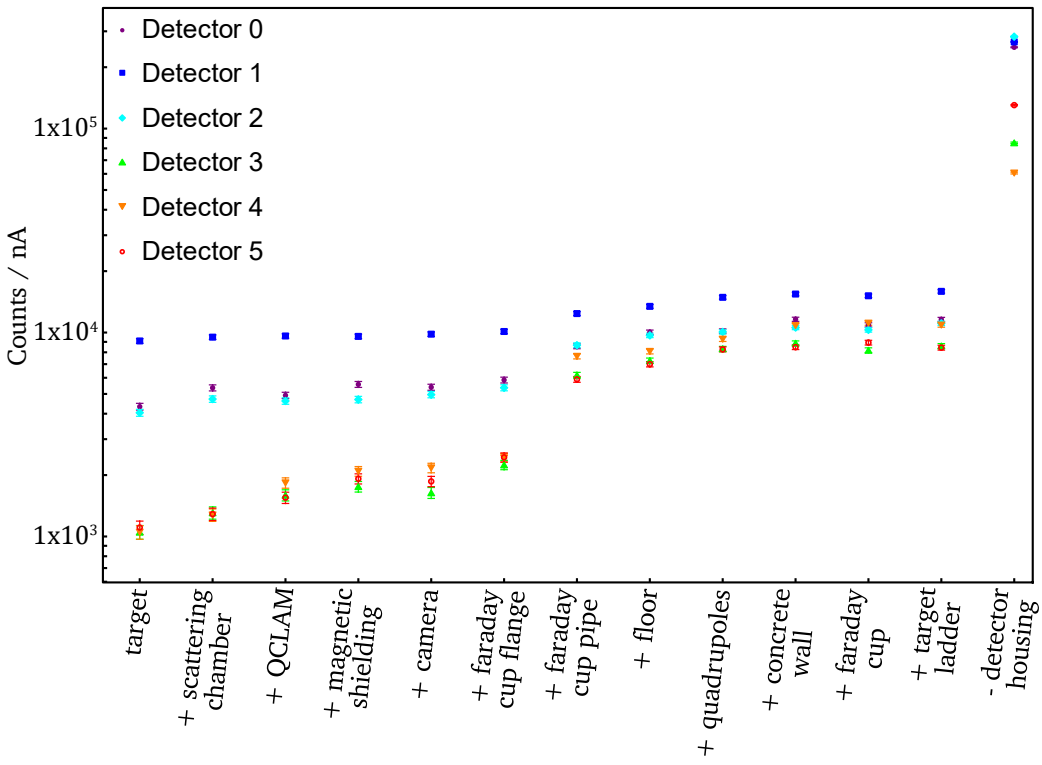

Figure 106: Using the new (e,e'γ) scattering chamber, the background rate in the $LaBr_3$:Ce detectors increases slightly. Further geometry has only minor effects on the background in the detectors, except for the Faraday Cup beam pipe. If the lead shields of the detectors are removed, the background increases strongly.

9. ^{96}Ru Production Run

A first production run utilizing the full (e,e'γ) setup and data acquisition took place in September 2021. The aim of the measurement was the observation of the γ-decay branching ratio of the 2_3^+ state of ^{96}Ru. This state decays with a relative intensity of $I_{rel}(2_{ms}^+ \rightarrow 2_1^+) = 100(11)$ % via the 2_1^+ state and with $I_{rel}(2_{ms}^+ \rightarrow 0_1^+) = 7.2(9)$ % directly to the ground state (see Section 2.1). This chapter presents a preliminary analysis of the data.

9.1. Experimental Setup

During the ^{96}Ru production run, the full (e,e'γ) setup shown in Figure 107, consisting of the optimized beamline (see Section 4.1), detector array, magnetic field shielding, and the new (e,e'γ) scattering chamber, which was used for the first time. For an increased reaction rate, the QCLAM was positioned at a scattering angle of 46.3° to provide an increased Mott cross section. The filters in front of the $LaBr_3$:Ce detectors consisted of a 2 mm layer of copper and a 5 mm layer of lead. A plastic scintillator, which is also read out by the LaBr data acquisition, was placed in front of detector 5 to investigate the use of a veto to suppress recorded events from scattered electrons. For the calibration measurement of the scattering angles, the sieve slit was placed in the adapter between the scattering chamber and the spectrometer at a distance of 226 mm from the target.

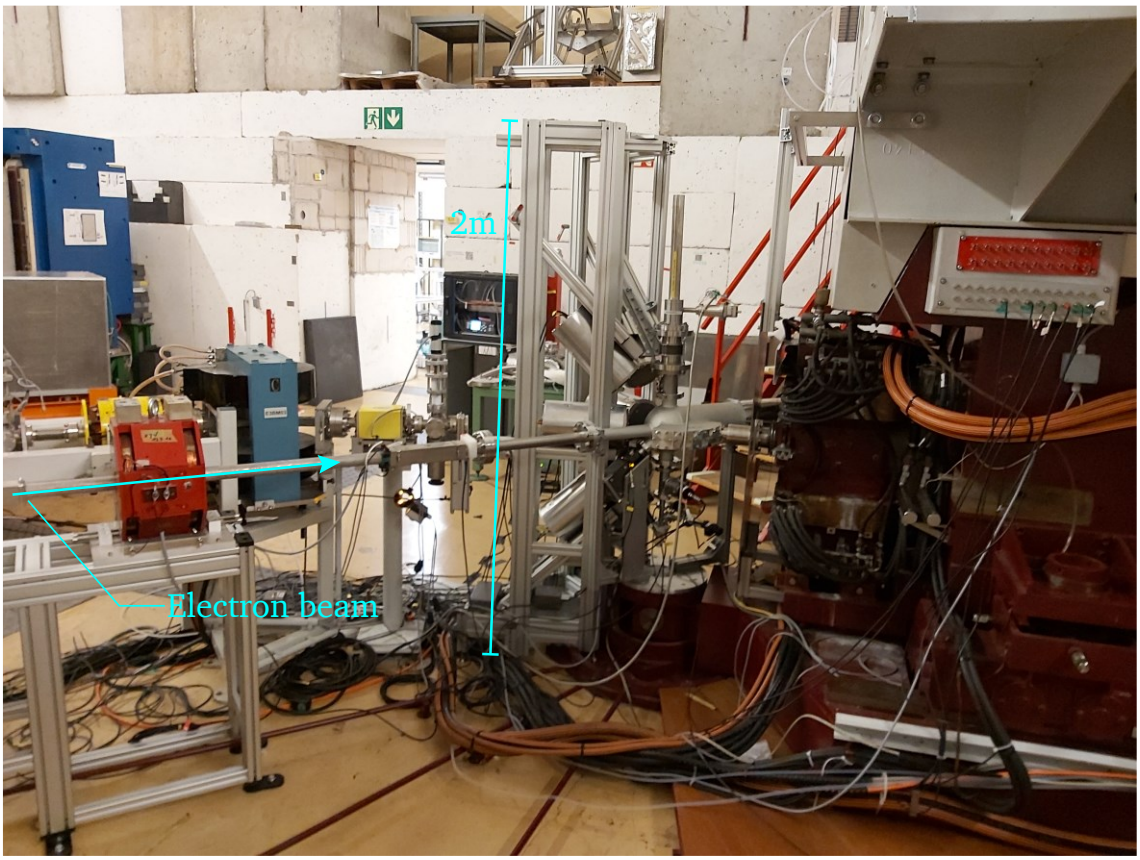

Figure 107: Experimental setup of the first (e,e'γ) production run. For the first time, the full setup including the new scattering chamber was used.

The setup was aligned according to the existing [39] and newly added marks at the QCLAM measurement site by using line lasers. The alignment tips of the $LaBr_3$:Ce detectors were used

to align the detectors in such a way that they are directly facing the target. Then, the inclination angles of the detectors were determined with a protractor of type PLR 50 C from Bosch. Table 24 lists the distances of the detectors from the target and their angles relative to the beam axis.

Table 24: Positions of the six $LaBr_3$:Ce detectors relative to the target position and beam axis.

Detector	Distance (mm)	Angle horizontal (deg)	Angle vertical (deg)
0	263 (2)	90	44.6(2)
1	172 (2)	90	0.0(2)
2	280 (2)	90	-43.9(2)
3	264 (2)	135	45.0(2)
4	171 (2)	135	0.0(2)
5	263 (2)	135	-44.1(2)

Three targets were mounted on the target ladder, which is shown in Figure 108. As described for the previous measurements, the second target position was kept free for beam and background optimization. The three targets were ^{96}Ru, ^{12}C and BeO. A 10 mg/cm^2 ^{12}C target was mounted in position 1 and was used for energy and efficiency calibration of the QCLAM spectrometer and for the (e,e'γ) commissioning at the beginning of the measurement. The ^{96}Ru target of the previous (e,e'γ) measurement, described in Section 8.1 was mounted at position 4.

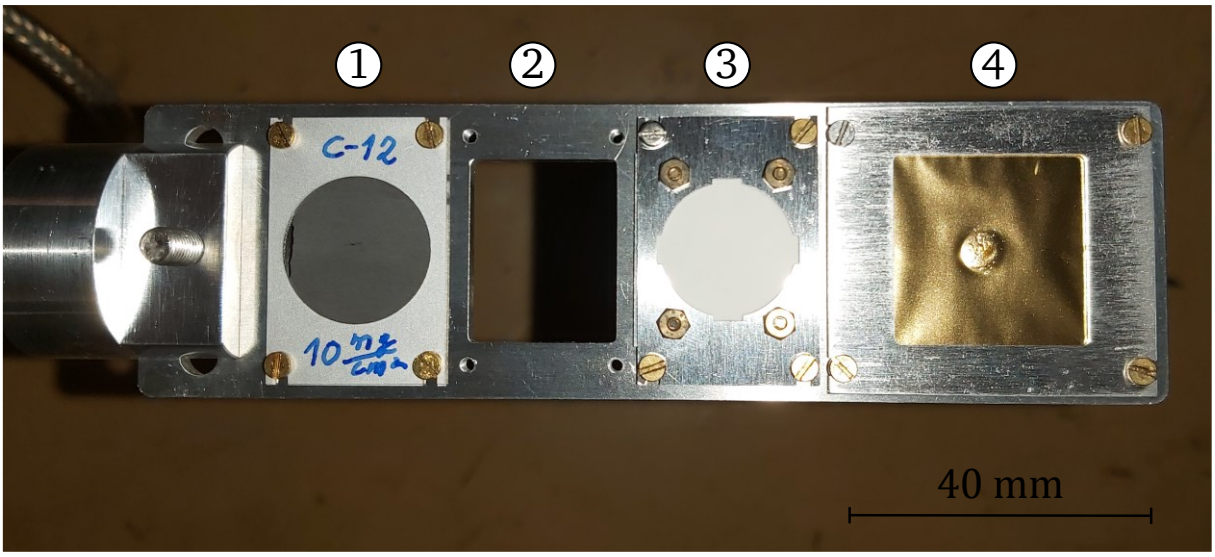

Figure 108: Three targets are mounted on the target ladder, the second slot was left free for beam optimizations. ① 10 mg/cm^2 ^{12}C, ② empty target, ③ BeO, ④ 28 mg/cm^2 ^{96}Ru with 13.6 mg/cm^2 ^{197}Au backing.

In this measurement, the (e,e'γ) data acquisition with the dead time lock (see Section 5.3) was used for the first time. Before starting the measurement, the delays of the coincidence circuit were optimized using three techniques. First, a $LaBr_3$:Ce detector was placed next to

the QCLAM scintillator and a ^{60}Co source was positioned between the two detectors so that coincident signals were measured. The additional time it requires for the signal to propagate along the cable when the detector is mounted at the correct position was calculated and subtracted. Second, a CAEN NTD6800 detector emulator, which allows the frequency, amplitude, and signal shape to be manipulated remotely, was used to simultaneously feed signals to the LaBr DAQ and the QCLAM DAQ. Third, the chosen delays were tested with all detectors mounted in the detector array around the scattering chamber using cosmic radiation hitting the QCLAM detector system and the $LaBr_3$:Ce detectors in the form of large-area showers. The three methods provided consistent results for the delays.

For energy calibration of the $LaBr_3$:Ce detectors, measurements were performed with a 1.2 MBq ^{60}Co source, a 2.2 MBq ^{226}Ra source, and with a ^{35}Cl(n,γ)^{36}Cl reaction using an Am/Be source. For the efficiency calibration, measurements were performed with the ^{60}Co and ^{226}Ra sources sequentially attached to the target ladder. To investigate the rate dependence of the $LaBr_3$:Ce detectors, a 20 MBq ^{60}Co source was positioned at different distances from the detectors.

9.2. Experimental Conditions

The measurement was performed over a period of three weeks starting on September 15th, 2021 and ending on October 7th, 2021. The beam current at the beginning of the measurement was 30 nA to 60 nA with a scraper opening of 10 mm (left 5 mm, right 5mm) and was increased towards the middle of the measurement to 60 nA to 100 nA by opening the scraper aperture up to 16 mm (left 8 mm, right 8 mm). The transmission of the electron beam from the gun to the experimental site was 20% because the electron beam was not optimally adjusted. This meant that the scraper could not improve the energy resolution of the electron beam, since the beam current and thus the count rate would have been reduced too much with a smaller scraper gap. The halo scrapers were not used because the background rate in the $LaBr_3$:Ce detectors increased with small slit size. Due to the coincidence condition of the three QCLAM photomultiplier tubes and at least on $LaBr_3$:Ce detector for generation of the trigger, a beam current could be used which would have corresponded to 20 times the maximum possible trigger rate in a singles measurement of the QCLAM spectrometer.

Due to the relatively low excitation energy of the states of interest, the elastic line was within the acceptance of the spectrometer and the trigger rate of the QCLAM spectrometer was up to 100 kcps with an accepted coincidence trigger rate of 3.6 kcps. The magnetic field setting was $I_{\mathrm{Dipole}} = 112$ A and $I_{\mathrm{Quadrupole}} = 140$ A, so that the elastic line was at the upper end of the detector system and excitation energies up to about 16 MeV were measured. The rates of the $LaBr_3$:Ce detectors were below 350 kcps at a threshold of 400 keV.

9.3. Preliminary Analysis

This section describes the corrections made and presents preliminary results of the measurement. The corrections are based on the experience of the previous ^{12}C measurements, described in Chapter 7, and have been improved. At the end of this chapter, spectra of the ^{96}Ru(e,e'γ) measurement are shown.

9.3.1. Correction of Spectrometer Aberration

The correction of the electron optical imaging properties of the QCLAM spectrometer was performed using the same procedure used in Section 7.3.1. In the first step, as shown in Figure 109, the ϕ dependence of the x-coordinate is corrected. For this correction, a run of the efficiency calibration measurements of the QCLAM detector system is used, which has no peak structures. The values of the correction parameters are listed in Table 25.

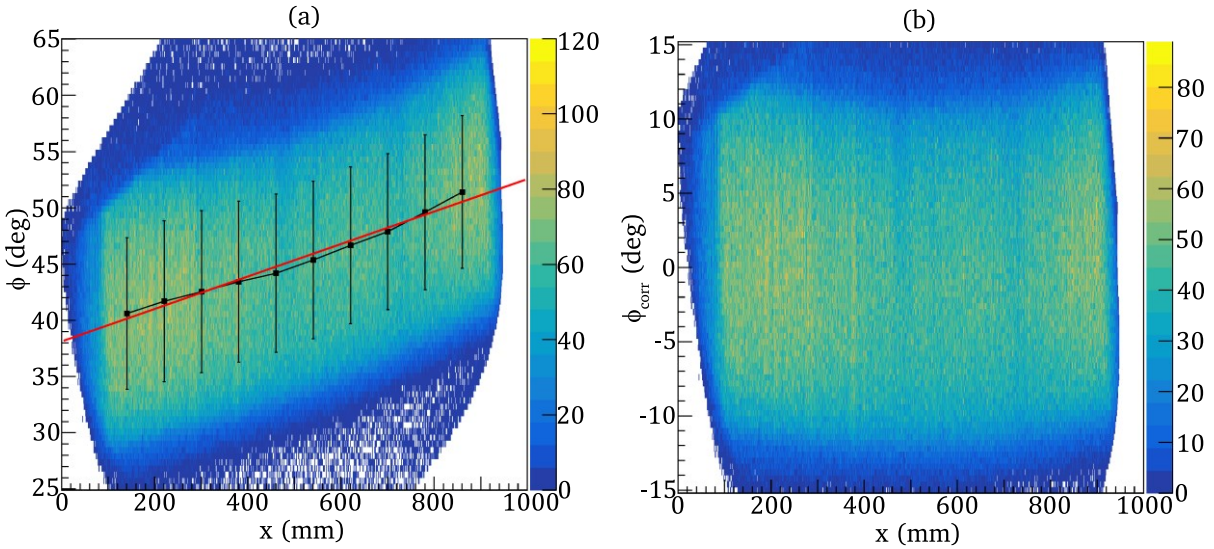

Figure 109: (a): The $x-\phi$ plot shows an approximately linear correlation between the angle ϕ and the x-coordinate. (b): After correction of the ϕ dependence of the x-coordinate, the $x-\phi$ plot shows a horizontal distribution.

Table 25: The listed parameters are used to correct the ϕ dependence of the x-coordinate according to Equation (7.2).

Parameter	Value
a	38.1(5)°
b	$1.44(95) \cdot 10^{-2}$°/mm

During this measurement, more different magnetic field settings were used than in the first commissioning experiment, so that the elastic lines of the ^{96}Ru target were shifted uniformly over the whole focal plane. This increases the reliability of the correction of the spectrometer abberation. The current of the QCLAM dipole magnet was increased from 106 A to 136 A in 3 A steps while keeping the ratio of quadrupole current to dipole current constant at 1.25. Using a higher number of uniformly distributed positions of the elastic lines improves the correction of the electron-optical imaging properties, since more data points are available for the fit and smaller areas have to be extrapolated when applying the correction. The summed-up runs of the measurements for correcting the electron optical imaging properties before and after correction are shown in Figure 110. The correction parameters used are listed in Table 26.

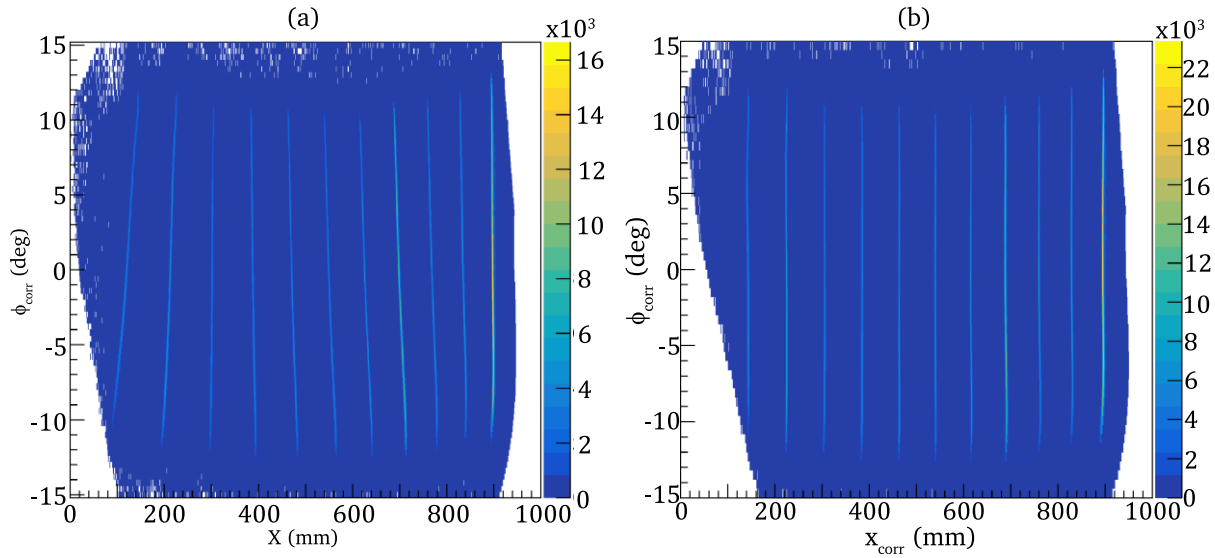

Figure 110: (a): In the two-dimensional $x - \phi$ plot of the summed runs, the curvatures of the elastic lines can be seen. (b): After correction of the x-coordinate, the elastic lines are straight, vertical lines.

Table 26: Listed are the correction parameters for the calculation of the corrected x-coordinate according to Equation (7.1).

Parameter	Value
$c_{0,0}$	$39.44(26)$ mm
$c_{0,1}$	$-3.933(25)$ mm/deg
$c_{0,2}$	$2.58(42) \cdot 10^{-2}$ mm/deg^2
$c_{1,0}$	$8.453(11) \cdot 10^{-1}$
$c_{2,0}$	$1.201(1) \cdot 10^{-4}$/mm
$c_{1,1}$	$1.613(11) \cdot 10^{-2}$/deg
$c_{1,2}$	$-1.60(17) \cdot 10^{-4}$/deg^2
$c_{2,1}$	$-1.286(10) \cdot 10^{-5}$/(mm deg)
$c_{2,2}$	$1.57(16) \cdot 10^{-7}$/(mm deg^2)

A comparison of the projections on the uncorrected x-coordinate and the corrected x-coordinate of the plots in Figure 110 is shown in Figure 111. A significant improvement in the resolution of the individual elastic lines can be seen.

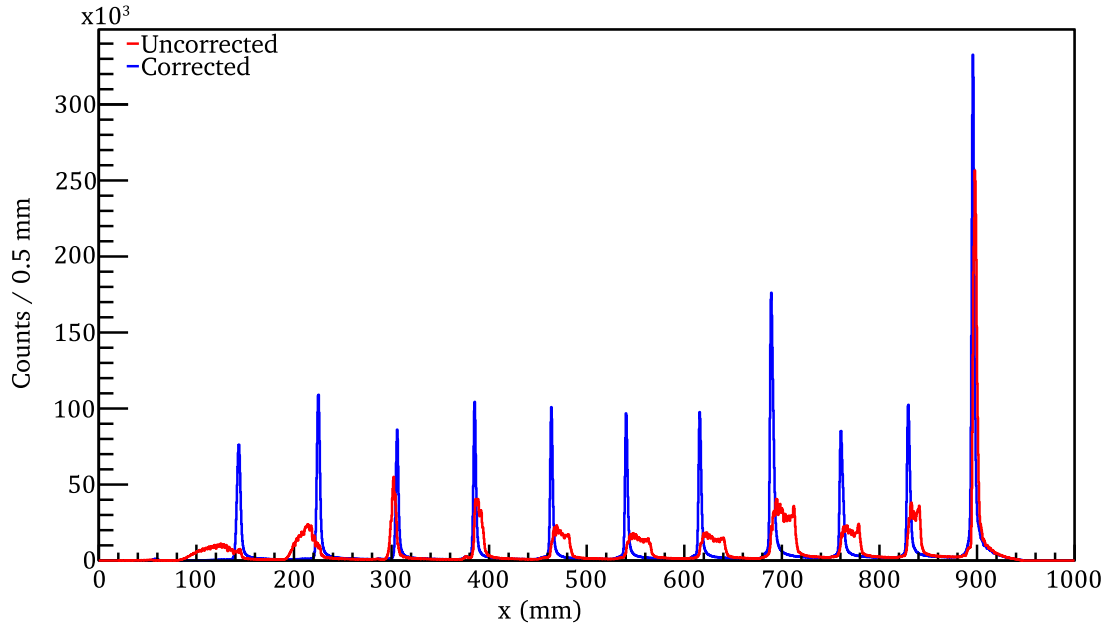

Figure 111: The projection of the uncorrected x-coordinates (red) has low and inconsistent resolution. After applying the correction of the x-coordinate, a better and approximately constant resolution is shown throughout the acceptance of the detector system.

The energy calibration of the electron data was done using the measurements with the ^{12}C target. In addition to the elastic line, the excited states at 4.44 MeV and 7.654 MeV (see Section 2.1) are visible in the spectrum, providing a total of three peaks. A second order polynomial

$$E_x(x_{corr}) = a + b\,x_{corr} + c\,x_{corr}^2 \tag{9.1}$$

with the parameters listed in Table 27 was used for the energy calibration to account for the non-linearity of the focal plane of the spectrometer. The calibrated excitation spectrum of ^{12}C is shown in Figure 112.

Table 27: Parameter of the energy calibration function shown in Equation (9.1).

Parameter	Value
a	$-9.197(11)$ MeV
b	$3.1766(4) \cdot 10^{-2}$ MeV/mm
c	$5.878(12) \cdot 10^{-6}$ MeV/mm^2

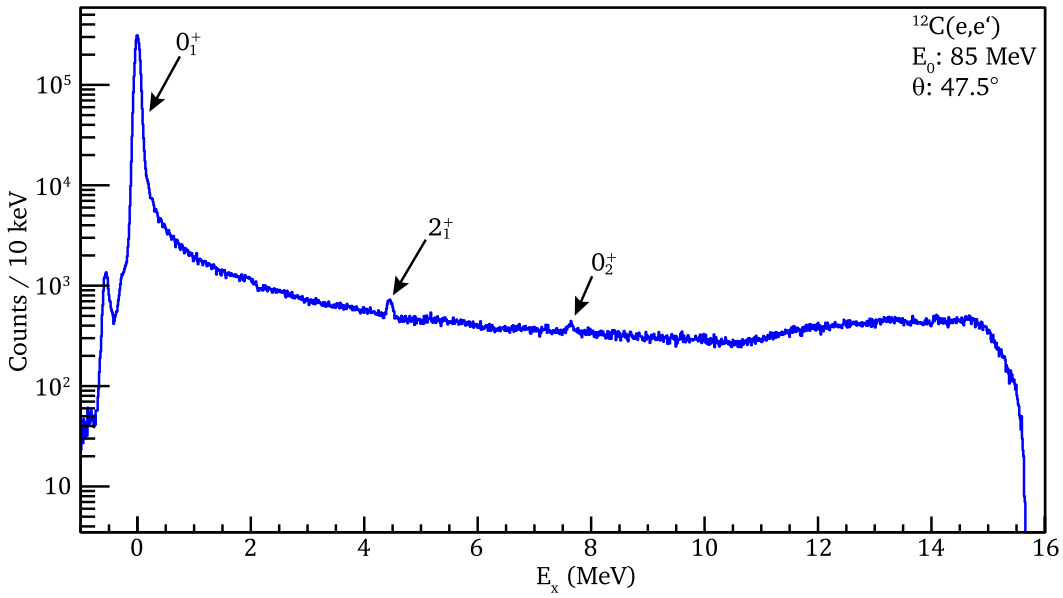

Figure 112: The ^{12}C excitation spectrum shows two peaks at 4.44 MeV and 7.654 MeV in addition to the elastic line. The peaks to the left of the elastic line of ^{12}C cannot be assigned to the target. It is possible that these are software artifacts, which requires further investigation.

There are shifts in the peak positions in the spectrum between the energy calibration measurements with the ^{12}C target and the measurements with the ^{96}Ru target. A constant offset arises due to the different masses of the target nuclei. In addition, fluctuations of the peak positions between the individual runs occur due to the experimental setup during the measurements. Both offsets are corrected by determining the position of the elastic line of the ^{96}Ru runs and shifting it to the position of the elastic line of the ^{12}C runs. Thereby the energy calibration of the ^{12}C measurement can be used. This ensures that the elastic line is assigned to excitation energy zero. The positions of the elastic lines of the ^{96}Ru runs are shown in Figure 113.

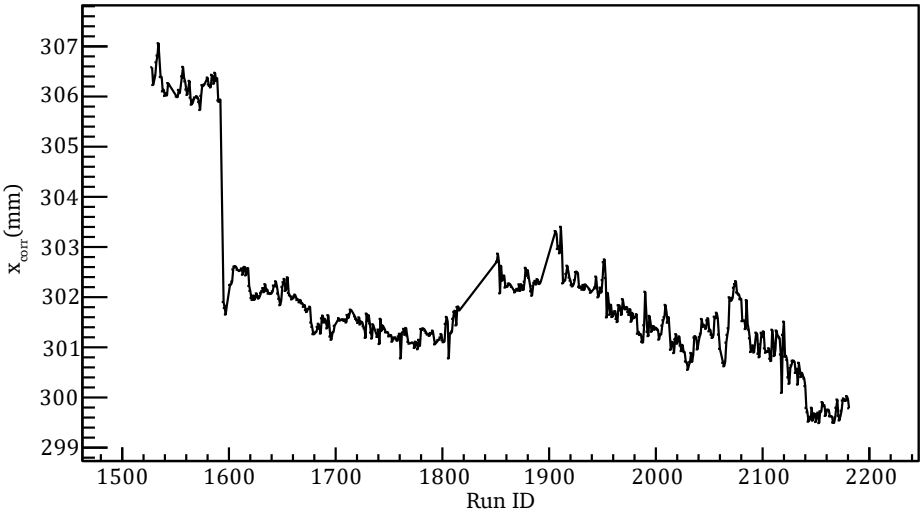

Figure 113: The position of the elastic line of the ^{96}Ru target shifts during the measurements.

In the energy-calibrated ^{96}Ru excitation spectrum shown in Figure 114, the elastic line is dominant and other peaks cannot be detected without an additional coincidence condition

due to the kinematics of the measurement. The energy resolution of the excitation spectrum is 110 keV.

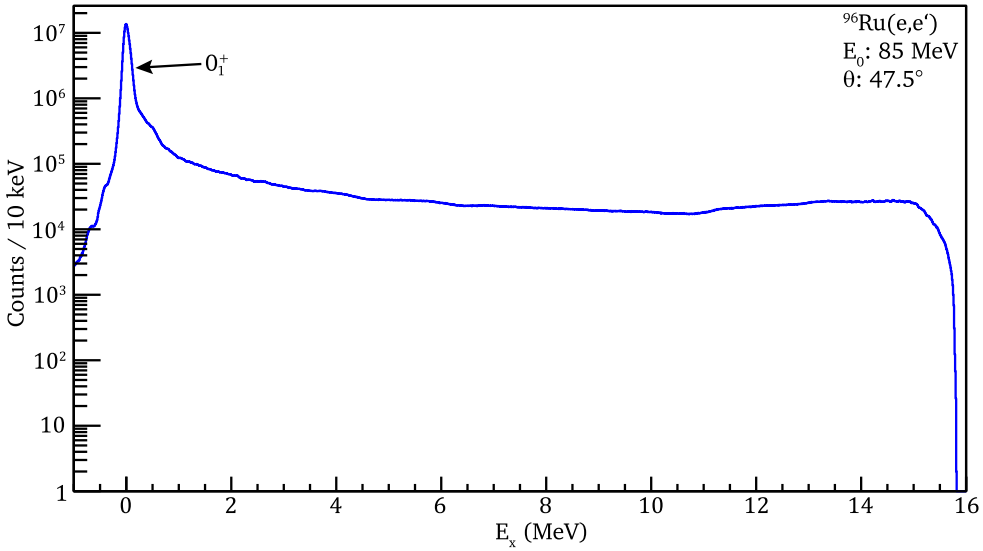

Figure 114: Without the use of a coincidence condition, the elastic line is the only visible peak in the excitation spectrum of the ^{96}Ru measurement.

9.3.2. Energy Calibration of $LaBr_3$:Ce Detectors

The energy calibration of the six $LaBr_3$:Ce detectors cannot be obtained from the electron beam runs because the spectra are dominated by background. Therefore, as described in Section 7.3.3, the energy calibration is performed using similar source measurements. Before the energy calibration can be performed, the rate-dependent shift of the peaks in the uncalibrated spectrum must be corrected. The rate dependence was experimentally determined by measurements with a 20 MBq ^{60}Co source by changing the distances between source and $LaBr_3$:Ce detectors. For the correction of the rate dependence, a model as simple as possible is used, which is compatible with the measurements. The rate-corrected integrated detector signals are calculated using

$$x_{corr,1}(r,x) = (1 + a\,r) \cdot b\,x, \tag{9.2}$$

which scales linearly with the rate r and is proportional to the integrated detector signal x. Detector 2 was the only detector to show strong deviations from Equation (9.2) at small rates, thus the model

$$x_{corr,2}(r,x) = \frac{d\,x}{r^a + b\,r^c} \tag{9.3}$$

is used for this detector. The parameter a, b, c and d, which are listed in Table 28, were obtained by fitting Equations (9.2) and (9.3) to the measured rate dependence of the $LaBr_3$:Ce detectors using the 1.174 MeV and 1.332 MeV peaks of the ^{60}Co source. The fits are shown in Figure 115.

Table 28: Parameters of rate dependence correction given by Equations (9.2) and (9.3). The parameters are determined for rates r in units of cps.

Detector	a	b	c	d
0	$-3.91(13)\ 10^{-8}$	0.28981(8)	-	-
1	$2.64(8)\ 10^{-9}$	0.20319(5)	-	-
2	0.1623(16)	0.0190(10)	0.5919(53)	0.3585(3)
3	$1.1(19)\ 10^{-9}$	0.13537(2)	-	-
4	$1.901(96)\ 10^{-8}$	0.04087(1)	-	-
5	$-1.161(19)\ 10^{-7}$	0.14489(5)	-	-

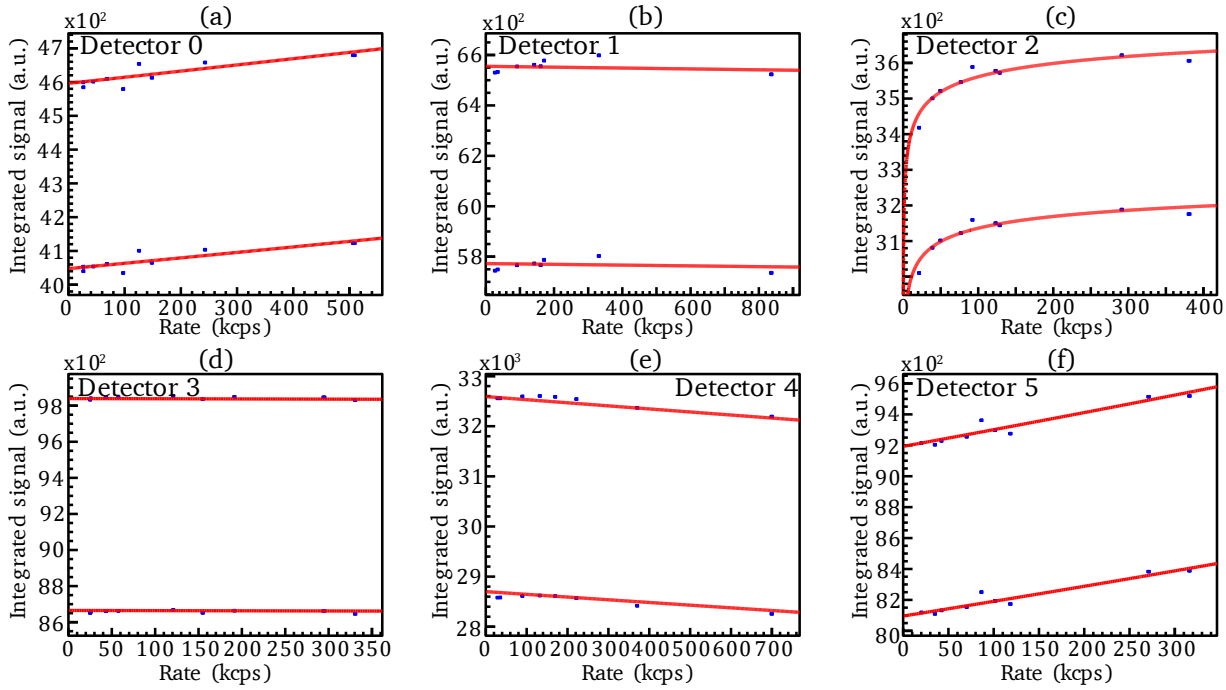

Figure 115: The rate dependence of the integrated signal shape of the $LaBr_3$:Ce detectors is determined by simultaneous fit (red) of the model functions given by Equations (9.2) and (9.3) to the data points (blue) of the two peaks of a ^{60}Co source measurement.

By correcting for rate dependence, the energy resolution of the ^{60}Co measurements was improved by up to 17%. Furthermore, measurements with sources of different activities can be used for energy calibration and the resulting energy calibration can be applied to data from electron beam measurements with fluctuating count rates.

The energy calibration was performed using a ^{226}Ra source for energies below 3 MeV and the ^{35}Cl(n,γ)^{36}C reaction (as described in Section 7.3.3) for energies greater than 3 MeV. Since both energy calibration measurements were incompatible even after rate correction and had different slopes of the calibration function, the ^{35}Cl(n,γ)^{36}Cl measurement was scaled to the measurement with the ^{226}Ra source based on the peak of the intrinsic activity of the $LaBr_3$:Ce

detectors at 1.46 MeV. A possible explanation for the change in gain of the $LaBr_3$:Ce detectors could be caused by a change in setup, since the scattering chamber had to be removed for the calibration measurements at higher energies and this could have had an effect on the magnetic field distributions at the detectors. The energy calibration of the $LaBr_3$:Ce detectors was then performed using a second order polynomial. The energy calibrated spectra of the ^{226}Ra and $^{35}Cl(n,\gamma)^{36}Cl$ measurements are shown in Figures 116 and 117.

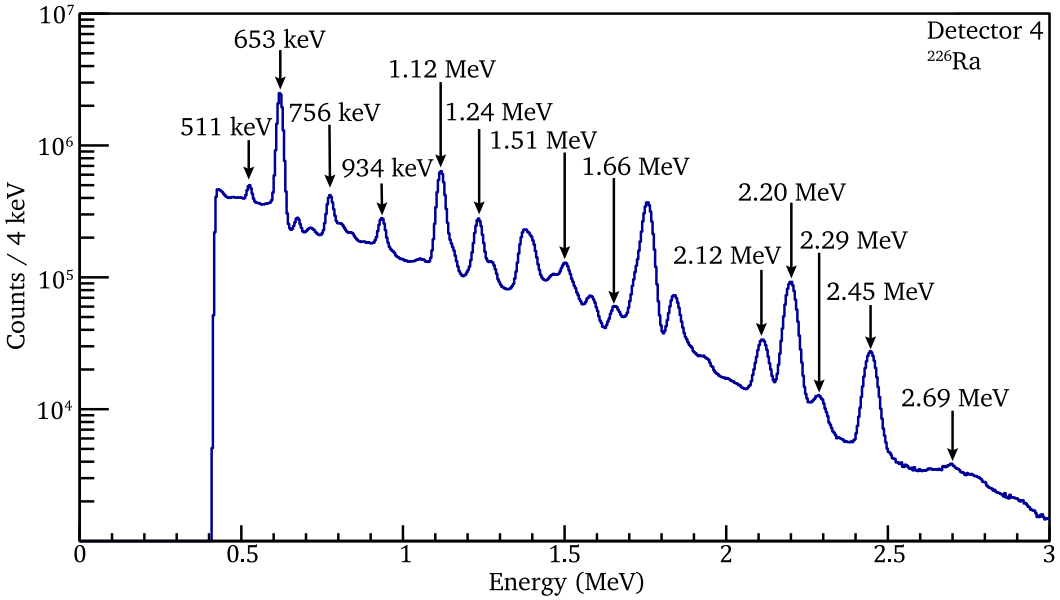

Figure 116: The spectrum of a ^{226}Ra source is used for energy calibration for energies lower than 3 MeV.

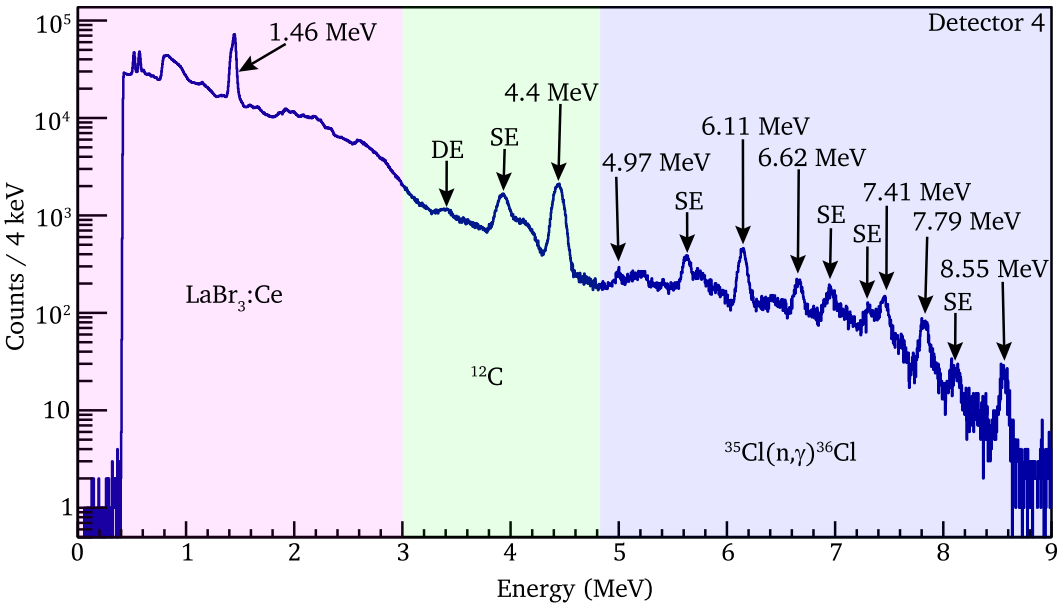

Figure 117: For energies above 3 MeV, a $^{35}Cl(n,\gamma)^{36}Cl$ reaction is used, producing photons with energies up to 8.55 MeV.

Table 29: Listed are the energy calibration parameters of the six $LaBr_3$:Ce detectors.

Detector	a (MeV)	b (MeV/ch)	c (MeV/ch^2)
0	$2.6(60) \cdot 10^{-3}$	$9.66(35) \cdot 10^{-4}$	$4.05(38) \cdot 10^{-9}$
1	$-1.94(42) \cdot 10^{-3}$	$1.014(3) \cdot 10^{-3}$	$-5.06(27) \cdot 10^{-9}$
2	$1(10) \cdot 10^{-4}$	$1.004(6) \cdot 10^{-3}$	$-8.7(71) \cdot 10^{-10}$
3	$1.5(48) \cdot 10^{-2}$	$9.932(31) \cdot 10^{-4}$	$-1.72(35) \cdot 10^{-9}$
4	$4.14(79) \cdot 10^{-2}$	$9.674(51) \cdot 10^{-4}$	$2.10(58) \cdot 10^{-9}$
5	$1.01(51) \cdot 10^{-2}$	$9.740(32) \cdot 10^{-4}$	$6.27(37) \cdot 10^{-9}$

The energy dependence of the energy resolution of the $LaBr_3$:Ce detectors was determined by a fit of Equation (7.9), analogous to Section 7.3.3. The energy resolutions for different energies were obtained by fitting Gaussians on linear background to the energy calibration measurements. Figure 118 shows the FWHM of detector 5 as a function of energy. The fit provides an energy resolution of 3.1 % at 662 keV, which is consistent than the specification of the manufacturer of 2.9 % [128].

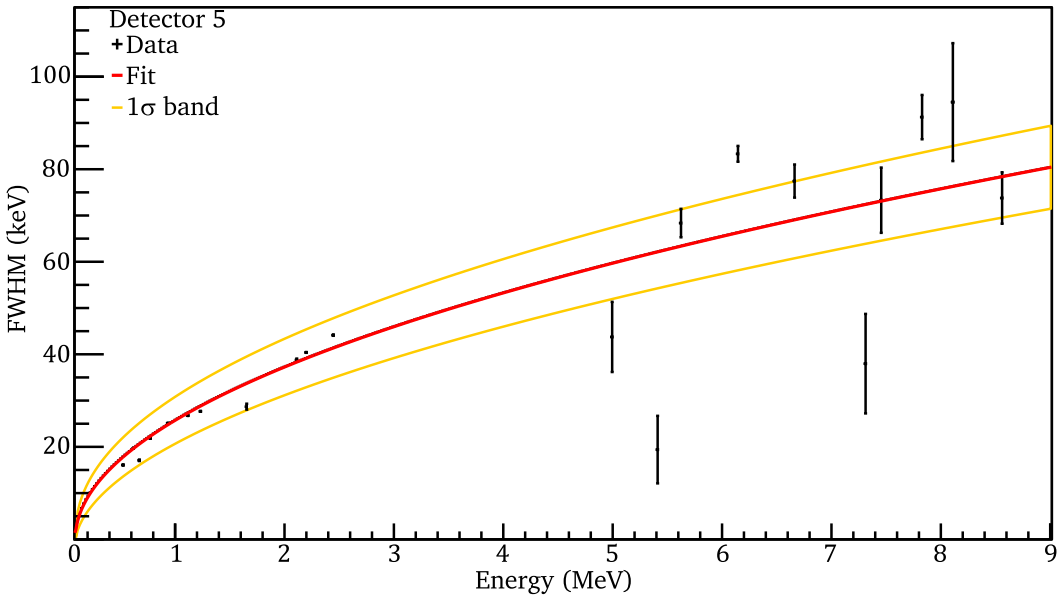

Figure 118: The energy resolution of $LaBr_3$:Ce detectors depends on the energy. At higher energy, the absolute width increases, but the relative resolution improves. Shown is the fill width at half maximum as a function of the energy of detector 5.

9.3.3. Time-of-Flight Correction

The uncorrected time resolution is deteriorated by the properties of the (e,e'γ) setup. These are the effects of the time-of-flight of electrons inside the QCLAM spectrometer and the energy dependent time effect of the $LaBr_3$:Ce detectors described in Section 7.4. Both effects are corrected by an empirical procedure by determining the dependencies by fits to the measured data.

The time-of-flight correction is performed using

$$t_{tof} = \sum_{i,j} a_{i,j} x^i \Phi^j, \tag{9.4}$$

which is a generalized form of Equation (6.7). The parameters $a_{i,j}$ of the dependencies of the time-of-flight on the dispersive coordinate x and the dispersive angle ϕ are determined iteratively, as shown in Figure 119. The time differences between the QCLAM spectrometer and the $LaBr_3$:Ce detector 1 were corrected using the $x2$-coordinate as the dispersive coordinate. The correction parameters thus obtained are listed in Table 30.

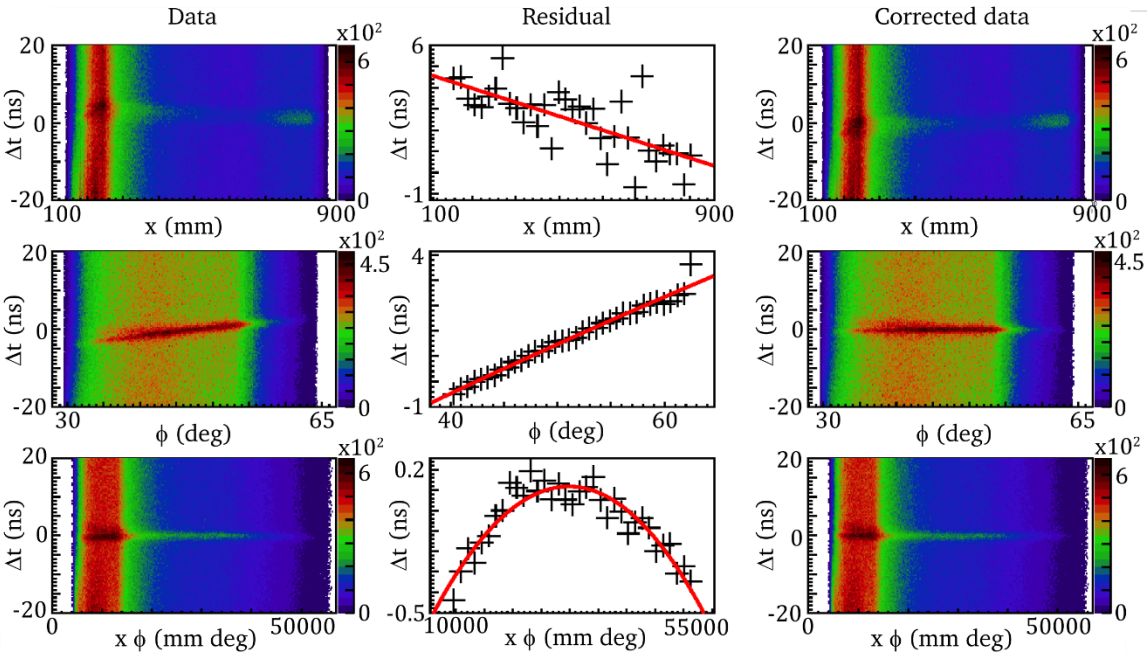

Figure 119: The time-of-flight of the electrons in the QCLAM spectrometer is determined iteratively by fits to the data. The left column shows the uncorrected data, the fit to the positions of the time peak is shown in the middle column and the right column shows the corrected data. For each subsequent line, the previous corrections are applied to the time difference. The rows show from top to bottom the correction of the x-dependence, the ϕ-dependence and the $x \cdot \phi$-dependence.

The correction of the electron's time-of-flight inside the QCLAM dipole magnet leads to an improvement of the time resolution, but a dependence on the time difference of the energy of the detected photons or the amplitude of the signals of the $LaBr_3$:Ce detectors is observed. A possible explanation for this effect is the dependence of the signal shape on the amplitude, which was discussed in the context of the pileup correction in Section 6.1.2. To ensure that a gate on the time difference peak does not cut events belonging to high energy photons, the energy-dependent time effect of the $LaBr_3$:Ce detectors must be corrected. The correction for the photon energy dependence on the time difference is accomplished by a fit of

$$t_{te} = a + b \cdot E_\gamma + \mathrm{c} \cdot E_\gamma^2 \tag{9.5}$$

to the measured data, as shown in Figure 120. The correction parameters a, b and c of all detectors obtained by this method are listed in Table 31.

Table 30: Listed are the values of the correction parameters $a_{i,j}$ of the time-of-flight correction according to Equation (9.4).

i	j	Value
0	0	$-5.95(60)$ ns
1	0	$-6.5(11) \cdot 10^{-3}$ ns/mm
0	1	$2.32(77) \cdot 10^{-1}$ ns/deg
0	2	$-4.1(75) \cdot 10^{-4}$ ns/deg^2
1	1	$6.56(49) \cdot 10^{-5}$ ns/(mm deg)
2	2	$-1.101(79) \cdot 10^{-9}$ ns/(mm^2 deg^2)
1	2	$-3(10) \cdot 10^{-4}$ ns/(mm deg^2)
2	1	$5.1(22) \cdot 10^{-8}$ ns/(mm^2 deg)

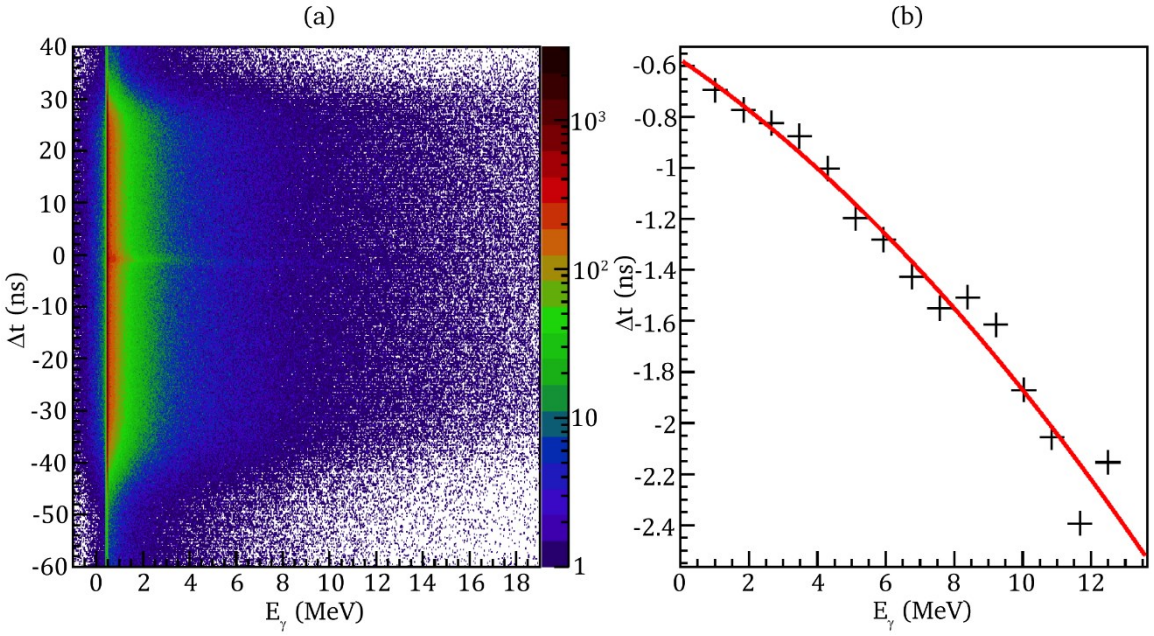

Figure 120: (a): In the two-dimensional plot of the time-of-flight corrected time difference versus photon energy measured by detector 5 an energy dependence of the time difference peak can be seen. (b): For the correction of the effect, Equation (9.5) is fitted to the time difference-energy values.

By applying both corrections, the time resolution of the coincidence peak was reduced from 5.6 ns to 1.9 ns FWHM. Figure 121 shows a comparison of the time resolutions before and after correction and when using the correction obtained from a CST simulation in Section 6.3.

The correction performed using the fits to the measured data provide better results than the correction based on the CST simulation of 2.3 ns. The deviation of 0.4 ns between both time-of-flight corrections is probably caused by the positioning of the detector system, which is not known and was estimated for the simulation. The peak to background ratio is 0.383(1).

Table 31: Listed are the parameters for correcting the energy-dependent time effect of the $LaBr_3$:Ce detectors based on Equation (9.5).

Detector	a (ns)	b (ns/MeV)	c (ns/MeV^2)
0	1.801(39)	$-5.5(11) \cdot 10^{-2}$	$1.48(72) \cdot 10^{-3}$
1	$1.45(33) \cdot 10^{-1}$	$-7.4(97) \cdot 10^{-3}$	$-2.46(67) \cdot 10^{-3}$
2	2.344(63)	$-2.8(19) \cdot 10^{-2}$	$-2.0(11) \cdot 10^{-3}$
3	$-5.76(96) \cdot 10^{-1}$	$-9.1(32) \cdot 10^{-2}$	$-3.8(24) \cdot 10^{-3}$
4	$-6.9(17) \cdot 10^{-1}$	$5.6(63) \cdot 10^{-2}$	$-2.56(48) \cdot 10^{-2}$
5	5.396(83)	$-1.34(28) \cdot 10^{-1}$	$-1.5(20) \cdot 10^{-3}$

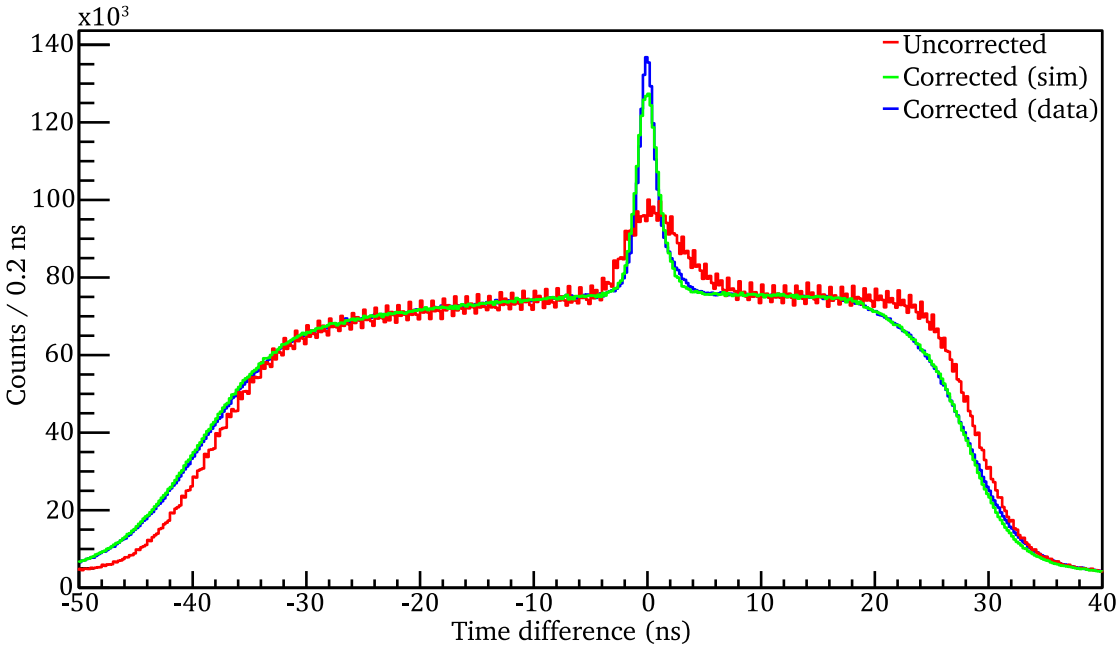

Figure 121: The uncorrected time resolution (red) is improved by using the time-of-flight correction and the correction of the energy-dependent time effect in the $LaBr_3$:Ce detectors. The time-of-flight correction from the measured data (blue) provides a better result than the correction from a simulation (green).

9.4. QCLAM and $LaBr_3$:Ce Efficiency

The efficiency measurement and evaluation of the relative QCLAM efficiency was performed analogously to the commissioning experiment described in Section 7.5.1. The relative efficiencies shown in Figure 122 corresponds to an analysis with the QCLAMon version from September 2021, used during the measurement campaign, and the newer version from February 2022. A comparison shows the improved and more uniform relative efficiency due to an improved reconstruction algorithm of the trajectories of the electrons based on the drift time distributions. In the efficiency spectrum, structures and strong fluctuations in the range between 300 mm and 400 mm can also be seen with the new algorithm, but they are less pronounced in the data of the newer QCLAMon version. Since February 2022, QCLAMon has

been continuously improved. Thanks to a continuous improvement on the tracking algorithm a further increase on the achievable efficiency is possible.

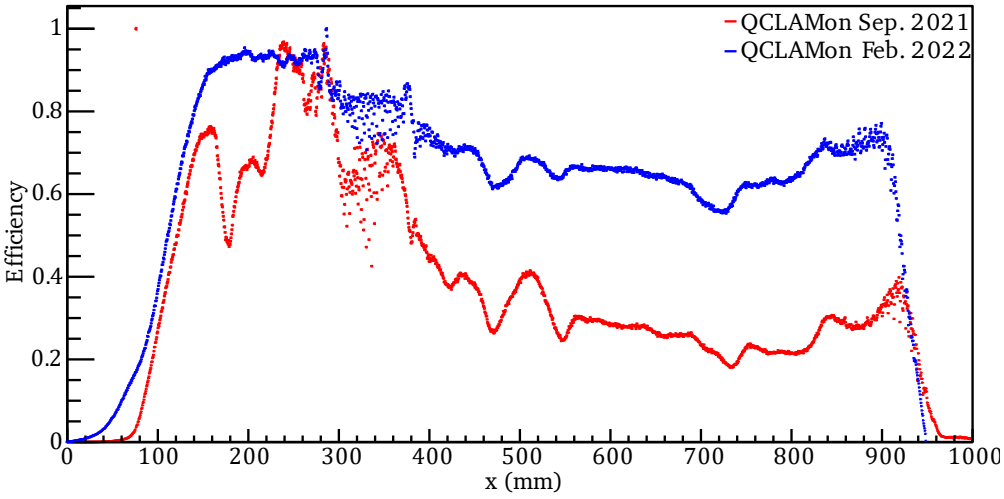

Figure 122: The reconstruction algorithm of the QCLAMon version from February 2022 (blue) provides higher efficiency compared to the reconstruction algorithm of the older QCLAMon version from September 2021 (red).

Efficiency calibrated ^{96}Ru(e,e') spectra using the two efficiency corrections are shown in Figure 123. The efficiency correction of the February 2022 version of QCLAMon results in a smoother curve.

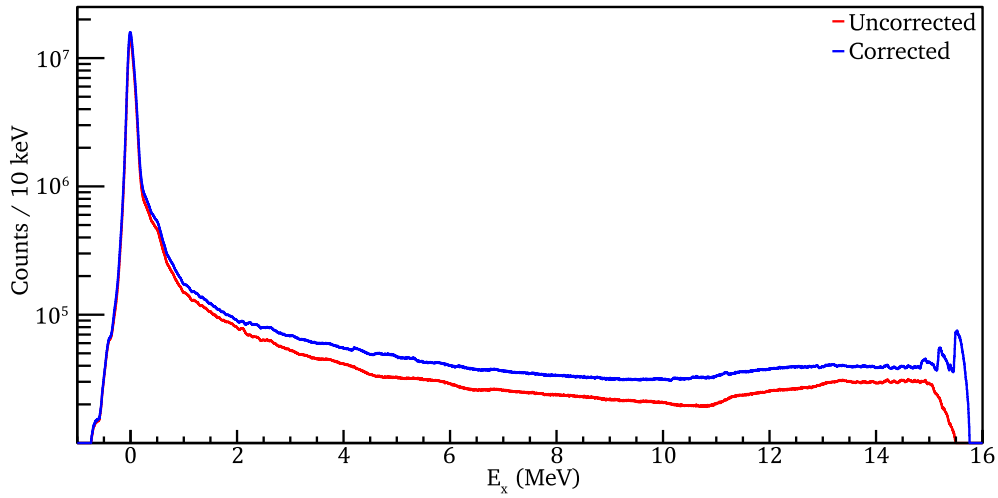

Figure 123: The ^{96}Ru(e,e') spectrum is flatter in the range between 2 MeV and 14 MeV after correction of the relative efficiency, but shows small structures.

9.5. Status of Preliminary Analysis

The background subtraction was performed analogously to the evaluation of the measurement at ^{12}C. The background subtracted $E_x - E_\gamma$ matrix is shown in Figure 124. The background caused by bremsstrahlung can be seen along the $E_x = E_\gamma$ line and decreases with increasing energy loss of the electrons, i.e., with increasing excitation energy. Above the $E_x = E_\gamma$ line, the counts fluctuate around zero, confirming the quality of the background subtraction of random coincidences. At small excitation energies, isolated states can be seen. Above the

neutron separation threshold S_n of 10.7 MeV [68], an increase in events with photon energies less than 2 MeV is observed.

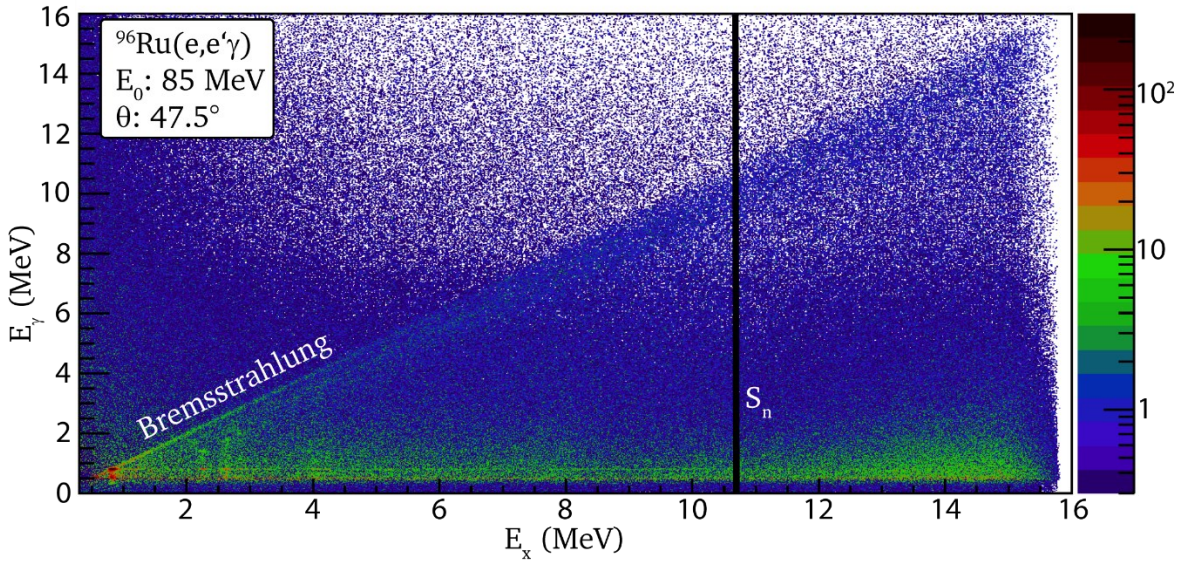

Figure 124: Background subtracted $E_x - E_\gamma$ matrix. Isolated states are visible at small excitation energies. At energies above the neutron separation threshold S_n, an accumulation of photons with energies below 2 MeV is observed. The $E_x - E_\gamma$ line is caused by bremsstrahlung.

A better understanding of the increased number of counts above the neutron separation threshold is provided by projecting events with excitation energies above S_n onto the E_γ axis, which is shown in Figure 125. When excited to states above the neutron separation threshold, ^{96}Ru predominantly decays via neutron emission to ^{95}Ru, which subsequently equilibrates by one or more γ-decays. In the γ-spectrum three peaks with energies between 788 keV and 1141 keV can be seen, which can be assigned to known low lying states of ^{95}Ru.

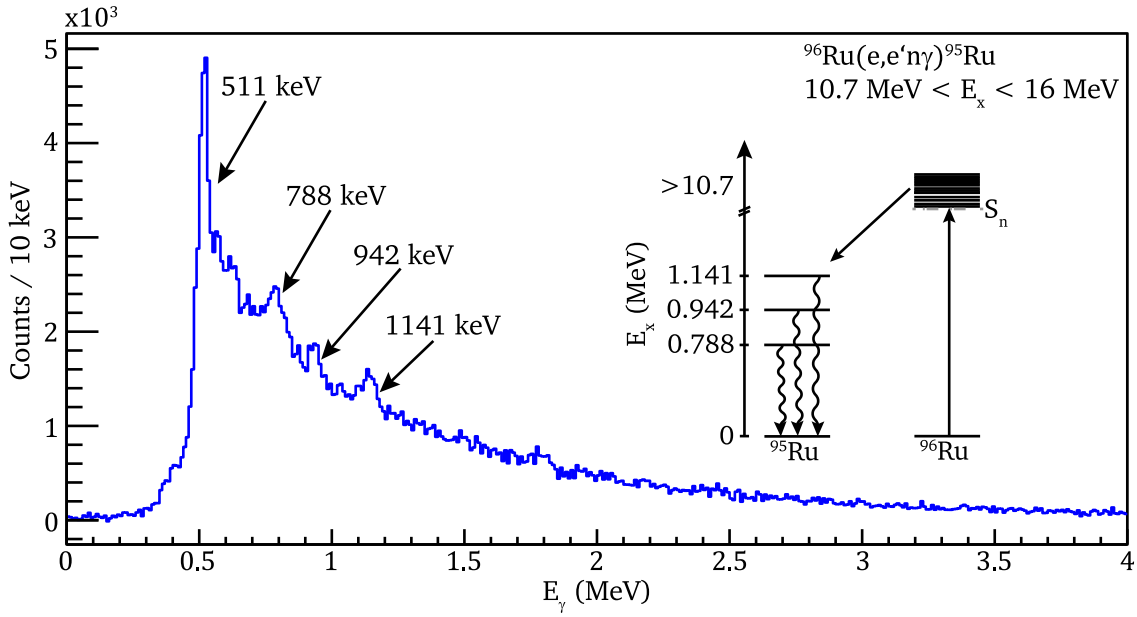

Figure 125: At excitation energies above the neutron separation threshold of 10.7 MeV, ^{96}Ru decays predominantly via neutron emission to ^{95}Ru. Using a gate on excitation energies above the neutron separation threshold, depopulations of low-lying states of the resulting ^{95}Ru are observed in the γ-ray detectors.

A zoom of the $E_x - E_\gamma$ matrix to energies below 5 MeV is shown in Figure 126. On the $E_x = E_\gamma$ line, the excitation, and the subsequent ground state decay of the 2_1^+ state of ^{96}Ru can be seen with high intensity. At an excitation energy of 2.284 MeV, a γ-decay branch of the 2_3^+ state via the 2_1^+ state is observed. The ground state decay of the 2_3^+ state could not be observed due to its low probability and the bremsstrahlung background. At excitation energies above 2.5 MeV, states depopulating via the 2_1^+ state are further observed.

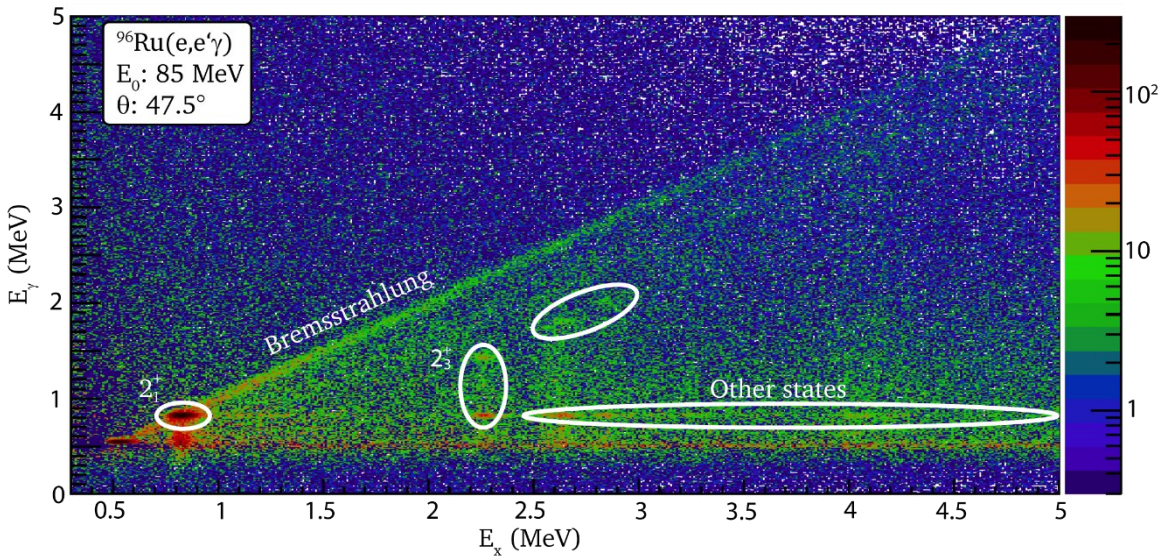

Figure 126: Isolated states of ^{96}Ru in the range up to 5 MeV are visible. The 2_1^+ state is excited and decays to the ground state. Other states at higher excitation energies decaying via the 2_1^+ state have been observed.

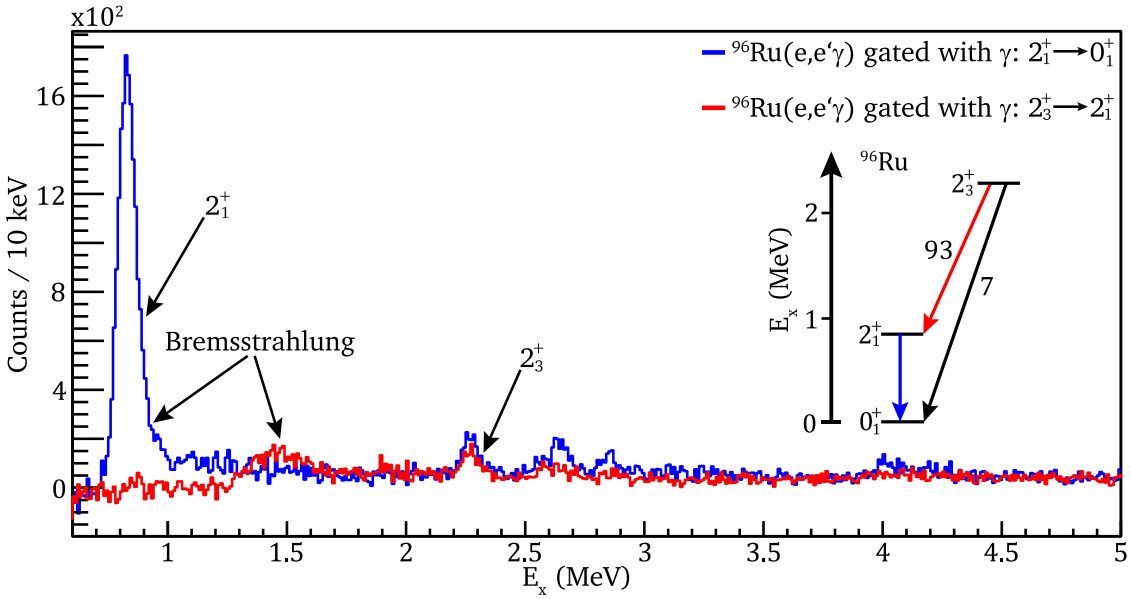

Figure 127: Using a gate on the transition $2_1^+ \rightarrow 0_1^+$ (blue), the excitation and decay of the 2_1^+ state superimposed with bremsstrahlung can be seen dominantly. At higher excitation energies, additional states can be seen decaying via the 2_1^+ state. A gate to the transition $2_3^+ \rightarrow 2_1^+$ (red) shows two structures in the spectrum, namely bremsstrahlung at the energy of the transition and the excited 2_3^+ state.

Projections on the E_x axis using gates on the γ-decays $2_1^+ \rightarrow 0_1^+$ and $2_3^+ \rightarrow 2_1^+$ are shown in Figure 127, which depicts a γ-decay branch of the 2_3^+ state. Since both transitions belong to a

γ-decay branch of the 2_3^+ state, this state can be seen in both spectra. The bremsstrahlung has a peak at $E_x = E_\gamma$, which makes the observation of ground state decays of an excited state difficult. By gating on a transition with $E_x \neq E_\gamma$, the excited state and bremsstrahlung peaks are separated in the excitation spectrum. A complete evaluation of the recorded data is to be done, but a preliminary measured angular distribution of the 2_1^+ state of ^{96}Ru will be discussed in the next section.

9.6. Results

On top of the 2_1^+ excitation and ground-state decay and a γ-decay branch of the 2_1^+ state, other states were observed that directly or indirectly populate the 2_1^+ state. The energies of the states were determined by a fit of the electron scattering peak shape and assigned in Table 32 to the energies of known states decaying via the 2_1^+ state.

Table 32: Listing of measured peaks in the electron spectrum with excitation energies above the 2_3^+ and the associated known energies and angular momentum J and parity π. The data are taken from [70].

Fitted energy (MeV)	Known energy (MeV)	J^π
2.711(2)	2.73978(12)	(2^+)
2.925(4)	2.89761(13)	$3^{(+)}$
4.070(2)	4.05752(20) 4.08028(15)	(5,6) $(5,6,7)^+$

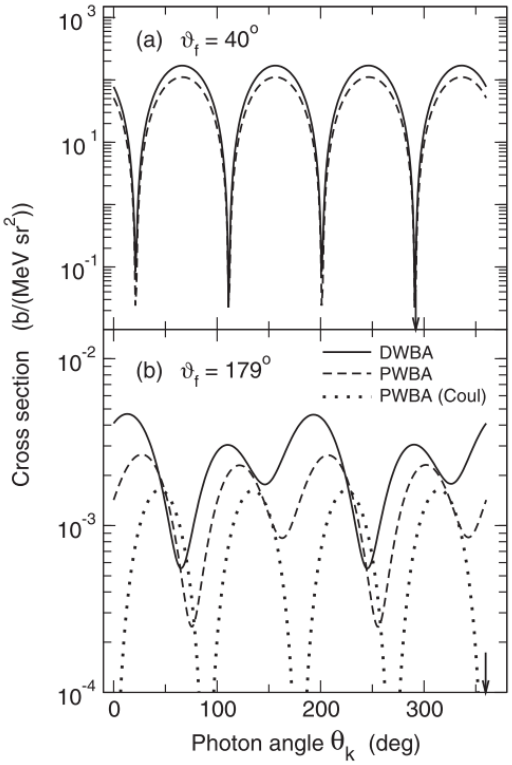

Figure 128: Comparison between PWBA and DWBA calculations for the 2_2^+ state in a ^{92}Zr(e,e'γ) reaction at a beam energy of 75 MeV and scattering angles of 40° (top) and 179° (bottom). Figure taken from [75]. Reprinted Figure 128 with permission from [75] Copyright 2022 by the American Physical Society.

As the number of protons increases, PWBA calculations become less accurate and DWBA calculations must be performed. However, Figure 128 shows that for conditions like those of the ^{96}Ru measurement the difference between PWBA and DWBA is small.

By gating on the excitation of the 2_1^+ state, the quadrupole pattern of the E2 transition to the ground state shown in Figure 129 could be observed. Table 33 lists the values of the calculated double differential cross sections and the scaled counts after efficiency correction. The quadrupole pattern of the E2 transition was successfully measured, demonstrating the ability of the (e,e'γ) setup to measure angular distributions.

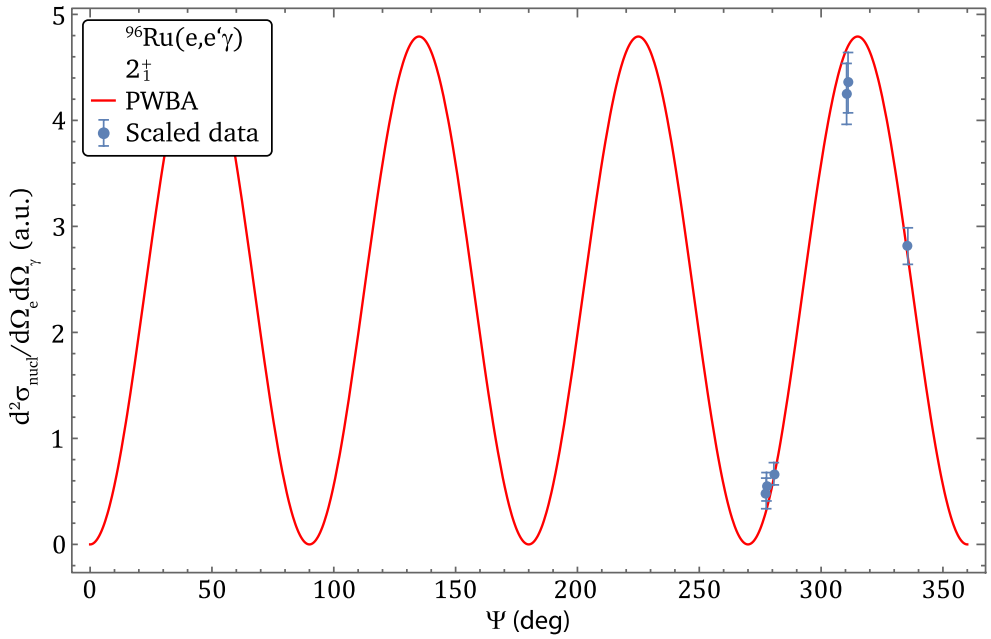

Figure 129: The measured counts in the LaBr$_3$:Ce detectors (blue dots) were scaled to the calculated angular distribution of the quadrupole pattern of the 2_1^+ state of ^{96}Ru (red line).

Table 33: Comparison of the calculated double differential cross sections of the 2_1^+ state of ^{96}Ru with the scaled counts in the LaBr$_3$:Ce detectors. The numbering of the detectors corresponds to the numbering from Table 24. The angles Ψ and Φ correspond to the angles in the coordinate system introduced in Figure 9.

Detector	Ψ (deg)	Φ (deg)	Calculated $\frac{d^2\sigma}{d\Omega_e\, d\Omega_\gamma}$ (a.u.)	Scaled counts
0	310.5	67.2	47	42(3)
1	335.6	0	27	28(2)
2	311.1	-67.7	47	44(3)
3	277.5	45.5	3.2	4.8(14)
4	280.6	0	6.2	6.7(10)
5	277.6	-44.6	3.2	5.4(13)

10. Discussion

A new setup for (e,e'γ) experiments was designed, constructed, commissioned and used for an initial physics run. Data from the LaBr and QCLAM data acquisitions were successfully merged and analyzed. This chapter presents simulations to estimate the expected background for future measurements, possibilities to extend the setup and the challenges of the coincident bremsstrahlung background.

10.1. Subtraction of Bremsstrahlung Background

A challenge in extracting the branching ratio of the 2_3^+ state of ^{96}Ru is the coincident background from bremsstrahlung, which cannot be corrected by the background subtraction described in Section 7.6. This is more evident from the γ-ray spectrum in Figure 130, which was produced using a gate in the electron spectrum on the excitation of the 2_3^+ state. The bremsstrahlung present in the γ-ray spectrum has the same energy as the photons from the decay to the ground state.

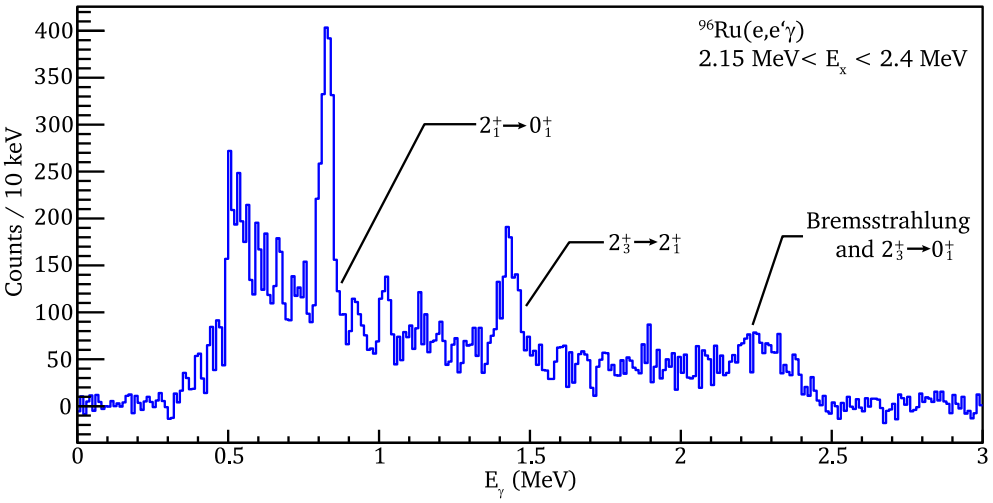

Figure 130: In the γ-ray spectrum with gate on the excitation of the 2_3^+ state of ^{96}Ru. The two peaks of the γ-decay cascade $2_3^+ \rightarrow 2_1^+ \rightarrow 0_1^+$ can be seen. The direct decay to the ground state with a branching ratio of about 7 % cannot be easily distinguished from the bremsstrahlung in this energy interval.

To illustrate the challenges of the background subtraction, a simple subtraction of the background is shown in Figure 131. The γ-ray spectra (blue) with gate on the excitation energy of the 2_1^+ state of ^{96}Ru (a) and the 2_3^+ state of ^{96}Ru (b) as well as pure background spectra with gates on smaller (green) and larger (red) excitation energy show a bremsstrahlung bump in the corresponding energy interval according to the gate used. Because of the different energies of the bremsstrahlung bumps, the background cannot be subtracted directly, but must be scaled to the energy of the gate of the state of interest as shown in (c) and (d). The corresponding bremsstrahlung corrected spectra are shown in (e) and (f). As can be seen in (f) at energies above 1.5 MeV, the bremsstrahlung bump and the associated detector response could be successfully subtracted. The difficulty of this background subtraction method is the use of the gates for the pure bremsstrahlung background, since it must be ensured that there are no contributions from the decay of excited states of the target in this region. The orange arrows in (a) and (b) mark peaks at the energies expected in the decay of the corresponding excited state for which the

bremsstrahlung is to be subtracted. This is due to the radiative tail of the electron scattering peak shape extending into the gate for the background at higher excitation energy, thus higher energy loss of the scattered electrons. To prevent this, a sufficiently large distance from the peak of interest must be used while avoiding to gate on another excitation of the nucleus. In the past, when evaluating a Lintott spectrum to calculate the peak area, the radiative tail in a 5 σ interval of the right half of the asymmetric Gaussian was used [179]. The peak pointed to by the orange arrow in (b) could also contain a contribution from neighboring states that also decay to the ground state via the 2_1^+ state. An indication of this is the low amplitude of the peak at 1.5 MeV that originates from the decay of the 2_3^+ state to the 2_1^+ state in the red histogram. In (a), the peak in the red spectrum has been shifted by scaling so that the peak area of the 2_1^+ state in the blue histogram is unaffected. The purple arrow in (a) and (c) points to a peak at an excitation energy of about 550 keV, possibly due to the 547 keV state of the ^{197}Au baking or an incomplete background subtraction as indicated by the negative counts next to it.

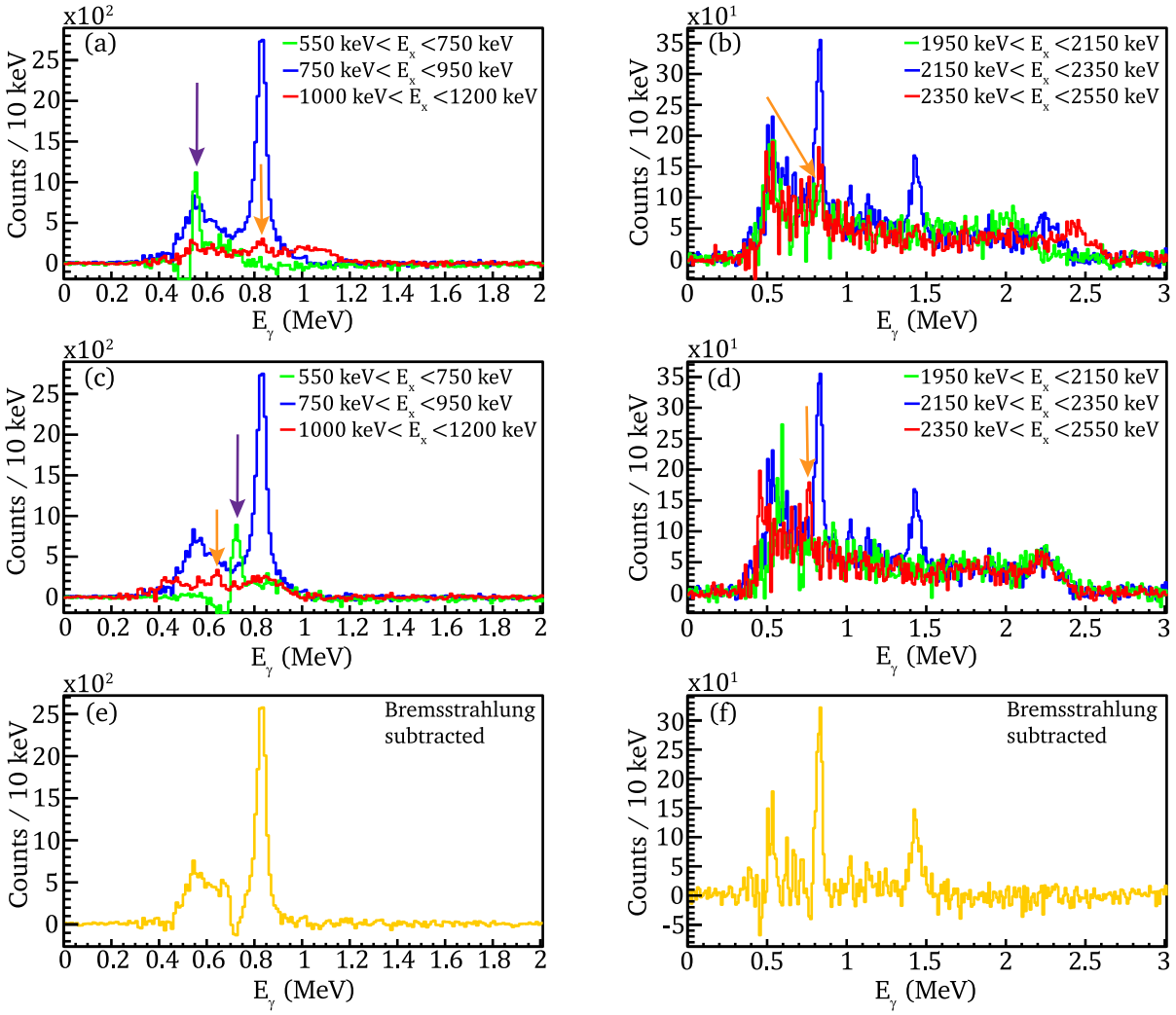

Figure 131: γ-ray spectra with gates on the excitation energy of the 2_1^+ state (a) and the 2_3^+ state (b) of ^{96}Ru. For the extraction of the bremsstrahlung, gates on smaller excitation energy (green) and on larger excitation energy (red) are used. In the next step, the obtained bremsstrahlung spectra are scaled to the energy of the gate on the peak of interest, as seen in (c) and (d). The bremsstrahlung corrected spectra are shown in (e) and (f). The arrows point to peaks in the bremsstrahlung spectra, illustrating the difficulty of this procedure.

Despite the low statistics, the ground-state branching ratio of the 2_3^+ state of ^{96}Ru is determined from the bremsstrahlung corrected spectrum in Figure 131 (f). The peak at 1.45 MeV corresponding to the $2_3^+ \rightarrow 2_1^+$ transition has a peak area of 986(42) counts, from which, taking into account the literature branching ratio of 7.2(9) [67] and the full energy efficiency of the $LaBr_3$:Ce detectors at the respective γ-ray energies, about 54(8) counts are expected for the ground-state transition of the 2_3^+ state. An integration of the γ-ray spectrum after subtraction of the bremsstrahlung in a FWHM interval (corresponding to 75 keV) around the $2_3^+ \rightarrow 0_1^+$ transition energy of 2.283 MeV gives 55(36) counts. The resulting branching ratio of this preliminary analysis is 7.3(45) % and is in good agreement with the previously measured value of 7.2(9) % even though the relative uncertainty is about 62 %.

A possible background subtraction method is the use of a two-dimensional model function $f_{\mathrm{brems}}(E_x, E_\gamma)$ for the description of the bremsstrahlung. This model can be benchmarked to energy regions where no nuclear excitations are present, i.e., of pure bremsstrahlung and thus describe the bremsstrahlung background of the nuclide to be investigated. This method, in combination with higher solid angle acceptance using more detectors, could allow the observation of weak ground-state decays and of isolated levels as well as the analysis of ground-state decays in the (quasi-)continuum region.

10.2. Simulations of Background Count Rates

Knowledge of the expected background in the $LaBr_3$:Ce detectors is helpful for planning future experiments. Therefore, further simulations were performed. An important factor in the planning of electron scattering experiments is the area mass density of the targets, which linearly affects the reaction rate of the state of interest, but also increases the background and reduces the energy resolution of the electron spectrum. The effect of area mass density on the background count rate in the $LaBr_3$:Ce detectors was simulated for area mass densities between 10 mg/cm^2 and 50 mg/cm^2 for the targets ^{12}C, ^{40}Ca, ^{96}Ru, ^{140}Ce, and ^{208}Pb. In the first order, the background count rate is expected to increase proportionally to the number of nuclei per area and thus to the thickness of the target. As can be seen in Figure 132, the results of the simulations show an additional quadratic component, so a second-order polynomial was fitted. For a ^{208}Pb target, the background is a factor of 6.9 larger when using a 50 mg/cm^2 target compared to the background caused by a 10 mg/cm^2 target. Illustrating the nonlinear increase in background count rate.

In further simulations, the influence of the energy of the electron beam on the background count rate in the $LaBr_3$:Ce detectors was investigated. The simulations were performed on ^{12}C, ^{40}Ca, ^{96}Ru, ^{140}Ce and ^{208}Pb targets of 20 mg/cm^2 area mass density. The decreasing background count rate can be explained by the $1/E_i^2$ dependence of the Mott cross section (see Equation (2.32) of elastically scattered electrons and the stronger focusing of the bremsstrahlung cone in the direction of the incoming electron beam. The results of these simulations are shown in Figure 133.

Another way to reduce background in γ-ray detectors is to use additional lead shielding elements to protect the detectors against the background from backscattered radiation from upstream of the target. For this purpose, two lead components were added, as shown in Figure 134, to provide additional suppression of background radiation. Simulations showed a reduction of the background up to 17(3) %. This shows that the experimental setup is already optimized for a low background count rate, as can be seen in Figure 106.

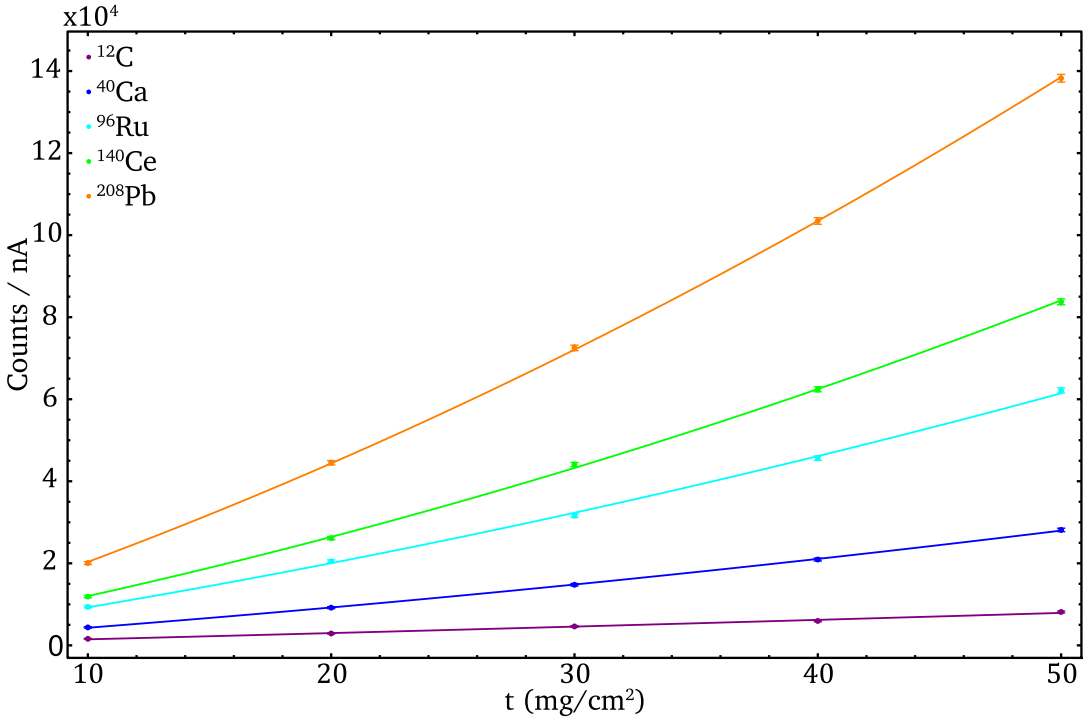

Figure 132: The background for different target materials increases with the thickness of the targets in the investigated interval. Plotted is the sum of the rates of the six detectors.

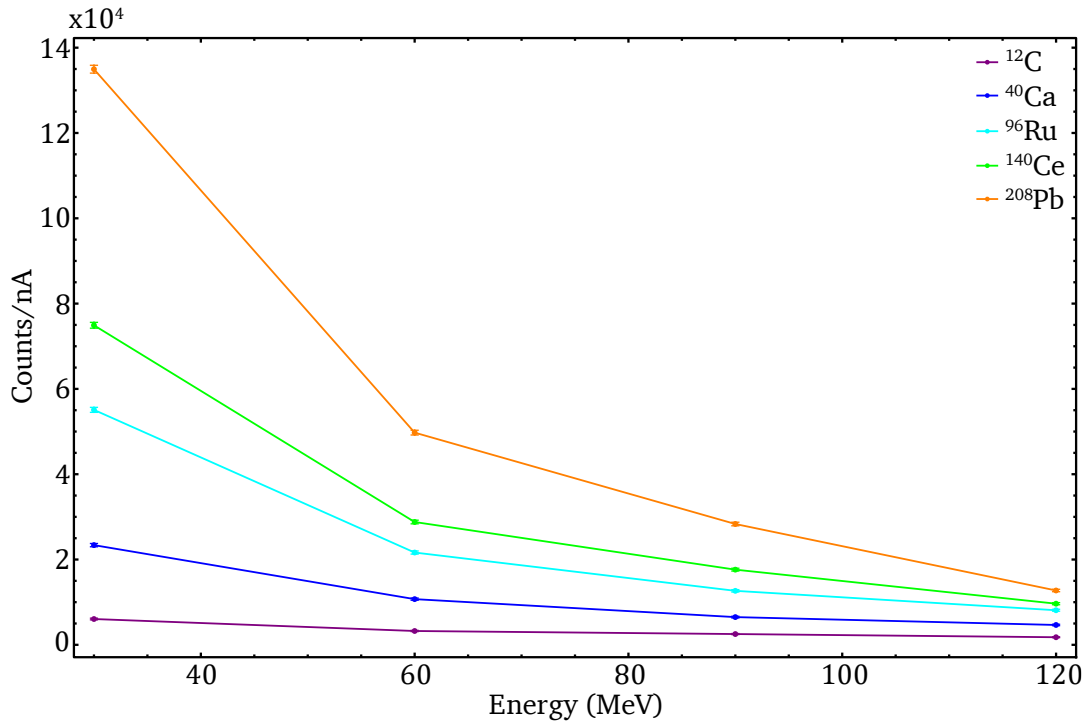

Figure 133: The background count rate in the $LaBr_3$:Ce detectors decreases as the energy of the electron beam increases. For the simulations, 20 mg/cm² targets corresponding to the alignment for a spectrometer angle of 47.5° were used. Plotted is the sum of the rates of the six detectors.

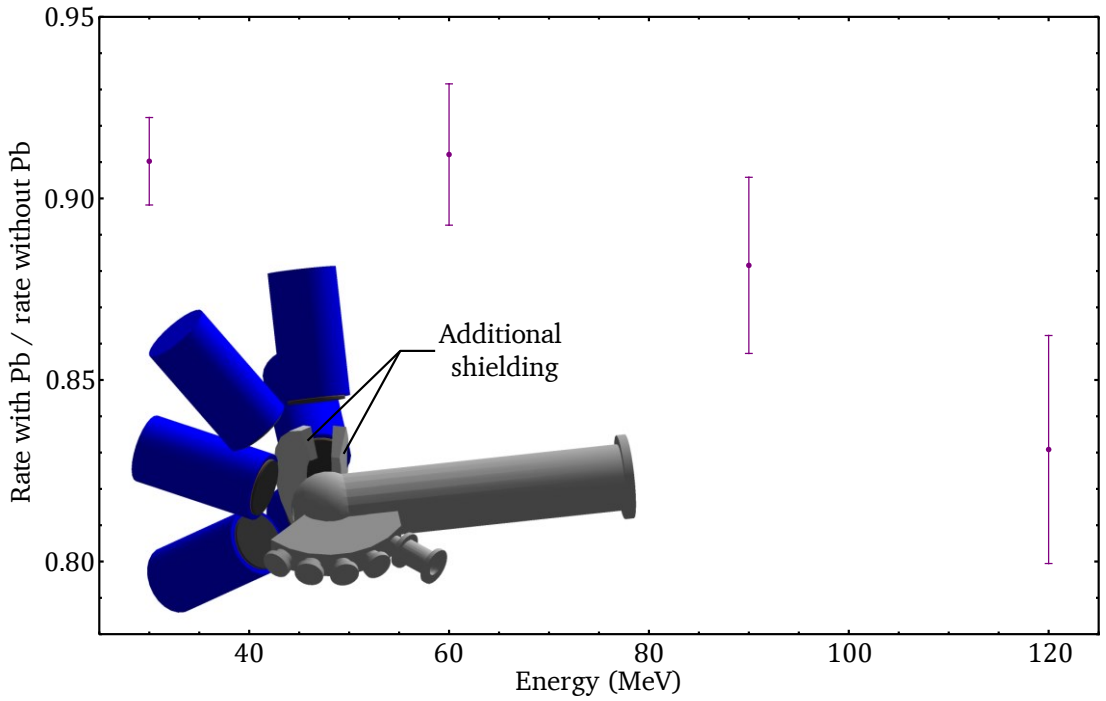

Figure 134: Adding lead shielding elements reduce the background marginally. Plotted is the sum of the rates of the six γ-ray detectors.

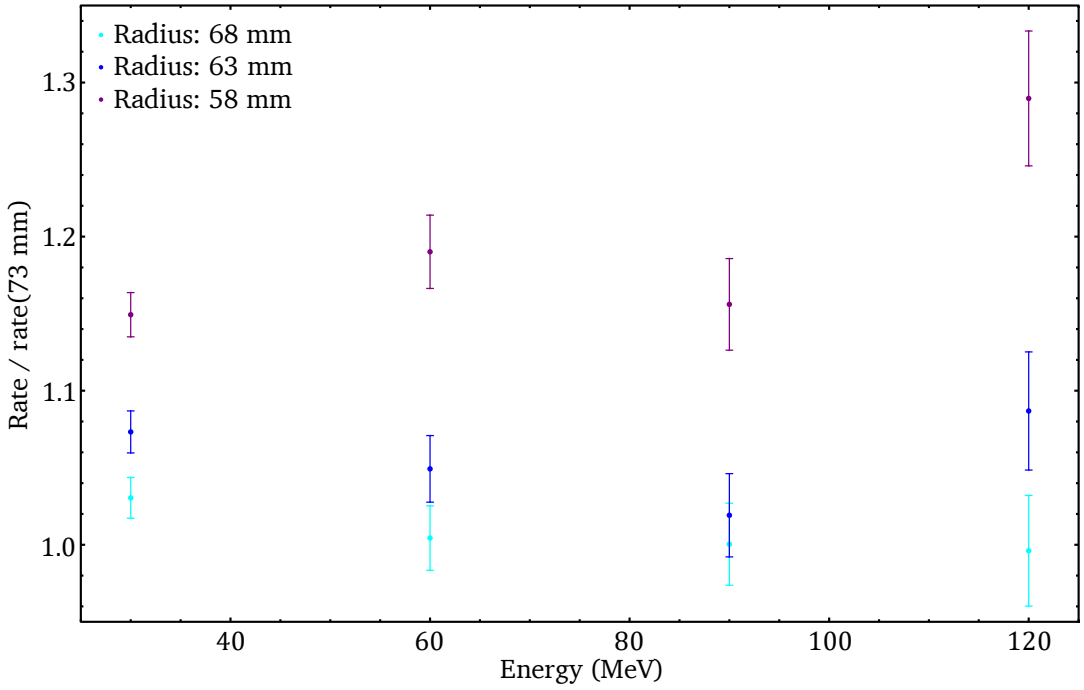

Figure 135: Reducing the radius of the lead shielding of the $LaBr_3$:Ce detectors by 5 mm, 10 mm, and 15 mm was investigated in simulations. Plotted is the sum of the rates of the six detectors.

Due to the cylindrical detector housings with a diameter of 166 mm, the number of $LaBr_3$:Ce detectors is geometrically limited. Reducing the diameter or using tapered detector housings can increase the number of detectors that fit in the existing two tower holding structures. To be able to reduce the radius of the detector housings, the thickness of the lead shielding in the housing must be reduced. The lead shielding consists of a hollow cylinder with an outer radius of 73 mm. The thickness of the cylinder wall is 30 mm at the crystal of the detector and

20 mm at the PMT. As can be seen in Figure 135, a 15 mm reduction of the wall thickness increases the background count rate by a maximum of 29(4) % at electron energies of 120 MeV.

10.3. Improvements of the Setup

The demonstrated reasonable increase in background count rates when reducing the thickness of the lead shielding of the detector housings by 15 mm would allow to increase the number of detectors per tower from three to five, as shown in Figure 136, providing per tower two additional data points for measurements of the angular distribution and increased efficiency. Subfigure (a) represents the geometry of the ^{96}Ru(e,e'γ) measurement discussed in Section 9.1, where the positioning of the $LaBr_3$:Ce detectors was further constrained by the stability required due to the high mass of the lead shielding. (b) the reduction of the lead shielding decreases the mass of the detectors by 2/3, so that the detectors can be positioned at steeper angles of 55° and closer to the target due to the smaller radii of the detector housings.

By using tapered detector housings, five detectors can be mounted in a single tower. The solid angle can be maximized by placing three detectors closer to the target (c). Alternatively, the detectors can be placed with equal distances to the target providing the same solid angle for each detector (d). The solid angle coverage for all configurations is listed in Table 34. Assuming ideal conditions, the solid angle could be increased by a factor of 2.43 with respect to configuration (a).

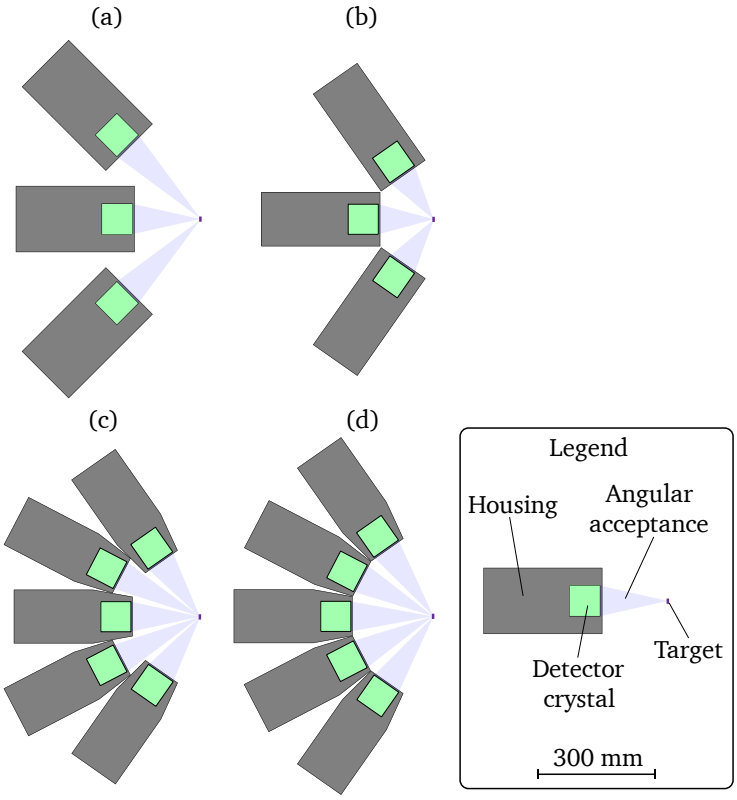

Figure 136: Side view of the detectors in a tower. (a) Geometry for use with the original lead shields of the $LaBr_3$:Ce detectors. (b) Reducing the thickness of the lead shielding in the detector housings allows to move the detectors closer to the target. (c) The additional use of tapered designs allows the detectors to be brought closer to the target. (d) Alternative geometry with tapered design and equal distances between the detectors and the target.

Table 34: Summed solid angles of the detectors in a tower for the geometries shown in Figure 136.

Geometry	Solid angle (%)
(a)	2.3
(b)	5.6
(c)	5.0
(d)	4.2

To obtain additional measurement points over a larger angular interval and to increase the solid angle, the modular design can be extended to include another tower between the QCLAM spectrometer and the beamline at a horizontal scattering angle of 145° as shown in Figure 137. This would allow to use three towers with angular offsets of 55° and 70° in the scattering plane providing a larger interval for measurements of angular distributions. The addition of detectors to the setup will require upgrading the readout electronics. In particular, the increased data rate may lead to an increase in dead time. In this case either the length of the trace must be reduced or the SIS3316 module must be read out via the network connector in the front of the module to bypass the data transfer bottleneck of the VME bus.

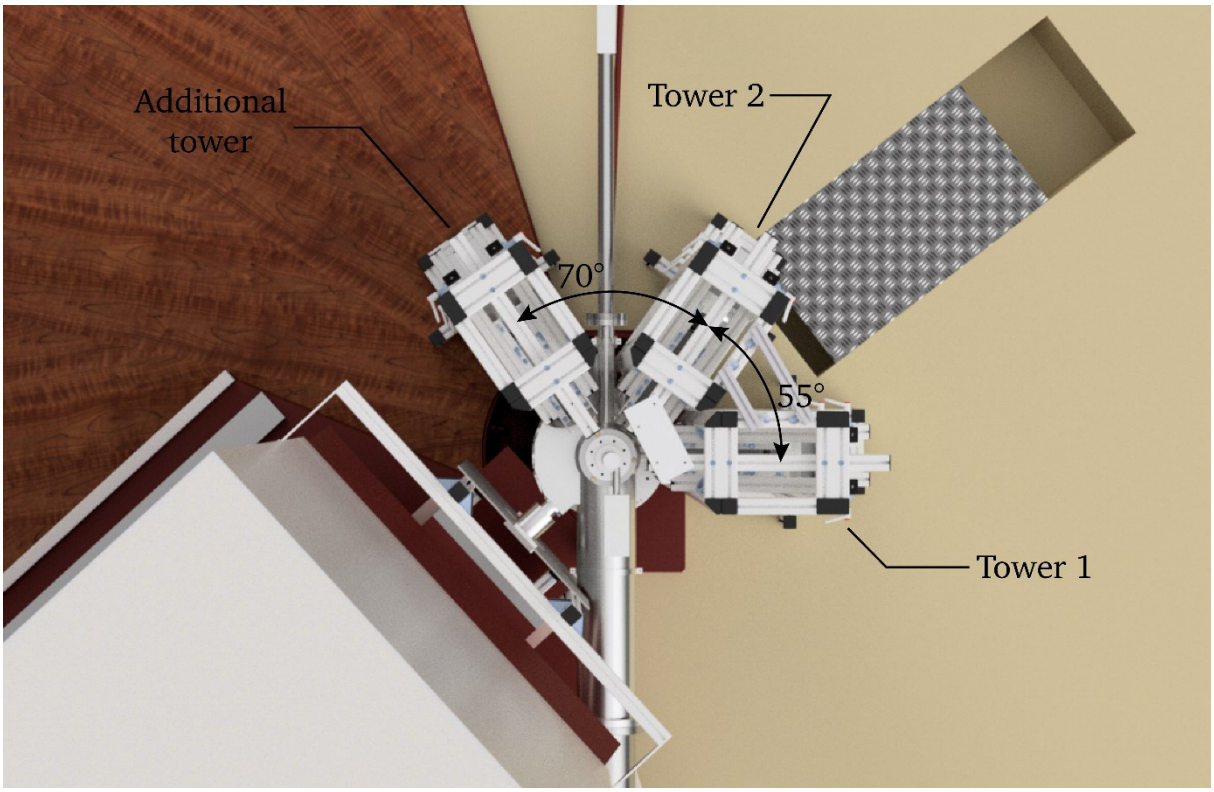

Figure 137: Top down view on the (e,e'γ) setup. The modular design allows the extension by adding detector towers to increase the number of detectors. A suitable location for an additional detector tower is between the QCLAM spectrometer and the beamline.

11. Summary and Conclusion

In this work, a new (e,e'γ) setup at the S-DALINAC was designed, constructed, commissioned and used for first nuclear structure measurements. It represents a novel tool for future nuclear physics investigations and enables (e,e'γ) coincidence measurements at the S-DALINAC for the first time. Furthermore, the new setup is the first setup for coincidence measurements utilizing the new QCLAM data acquisition. Future exclusive electron scattering experiments such as the planned electro-fission experiment in the LOEWE cluster project ELEMETNS will benefit from the developments and achievements of this work.

Data from the QCLAM and LaBr DAQs of the ^{12}C(e,e'γ) commissioning experiment were combined into an electron-γ coincidence data set and analyzed. The time difference spectra of the measurements of the 2_1^+ and 1_2^+ states of ^{12}C showed a distinct coincidence peak, and both were observed in the E_γ-E_x matrix. This demonstrated the functionality of the coincidence DAQ.

To improve the setup, a new scattering chamber, which is optimized for low background count rates in the $LaBr_3$:Ce detectors, was designed based on experience from the ^{96}Ru test experiment and GEANT4 simulations. This made the successful ^{96}Ru(e,e'γ) measurement possible, which represents the first (e,e'γ) measurement of a nucleus with charge number larger than $Z = 8$, where isolated states decaying to the ground state via the 2_1^+ state were observed at excitation energies below the neutron separation threshold. An evaluation of the excitation and subsequent ground-state γ-decay of the 2_1^+ state provided an angular distribution consistent with the expected quadrupole pattern of the E2 transition. This clearly demonstrated the ability of the setup to measure angular distributions. At excitation energies above the neutron separation threshold, peaks in the low-energy part of the γ-ray spectrum were observed and assigned to the depopulations of low-lying states of ^{95}Ru. This potentially provides a method to study the neutron emission channel of ^{96}Ru.

By using new developments like the $LaBr_3$:Ce detectors, a FWHM time resolution of 1.9 ns was achieved. This is an improvement of a factor of 10 compared to the 20 ns time resolution of the first (e,e'γ) measurement [22], resulting in an increased peak-to-background ratio in the time difference histograms. The measured time resolution of the new (e,e'γ) setup is close to the time resolution of the detector system of the QCLAM spectrometer, which therefore is the limiting factor. This will be improved within the scope of the upcoming electro-fission project by segmenting the scintillator of the QCLAM detector system to achieve time resolutions of 120 ps [180].

The modular design of the (e,e'γ) setup allows to increase the number of detectors for future measurements to provide more data points for angular distributions and increase the efficiency of the setup. By adding a tower and increasing the number of detectors per tower from three to five, up to 15 detectors could be used. To read out this number of detectors, an extension of the readout electronics is required.

The coincident background caused by bremsstrahlung makes (e,e'γ) measurements of ground state transitions challenging. In particular, low-intensity transitions are difficult to observe. To separate the bremsstrahlung background from γ-decays of excited nuclei, a new method for background subtraction will be developed in the near future.

The established setup is ready for future (e,e'γ) measurements. For 2023, an experiment on ^{140}Ce is planned to study dipole excitations such as the PDR and the GDR. To distinguish these excitation modes from higher-order multipoles (E2, M2, …) a coincident measurement of the scattered electrons and the ground-state γ-ray decay is exploited.

Closely related is the study of the toroidal dipole mode in ^{24}Mg(e,e'γ) [181] and ^{58}Ni(e,e'γ) [182] reactions. Unlike other E1 modes, toroidal modes are predicted to have a negative relative sign for longitudinal and transverse form factors, which is accessible by the measurement of their interference term in the (e,e'γ) experiments.

12. Appendix

12.1. (e,e'γ) Scattering Chamber

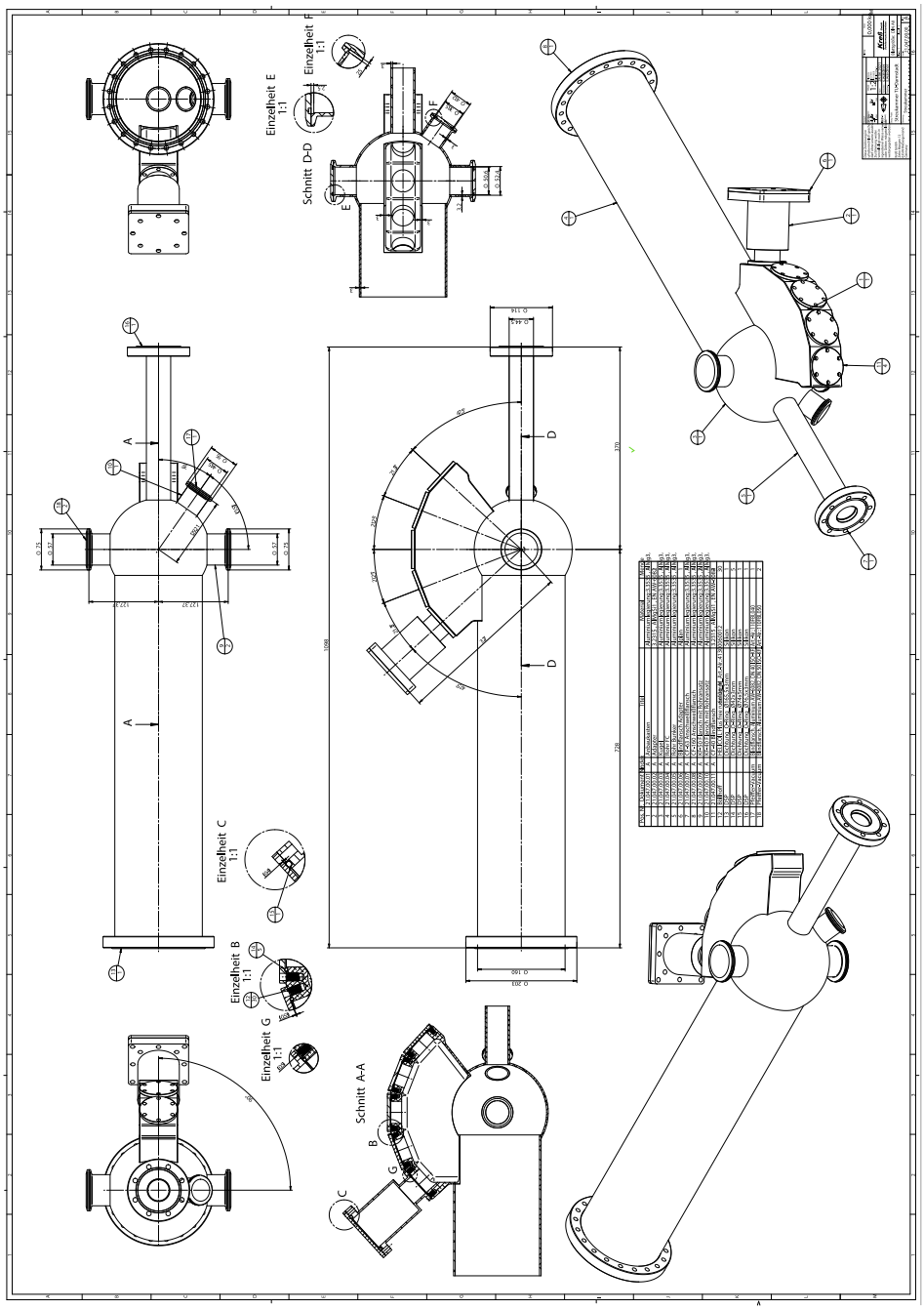

Figure 138: Technical drawing of the new scattering chamber.

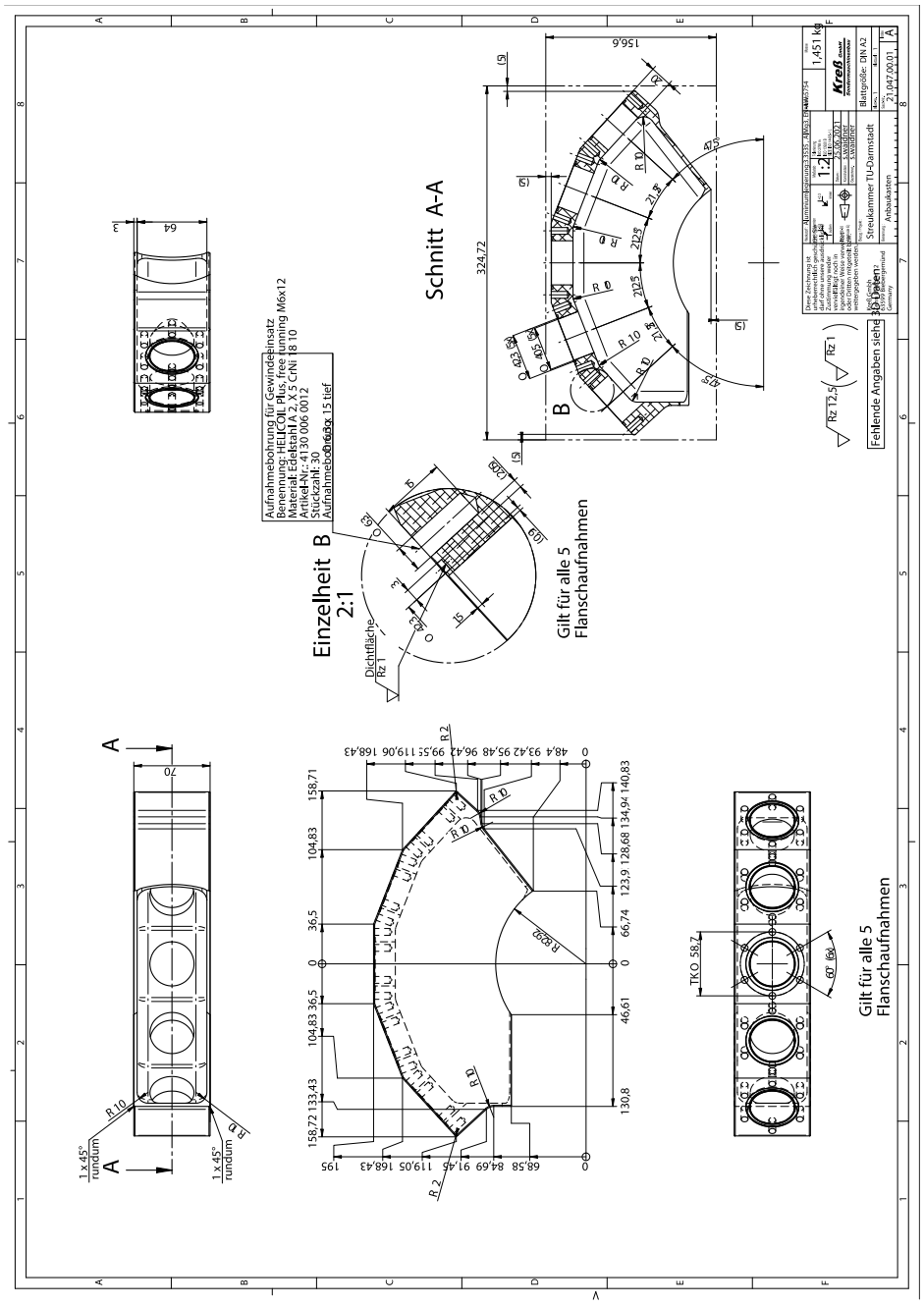

Figure 139: Technical drawing of the new scattering chamber.

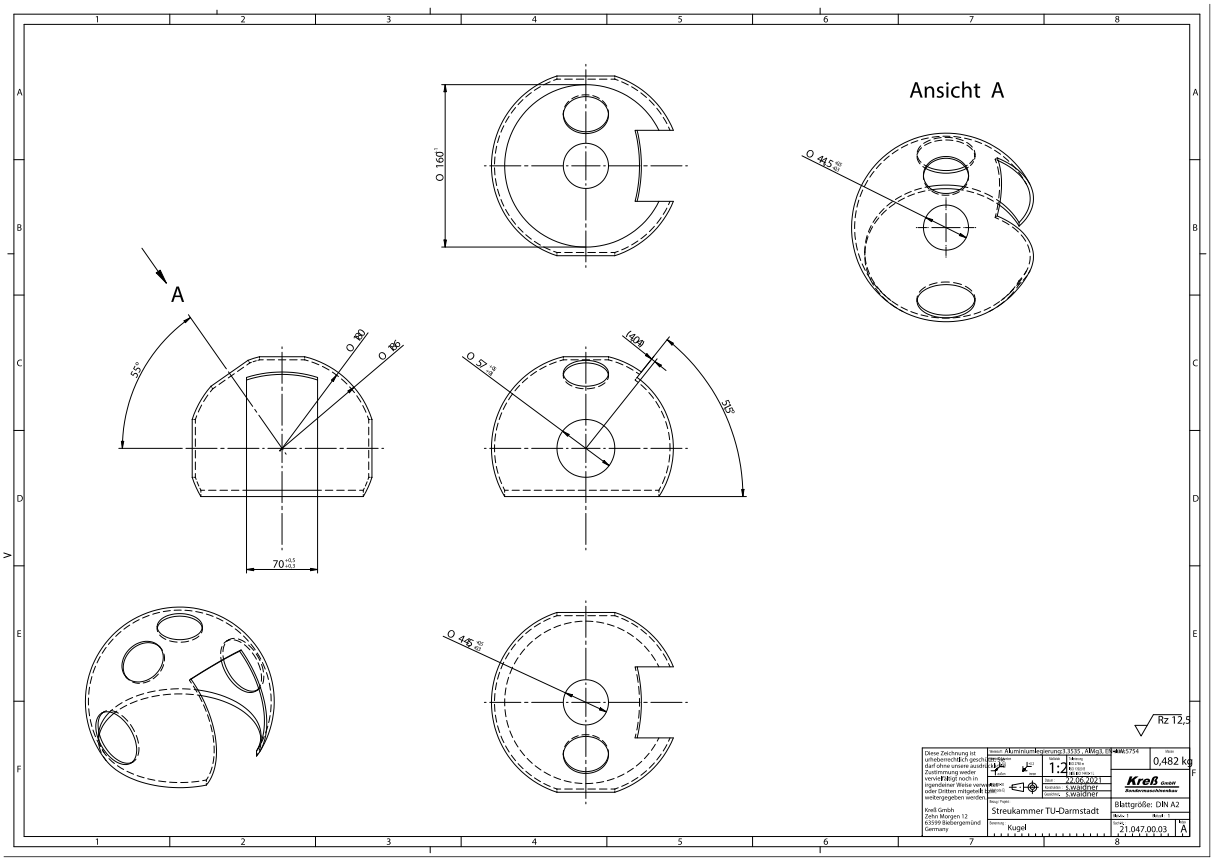

Figure 140: Technical drawing of the new scattering chamber.

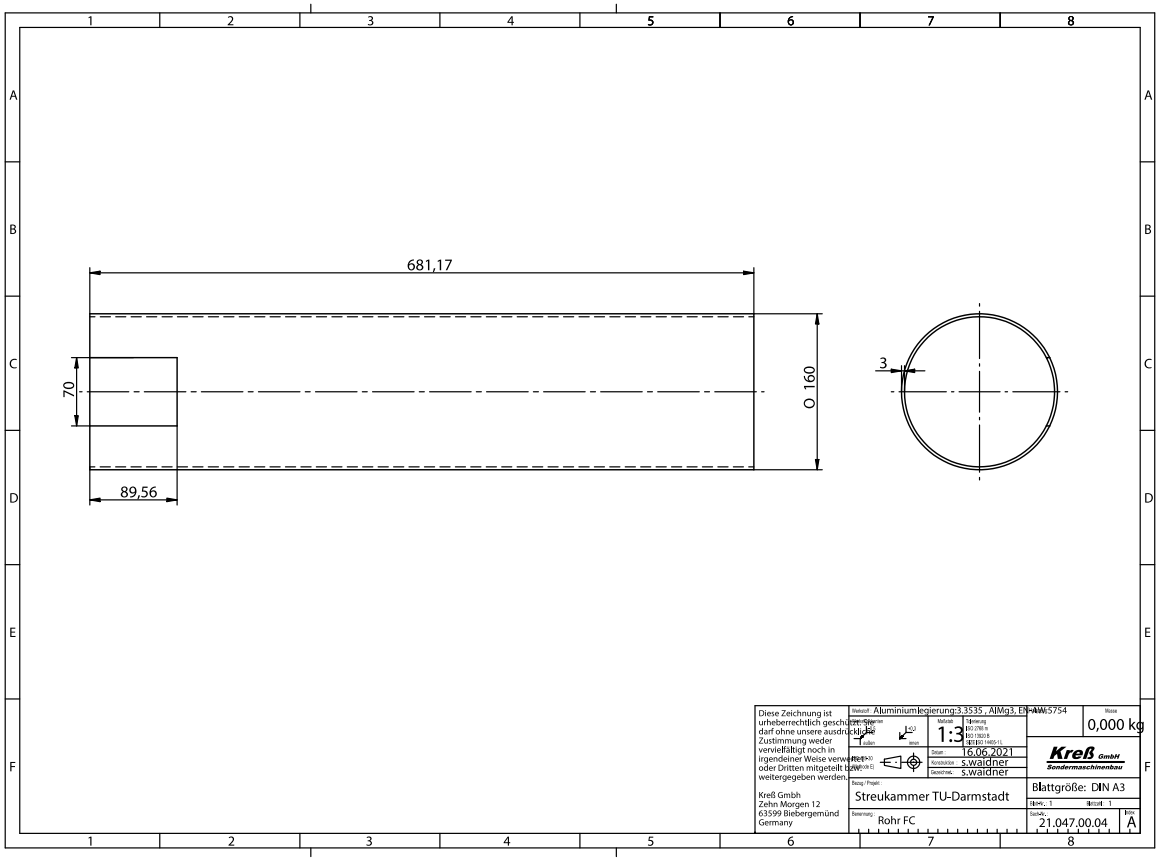

Figure 141: Technical drawing of the new scattering chamber.

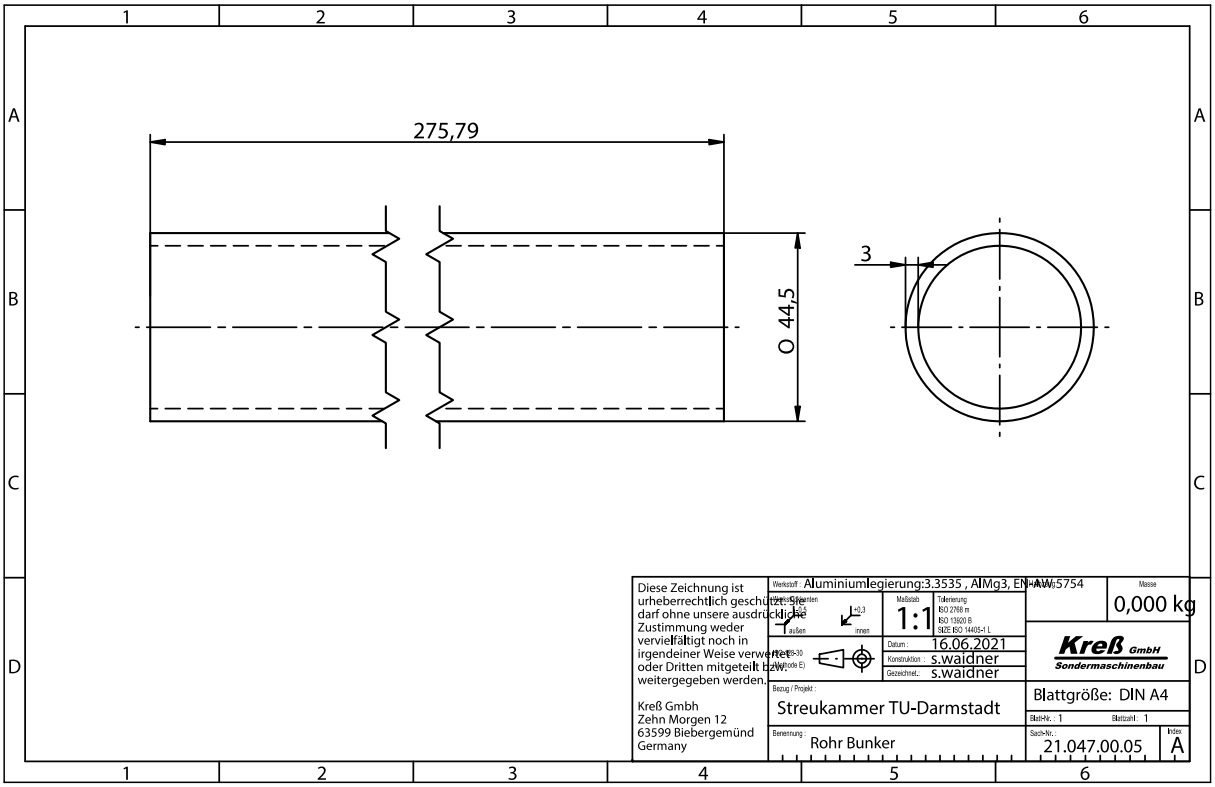

Figure 142: Technical drawing of the new scattering chamber.

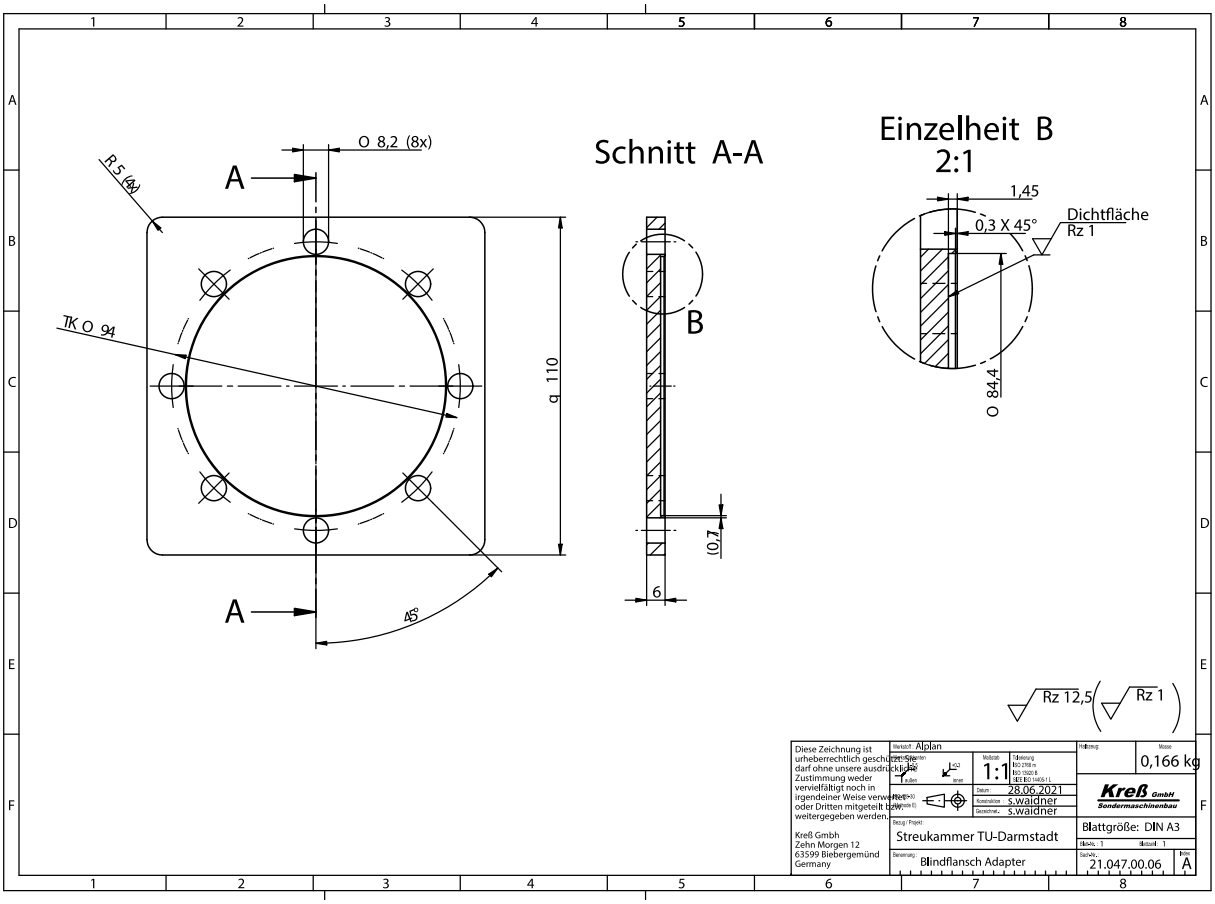

Figure 143: Technical drawing of the new scattering chamber.

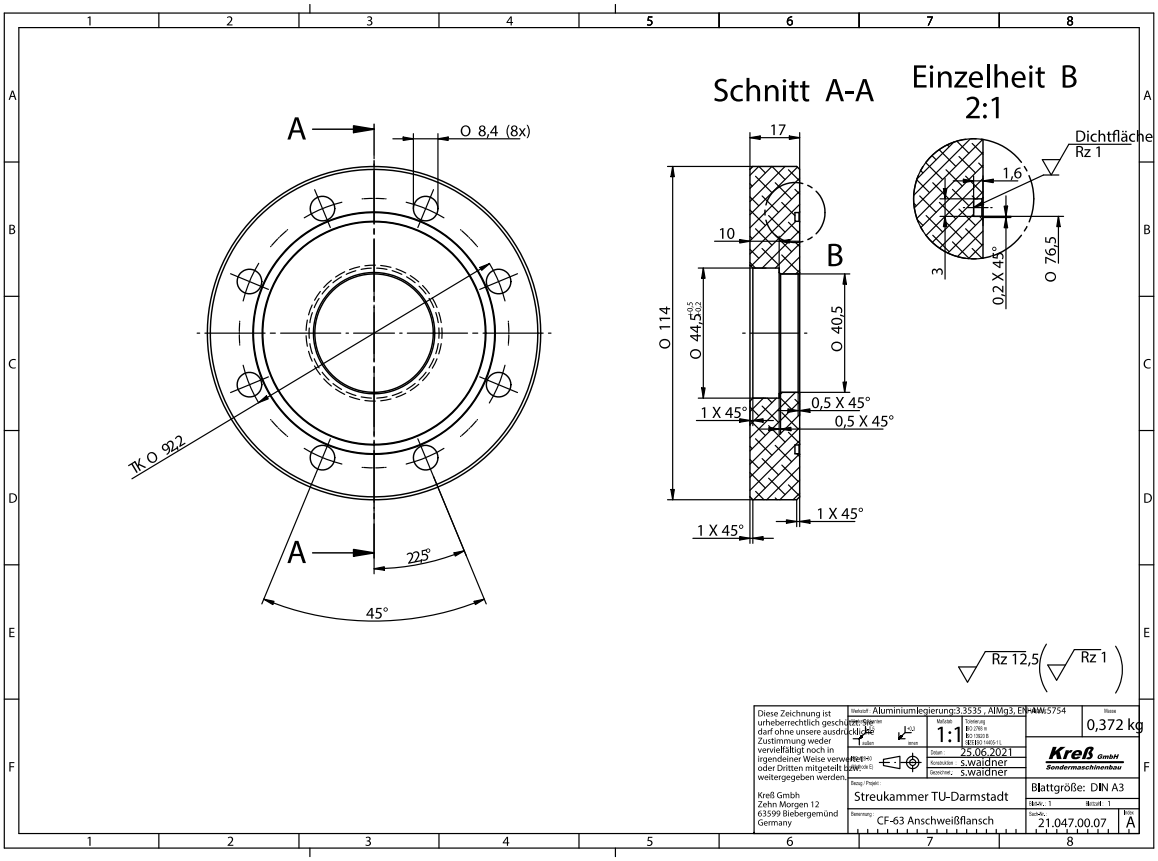

Figure 144: Technical drawing of the new scattering chamber.

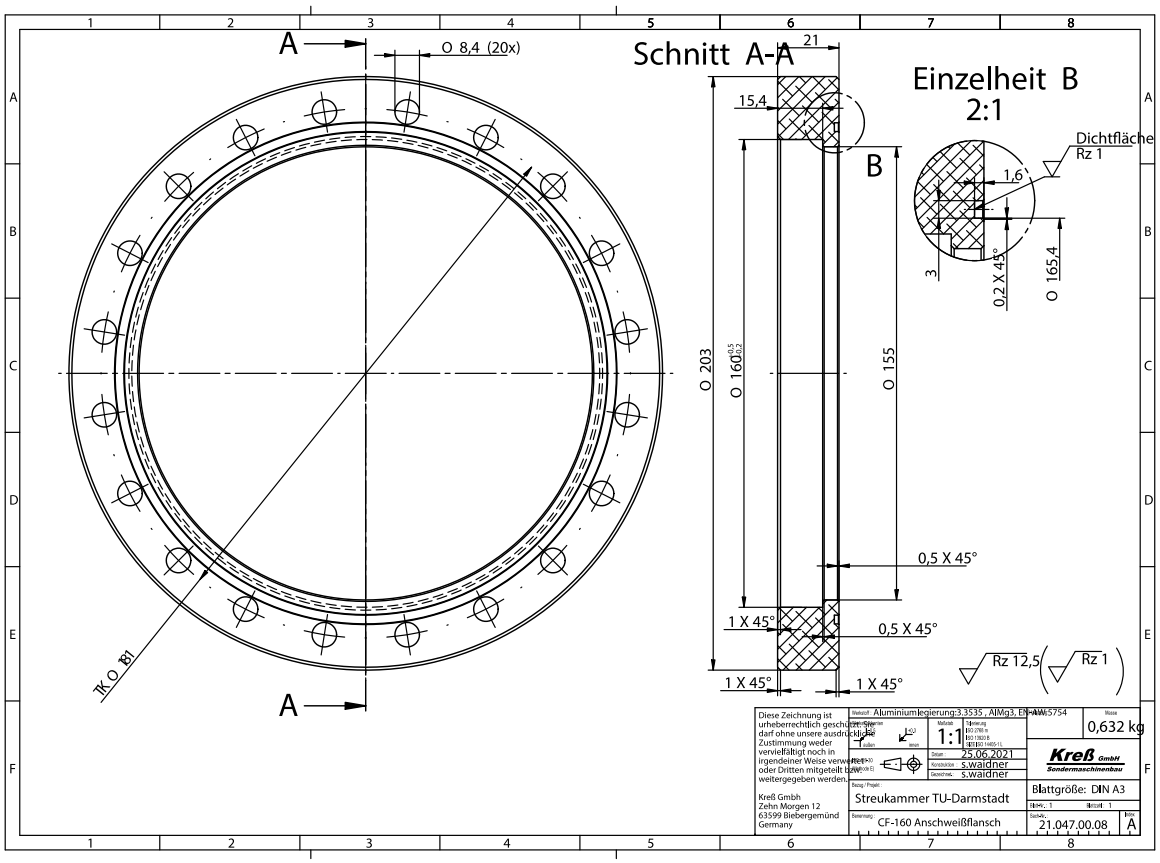

Figure 145: Technical drawing of the new scattering chamber.

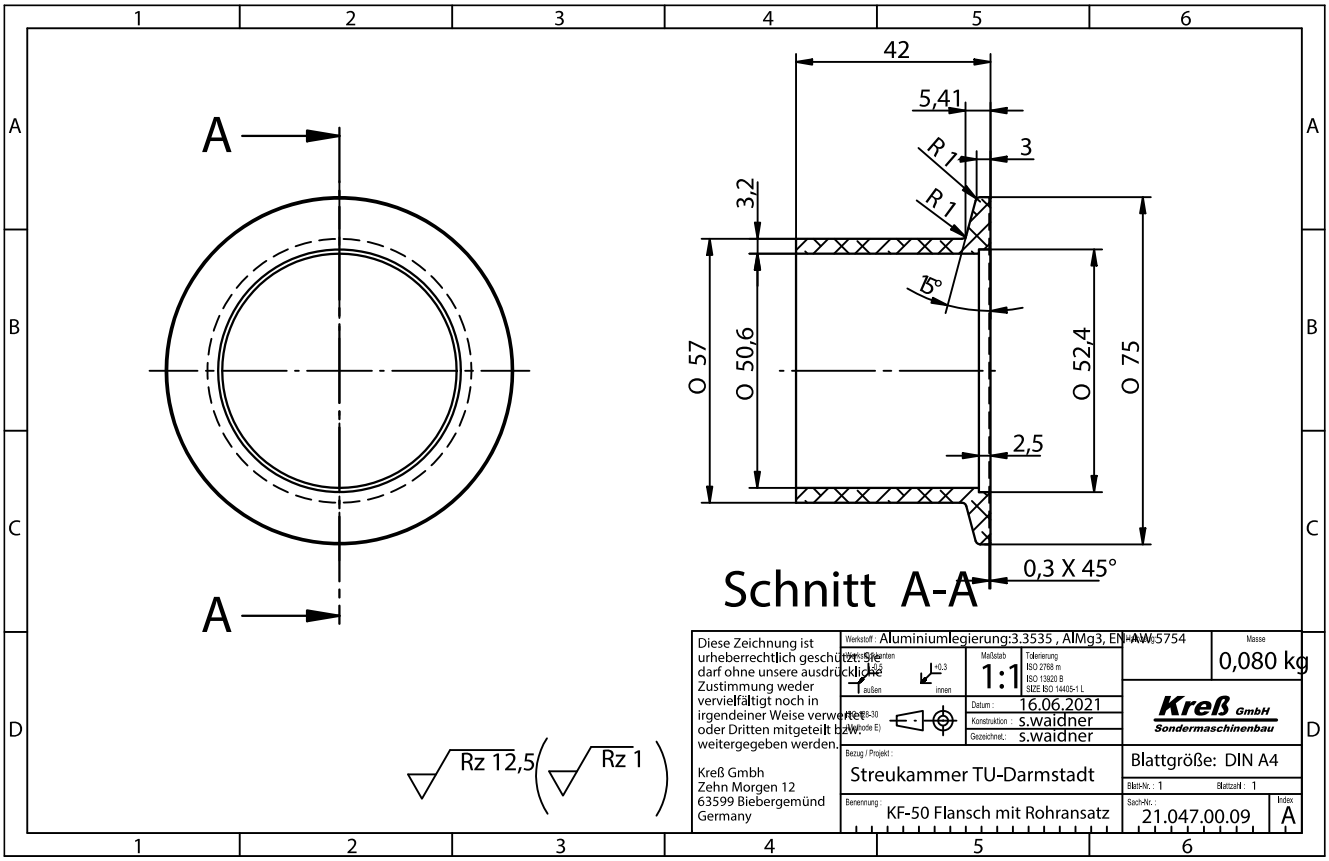

Figure 146: Technical drawing of the new scattering chamber.

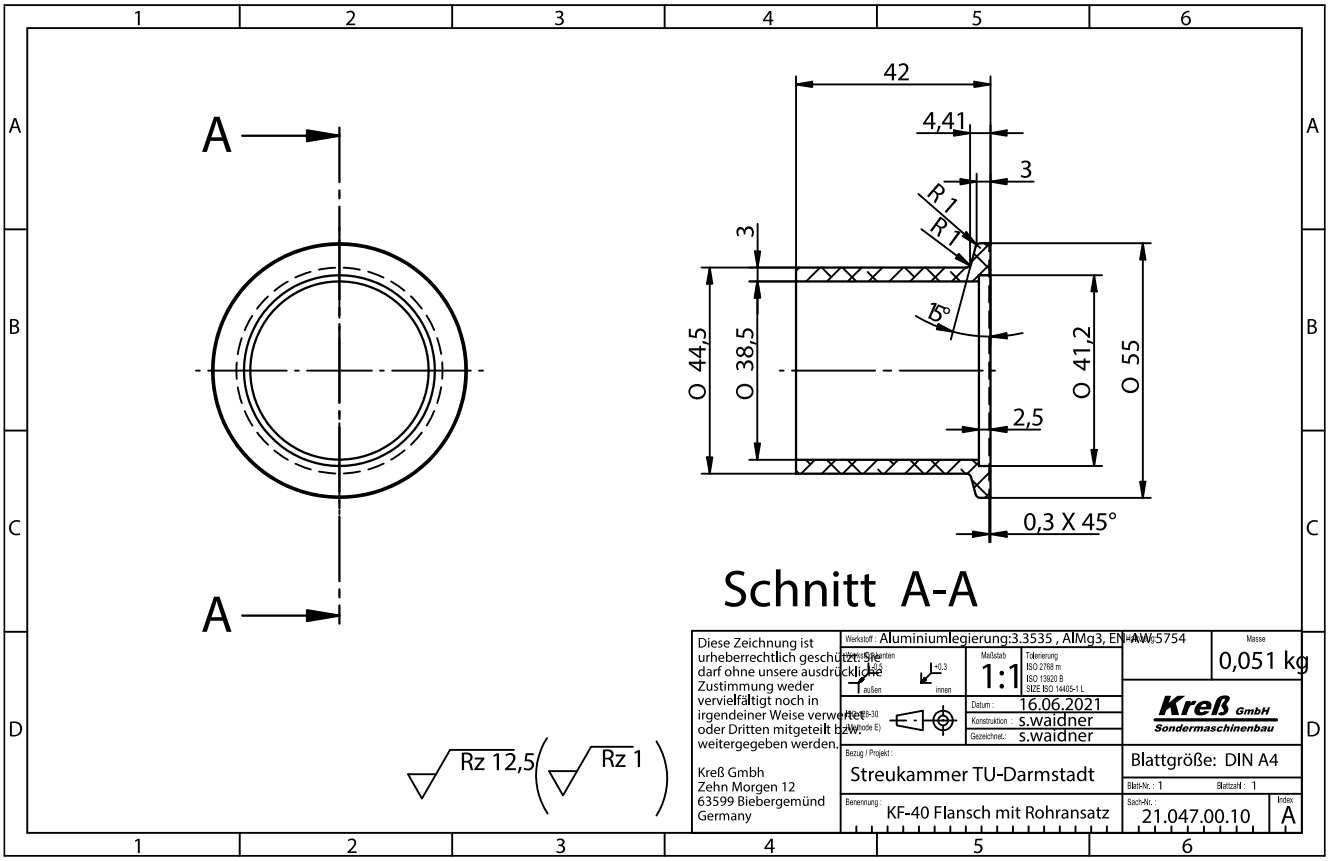

Figure 147: Technical drawing of the new scattering chamber.

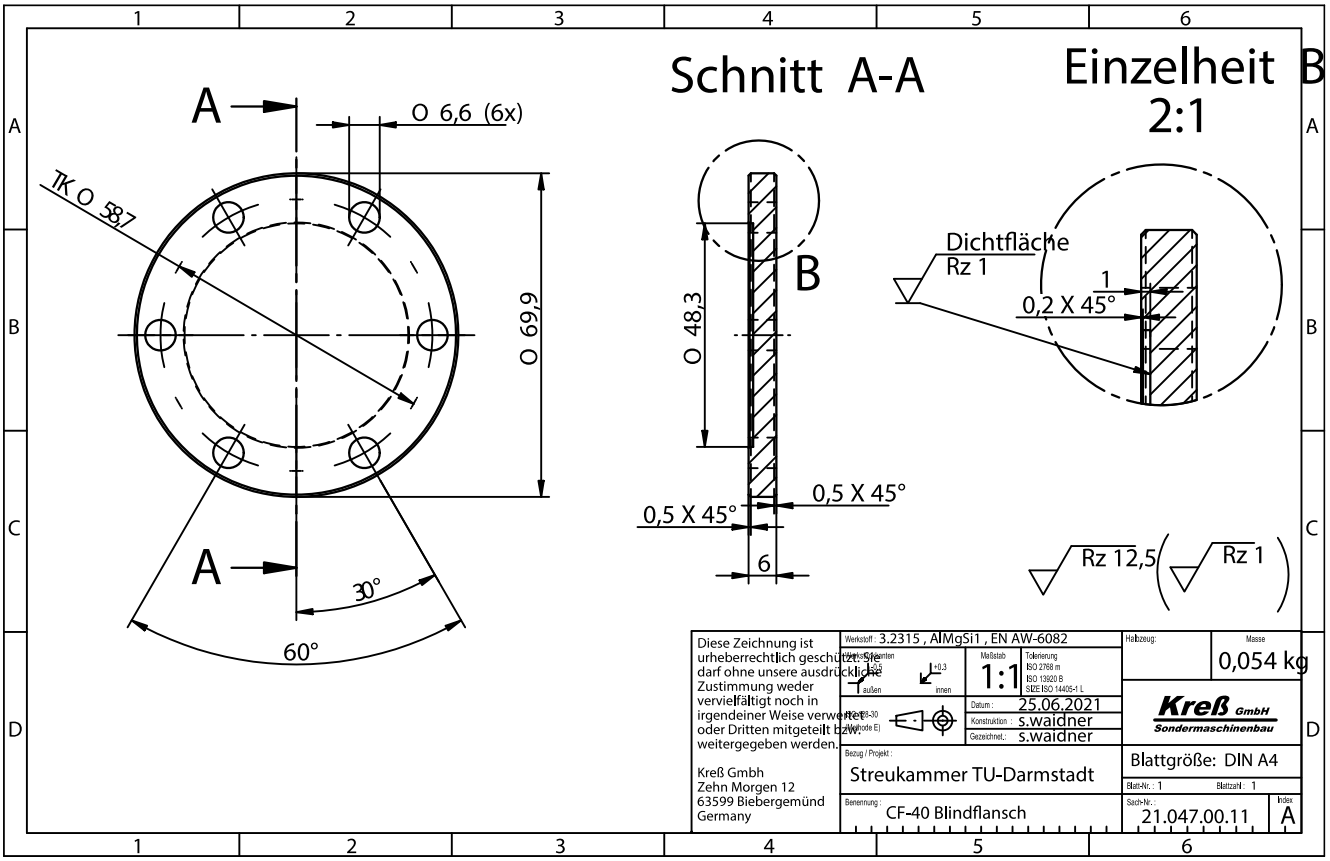

Figure 148: Technical drawing of the new scattering chamber.

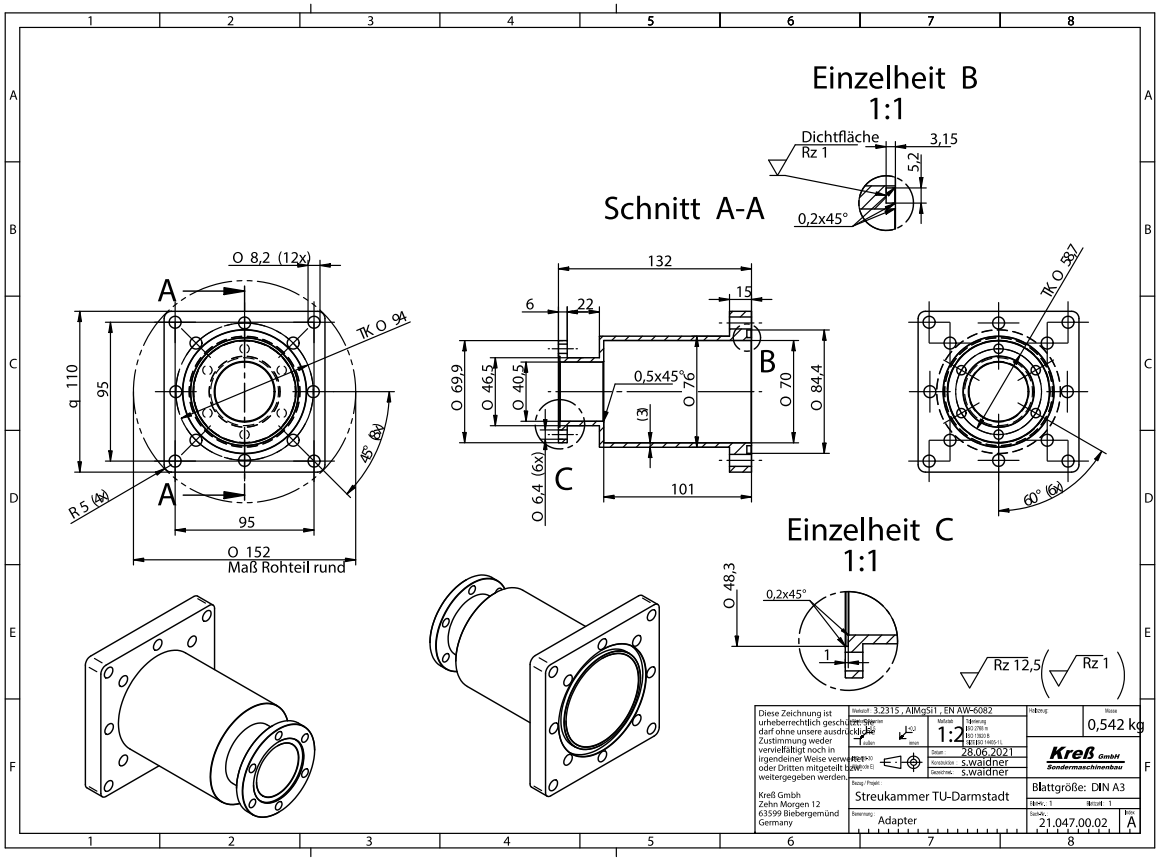

Figure 149: Technical drawing of the new adapter.

12.2. Target Ladder and Target Frames

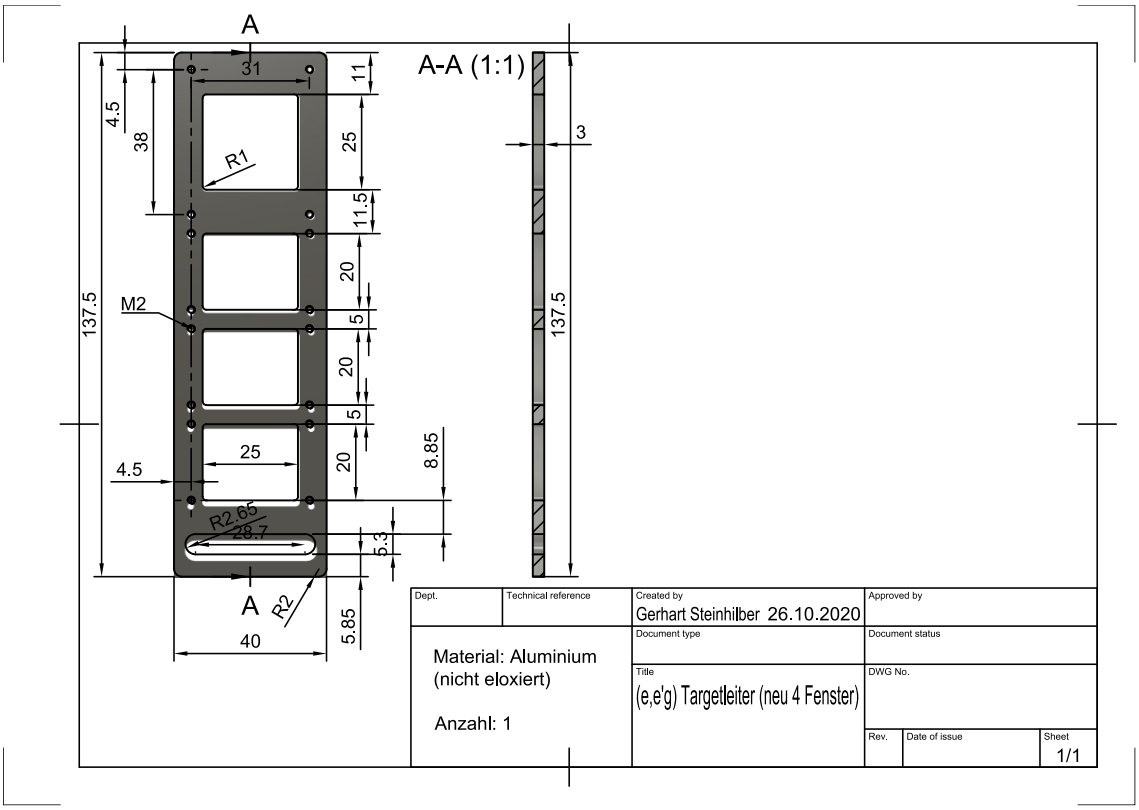

Figure 150: Technical drawing of the target ladder.

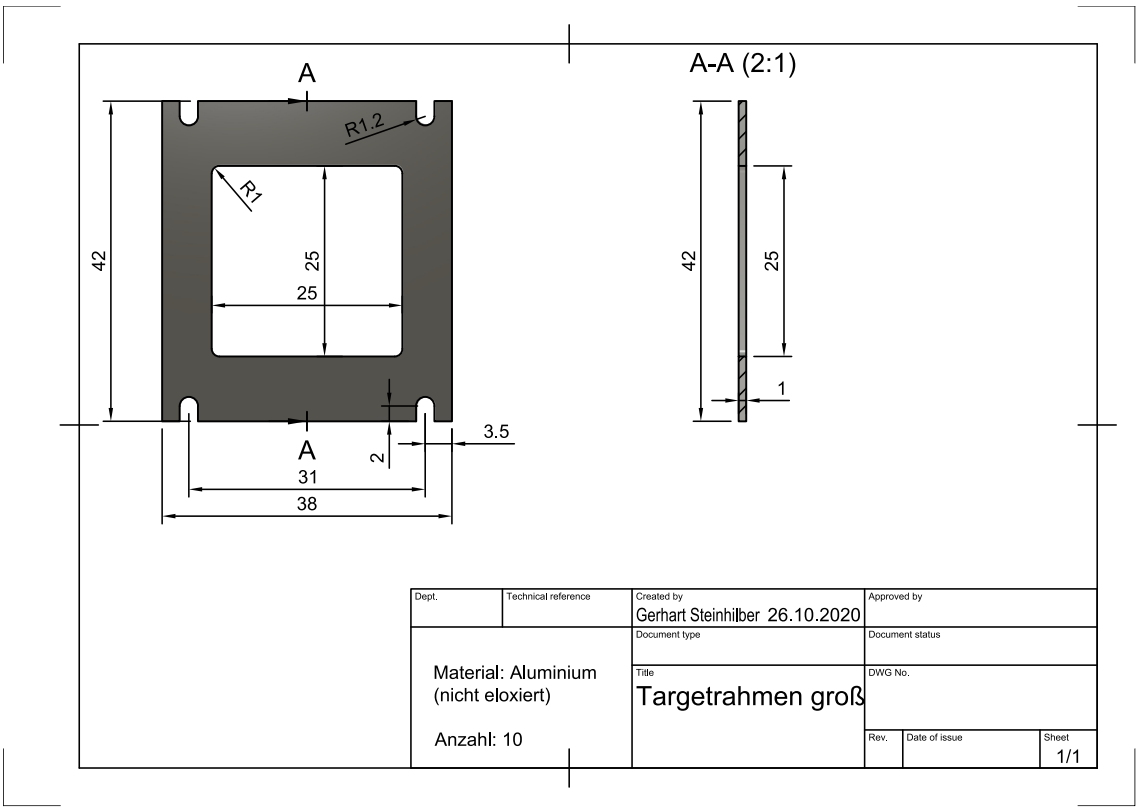

Figure 151: Technical drawing of the large target frame.

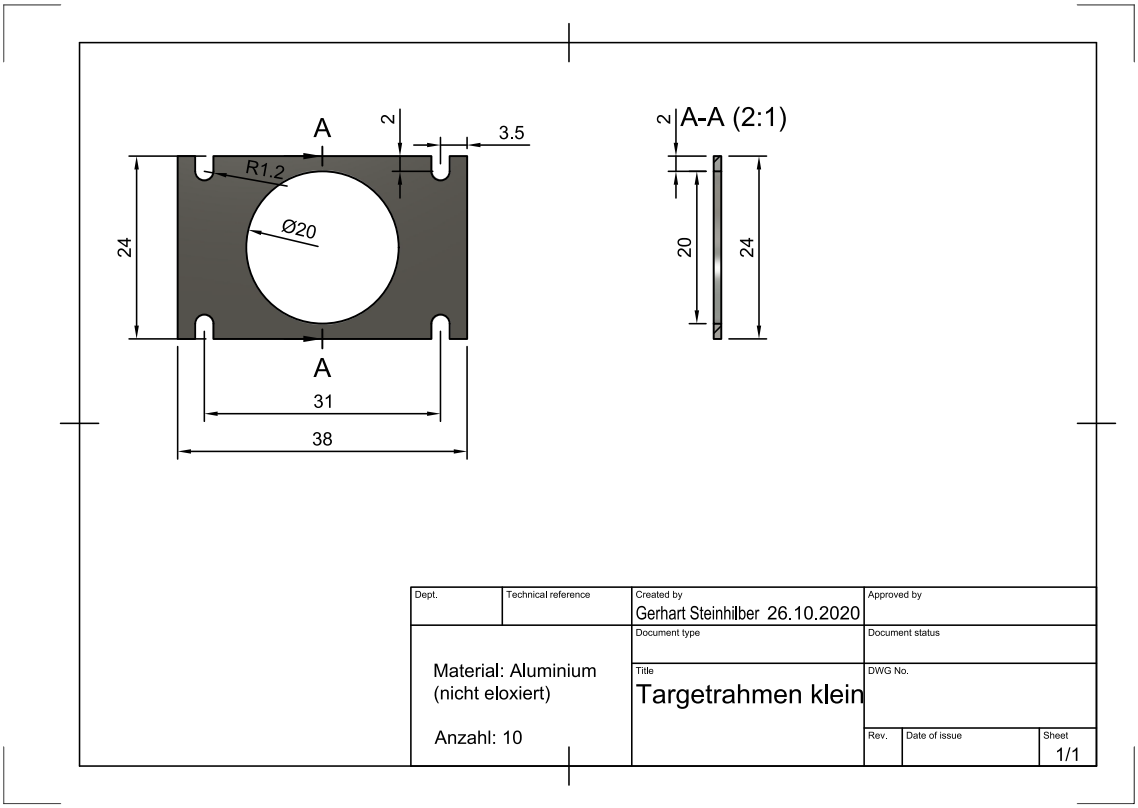

Figure 152: Technical drawing of the small target frame.

12.3. Scattering Chamber Mount

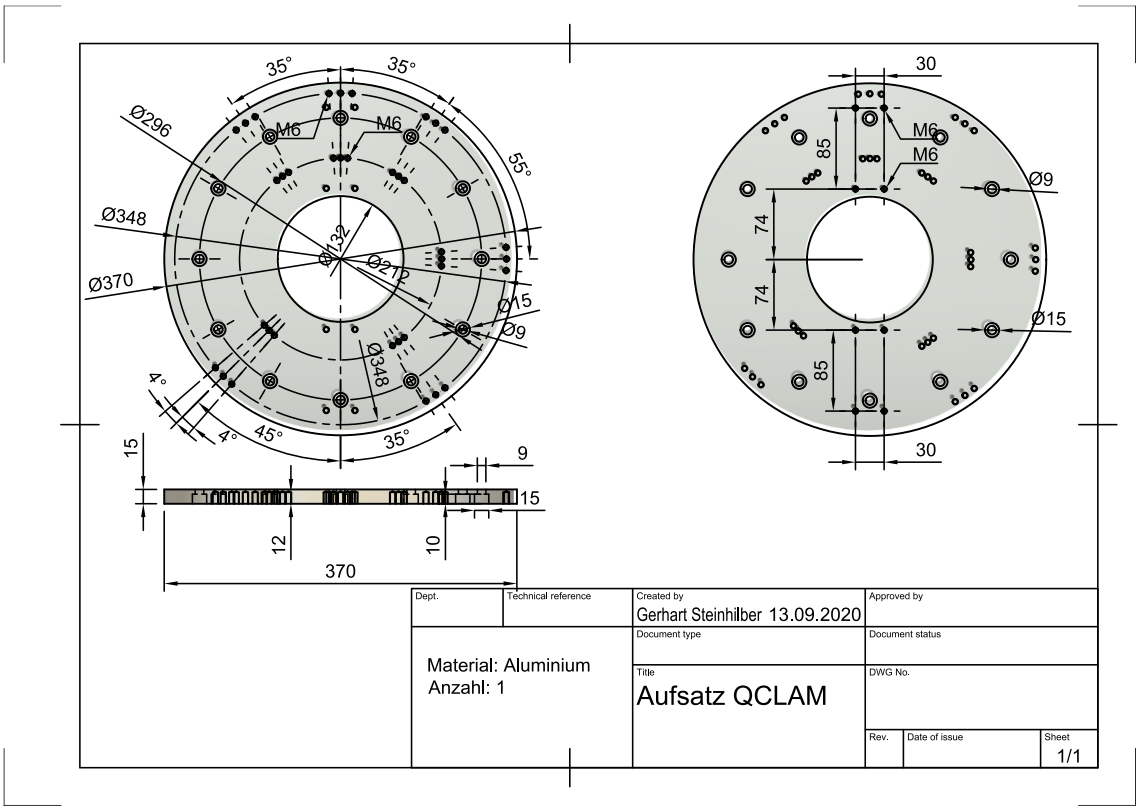

Figure 153: Technical drawing of the attachment for the rotation center of the QCLAM spectrometer.

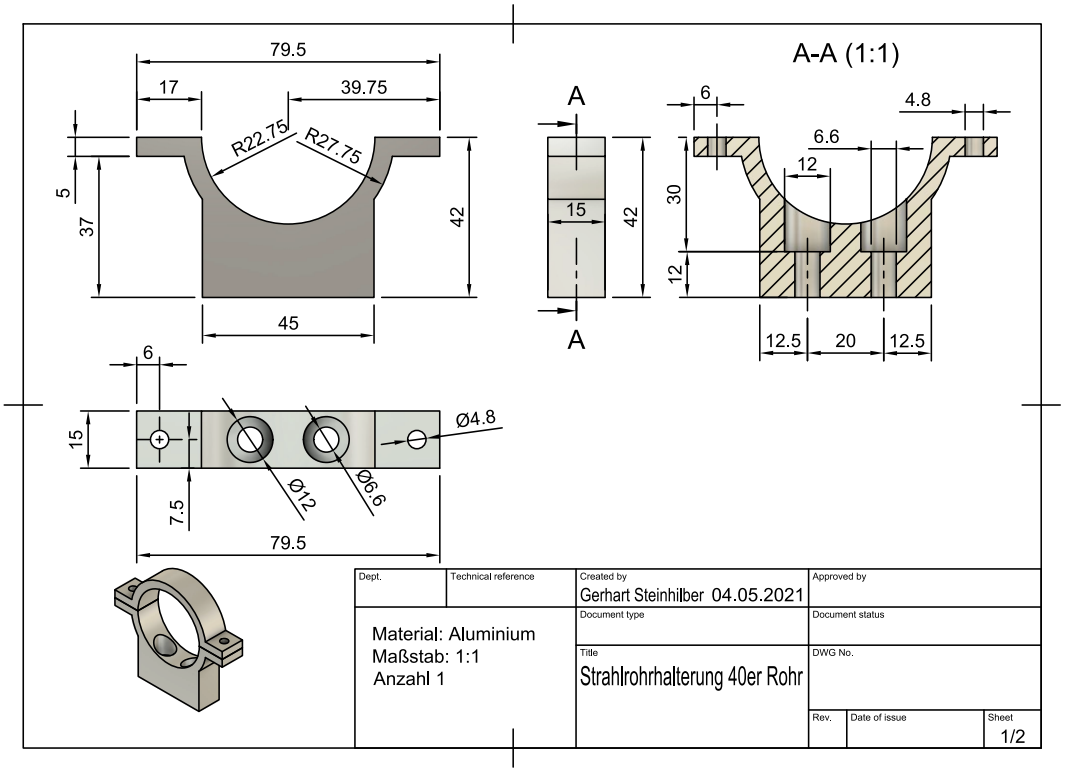

Figure 154: Technical drawing of the lower half of the small beam pipe holding clamp.

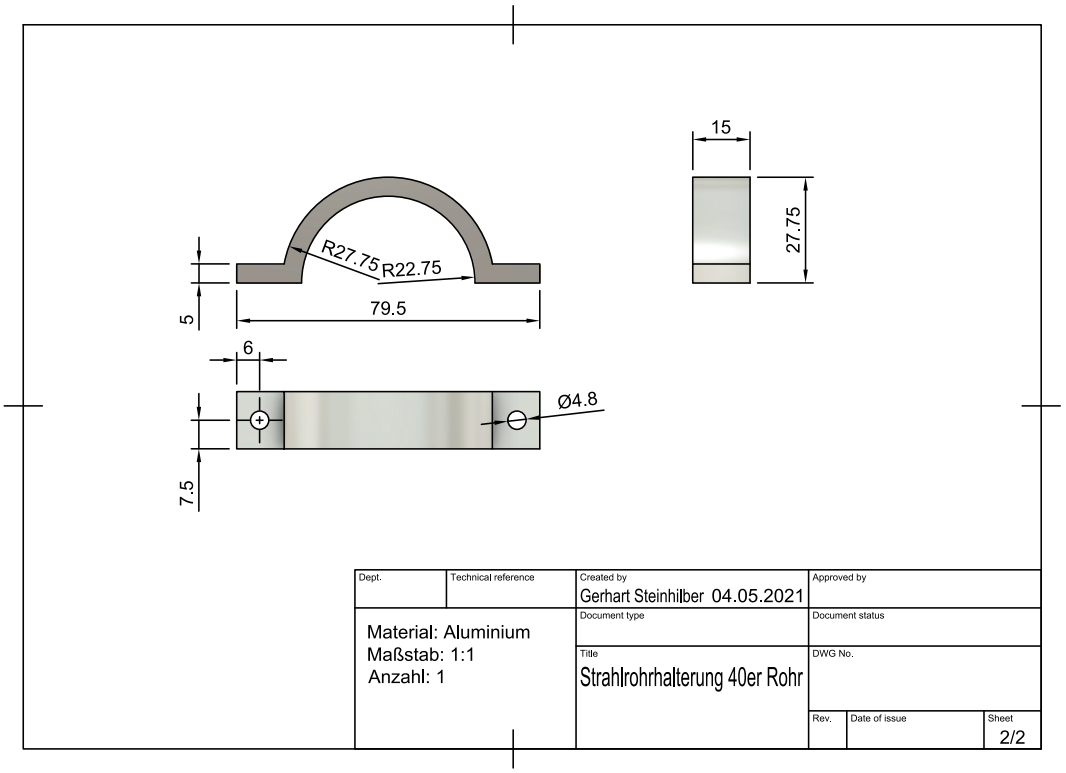

Figure 155: Technical drawing of the upper half of the small beam pipe holding clamp.

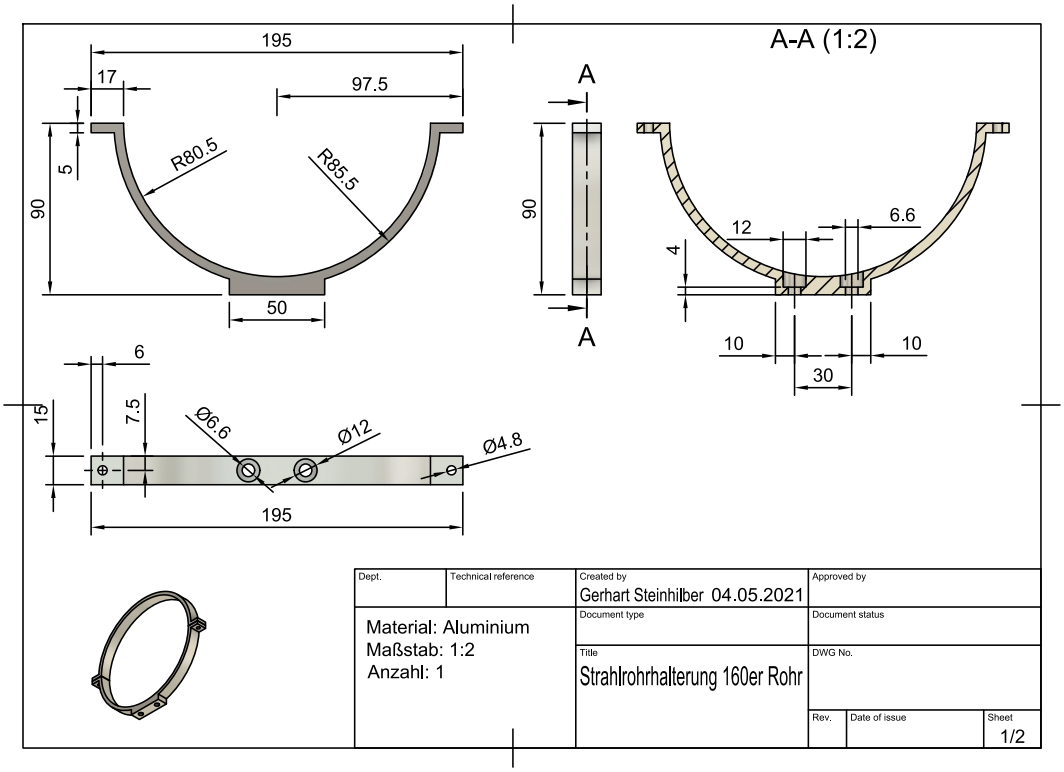

Figure 156: Technical drawing of the lower half of the large beam pipe holding clamp.

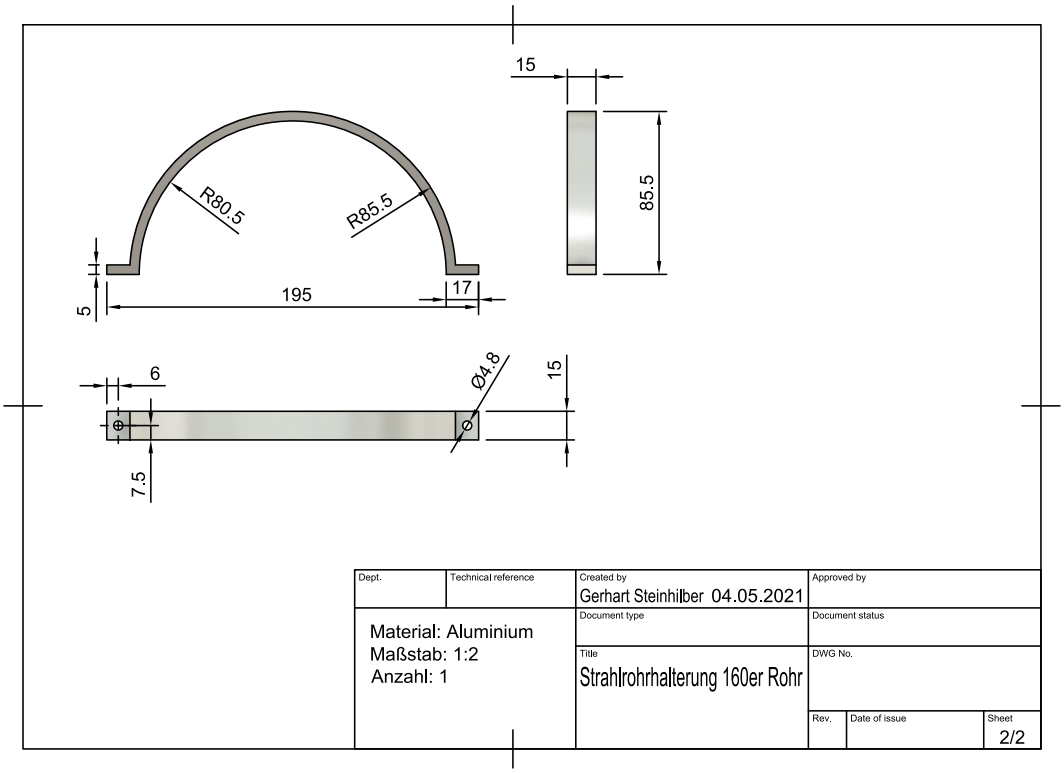

Figure 157: Technical drawing of the upper half of the large beam pipe holding clamp.

12.4. Detector Housing and Sled

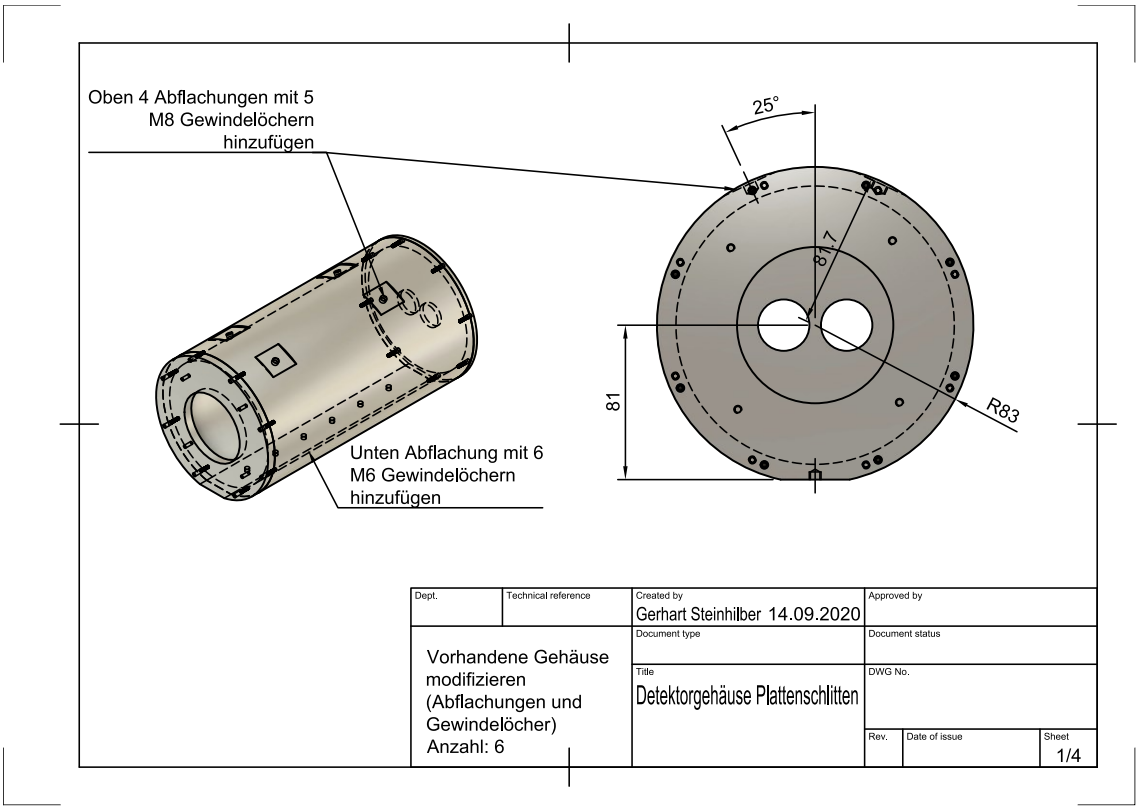

Figure 158: Technical drawing of the detector housing.

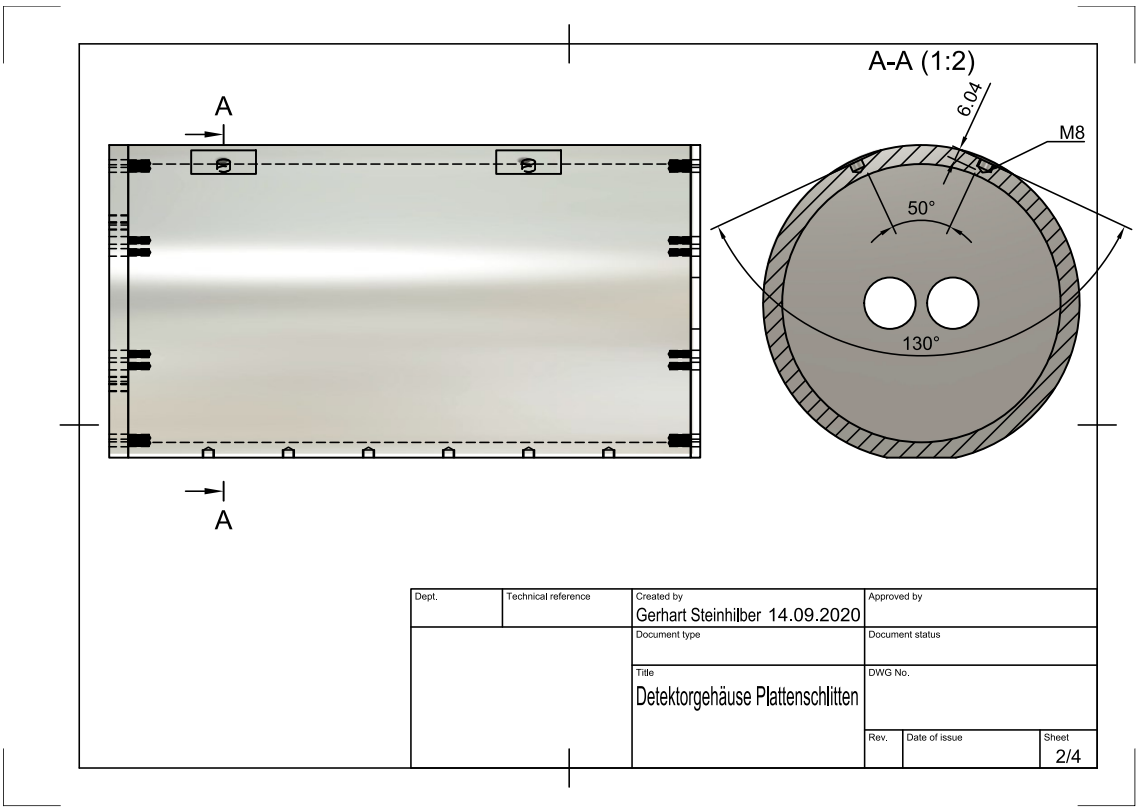

Figure 159: Technical drawing of the detector housing.

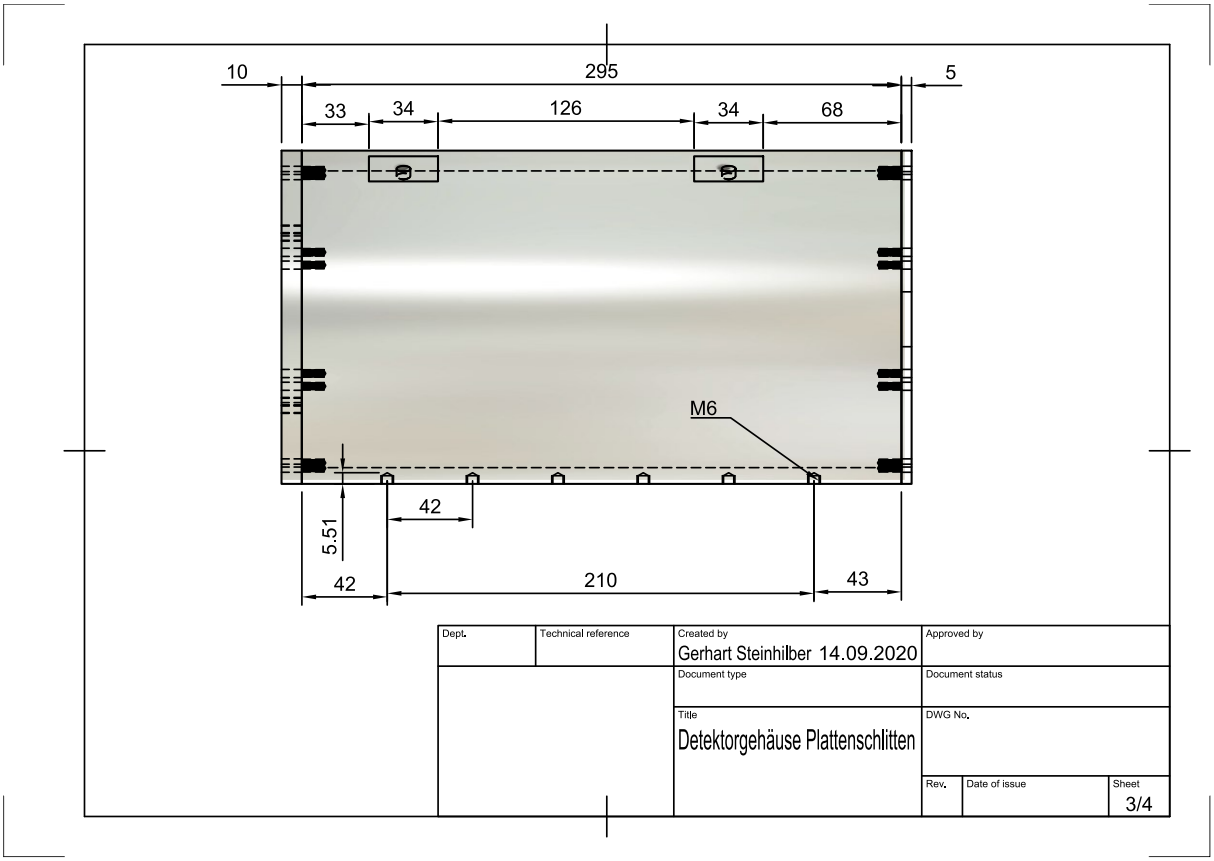

Figure 160: Technical drawing of the detector housing.

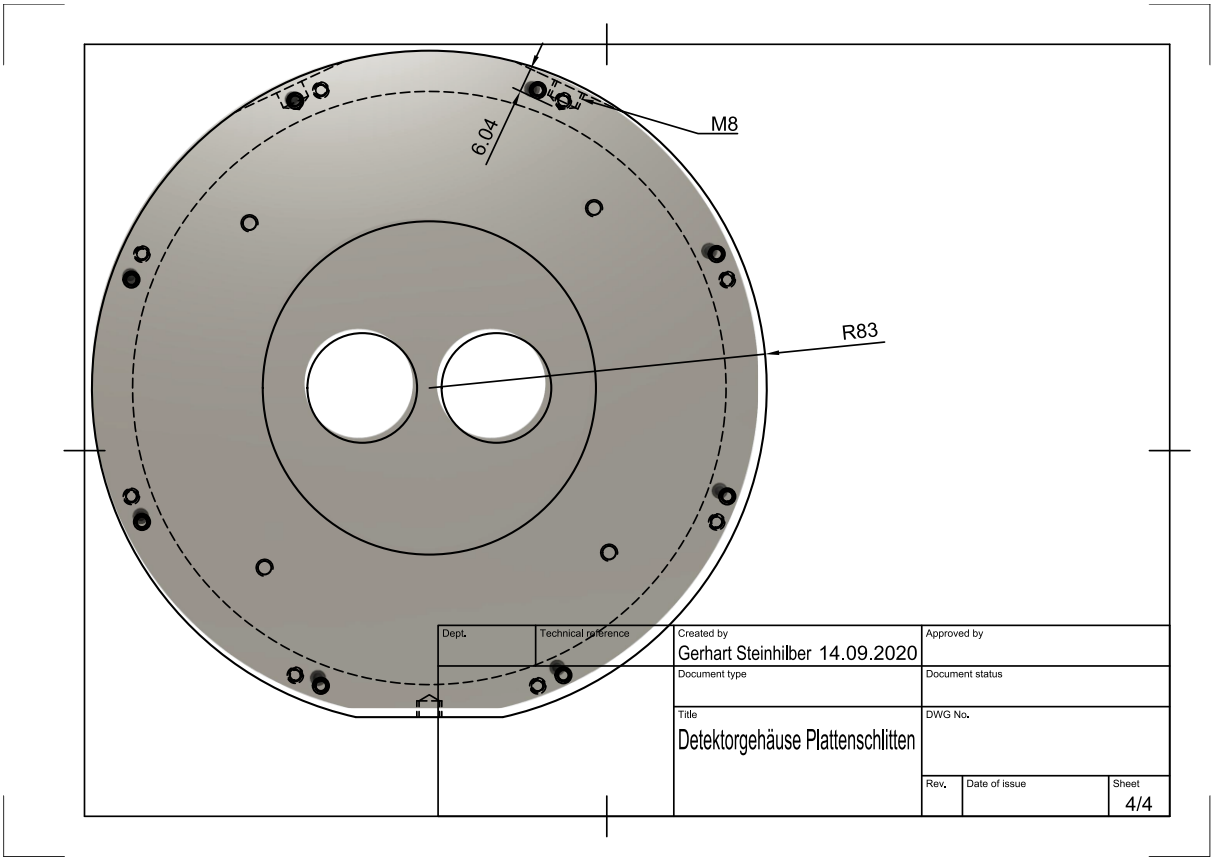

Figure 161: Technical drawing of the detector housing.

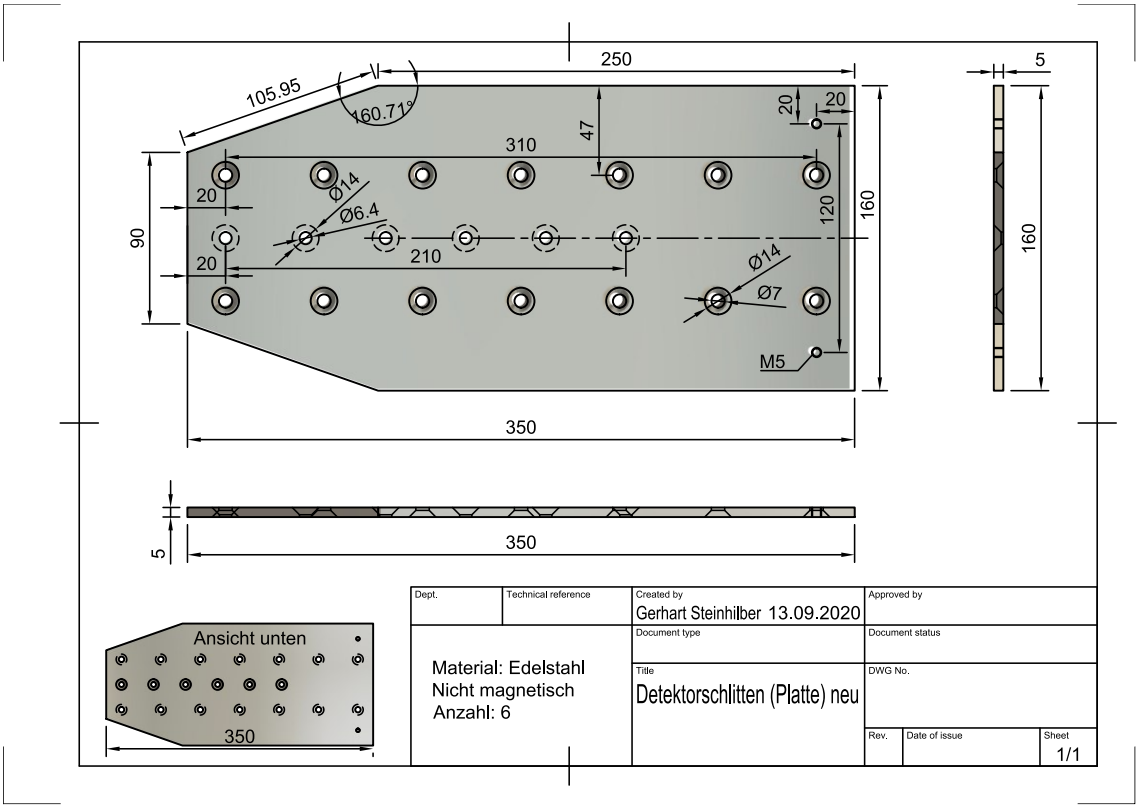

Figure 162: Technical drawing of the detector sled.

12.5. Magnetic Field Shielding

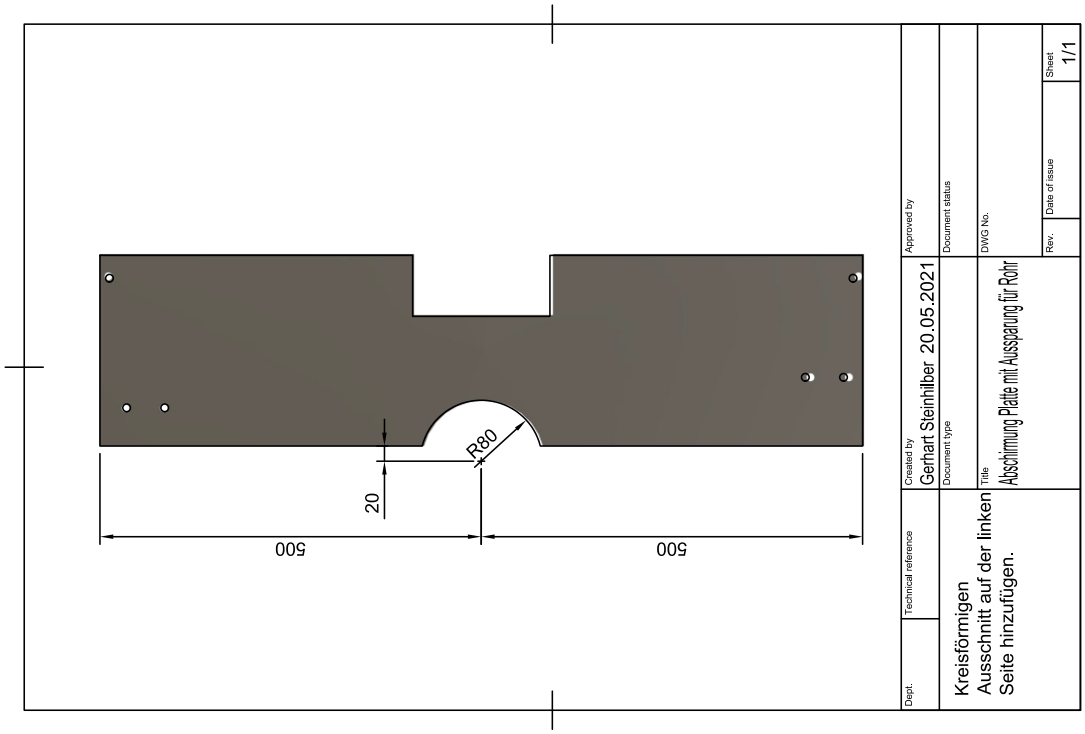

Figure 163: Technical drawing of the magnetic field shielding, which is attached to the front of the QCLAM spectrometer.

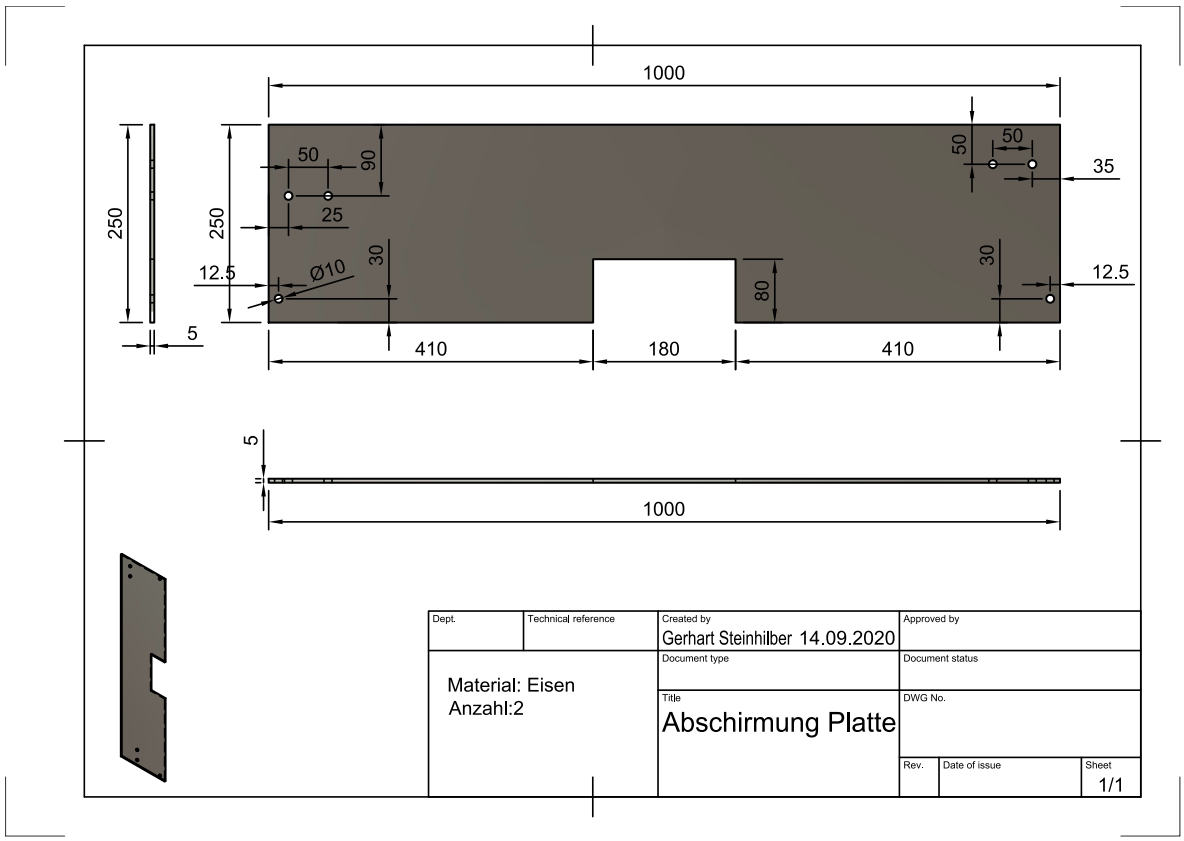

Figure 164: Technical drawing of the magnetic field shielding, which is attached to the front of the QCLAM spectrometer.

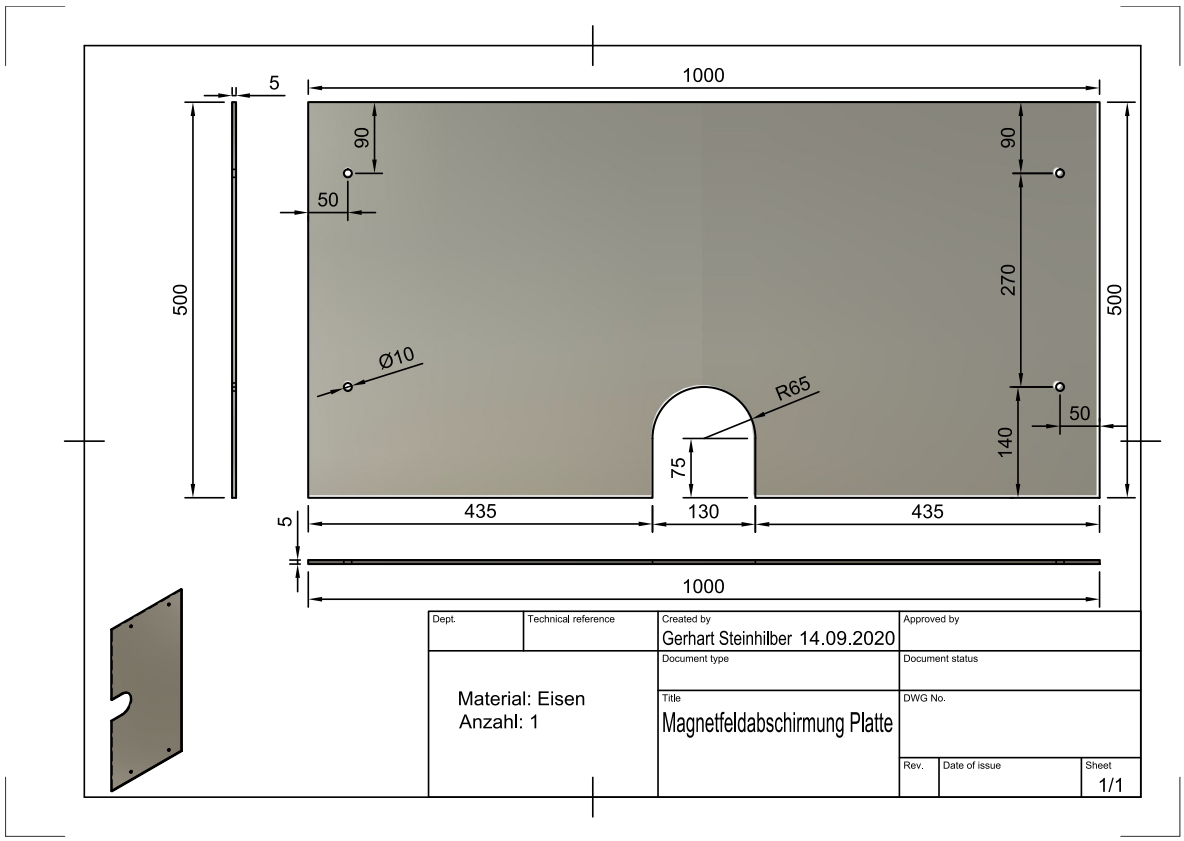

Figure 165: Technical drawing of the magnetic field shielding, which is attached to the side of the tower.

12.6. Instructions to Mount Scattering Chamber Holder

Instructions for assembling the beam pipe holding structure:

1. If a different scattering chamber is mounted, remove it and the corresponding mounting device underneath.
2. Align and attach the adapter plate using the alignment marks at the QCLAM measuring site.
3. Align and mount the struts of the beam tube holder.
4. Align detector array and attach to adapter plate.
5. Attach and align detectors in the detector array.
6. Mount scattering chamber and check alignment.

12.7. Instructions to Mount $LaBr_3$:Ce Detector in Housing

Procedure for installation of the detectors in the detector housings:

1. Attach the front to the aluminum case and place the case on the front.
2. First lower the front of the lead shielding and then the middle lead shielding into the aluminum housing.
3. Place the housing on its side and slide the detector in.
4. Connect high Voltage and signal cables to the detector, mount aft lead shielding and close aluminum case.

12.8. Spikes for $LaBr_3$:Ce Detector Alignment

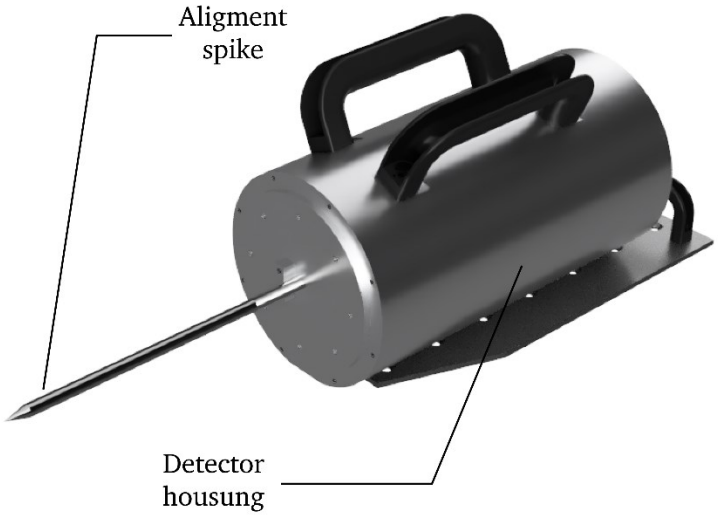

Figure 166: The spike for aligning the $LaBr_3$:Ce detectors is attached to the front of the detector housing instead of the copper and lead filters.

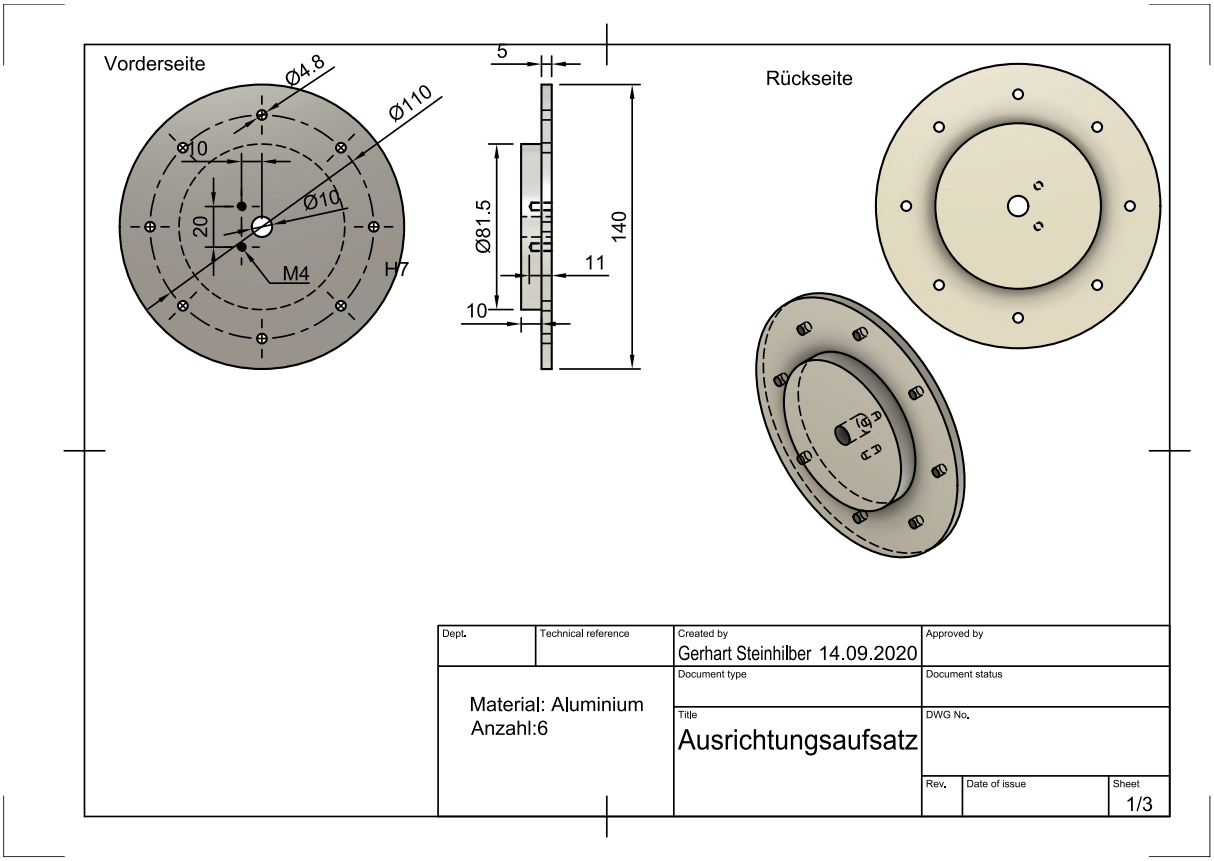

Figure 167: Technical drawing of the attachment for alignment of $LaBr_3$:Ce detectors.

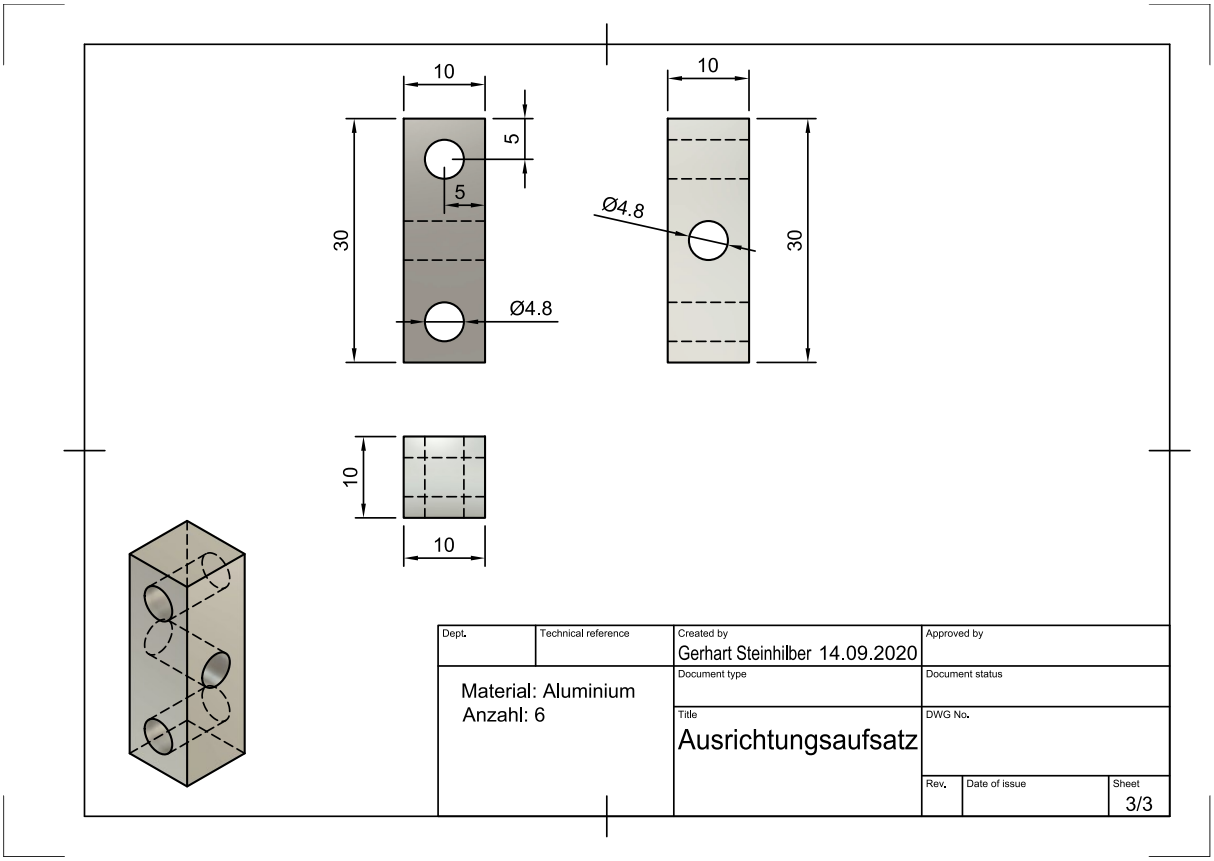

Figure 168: Technical drawing of the attachment for alignment of $LaBr_3$:Ce detectors.

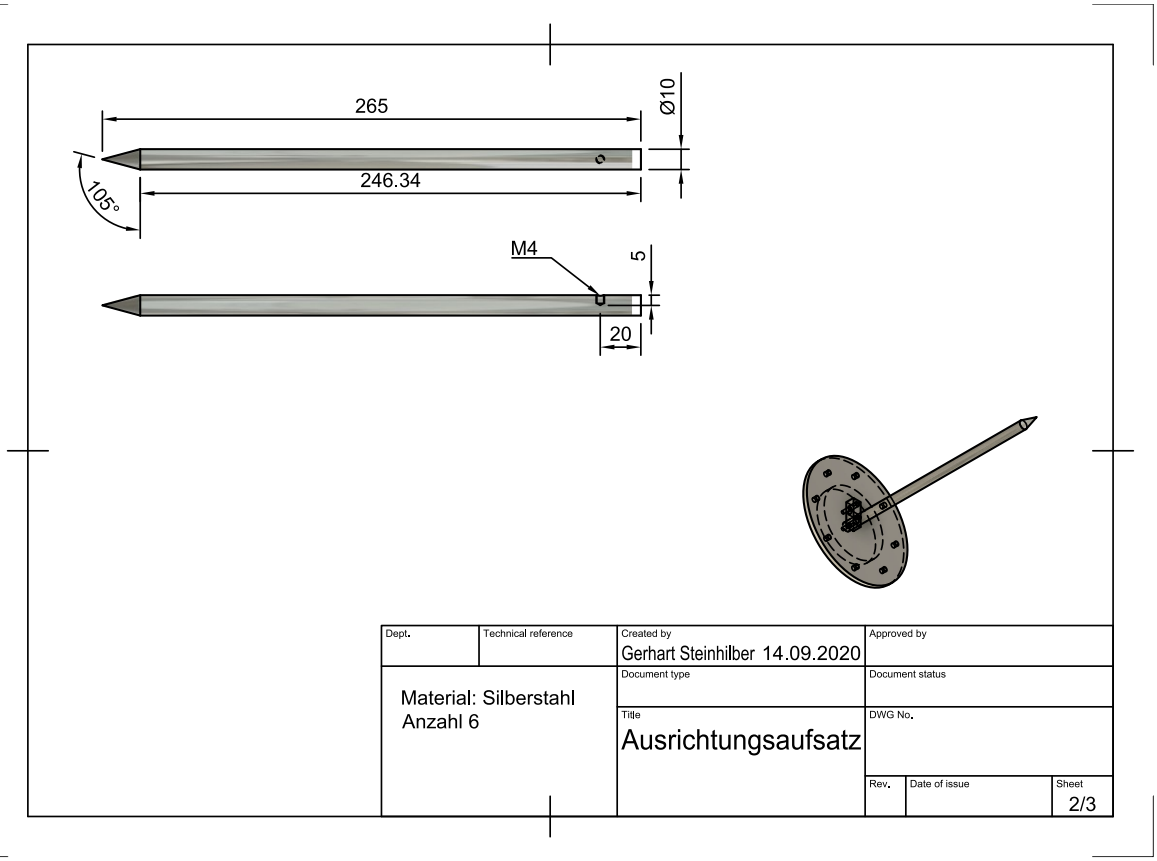

Figure 169: Technical drawing of the attachment for alignment of $LaBr_3$:Ce detectors.

12.9. Instructions to Attach Detector Towers to Scattering Chamber Holder

Assembly instructions:

1. Place both towers at the center of rotation of the QCLAM spectrometer and align them perpendicular to the floor using the adjustable stands.
2. Attach the towers to the adapter plate and attach the towers with screws at the upper end to fix the position.
3. Fill lead weights in the baskets.
4. Roughly align the detector rails and position the detectors.
5. Set the distance of the detectors to the target and optimize the alignment of the detectors.

12.10. DAQ Map

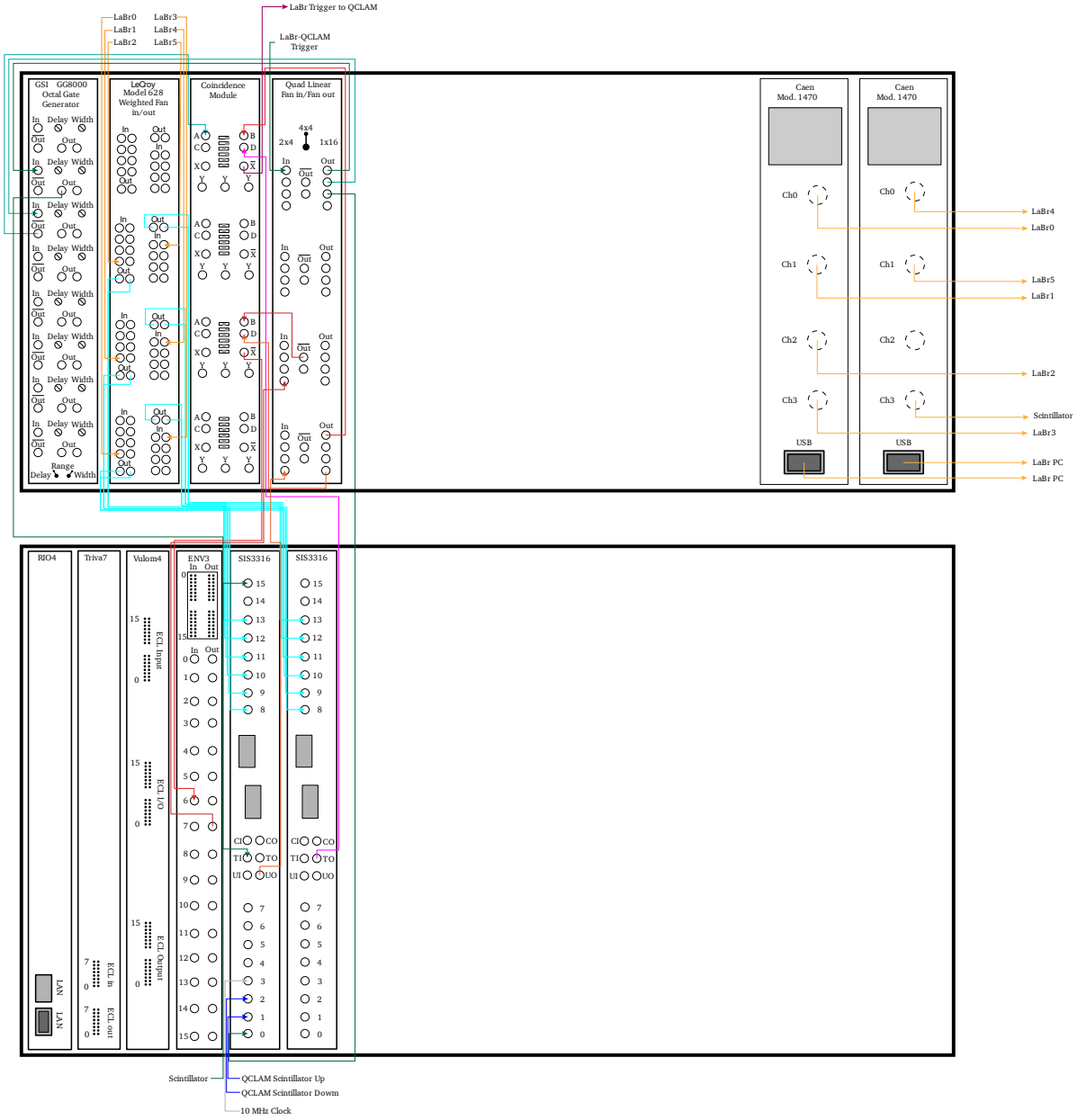

Figure 170: Complete map of VME and NIM crates of the LaBr Electronics.

12.11. Timing of Coincidence DAQ

The timing of the most important signals in both data acquisitions is shown in Figure 171.

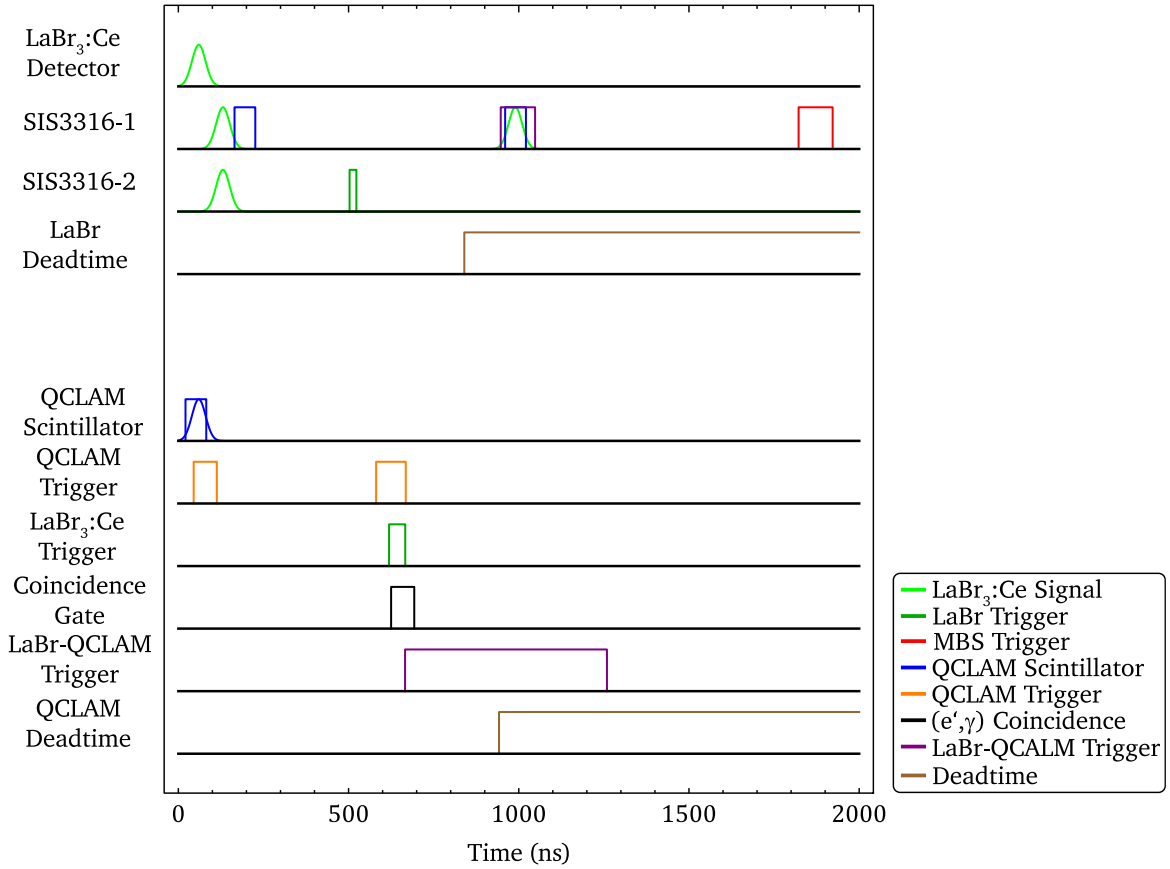

Figure 171: The time sequence of the signals of a single coincident event in both data acquisitions is shown. Shortly after the scattering process, the scattered electron in the QCLAM trigger detector system generates the QCLAM trigger, which is delayed until the LaBr trigger generated shortly thereafter in the LaBr electronics arrives. In the QCLAM trigger logic, the coincidence trigger is generated and distributed to both DAQs. In the QCLAM DAQ the readout of the drift times and the dead time latching starts. In the LaBr DAQ, the LaBr QCLAM trigger opens a gate for the previously delayed signal of the $LaBr_3$:Ce detector and the dead time latching starts.

12.12. Coincidence DAQ Operation

Three scripts are available to simplify the operation of the LaBr DAQ, the QCLAM DAQ and the combined coincidence DAQ.

- daqlogin /daqlogin_labr /daqlogin_qclam:
  daqlogin creates a new screen session on the server so that in case of connection loss of the computer to the server, the data acquisition continues operating. Subsequently, an automatic connection with the RIO4 and the change into the directory of the data acquisition software are executed.
- daqscreen_labr/daqscreen_qclam1/ daqscreen_qclam2:
  daqscreen establishes a connection to the screen session of the data acquisition system. This can be used, for example, to monitor the data acquisition.
- daqcontrol/daqcontrol_labr/daqcontrol_qclam:
  daqcontrol is used to send commands to the data acquisition. Commands that are sent

can consist of one or two parts (e.g. *daqcontrol @runstart* to start a new run; *daqcontrol show acquisition* to show the current status of the data acquisition).

LaBr DAQ settings can be changed in three text files in the “files” subdirectory of the data acquisition software. The three categories of settings are general settings (setup_file.txt), settings per group (group.txt) and settings per channel (channel.txt). General settings contain settings for the data acquisition, e.g., switching between coincidence and singles mode. In the SIS3316 module, four channels are combined in a group, whose settings contain, for example, the length of the trace. Settings for the individual channels contain the internal delay and the thresholds. Outsourcing these settings to text files reduces the necessity for code changes and time-consuming compilations when values are changed. Changes are applied when the data acquisition is restarted by either restarting MBS or stopping and starting the acquisition while MBS is running.

12.13. Data Structure of Unpacker Output File

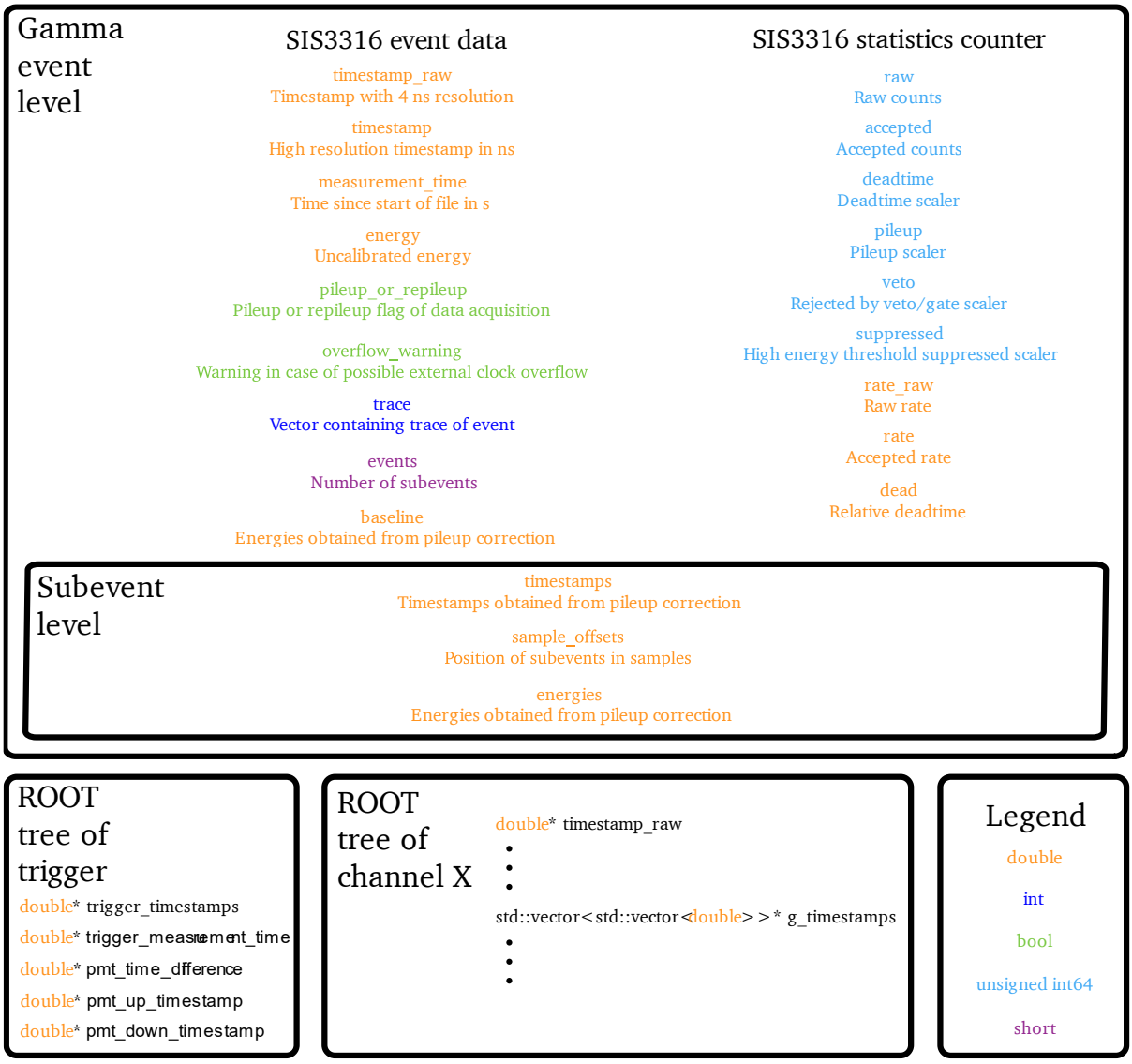

Figure 172: Data structure of the file containing the data of $LaBr_3$:Ce detectors. A $LaBr_3$:Ce event consists of two levels, the information about the event and, if using the pileup correction for each subevent, an entry in the subevent level. On the event level the SIS3316 event data are calculated for each event, the SIS3316 statistics counter information are constant until the next statistics counter readout. The file contains a tree with the time data of the electron trigger and a tree for each channel of the SIS3316 module.

12.14. Data Structure of Gamma Analyzer File

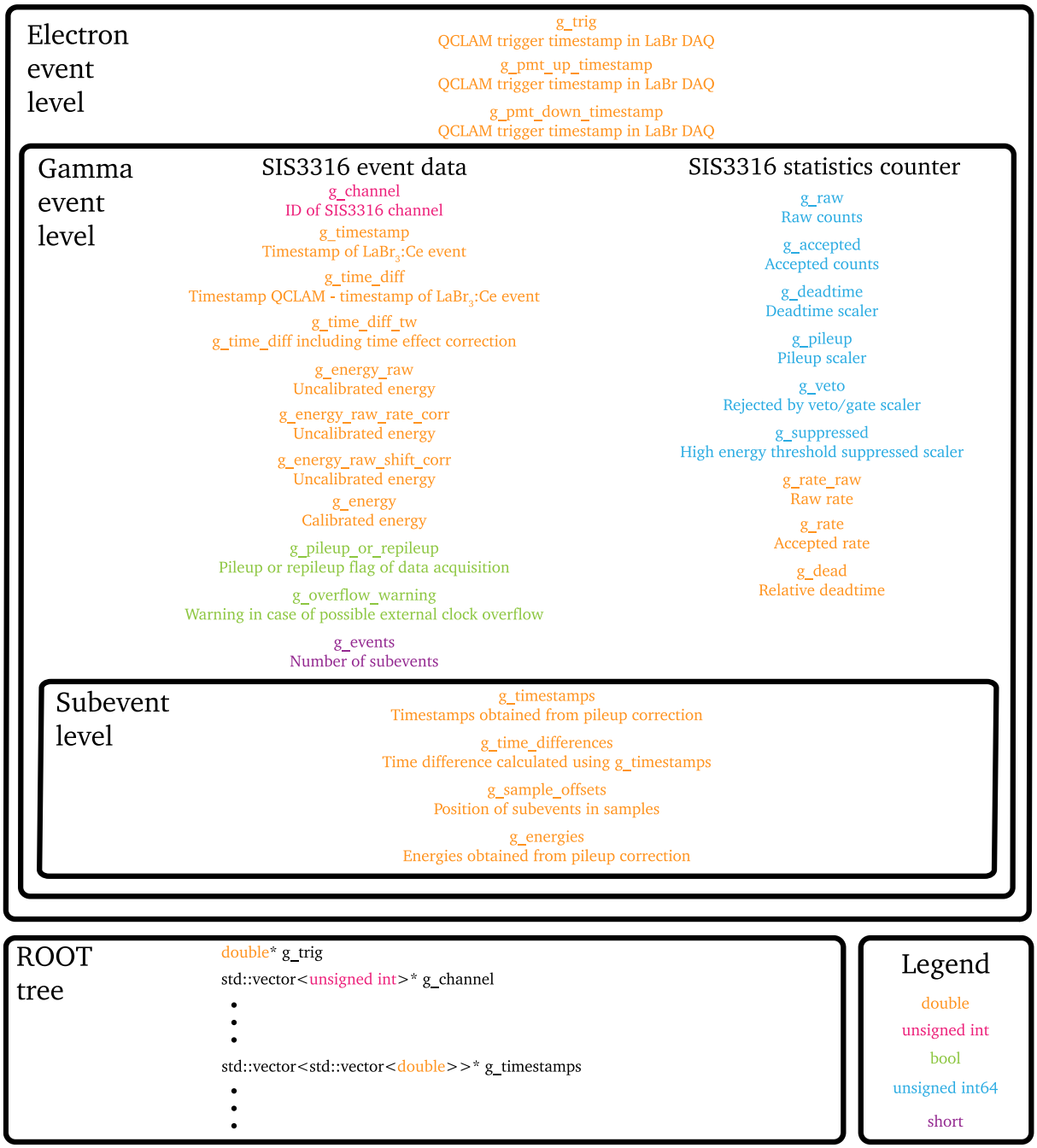

Figure 173: Data structure of the ROOT tree of coincident $LaBr_3$:Ce data. A coincident event consists of the coincidence trigger timestamp and its assigned $LaBr_3$:Ce events that have at least one subevent when using the pileup correction. In the upper area the event levels are illustrated, and the structure of the ROOT tree is indicated in the lower area.

12.15. Data Structure of Electron Analyzer File

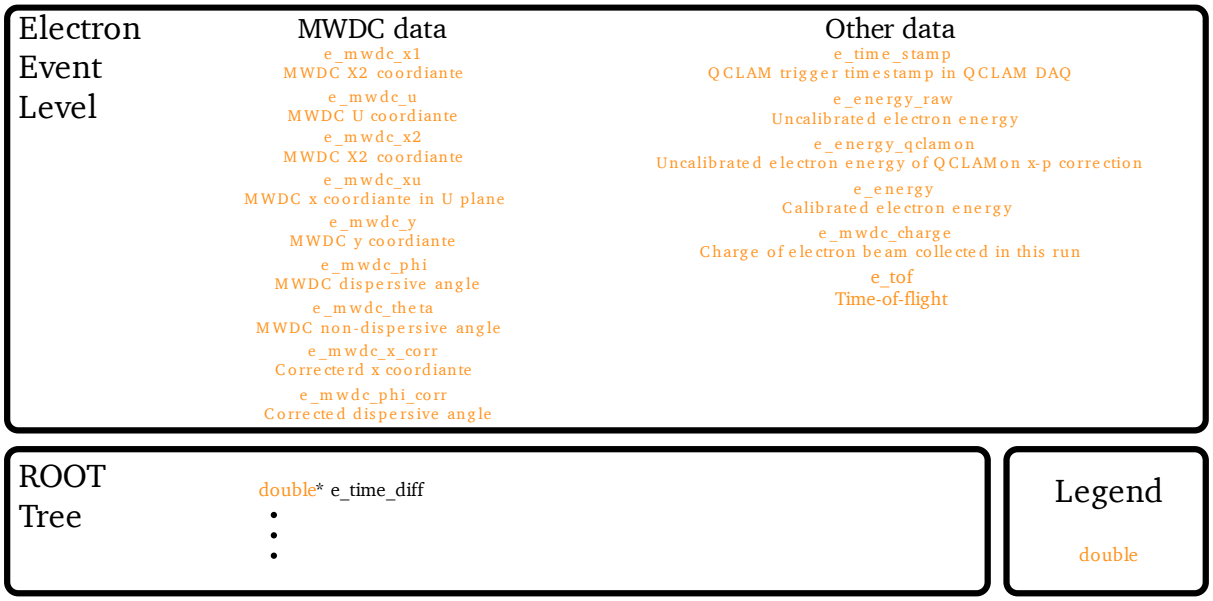

Figure 174: As QCLAM data acquisition does not store information about the events of $LaBr_3$:Ce detectors, there is only the electron event level in the data.

12.16. Data Structure of Trig Match File

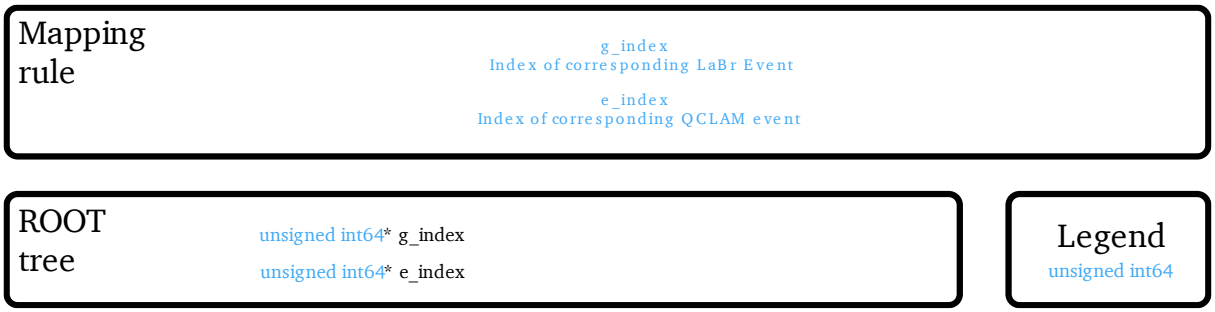

Figure 175: The data structure of Trig Match contains the indices of the QCLAM and LaBr events belonging to a coincidence event.

12.17. Data Structure of Coin Merger File

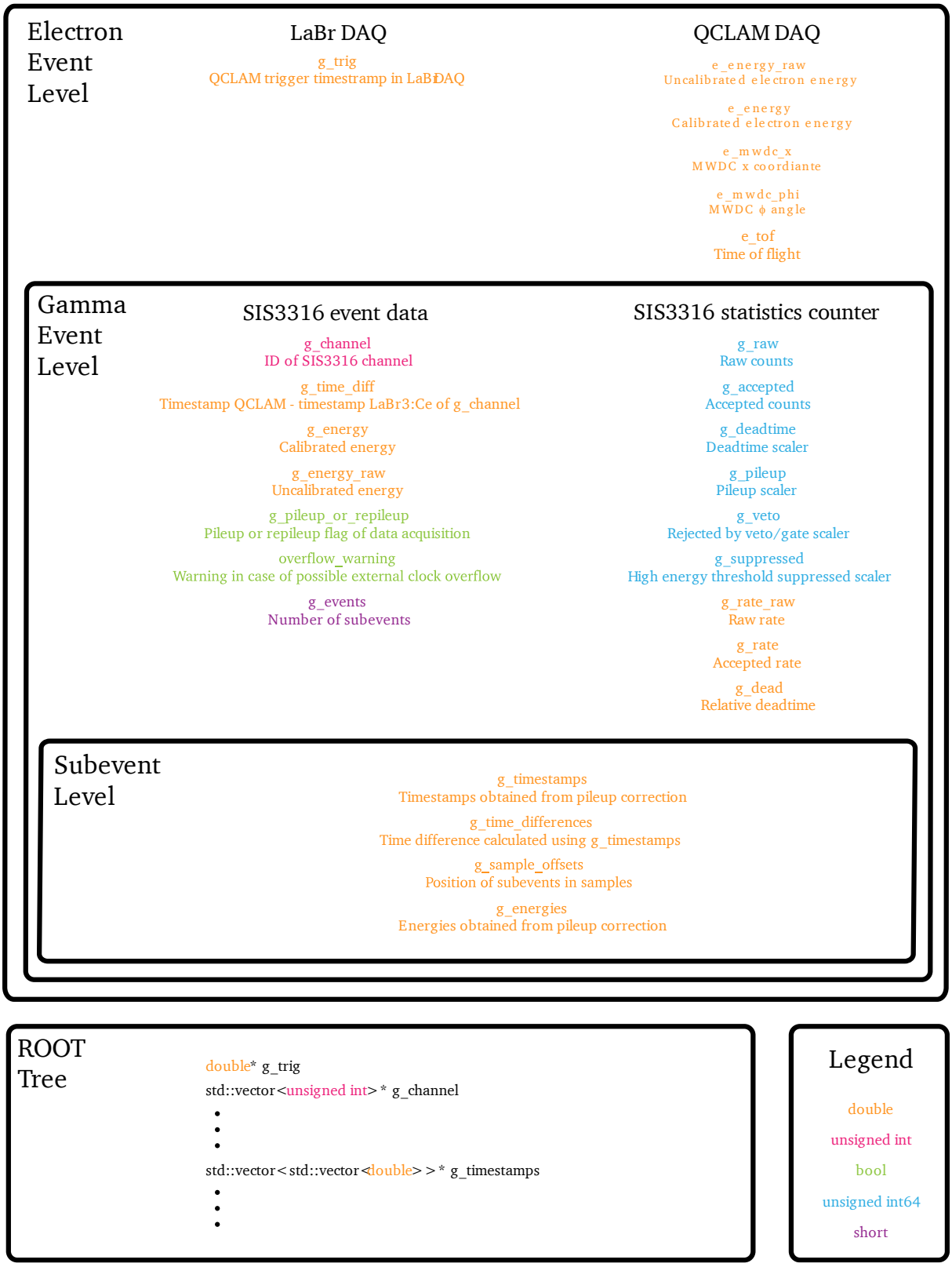

Figure 176: The data structure of the merged data is shown. Each coincidence event contains the data of the associated QCLAM event and a timestamp of the coincidence trigger in the LaBr data acquisition. The timestamp of the LaBr DAQ is used because of its higher time resolution. In addition, the coincidence event contains the events of all assigned detectors that registered a coincident hit. If a pileup correction has been used, the subevents of the $LaBr_3$:Ce detector event are stored in a vector.

12.18. Signal Shape Parameter

Table 35: Signal shape parameter of Equations (6.2) and (6.3) of the three detectors of the first commissioning experiment (See Chapter 7). Listed are the parameter for 511 keV photons.

Parameter	Detector 0	Detector 1	Detector 2
η	1.55589e+00	1.30589e+00	1.33219e+00
γ	1.87469e+00	1.68738e+00	2.82936e+00
a_0	6.31800e-01	6.52313e-01	5.33875e-01
a_1	4.38438e-01	4.08063e-01	5.15261e-01
a_2	2.31002e-02	2.58838e-02	2.84345e-02
a_3	-5.99037e-03	-3.50116e-02	-6.18900e-03
x_1	3.13823e+00	2.71072e+00	2.46260e+00
x_2	3.25908e+01	5.38968e+01	1.89897e+01
x_3	4.07466e+01	5.25251e+01	4.07384e+01
$\bar{\sigma}_{0,l}$	2.42189e+00	2.20159e+00	2.33593e+00
$\bar{\sigma}_{0,r}$	5.92802e+00	6.21404e+00	5.84657e+00
$\bar{\sigma}_{1,l}$	2.77739e+00	2.26028e+00	2.69603e+00
$\bar{\sigma}_{1,r}$	7.86789e+00	7.51178e+00	7.71272e+00
$\bar{\sigma}_{2,l}$	1.35877e+01	9.45887e+00	3.36848e+00
$\bar{\sigma}_{2,l}$	4.46980e+00	1.71930e+01	1.33304e+01
$\bar{\sigma}_{3,l}$	7.65202e+00	9.96759e+00	2.02123e+00
$\bar{\sigma}_{3,r}$	1.99810e+01	1.94071e+01	1.18093e+01

Table 36: Signal shape parameter of Equations (6.2) and (6.3) of the three detectors of the first commissioning experiment (See Chapter 7). Listed are the parameter for 15 MeV photons

Parameter	Detector 0	Detector 1	Detector 2
η	1.20992e+00	1.43461e+00	1.40377e+00
γ	2.83419e+00	1.20325e+00	2.33840e+00
a_0	6.17353e-01	6.35613e-01	6.52739e-01
a_1	4.49632e-01	4.30571e-01	4.00217e-01
a_2	7.11827e-03	-6.16992e-03	-1.17840e-03
a_3	-1.88715e-02	-1.40232e-02	-1.02616e-02
x_1	3.84938e+00	3.57170e+00	3.56151e+00
x_2	5.65931e+01	4.64570e+01	2.99790e+01
x_3	4.32860e+01	5.82189e+01	4.74428e+01
$\bar{\sigma}_{0,l}$	2.20302e+00	2.27018e+00	2.39160e+00
$\bar{\sigma}_{0,r}$	7.90603e+00	7.65411e+00	9.09499e+00
$\bar{\sigma}_{1,l}$	3.05633e+00	2.91799e+00	3.36954e+00
$\bar{\sigma}_{1,r}$	6.78258e+00	7.10491e+00	7.29615e+00
$\bar{\sigma}_{2,l}$	1.78906e+01	2.82770e+01	4.96250e+01
$\bar{\sigma}_{2,l}$	1.10546e+01	9.99263e+00	4.81180e+01
$\bar{\sigma}_{3,l}$	3.38596e+00	2.64576e+01	9.91573e+00
$\bar{\sigma}_{3,r}$	1.99941e+01	5.82189e+01	1.99984e+01

13. References

[1] R. Hofstadter, Rev. Mod. Phys. **28**, 214 (1956).
[2] L. de Broglie, Ann. Phys. **10**, 22 (1925).
[3] H. Überall, *Electron Scattering from Complex Nuclei. Part A* (Academic Press, New York, 1971), Vol. 1.
[4] T. Suda and H. Simon, Prog. Part. Nucl. Phys. **96**, 1 (2017).
[5] T. de Forest and J. D. Walecka, Advances in Physics **15**, 1 (1966).
[6] A. Zilges, D. L. Balabanski, J. Isaak, and N. Pietralla, Prog. Part. Nucl. Phys. **122**, 103903 (2022).
[7] P. von Neumann-Cosel and A. Tamii, Eur. Phys. J. A **55**, 110 (2019).
[8] G. A. Proca and D. B. Isabelle, Nucl. Phys. A **109**, 177 (1968).
[9] R. Huby, Rep. Prog. Phys. **21**, 59 (1958).
[10] P. Napiralla *et al.*, Eur. Phys. J. A **56**, 147 (2020).
[11] J. Goldemberg and R. H. Pratt, Rev. Mod. Phys. **38**, 311 (1966).
[12] A. Richter, Nucl. Phys. A **522**, 139 (1991).
[13] F.-P. Juster *et al.*, Phys. Rev. Lett. **55**, 2261 (1985).
[14] F. J. Kline *et al.*, Nucl. Phys. A **209**, 381 (1973).
[15] H. Baghaei *et al.*, Phys. Rev. C **42**, 2358 (1990).
[16] M. Wakasugi *et al.*, Nucl. Instrum. Methods Phys. Res. B **317**, 668 (2013).
[17] C. N. Papanicolas, Nucl. Phys. A **446**, 249 (1985).
[18] P. von Neumann-Cosel *et al.*, Nucl. Phys. A **569**, 373 (1994).
[19] G. O. Bolme *et al.*, Phys. Rev. Lett. **61**, 1081 (1988).
[20] T. Weber *et al.*, Phys. Rev. Lett. **59**, 2028 (1987).
[21] T. Weber *et al.*, Phys. Rev. Lett. **62**, 129 (1989).
[22] S. E. Williamson, PhD Thesis, University of Illinois, 1981 (unpublished).
[23] C. N. Papanicolas *et al.*, Phys. Rev. Lett. **54**, 26 (1985).
[24] H. Crannell, Phys. Rev. **148**, 1107 (1966).
[25] J. H. Fregeau and R. Hofstadter, Phys. Rev. **99**, 1503 (1955).
[26] M. Bernheim, T. Stovall, and d. Vinciguerra, Phys. Lett. B **25**, 461 (1967).
[27] J. B. Flanz *et al.*, Phys. Rev. Lett. **41**, 1642 (1978).
[28] M. N. Rosenbluth, Phys. Rev. **79**, 615 (1950).
[29] J. R. Deininger, Ph.D. Thesis, University of Illinois, 1996.
[30] P. E. Mueller, Ph.D. Thesis, University of Illinois, 1993.
[31] E. Fein *et al.*, Nucl. Phys. A **468**, 301 (1987).
[32] B. Rasmussen, BrilLanCe 380 Scintillation Material, 2004.
[33] N. Pietralla, Nucl. Phys. News **28**, 4 (2018).
[34] D. Bohle *et al.*, Phys. Lett. B **137**, 27 (1984).
[35] A. Richter, Nucl. Phys. A **507**, 99 (1990).
[36] C. Walz *et al.*, Phys. Rev. Lett. **106**, 62501 (2011).
[37] O. Burda *et al.*, Phys. Rev. Lett. **99**, 92503 (2007).
[38] S. Strauch *et al.*, Phys. Rev. Lett. **85**, 2913 (2000).
[39] M. Knirsch, Ph.D. Thesis, Technische Hochschule Darmstadt, 1991.
[40] L. Rezzolla and N. Pietralla, *Funding Proposal for Cluster Project ELEMENTS: Exploring the Universe from microscopic to macroscopic scales* (2020).
[41] F. Hoyle, Astrophys. J. Suppl. Ser. **1**, 121 (1954).

[42] M. Salaris, *Evolution of Stars and Stellar Populations* (John Wiley & Sons Incorporated, Newark, 2005).
[43] J. H. Kelley, J. E. Purcell, and C. G. Sheu, Nucl. Phys. A **968**, 71 (2017).
[44] M. Goeppert-Mayer, Phys. Rev. **74**, 235 (1948).
[45] M. Goeppert-Mayer, Phys. Rev. **75**, 1969 (1949).
[46] F. Iachello, Phys. Rev. Lett. **53**, 1427 (1984).
[47] H. Klein *et al.*, Phys. Rev. C **65**, 44315 (2002).
[48] N. Pietralla *et al.*, Phys. Rev. C **64**, 031301(R) (2001).
[49] A. Arima and F. Iachello, Phys. Rev. Lett. **35**, 1069 (1975).
[50] A. Arima, T. Ohtsuka, F. Iachello, and I. Talmi, Phys. Lett. B **66**, 205 (1977).
[51] T. Otsuka, A. Arima, and F. Iachello, Nucl. Phys. A **309**, 1 (1978).
[52] G. Siems *et al.*, Phys. Lett. B **320**, 1 (1994).
[53] N. Pietralla *et al.*, Phys. Rev. Lett. **73**, 2962 (1994).
[54] N. Pietralla, P. von Brentano, T. Otsuka, and R. F. Casten, Phys. Lett. B **349**, 1 (1995).
[55] T. Otsuka and K. H. Kim, Phys. Rev. C **50**, R1768 (1994).
[56] N. Pietralla, P. von Brentano, and A. Lisetskiy, Prog. Part. Nucl. Phys. **60**, 225 (2008).
[57] O. Burda, Ph.D. Thesis, Technische Universität Darmstadt, 2007.
[58] W. D. Hamilton, A. Irbäck, and J. P. Elliott, Phys. Rev. Lett. **53**, 2469 (1984).
[59] N. Pietralla *et al.*, Phys. Rev. Lett. **83**, 1303 (1999).
[60] A. F. Lisetskiy *et al.*, Nucl. Phys. A **677**, 100 (2000).
[61] S. R. Lesher *et al.*, Phys. Rev. C **75**, 34318 (2007).
[62] V. Werner *et al.*, Phys. Lett. B **550**, 140 (2002).
[63] E. Elhami *et al.*, Phys. Rev. C **75**, 011301(R) (2007).
[64] J. D. Holt *et al.*, Phys. Rev. C **76**, 34325 (2007).
[65] V. Werner *et al.*, Phys. Rev. C **78**, 031301(R) (2008).
[66] A. Hennig *et al.*, Phys. Rev. C **90**, 51302 (2014).
[67] A. Hennig *et al.*, Phys. Rev. C **92**, 64317 (2015).
[68] M. Wang *et al.*, Chin. Phys. C **36**, 1603 (2012).
[69] J. R. Beene *et al.*, Phys. Rev. C **41**, 1332 (1990).
[70] D. Abriola and A. A. Sonzogni, Nucl. Data Sheets **109**, 2501 (2008).
[71] H. L. Acker and M. E. Rose, Ann. Phys. **44**, 336 (1967).
[72] D. F. Hubbard and M. E. Rose, Nucl. Phys. **84**, 337 (1966).
[73] D. Drechsel and H. Überall, Phys. Rev. **181**, 1383 (1969).
[74] T. A. Griffy and Don Whitehill, Phys. Rev. C **2**, 441 (1970).
[75] D. H. Jakubassa-Amundsen and V. Y. Ponomarev, Phys. Rev. C **95**, 24310 (2017).
[76] D. H. Jakubassa-Amundsen, Phys. Rev. A **93**, 52716 (2016).
[77] D. H. Jakubassa-Amundsen and V. Y. Ponomarev, Eur. Phys. J. A **56**, 162 (2020).
[78] C. García-Recio, T. W. Donnelly, and E. Moya De Guerra, Nucl. Phys. A **509**, 221 (1990).
[79] T. de Forest, Nucl. Phys. A **132**, 305 (1969).
[80] M. E. Rose, *Multipole Fields* (Wiley, 1955), Vol. 8.
[81] N. F. Mott, Proc. R. Soc. Lond. A **124**, 425 (1929).
[82] H. Bethe and W. Heitler, Proc. R. Soc. Lond. A **146**, 83 (1934).
[83] K. Sonnabend *et al.*, Nucl. Instrum. Methods Phys. Res. A **640**, 6 (2011).
[84] M. Arnold, Ph.D. Thesis, Technische Universität Darmstadt, 2016.
[85] M. Arnold *et al.*, Proceedings of the 9th International Particle Accelerator Conference (2018).
[86] D. Savran *et al.*, Nucl. Instrum. Methods Phys. Res. A **613**, 232 (2010).

[87] A. Krugmann and O. Burda, Performing Electron Scattering Experiments with the LINTOTT Spectrometer at the S-DALINAC, 2013.
[88] T. Walcher *et al.*, Nucl. Instrum. Methods **153**, 17 (1978).
[89] L. Jürgensen, Ph.D. Thesis, Technische Universität Darmstadt, 2018.
[90] L. Jürgensen (private communications).
[91] M. Dutine, Master Thesis, Technische Universität Darmstadt, 2018.
[92] F. Neumeyer, Ph.D. Thesis, Technische Universität Darmstadt, 1997.
[93] G. C. Lüttge, Ph.D. Thesis, Technische Hochschule Darmstadt, 1994.
[94] M. Singer (private communications).
[95] M. Singer, Ph.D. Thesis, Technische Universität Darmstadt, 2019.
[96] Y. Kalmykov, *(e,e'x) and (e,e') at 180° Experiments at the S-DALINAC QClam Spectrometer* (Darmstadt, 2003).
[97] A. D'Alessio, Masterarbeit, Technische Universität Darmstadt, 2016.
[98] M. Lösler *et al.*, zfv – Zeitschrift für Geodäsie, Geoinformation und Landmanagement, 346 (2015).
[99] S. Dietrich, Diploma thesis, Technische Universität Darmstadt, 1998.
[100] K.-D. Hummel, Ph.D. Thesis, Technische Hochschule Darmstadt, 1992.
[101] A. D'Alessio, Ph.D. Thesis, Technische Universität Darmstadt, 2020.
[102] W. R. Leo, *Techniques for nuclear and particle physics experiments* (Springer, 1994).
[103] J. Horn, Ph.D. Thesis, Technische Hochschule Darmstadt, 1997.
[104] B. Reitz, Ph.D. Thesis, Technische Universität Darmstadt, 2000.
[105] I. Pysmenetska, Ph.D. Thesis, Technische Universität Darmstadt, 2009.
[106] Autodesk Inc., Autodesk Fusion 360 (Autodesk Inc., San Rafael, 2020).
[107] item Industrietechnik GmbH, 2022, https://de.item24.com/index.html.
[108] M. Steinhorst (private communications).
[109] T. Klaus (private communication).
[110] M. W. Kuss, Diploma Thesis, Technische Hochschule Darmstadt, 1990.
[111] M. Hilcker, Ph.D. Thesis, Technische Universität Darmstadt, 2020.
[112] M. B. Mathy, Ph.D. Thesis, Technische Universität Darmstadt, 2021.
[113] M. Chernykh, Ph.D. Thesis, Technische Universität Darmstadt, 2008.
[114] S. Agostinelli *et al.*, Nucl. Instrum. Methods Phys. Res. A **506**, 250 (2003).
[115] J. Allison *et al.*, Nucl. Instrum. Methods Phys. Res. A **835**, 186 (2016).
[116] J. Allison *et al.*, IEEE Trans. Nucl. Sci. **53**, 270 (2006).
[117] thyssenkrupp Materials Schweiz AG, Werkstoffdatenblatt EN AW-5754 / Al Mg3, 2017.
[118] V. P. Singh and N. M. Badiger, Radioprotection **48**, 431 (2013).
[119] S. Seltzer and J. H. Hubbell, Tables of X-Ray Mass Attenuation Coefficients and Mass Energy-Absorption Coefficients, NIST Standard Reference Database 126, 1996.
[120] Kreß GmbH, *Kreß GmbH*, https://www.kress-gmbh.de/impressum.html, accessed Jul 6, 2021.
[121] Institut für Kernphysik, Technische Universität Darmstadt, *Bleistein Kamera*, http://ikpweb.ikp.physik.tu-darmstadt.de/mediawiki/index.php/Bleistein-Kamera, accessed Oct 31, 2021.
[122] Mclennan, 17HS-240E Data Sheet, 2019.
[123] Applied Motion Products, Inc., ST-Datasheet 925-0007, 2011.
[124] Applied Motion Products, Inc., *ST Configurator*, https://www.applied-motion.com/products/software/st-configurator, accessed Oct 29, 2021.

[125] Applied Motion Products, Inc., *Q Programmer*, https://www.applied-motion.com/products/software/q-programmer, accessed Oct 29, 2021.
[126] E. van Loef *et al.*, Appl. Phys. Lett. **79**, 1573 (2001).
[127] A. Giaz *et al.*, Nucl. Instrum. Methods Phys. Res. A **729**, 910 (2013).
[128] Saint-Gobain Crystals, Lanthanum Bromide Scintillators Performance Summary, (2019).
[129] R. Casanovas, J. J. Morant, and M. Salvadó, Nucl. Instrum. Methods Phys. Res. A **675**, 78 (2012).
[130] A. Iltis *et al.*, Nucl. Instrum. Methods Phys. Res. A **563**, 359 (2006).
[131] B. Löher *et al.*, Nucl. Instrum. Methods Phys. Res. A **686**, 1 (2012).
[132] A. F. Iyudin *et al.*, Instrum. Exp. Tech. **52**, 774 (2009).
[133] G. F. Knoll, *Radiation detection and measurement* (Wiley, New York, NY, 2000).
[134] Hamamatsu Photonics K.K., *Photomultiplier tube R6233*, https://www.hamamatsu.com/eu/en/product/type/R6233/index.html, accessed Oct 30, 2021.
[135] D. Symochko (private communications).
[136] G. Esposito, N1470 Programmable HV Power Supply, 2021.
[137] G. Esposito, GECO2020 GEneral COntrol Software for CAEN HV Power Supplies, 2020.
[138] T. Klaus (private communication).
[139] M. Ciemała *et al.*, Nucl. Instrum. Methods Phys. Res. A **608**, 76 (2009).
[140] G. Steinhilber, Masterthesis, Technische Universität Darmstadt, 2016.
[141] Dassault Systémes, CST Studio Suite 2020.00 - Release Notes, 2019.
[142] R. Hawkes *et al.*, IEE Nucl. Sci. Symp. Conf. Rec., 3400 (2007).
[143] P. von Neumann-Cosel *et al.*, Phys. Rev. Lett. **88**, 202 (2002).
[144] VITA Technologies, *VMEbus Technology*, 2020, https://web.archive.org/web/20200813001829/https://www.vita.com/page-1855175, accessed May 25, 2021.
[145] L. Costrell *et al.*, Standard NIM Instrumentation System, 1990.
[146] ELB-Elektroniklaboratorien Bonn UG, *ELB-VME-VFB6 Modul*, https://web.archive.org/web/20191111215825/https://www.elbonn.de/cms/item.php?theme=elb-vme-vfb6&language=de, accessed May 11, 2022.
[147] GSI Helmholzzentrum für Schwerionenforschung GmbH, *GSI Multi Branch System*, 2020, https://web.archive.org/web/20201022154112/https://www.gsi.de/work/forschung/experimentelektronik/datenverarbeitung/datenerfassung/mbs.htm, accessed May 25, 2021.
[148] GSI Helmholtzzentrum für Schwerionenforschung GmbH, https://www.gsi.de/en/start/news, accessed Mar 1, 2022.
[149] N. Kurz, MBS Multi Branch System. The General Purpose Data Acquisition System MBS at GSI (and elsewhere), 2019.
[150] CES, RIO4-8072. Freescale-Based 6U VME Single Board Computer, 2013.
[151] Lynx Software Technologies, *Lynx OS*, 2021, https://www.lynx.com/products/lynxos-posix-real-time-operating-system-rtos, accessed Aug 1, 2021.
[152] J. Hoffmann, N. Kurz, and M. Richter, TRIVA, VME Trigger Module, 2011.
[153] J. Hoffmann, *Dead Time Locker and Trigger Priority Encoder*, 2010, https://www.gsi.de/work/forschung/experimentelektronik/digitalelektronik/digitalelektronik/module/vme/vulom/vulom4, accessed Nov 11, 2021.
[154] D. Symochko (private communications).
[155] SIS GmbH, SIS3316 16 Channel VME Digitizer User Manual, 2016.
[156] B. Löher (private communications).

[157] D. Symochko (private communications).
[158] J. F. Groß, BSc. Thesis, Technische Universität Darmstadt, 2021.
[159] L. Stobbe (private communications).
[160] M. Singer (private communications).
[161] ROOT Team, *ROOT data analysis framework*, https://root.cern.ch/, accessed May 27, 2021.
[162] H. T. Johansson, The UCESB unpacker generator, 2010.
[163] B. Löher *et al.*, Nucl. Instrum. Methods Phys. Res. A **686**, 1 (2012).
[164] P. Adrich and I. Zychor, Nucl. Instrum. Methods Phys. Res. A **990**, 164962 (2021).
[165] R. E. Segel, Phys. Rev. **113**, 844 (1959).
[166] *SQLite*, https://sqlite.org/, accessed Nov 26, 2021.
[167] M. Spall (private communications).
[168] H. Theissen, *Springer tracts in modern physics. Ergebnisse der exakten Naturwissenschaften* (Springer, Berlin, Heidelberg, New York, 1972), Vol. 65.
[169] A. Schmidt, B.Sc. Thesis, Technische Universität Darmstadt, 2017.
[170] B. Krusche *et al.*, Nucl. Phys. A **386**, 245 (1982).
[171] E. Browne and J. K. Tuli, Nucl. Data Sheets **114**, 1849 (2013).
[172] L. C. Biedenharn and M. E. Rose, Rev. Mod. Phys. **25**, 729 (1953).
[173] V. Y. Ponomarev and A. Krasznahorkay, Nucl. Phys. A, 150 (1992).
[174] S. K. Basu, G. Mukherjee, and A. A. Sonzogni, Nucl. Data Sheets **111**, 2555 (2010).
[175] T. Wieczorek, B.Sc. Thesis, Technische Universität Darmstadt, 2020.
[176] A. Blazhev (private communications).
[177] U. Friman-Gayer, *New Upstream Target Room*, 2020, https://github.com/uga-uga/nutr.
[178] T. Klaus (private communications).
[179] C. Kremer, Thesis, Technische Universität Darmstadt, 2016.
[180] M. L. Cortés (private communications).
[181] V. O. Nesterenko, A. Repko, J. Kvasil, and P.-G. Reinhard, Phys. Rev. Lett. **120**, 182501 (2018).
[182] P. von Neumann-Cosel (private communications).

14. List of Figures

15. List of Tables

List of Publications

F. C. L. Crespi, A. Bracco, E. G. Lanza et al., Phys. Lett. B **816**, 136210 (2021)
M. Hilcker, J. Birkhan, A. D'Alessio et al., Nucl. Instr. Meth. **957**, 163418 (2020)
S. Bassauer, P. von Neumann-Cosel, P.-G. Reinhard et al., Phys. Lett. B **810**, 135804 (2020)
S. Bassauer, P. von Neumann-Cosel, P.-G. Reinhard et al., Phys. Rev. C **102**, 034327 (2020)
A. D'Alessio, T. Mongelli, M. Arnold et al., Phys. Rev. C **102**, 011302(R) (2020)
F. C. L. Crespi, A. Bracco, A. Tamii et al., JPCS 1014, 012002 (2018)
C. Kremer, S. Aslanidou, S. Bassauer et al., Phys. Rev. Lett. **117**, 172503 (2016)

Acknowledgement

I would like to take this opportunity to thank the people who have supported me over the past years.

First of all, I would like to thank **Prof. Dr. Dr. h.c. mult. Norbert Pietralla** for the opportunity to work in his group on this interesting and challenging topic. The discussions on the development of the setup were always purposeful and I look forward to further discussion during the analysis of the (e,e'γ) data. Furthermore, I would like to thank **Prof. Dr. Peter von Neumann-Cosel** for the helpful discussions and the participation in business trips to the Research Center for Nuclear Physics in Osaka, Japan. These trips were interesting to get to know the working methods in other institutes as well as a distant country.

Also, the collaboration with **Dr. Martha Liliana Cortés Sua**, **Dr. Johann Isaak**, **Dr. Maxim Singer**, and **Dr. Dmytro Symochko** was helpful for the progress of the project. I enjoyed working with the spectrometer group, which also actively helped in the preparation of the experiments. Therefore, in addition to the members of the spectrometer group already mentioned, I would like to thank **Dr. Jonny Birkhan**, **Isabelle Brandherm**, **Igor Jurosevic**, and **Maximilian Spall**, as well as former members **Dr. Michaela Hilcker**, **Dr. Sergej Bassauer**, **Dr. Antonio D'Alessio**, and **Dr. Andreas Krugmann**. I would also like to thank **Dr. Udo Friman-Gayer** for the pleasant collaboration and **Dr. Michael Mathy** for the fun joint work on vacuum systems.

A special thanks goes to the accelerator group, which has always worked hard to prepare the electron accelerator for the experiments. In particular, I would like to thank **Dr. Michaela Arnold** and **Dr. Lars Jürgensen** for their efforts. I would also like to thank the operations group and the mechanics workshop for their support in planning the setup, as well as the administration of the IKP for their organizational work.

For the support outside of the work, I want to thank my parents **Gerhild** and **Hartmut** and my siblings **Anna** and **Reinhard** for their support. A special thanks for the regular joint planning of the fun evenings of the GSPB organization goes to **Thomas Müller** and **Benno Schmid**.

Finally, I would like to thank all those who have not been mentioned by name, but who have contributed to this work through exciting discussions.